(In,Al)N-based blue microcavity lasers

THÈSE N^{O} 5675 (2013)

PRÉSENTÉE LE 17 MAI 2013

À LA FACULTÉ DES SCIENCES DE BASE
LABORATOIRE EN SEMICONDUCTEURS AVANCÉS POUR LA PHOTONIQUE ET L'ÉLECTRONIQUE
PROGRAMME DOCTORAL EN PHOTONIQUE

ÉCOLE POLYTECHNIQUE FÉDÉRALE DE LAUSANNE

POUR L'OBTENTION DU GRADE DE DOCTEUR ÈS SCIENCES

PAR

Gatien COSENDEY

acceptée sur proposition du jury:

Prof. C. Moser, président du jury
Prof. N. Grandjean, directeur de thèse
Dr A. Avramescu, rapporteur
Prof. E. Kapon, rapporteur
Prof. A. Larsson, rapporteur

ÉCOLE POLYTECHNIQUE
FÉDÉRALE DE LAUSANNE

Suisse
2013

One does not simply walk into Mordor.
Its black gates are guarded by more than
just orcs. There is evil there that does
not sleep. The great eye is ever watchful.
It is a barren wasteland, riddled with
fire, ash, and dust. The very air you
breathe is a poisonous fume. Not with ten
thousand men could you do this. It is folly.
— Boromir
(J. R. R. Tolkien, *The Fellowship of the Ring*)

A mes parents, qui m'ont toujours encouragé.
A Maël, Killian, Audran, mes compagnons de toujours.
A Muriel, ma meilleure moitié et future épouse.

Remerciements

Je tiens tout d'abord à exprimer ma profonde et sincère gratitude au Prof. Nicolas Grandjean, mon directeur de thèse, pour m'avoir offert la possibilité de vivre cette aventure formidablement enrichissante qu'est la poursuite d'une thèse. Il a toujours été disponible pour me fournir aide et conseils précieux, tout en me laissant libre de mener mes recherches à ma guise. Je lui sais gré de n'avoir jamais douté de moi, si ce n'est des V(E)CSELs eux-mêmes... Par ailleurs, ce fut un réel plaisir que de collaborer avec lui à l'enseignement de la physique générale pour les ingénieurs de première année.

Je souhaite ensuite remercier le Prof. Christophe Moser pour avoir présidé mon jury de thèse, ainsi que les rapporteurs qui ont accepté de lire et de juger le présent travail : le Prof. Anders Larsson, le Dr. Adrian Avramescu et le Prof. Elyahou Kapon.

Je voudrais remercier tous ceux qui ont contribué au succès de ce travail. Merci à Nino et Julien pour m'avoir formé à l'utilisation des salles blanches et aux techniques et procédés de microfabrication, merci à Jean-François pour son aide concernant la croissance épitaxiale, merci à Arnaud et Nino pour leurs conseils avisés concernant le développement des VCSELs, merci à Xi et Marlene pour leur collaboration sur les VECSELs. Merci à Jacques et Georg pour l'assistance qu'ils m'ont fournie concernant la spectroscopie et merci à Nils pour m'avoir appris à utiliser l'AFM, ainsi que pour m'avoir exposé la théorie concernant la barrière d'Ehrlich-Schwoebel. Je suis également redevable à Raphaël pour la relecture critique et les corrections des différents articles que j'ai rédigés, ainsi que du présent manuscrit. Les pages couvertes de stylo rouge qui en résultaient invariablement n'en étaient pas moins gage de qualité... Merci également aux étudiants dont j'ai supervisé le travail de master : Luca, Mikafil et Raphaël. Leur collaboration m'a été fort précieuse. Je remercie ceux grâce à qui le travail en salle blanche a toujours été un vrai plaisir, Nicolas, Damien, Yoan et Philippe. Merci à Roger pour son aide précieuse pour tout ce qui touche à la mécanique. Je suis redevable à tous ceux qui m'ont assisté lors de ma quête d'un TCO convenable : Sylvain et Mauro, Hanspeter et Sylvia d'Evatec. Merci enfin à Åsa pour les discussions enrichissantes sur les VCSELs.

Si cette thèse fut une expérience formidable, c'est aussi (surtout?...) grâce à mes collègues et amis Jacques, Pierre et Georg. Les gallères épisodiques ponctuant notre travail d'assistanat furent plus aisément surmontées à deux... L'ex future start-up GanOptix fut également une expérience d'anthologie.

Merci à tous les membres du LASPE, qui contribuent tous à rendre l'atmosphère non seulement agréable mais également stimulante : Jacques, Georg, Nils, Nicolas, Raphaël, Marlene, Marco M., Lorenzo, Christian, Guillaume, Marcel, Noelia, Luca, Jean-Michel, Alexei, Nino, Etienne, Lise, Eric, Julien, Marco R., Jean-François et Aline, ainsi qu'à tous les anciens : Yoshi, Arnaud, Jérôme, Amélie, Gab, Dobri, Sylvain, Marcus, Tiankai et Rémy.

Last but not least, je remercie ma famille, tout particluièrement mes parents, Bernard et Dinah, pour leur soutien sans faille et leur confiance inconditionnelle, et mes frères Maël, Killian et Audran, sur qui j'ai toujours pu compter. Et finalement, un immense merci à celle qui partage mes joies et mes peines depuis bientôt dix ans, et qui a accepté de continuer pour encore de nombreuses années, ma fiancée Muriel. Elle a toujours su trouver les mots pour me rassurer lors des périodes de doutes, et m'a (sup)porté pendant ces presque cinq années de travail de thèse.

Lausanne, janvier 2013 G. C.

Abstract

Over the past decade, III-nitride semiconductors have proven to be of the highest interest for optoelectronic applications in the short-wavelength range. White, blue and green light emitting diodes as well as violet and blue laser diodes are nowadays used in mass consumer products such as domestic solid-state lighting sources or outdoor displays. More sophisticated devices like electrically-driven vertical-cavity surface-emitting lasers (VCSELs) and optically-pumped vertical external cavity surface-emitting lasers (VECSELs), which are both microcavity-based lasers, have also been recently demonstrated. VCSELs are well-known to offer several advantages compared to conventional edge-emitting lasers, e.g. single longitudinal mode, low operating current and power consumption, circular emission beam, high-speed modulation ability, and the possibility to easily process them into 2D arrays. Additionally, the VECSEL external cavity enables the insertion of intracavity elements such as saturable absorbers or absorption cells, which opens the way for compact atomic clocks or absorption spectroscopy devices.

Nevertheless, blue VCSELs still suffer from many issues, like challenging current injection schemes and a lack of suitable distributed Bragg reflector (DBR) system. We face either defective AlGaN/GaN DBRs or implement a bottom dielectric DBR that requires challenging processing steps. In this context, the use of a bottom lattice-matched InAlN/GaN DBR grown on a free-standing (FS) GaN substrate would allow improving both the device lifetime and thermal management while keeping the process flow simple. Such DBRs would also greatly benefit to VECSEL devices, enabling the overgrowth of a high crystalline quality active region and an efficient thermal management.

The goal of the present work was the realization of such blue microcavity-based lasers, by making use of high-quality highly-reflective InAlN-based DBRs. Consequently, the first step consists in the study and optimization of the key elements constituting microcavity-based laser devices. Thus, the growth mechanisms of InAlN layers are addressed. Such layers are shown to be subject to kinetic roughening, which yields a huge degradation of the crystalline quality of InAlN layers exceeding a critical thickness. The InAlN growth conditions are then optimized in order to minimize this effect. Subsequently, the optimized growth parameters are used for the realization of high-quality highly-reflective InAlN-based DBRs grown on FS GaN substrates, exhibiting a reflectivity value exceeding 99.5%, and several parameters impacting on the quality of such structures are discussed. The second key element required for the

realization of electrically-driven VCSELs, namely transparent conductive oxide(TCO)-based contacts to *p*-type GaN, is then considered. The plasma used in several TCO deposition techniques is shown to have a strong negative impact on the electrical properties of such contacts. Thus, different TCOs and deposition techniques are compared, and the effect of a thin metallic interlayer in-between the *p*-type GaN layer and the TCO contact is discussed. Low-resistance indium tin oxide-based transparent contacts to *p*-type GaN layers, suited for VCSEL applications, are eventually described.

In the last part of this PhD dissertation, the realization of microcavity-based devices is addressed, making use of the optimized building blocks. The epitaxial structure and process flow of our VCSELs are presented. Lasing is demonstrated in electrically-driven VCSELs at room temperature under pulsed injection. The characteristics of such devices are detailed, and several improvements that should allow achieving CW lasing are addressed. The development of the active region of VECSELs is then described, and two different designs are compared in terms of sample surface morphology and photoluminescence intensity. The best one is subsequently integrated in our VECSELs devices, which are characterized under optical pumping in VCSEL configuration in order to validate our approach. The VECSEL samples are then mounted in external cavity configuration, and lasing under optical pumping is demonstrated with an external cavity length up to 50 mm, enabling the insertion of intra-cavity elements. This opens the way for the realization of compact III-nitride based atomic clocks.

Keywords: III-nitrides, gallium nitride, vertical-cavity surface-emitting laser, vertical external cavity surface-emitting laser, indium aluminum nitride, indium tin oxide, microcavity, laser diode, light-emitting devices, distributed Bragg reflector.

Résumé

Au cours de la dernière décennie, les semiconducteurs à base de nitrures d'éléments III ont prouvé leur intérêt pour la réalisation de dispositifs optoélectroniques émettant dans la gamme des courtes longueurs d'onde. Les diodes électroluminescentes blanches, bleues et vertes, ainsi que les diodes lasers violettes et bleues sont aujourd'hui utilisées dans de nombreux produits de consommation de masse, tels que l'éclairage domestique, les écrans de télévision ou les panneaux d'affichage lumineux. Des dispositifs plus sophistiqués comme les lasers à cavité verticale à émission par la surface (VCSELs) injectés électriquement et les laser à cavité verticale externe à émission par la surface (VECSELs) pompés optiquement, tous deux étant des lasers à microcavité, ont également été réalisés récemment. Les VCSELs présentent certains avantages reconnus face aux lasers à émission par la tranche conventionnels, comme une émission monomode longitudinale, un faible courant de fonctionnement, une faible consommation électrique, l'émission d'un faisceau circulaire, la possibilité d'être modulé à haute fréquence et d'effectuer la microfabrication de matrices bidimensionnelles de dispositifs. De plus, la cavité externe des VECSELs permet l'insertion d'éléments intracavités comme des absorbants saturables ou des cellules d'absorption, ce qui ouvre la voie à la réalisation d'horloges atomiques compactes et de dispositifs pour spectrométrie d'absorption.

Néanmoins, les VCSELs bleus souffrent de plusieurs problèmes, comme une injection électrique délicate et un manque de miroirs de Bragg adaptés. En effet, nous devons faire face soit à des miroirs de Bragg utilisant des bicouches AlGaN/GaN défectueues, soit il faut utiliser un miroir de Bragg inférieur à base de diélectriques, ce qui complique la microfabrication. Dans ce contexte, l'utilisation d'un miroir de Bragg inférieur utilisant des paires InAlN/GaN en accord de maille crûs sur des substrats de GaN permettrait d'améliorer sensiblement la durée de vie ainsi que la dissipation thermique tout en gardant le procédé de microfabrication aisé. De tels miroirs de Bragg seraient également d'une grande utilité pour les VECSELs en permettant la croissance d'une zone active de grande qualité cristalline et une dissipation thermique efficace.

Le but de ce travail est la réalisation de tels lasers bleus à microcavité, en utilisant des miroirs de Bragg hautement réfléchissant et de grande qualité à base d'InAlN. En conséquence, la première étape consiste en l'étude et l'optimisation des éléments clés constituant les dispositifs lasers à microcavité. C'est pourquoi les mécanismes de croissance des couches d'InAlN sont abordés. De telles couches sont sujettes au phénomène de rugosité cinétique, ce qui conduit

à une importante dégradation de la qualité cristalline des couches d'InAlN dépassant une épaisseur critique. Les conditions de croissance des couches d'InAlN sont par conséquent optimisées afin de minimiser cet effet. Par la suite, ces conditions de croissance optimisées sont utilisées afin de réaliser des miroirs de Bragg hautement réfléchissant et de grande qualité composés de bicouches d'InAlN/GaN et crûs sur des substrats de GaN, dont la réflectivité excède 99,5%, et plusieurs paramètres influançant la qualité de telles structures sont discutés. Le second élément clé requis pour la réalisation de VCSELs injectés électriquement, c'est-à-dire les contacts de type *p* à base d'oxydes transparents conducteurs (OTCs), est ensuite considéré. Les plasmas utilisés par de nombreuses techniques de déposition d'OTCs ont un impact négatif important sur les propriétés électriques de tels contacts. C'est pourquoi différents OTCs ainsi que différentes techniques de déposition sont comparés, et les effets de la déposition d'une fine couche métallique entre la couche de GaN de type *p* et et le contact d'OCT sont discutés. Finalement, des contacts au GaN de type *p* à base d'oxyde d'indium-étain ayant une faible résistance, adaptés pour des applications VCSELs, sont décrits.

Dans la dernière partie de ce travail de thèse, la réalisation de dispositifs à microcavité est abordée en utilisant les éléments clé précédemment optimisés. La structure épitaxiale ainsi que le processus de fabrication de nos VCSELs sont présentés. Le lasage de nos VCSELs est démontré sous injection électrique pulsée à température ambiante. Les caractéristiques de ces dispositifs sont détaillées, et plusieurs améliorations devant permettre à ces dispositifs de laser sous injection électrique continue sont abordées. Le développement de la zone active des VECSELs est ensuite décrite, dont deux géométries différentes sont comparées en terme de morphologie de surface et d'intensité de photoluminescence. La meilleure des deux géométries est ensuite intégrée dans nos dispositifs VECSEL, qui sont caractérisés sous pompage optique en configuration VCSEL afin de valider notre approche. Les échantillons VECSELs sont ensuite montés en configuration cavité externe, et le lasage sous pompage optique est démontré pour des cavités externes dont la longueur atteint 50 mm, ce qui permet l'insertion d'éléments intracavités. Ceci ouvre la voie à la réalisation d'horloges atomiques compactes à base de nitrures d'éléments III.

Mots-clé : Nitrures d'éléments III, nitrure de gallium, laser à cavité verticale à émission par la surface, laser à cavité verticale externe à émission par la surface, nitrure d'indium-aluminium, oxyde d'indium-étain, microcavité, diode laser, dispositifs émetteurs de lumière, miroir de Bragg.

Contents

Remerciements iii

Abstract v

Résumé vii

Table of contents ix

Introduction 1

Overview of III-nitride based optoelectronic devices . . . 1
On the interest of microcavity lasers . . . 2
Thesis objectives . . . 2
Outline of this PhD dissertation . . . 3

1 III-nitride compound properties **5**

1.1 Structural properties . . . 5
1.1.1 Crystalline structure and mechanical properties . . . 5
1.1.2 Polarization . . . 9
1.2 Growth . . . 10
1.3 Optical properties . . . 13
1.3.1 Bandgap . . . 13
1.3.2 Refractive index . . . 14
1.3.3 Quantum confined Stark effect . . . 15
1.4 Electrical properties . . . 17
1.4.1 *n*-type doping . . . 18
1.4.2 *p*-type doping . . . 18

2 Microcavity lasers **21**

2.1 Semiconductor laser diodes . . . 21
2.2 Planar microcavities . . . 26
2.2.1 Distributed Bragg reflectors . . . 27
2.2.2 The transfer matrix method . . . 29
2.2.3 Optical field distribution and related features . . . 33
2.3 The VCSEL . . . 34
2.3.1 Standard III-V VCSELs . . . 35

2.3.2 III-nitride based VCSEL specificities 36
2.3.3 Nitride-based VCSEL diodes: state-of-the-art 36
2.3.4 Our approach 37
2.4 The VECSEL 37
2.4.1 Standard III-V VECSELs 38
2.4.2 Nitride-based VECSELs: state-of-the-art 38
2.4.3 Nitride-based VECSELs for atomic clocks (the RbGaN project) 38

3 InAlN-based distributed Bragg reflectors 41
3.1 On the interest of InAlN for Bragg mirrors 41
3.2 Optical properties of InAlN 43
3.3 Growth and structural properties of InAlN layers 44
3.3.1 Growth parameters 45
3.3.2 The lattice-matched condition to GaN 47
3.3.3 Structural properties, defects, and critical thickness 47
3.4 Distributed Bragg reflectors 51
3.4.1 DBRs grown on sapphire substrates 53
3.4.2 DBRs grown on free-standing GaN substrates 54
3.4.3 UV DBRs for cavity polariton study and UV VCSELs 62
3.5 Further improvements 64

4 Transparent conductive oxides as *p*-type contacts 65
4.1 Metal-semiconductor contacts 65
4.1.1 Band alignment 66
4.1.2 Transport processes 69
4.2 Transparent conductive oxide properties 70
4.3 TCO contacts to *p*-type GaN 72
4.3.1 Plasma damage effects on *p*-type GaN 73
4.3.2 The quest for the right material/deposition method 73
4.3.3 Inserting a metallic interlayer 79
4.3.4 Optimized sputtered ITO contacts to *p*-type GaN from Evatec 80

5 Vertical-cavity surface-emitting lasers 83
5.1 Building blocks 83
5.2 Dielectric DBRs 85
5.3 Current confinement scheme 88
5.3.1 InAlN lateral oxidation 88
5.3.2 TCO and dielectric current confinement layer 89
5.3.3 TCO and plasma-based surface passivation 90
5.3.4 Buried current confinement layer 91
5.4 Final VCSEL design 91
5.4.1 Process flow 93
5.5 Results 95

5.6 Outlook 106

6 Vertical external cavity surface-emitting lasers **107**

6.1 Active region design 107

6.1.1 Thick InGaN barriers 108

6.1.2 Multiple quantum well approach 112

6.2 Results 114

6.2.1 Operation as a VCSEL 114

6.2.2 Operation in an extended external cavity configuration 116

6.3 Outlook 118

Conclusion **121**

Summary 121

Outlook and perspectives 123

Bibliography **125**

Curriculum Vitae **149**

Introduction

Thanks to their direct bandgap and the broad range of wavelengths that can be covered using their ternary alloys, III-nitride semiconductors are of high interest for optoelectronic applications. In this introduction chapter, a brief overview of nitride-based optoelectronic devices is first presented. The interest of microcavity lasers is then discussed. Finally, the outline of this PhD dissertation is detailed.

Overview of III-nitride based optoelectronic devices

For a long time, the main drawback towards the realization of GaN-based optoelectronic devices was the achievement of efficient *p*-type doping, which has been eventually reported by Amano *et al.* in 1989 [1]. In 1991, Nakamura and coworkers used a GaN buffer in order to improve the *p*-type GaN crystalline quality [2], enabling the demonstration of high power GaN-based light emitting diodes (LEDs) [3] followed three years later by candela-class blue LEDs [4]. The first blue laser diode (LD) was then reported in 1996 by Nakamura *et al.* [5]. Nowadays, both GaN-based LEDs and LDs are widely introduced in mass consumption applications like domestic solid-state lighting, high density optical data storage systems or displays [6]. Lately, more advanced nitride-based optoelectronic devices have been demonstrated, such as superluminescent light emitting diodes (SLEDs) [7, 8, 9], which are devices based on amplified spontaneous emission exhibiting properties in between those of LEDs and LDs, namely a large spatial coherence (highly directional light beam) and a small temporal coherence (broad emission spectrum), and vertical-cavity surface-emitting lasers (VCSELs) [10, 11], which benefit from several advantages when compared to standard edge-emitting LDs that will be summarized hereafter. Schematic drawings of these devices are depicted in Fig. 1.

Other advanced III-nitride based optoelectronic devices have also been reported recently, such as photonic crystal surface-emitting laser diodes [12, 13]. Besides, our laboratory is currently spending great efforts on the realization of polariton LDs [14, 15]. Finally, a few optically pumped devices are worth mentioning: vertical external cavity surface-emitting lasers (VECSELs) [16] and polariton lasers [17].

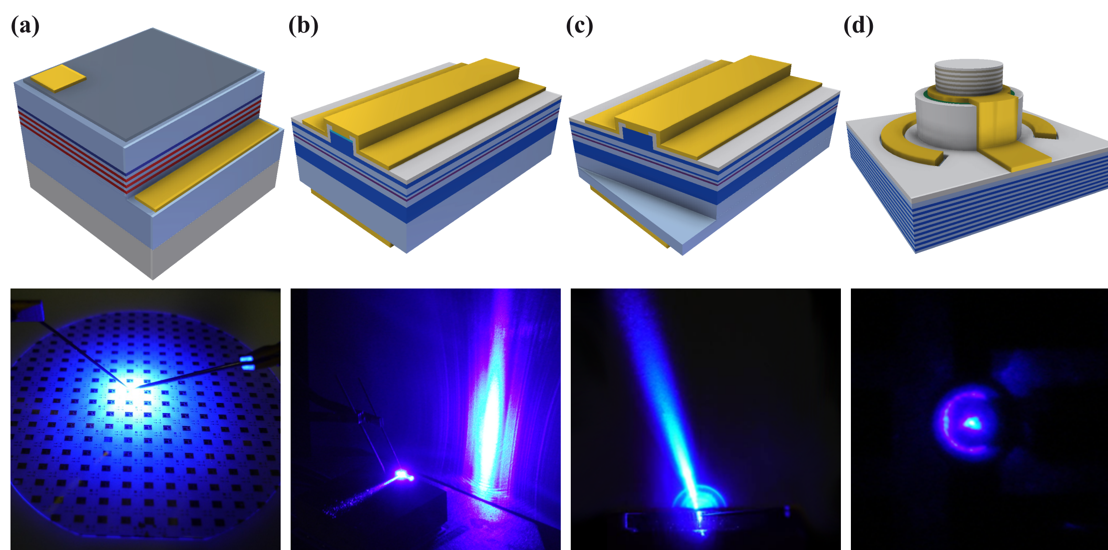

Figure 1: Schematic drawings and photographs of (a) an LED, (b) an LD, (c) an SLED, (e) a VCSEL.

On the interest of microcavity lasers

As conventional semiconductor lasers, microcavity lasers are compact sources of coherent light, which can efficiently convert electricity into light. Indeed, the wall-plug efficiency of semiconductor-based LDs is of the order of 50%, whereas that of gas-based laser only amounts to 1%. In addition, microcavity lasers exhibit many specific features: surface emission that permits on-wafer testing and the realization of 2D arrays of devices, a small active volume yielding a low threshold and enabling high-speed modulation and a circular emitted beam with a low divergence angle allowing an efficient coupling to optical fibers. Moreover, the short cavity length of VCSELs leads to single longitudinal mode emission, and intracavity elements such as saturable absorbers for mode locking can be introduced into VECSELs. Standard III-V microcavity lasers have proven or could be useful in many applications, such as optical communications (e.g. Ethernet protocol), optical mice, printers, displays and projectors, or gas and biomedical sensing. Properties and applications of VCSELs and VECSELs will be described in further details in chapter 2.

Thesis objectives

The objectives of this thesis deal with the development of III-nitride based microcavity lasers, in particular VCSELs and VECSELs. The work on the former focused on the development of highly reflective DBRs, made either of InAlN/GaN (for the bottom one) or dielectric bilayers (for the upper mirror), on the improvement of the electrical properties of transparent conductive oxide (TCO)-based hole spreading layers, and in the design of an efficient VCSEL structure and process flow, in order to achieve lasing in electrically-driven VCSEL diodes at room

temperature (RT). The aim of the work on VECSELs was the development of an optically pumped device including a long external cavity suited for the insertion of intracavity elements such as a saturable absorber, using the knowledge acquired on highly-reflective distributed Bragg reflectors (DBRs). It involved the optimization of the active region and the growth conditions of the whole cavity in order to ensure high quality samples compatible with these objectives.

Outline of this PhD dissertation

The aim of this PhD dissertation is the description of the development and realization of two types of blue nitride-based surface-emitting lasers, namely electrically-driven VCSELs and optically pumped VECSELs.

A brief overview of the main structural, optical and electrical properties of the wurtzite III-nitride material system is reviewed in chapter 1. In particular, the effects arising from the lattice-parameter mismatch as well as the total polarization mismatch between the different binary alloys are addressed. The impact of this polarization mismatch is discussed in terms of radiative efficiency. Finally, the impact of plasma damage on *p*-type GaN is presented, as it proved to be a key element in the realization of our VCSELs, for both the TCO deposition and current confinement.

The basics of LDs and semiconductor-based planar microcavities are summarized in chapter 2. VCSEL and VECSEL features are presented, as well as an overview of standard III-V (arsenide-, phosphide- and antimonide-based) devices and their commercial applications. Finally, the specificities of such devices made from III-nitride materials are given and the current state-of-the-art is reviewed.

The large in-plane lattice constant mismatch between the different III-nitride binary compounds makes the realization of high-quality highly-reflective DBRs challenging. In this context, InAlN is a material of choice to realize such structures, thanks to its ability to be grown lattice-matched to GaN. Consequently, InAlN-based DBRs, which represent a key building block for the realization of both VCSELs and VECSELs, are discussed in chapter 3. A particular attention has been brought to the growth and structural properties of InAlN layers. The thick InAlN layer quality degradation mechanism is explained in terms of kinetic roughening. The realization of highly-reflective InAlN-based DBRs grown on sapphire and free-standing (FS) GaN substrates is described, and the impact of several parameters affecting the overall quality of the DBRs is considered.

Highly transparent intra-cavity current spreading layers are a requirement for the realization of III-nitride based VCSELs, because of the low conductivity of *p*-type doped GaN. As TCOs exhibit both an efficient electrical conduction and a low absorption in the blue-violet range, they are candidates of choice for the realization of such current spreading layers. However, because of the large work function difference between TCOs and *p*-type GaN and the high

sensitivity of the latter to any plasma damage, obtaining low resistivity TCO-based contacts to *p*-type GaN is challenging. The development of such contacts is presented in chapter 4. First, the basics about metal-semiconductor contacts and TCO properties are recalled in order to better understand the issues related to the formation of such contacts. Then, several TCO materials and deposition techniques are investigated. Finally, high-quality ITO contacts to *p*-type GaN exhibiting a low contact resistance and enabling efficient VCSEL intracavity electrical injection are described.

The careful study and development of InAlN-based DBRs and TCO-based contacts to *p*-type GaN enables the realization of complete VCSEL diodes. Such devices are presented in chapter 5. First, the building blocks are summarized and dielectric DBRs and their deposition technique are detailed. Then, the most promising current confinement schemes are described. Our final VCSEL design is given, and the process flows are presented. Finally, the electrical and optical characteristics of our electrically-driven VCSELs are detailed, their current limitations are addressed and an outlook for further improvements is discussed.

The 6th and last chapter deals with the development of VECSEL devices. First, two different active region designs are studied and developed. Then, the characteristics of both types of device are compared. The most efficient one is first used in a VCSEL configuration in order to validate the approach. Eventually, the sample is mounted in a VECSEL configuration with an external cavity length up to 50 mm and results are presented.

Finally, the main experimental results are briefly summarized and an outlook on possible future work is proposed, including further improvements of the structures/devices presented in this PhD dissertation, but also perspectives on other photonic devices.

1 III-nitride compound properties

In this first chapter, the structural, optical, and electrical properties of the group III-nitride materials system are reviewed. In particular, the different binary compound lattice parameters are given and resulting strain issues are addressed. Polarization-related features are discussed and growth properties as well as available substrates are presented. Bandgap values and refractive index are detailed. Finally, the *n*- and *p*-type doping of GaN layers is considered.

1.1 Structural properties

In this first section, we present the structural properties of III-nitride compounds.

1.1.1 Crystalline structure and mechanical properties

III-nitride compounds can be found in either hexagonal (wurtzite) or cubic (zincblende) crystalline configuration. However, only the first one forms a stable phase, whereas the latter is metastable and can be obtained only under particular conditions [21, 22]. The wurtzite phase of GaN is actually made of two imbricated hexagonal close packed structures, one for the anions (the nitrogen atoms) and one for the cations (the metal atoms), which means that

Table 1.1: Lattice parameters, thermal expansion coefficients and densities of III-nitride binary compounds.

	GaN	AlN	InN
In-plane lattice constant a (Å) at 300 K [18]	3.189	3.112	3.545
Thermal expansion $d\ln a/dT$ (10^{-6}/K) [19]	5.6	4.2	3.8
Lattice constant c (Å) at 300 K [18]	5.185	4.982	5.703
Thermal expansion $d\ln c/dT$ (10^{-6}/K) [19]	3.2	5.3	2.9
Internal parameter u [20]	0.376	0.380	0.377
Density (g/cm^3) [19]	6.15	3.23	6.81

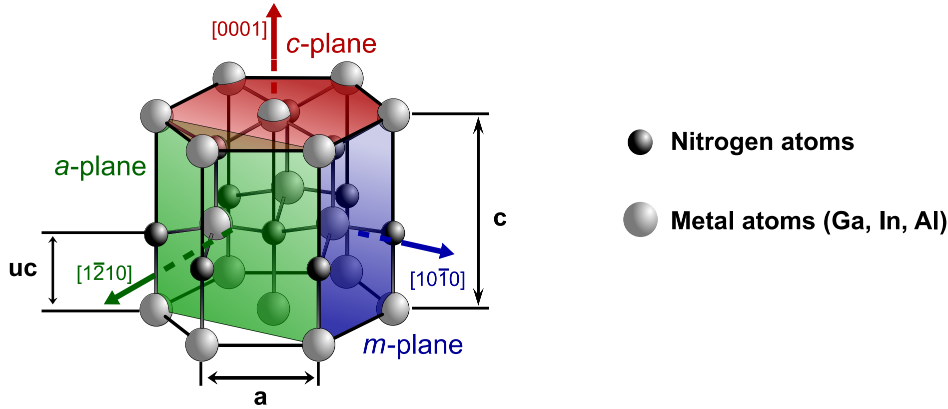

Figure 1.1: Wurtzite structure of III-nitride compounds. The polar *c*-plane and non polar *m*- and *a*-planes are depicted. Courtesy of G. Rossbach.

such crystals are anisotropic. A schematic drawing of III-nitride crystals is shown in Fig. 1.1, where the main polar and non polar planes are depicted. The present work focuses only on wurtzite material grown along the *c*-axis, which means that the lattice-matching condition for heterostructures implies identical a lattice parameters for the different materials. The internal parameter u gives the relative distance between nitrogen and metallic atoms along [0001]. The lattice constants a and c, and the internal parameter u for the different III-nitride binary compounds are given in Table 1.1, as well as the corresponding thermal expansion coefficients and their densities. The lattice parameter p ($p = a$ or c) for a ternary alloy $M_{1,x}M_{2,1-x}N$, where M_1 and M_2 are two different metal species amongst Al, In and Ga, can be deduced from the lattice parameters of the binary compounds using Vegard's law:

$$p(M_{1,x}M_{2,1-x}N) = x \cdot p(M_1N) + (1-x) \cdot p(M_2N) \, . \tag{1.1}$$

Because of the large lattice parameter mismatch existing between the different III-nitride alloys as well as the use of foreign materials substrates, a large strain builds up in heterostructures. On the one hand, this strain strongly impacts on the optical properties of the epitaxial structure. On the other hand, it results in important stress forces that eventually lead to the formation of cracks and/or dislocations, which strongly impair the performances of optoelectronic devices [23, 24, 25]. The stress field $\boldsymbol{\sigma}$ is proportional to the strain field $\boldsymbol{\varepsilon}$ in the linear elastic theory limit according to Hooke's law, which writes:

$$\boldsymbol{\sigma} = \hat{\mathrm{C}} \cdot \boldsymbol{\varepsilon} \tag{1.2}$$

Table 1.2: Elastic coefficients of wurtzite III-nitride binary materials [18].

C_{ij} (GPa)	GaN	AlN	InN
C_{11}	390	396	223
C_{12}	145	137	115
C_{13}	106	108	92
C_{33}	398	373	224
C_{44}	105	116	48

where $\hat{\mathbf{C}}$ is the elastic coefficient tensor that can be expressed, in the case of a hexagonal symmetry (wurtzite) crystal as:

$$\hat{\mathbf{C}} = \begin{pmatrix} C_{11} & C_{12} & C_{13} & 0 & 0 & 0 \\ C_{12} & C_{11} & C_{13} & 0 & 0 & 0 \\ C_{13} & C_{13} & C_{33} & 0 & 0 & 0 \\ 0 & 0 & 0 & C_{44} & 0 & 0 \\ 0 & 0 & 0 & 0 & C_{44} & 0 \\ 0 & 0 & 0 & 0 & 0 & \frac{1}{2}(C_{11}-C_{12}) \end{pmatrix}. \tag{1.3}$$

The elastic coefficients C_{ij} for the different binary compounds are given in Table 1.2. The values for ternary alloys can be obtained using Vegard's law (Eq. 1.1).

In the case of an epitaxial layer pseudomorphically grown along the c-axis, the in-plane strain resulting from a lattice mismatch between this layer and the underlying structure is given by:

$$\varepsilon_{xx} = \varepsilon_{yy} = \frac{a - a_0}{a_0} \tag{1.4}$$

where a_0 and a are the in-plane lattice constants of the relaxed material and strained layer, respectively. As no force is applied to the sample top surface, which is consequently stress free, the stress along the growth direction is null, which writes $\sigma_{zz} = 0$. This implies that the in-plane ε_{xx} and vertical ε_{zz} strains are linked according to:

$$\varepsilon_{zz} \equiv \frac{c - c_0}{c_0} = -\frac{C_{13}}{C_{33}}\varepsilon_{xx} \tag{1.5}$$

where c_0 and c are the lattice constants along the c-axis of the relaxed material and strained

layer, respectively. Thus, in the case of biaxial stress Hooke's law becomes:

$$\begin{pmatrix} \sigma_{xx} \\ \sigma_{xx} \\ 0 \end{pmatrix} = \begin{pmatrix} C_{11} & C_{12} & C_{13} \\ C_{12} & C_{11} & C_{13} \\ C_{13} & C_{13} & C_{33} \end{pmatrix} \begin{pmatrix} \varepsilon_{xx} \\ \varepsilon_{xx} \\ \varepsilon_{zz} \end{pmatrix}. \tag{1.6}$$

As a result, the in-plane stress σ_{xx} as a function of the in-plane strain ε_{xx} is simply expressed as:

$$\sigma_{xx} = \left(C_{11} + C_{12} - \frac{2C_{13}^2}{C_{33}} \right) \varepsilon_{xx}\,. \tag{1.7}$$

This in-plane stress can eventually result in the formation of misfit dislocations through plastic relaxation when the epitaxial layer thickness exceeds a critical value and the strain can no longer be elastically accommodated [26]. Holec and coworkers proposed a model comparing the energy E_d of a misfit dislocation when added to the system with the work W relieved by the misfit stress field during the introduction of the dislocation [27, 28]. The latter can be expressed as, per unit length of the dislocation:

$$W = \frac{(C_{11} + C_{12})C_{23} - 2C_{13}^2}{C_{33}} \varepsilon_{xx} b_{e,\parallel} h \tag{1.8}$$

where h is the layer thickness and $b_{e,\parallel}$ is the edge component of the dislocation Burgers vector in the layer-substrate interface plane. The energy of the dislocation $E_d = E_{elastic} + E_{core}$ is given by the sum of the elastic energy outside the dislocation core $E_{elastic}$, described by the inner and outer cutoff radius r_c and R, respectively, and the dislocation core energy E_{core}. Within an hexagonal approximation, $E_{elastic}$ writes:

$$E_{elastic} = A \cdot \ln \frac{R}{r_c} \tag{1.9}$$

where A is a numerical constant related to the elastic properties. Consequently, when W eventually exceeds E_d, it is energetically favorable for the system to plastically relax the strain through misfit dislocations. The different parameters for III-nitride binary compounds are given in Table 1.3, and the parameters for ternary alloys can be obtained through Vegard's law.

Table 1.3: Parameters involved in the estimation of the critical layer thickness for heterostructures under biaxial strain [28].

Material	Dislocation	r_c (nm)	E_{core} (eV/Å)	A (eV/Å)
GaN	$(a+c)$-type	0.72	3.12	2.12
GaN	a-type	0.60	1.61	0.81
AlN	a-type	0.83	1.71	0.90
InN	a-type	0.54	1.66	0.41

1.1.2 Polarization

As previously stated, the wurtzite structure of III-nitride compounds is made of two imbricated hexagonal close packed structures, one for the anions and one for the cations. This results in a shift between the barycenters of positive and negative charges. In addition the nitrogen-metal bonds exhibit a strong polarity, yielding a huge spontaneous polarization $\mathbf{P}_{sp}$ oriented along $[000\bar{1}]$. Thus, the c-plane is referred to as the polar plane. In addition to this spontaneous polarization, applying a biaxial strain in the c-plane to any wurtzite III-nitride materials leads to a displacement of the atoms along [0001] (Eq. 1.5), which generates a *direct* piezoelectric polarization $\mathbf{P}_{pz}$ that adds up to the spontaneous one, resulting in a macroscopic polarization field $\mathbf{P} = \mathbf{P}_{sp} + \mathbf{P}_{pz}$. In the general case, the piezoelectric polarization field is given by:

$$\mathbf{P}_{pz} = \hat{\mathbf{e}} \cdot \boldsymbol{\sigma} \tag{1.10}$$

where $\hat{\mathbf{e}}$ is the piezoelectric tensor and $\boldsymbol{\sigma}$ is the stress-field resulting from a deformation according to Eq. 1.2. In the specific case of biaxial strain, the piezoelectric polarization has a single component along the c-axis, which writes:

$$P_{pz} = \left(2e_{31} + 2\frac{C_{13}e_{33}}{C_{33}}\right)\varepsilon_{xx}\,. \tag{1.11}$$

The spontaneous polarization values and piezoelectric coefficients e_{ij} for the different III-nitride binary compounds are listed in Table 1.4. The total polarization field $\mathbf{P}$ in a single layer will thus depend on the layer material and the layer strain state, and is usually different within two contiguous layers i and j. Therefore, the polarization discontinuity at the interface creates a charge plane, which charge density is given by:

$$\sigma_{ij} = -\left(\mathbf{P}_j - \mathbf{P}_i\right) \cdot \mathbf{n}_{ij} \tag{1.12}$$

Table 1.4: Spontaneous polarization $\|\mathbf{P}_{sp}\|$ and piezoelectric coefficient e_{ij} of III-nitride binary materials.

	GaN	AlN	InN
$\|\mathbf{P}_{sp}\|$ (C/m^2) [30]	0.034	0.090	0.042
e_{31} (C/m^2) [30]	-0.37	-0.62	-0.45
e_{33} (C/m^2) [30]	0.67	1.50	0.81

where $\mathbf{n}_{ij}$ is the unitary surface vector pointing from layer i to layer j. The accumulated charges can be either positive, e.g. in the case of an AlN layer deposited on GaN, or negative, e.g. in the reverse case of a GaN layer deposited on AlN. Considering an infinite interface between those two layers, this charge plane yields an electric field $\mathbf{F}_{i(j)}$ in layer $i(j)$, respectively, which are expressed as:

$$\mathbf{F}_i = -\frac{\sigma_{ij}}{2\epsilon_0\epsilon_i}\mathbf{n}_{ij} \tag{1.13}$$

$$\mathbf{F}_j = \frac{\sigma_{ij}}{2\epsilon_0\epsilon_j}\mathbf{n}_{ij} \tag{1.14}$$

where ϵ_0 is the vacuum permittivity and $\epsilon_{i(j)}$ is the relative permittivity of material $i(j)$, respectively. However, in a bulk material (thick layer), this field is screened by free carriers. It is only in thin double heterostructures such as quantum wells (QWs) that a large electric field appears. For instance, the electric field in typical GaN/Al$_x$Ga$_{1-x}$N QWs with $0.1 < x < 0.2$ amounts to $1-2$ MV/cm [29]. This large electric field leads to the so-called quantum confined Stark effect (QCSE), which will be described in a forthcoming section. More details about polarization effects can be found for instance in Ref. [29].

1.2 Growth

The three most commonly used techniques for the epitaxy of III-nitride materials are hydride vapor phase epitaxy (HVPE), molecular beam epitaxy (MBE) and metal-organic vapor phase epitaxy (MOVPE). HVPE allows growing thick high quality layers with a high growth rate, which can exceed 500 μm/h, and thus usually serves to produce thick buffers with low dislocation densities [31]. It is also used for the production of epitaxial lateral overgrown free-standing (FS) GaN substrates, which is a technique allowing decreasing the threading dislocation density (TDD) of GaN buffers grown on sapphire [32] or GaAs [33] substrates. MBE is a growth technique performed under ultra high vacuum conditions, with an operating pressure typically of the order of 10^{-8} Pa, which presents a relatively low growth rate, usually not exceeding 1 μm/h. Thanks to the ability to monitor the growth with a submonolayer (ML) precision using reflection high energy electron diffraction, this is a technique of choice for

Table 1.5: Precursors for group-III metals, nitrogen and dopants used at LASPE for the MOVPE growth of III-nitride compounds.

Element	Precursor	Acronym or chemical formula	Phase
Ga	Trimethyl-gallium	TMGa	liquid
Ga	Triethyl-gallium	TEGa	liquid
In	Trimethyl-indium	TMIn	solid
Al	Trimethyl-aluminum	TMAl	liquid
Si	Silane	SiH_4	gaseous
Mg	Bis(Cyclopentadienyl)-magnesium	Cp_2Mg	liquid or solid
N	Ammonia	NH_3	gaseous

research applications, in particular concerning nanostructures. In addition, the lower growth temperatures when compared to the two alternative growth techniques is of high interest for the growth of indium rich InGaN alloys and subsequent overgrown *p*-type layers [34], which could be beneficial for the realization of green LDs [35]. However, so far the dominant technique for III-nitride optoelectronic applications is MOVPE, which offers a much better reproducibility and is well-suited for large scale production, enabling growth on wafers with diameters up to 12".

All samples studied in the present dissertation have been grown using this technique, in a 200/4 RF-S low pressure MOVPE reactor from Aixtron. This technique allows performing growth close to the thermodynamical equilibrium between the heated substrate and the precursor vapor phase. The typical growth temperature of GaN layers is about 1000°C, enabling a large adatom diffusion length. The different metal-organic precursors for the group-III metals as well as precursors for the dopants and nitrogen are listed in Table 1.5. Ammonia and silane are directly injected to the gas mixing system from pressurized bottles, whereas the metal-organic compounds are delivered using a carrier gas that passes through temperature controlled bubblers containing the group-III metal sources. This carrier gas can be either H_2 and/or N_2. Actually, H_2 should not be used as carrier gas for growing indium containing alloys, as it has been reported to reduce indium incorporation in both InGaN [36] and InAlN [37]. The layer growth rate r is controlled using an *in situ* reflectivity measurement monitoring system, which consists of a laser beam reflected at normal incidence on the wafer. The wavelength of this laser is $\lambda = 950$ nm. Thereby, for standard growth conditions (temperatures ranging from 750 to 1100°C), the refractive index of III-nitride compounds is estimated to be $n \approx 2.3$, which leads to this expression for r:

$$r = \frac{\lambda}{2n}\frac{1}{\Delta t} = \frac{206\ \text{nm}}{\Delta t} \tag{1.15}$$

Table 1.6: Lattice parameter mismatch to GaN $\Delta a/a$, thermal expansion coefficient mismatch to GaN $\Delta\alpha$ and thermal conductivity κ of commonly used substrates for the epitaxy of III-nitride crystals [38].

	Al_2O_3 (0001)	6H-SiC	Si (111)
$\Delta a/a$ (%)	-13.9	-3.5	17
$\Delta\alpha$ (10^{-6}/K)	1.7	-1.14	-3
κ (W cm^{-1} K^{-1})	0.25	3.8	1.56

where Δt is the growth time period corresponding to one oscillation of the measured reflectivity. This measurement is of the highest importance to precisely control the layer thicknesses for the realization of highly-reflective DBRs.

One of the main issues concerning the growth of III-nitride compounds is the lack of actual bulk GaN substrates, despite some promising techniques such as the ammonothermal method [39, 40]. This means that foreign substrates such as sapphire, silicon carbide or silicon have to be employed, which exhibit both quite large lattice parameter and thermal expansion coefficient mismatch to GaN. Their properties are listed in Table 1.6. Thereby, the resulting GaN buffers grown on such substrates suffer from a quite large TDD. Amongst those, sapphire, being cheap and widely available, is the most commonly used material. However, the fact that sapphire is an insulator, its poor thermal conductivity and the large TDD of GaN buffers grown on sapphire are critical drawbacks for the realization of advanced optoelectronic devices such as LDs and SLEDs. Interestingly, LEDs seem to be less sensitive to dislocations [41]. Thus, the growth of epitaxial structures for LD applications are usually performed on FS GaN substrates, which are not truly bulk substrates but offer the best characteristics at reasonable costs: a TDD$< 10^7$ cm^{-2}, a good thermal conductivity enabling efficient device thermal management, and a good conductivity allowing device back contacting. Therefore, all growth performed in this study were performed on c-plane FS GaN substrates (unless otherwise stated).

One last point which is worth being mentioned is the wedge inherent to our MOVPE reactor. Indeed, the inhomogeneity of both the precursor fluxes and the temperatures along the wafer radius during growth yields a variation of the material growth rate along the sample radius, and thus also to a thickness gradient, which is referred to as a wedge. This wedge has a strong impact on the stopband position of epitaxial DBRs, as the central wavelength λ_0 of such DBRs, which is defined by the Bragg condition $\lambda_0 = t \cdot (4n)$ with t being the thickness of a quarterwave layer whose refractive index is n, is sensitive to the thickness of those quarterwave layers. Therefore, the wedge along the sample radius leads to a shift of the stopband position along the DBR sample radius, which is usually parabolic.

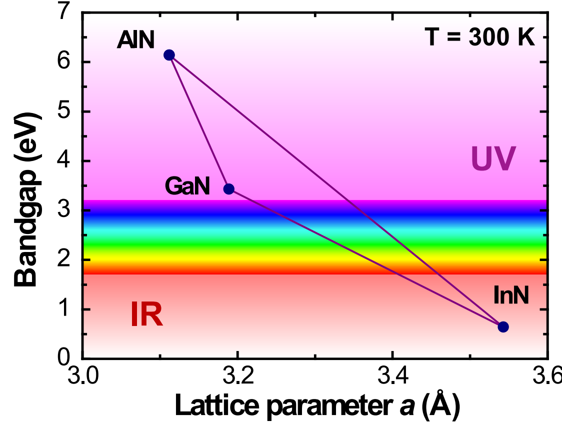

Figure 1.2: Bandgap of wurtzite III-nitride compounds versus their in-plane lattice constant a. The bowing parameter for the bandgap of ternary alloys is neglected. Values are taken from Tables 1.1 and 1.7.

1.3 Optical properties

In this section, the optical properties of III-nitrides are presented, including energy bandgap values, their variation as a function of the temperature and refractive index values. Finally, the QCSE is described, as well as its effects on the radiative efficiency and transition energy.

1.3.1 Bandgap

In addition to exhibiting a direct bandgap, one of the main interests of III-nitride compounds lies in the fact that the energy bandgap values of their ternary alloys cover a broad range of wavelengths from the near infrared to the deep ultraviolet, spanning across the whole visible spectrum (Fig. 1.2). The energy bandgap values E_g at low temperature (0 K) and room temperature (RT, 300 K) of binary compounds are given in Table 1.7. A modified version of Vegard's law (Eq. 1.1) gives the bandgap value of any ternary alloy $M_{1,x}M_{2,1-x}N$, where M_1 and M_2 are two different metal species amongst Al, In and Ga, from those of the corresponding binary materials:

$$E_g(M_{1,x}M_{2,1-x}N) = x \cdot E_g(M_1N) + (1-x) \cdot E_g(M_2N) - x(1-x) \cdot b_{M_1,M_2} \tag{1.16}$$

where b_{M_1,M_2} is the so-called bowing parameter, which accounts for the deviation from an ideal linear interpolation between binary alloys. For III-nitride materials, this bowing parameter is always positive, which reflects a reduction of the alloy energy gap. Once more, one has to stress the large lattice parameter mismatch between the different binary compounds that limits the actual wavelength window that can be reached. Bowing parameter values for the different gallium containing alloys are given in Table 1.7. The bowing parameter of $In_xAl_{1-x}N$

is dependent on the x value and will be discussed in section 3.2.

Obviously, the energy bandgap value E_g depends on the temperature T. This dependence is described by Varshni's semi-empirical law [45]:

$$E_g(T) = E_g(T=0) - \frac{\alpha T^2}{T+\beta} \tag{1.17}$$

where α and β are empirical independent parameters, whose typical values are given in Table 1.7. However, those values can strongly vary from one sample to another due to the thermal expansion coefficient mismatch between the different alloys and the substrate, giving rise to a temperature dependent strain affecting the temperature variation of the energy bandgap value of heterostructures. Thus, those Varshni parameters should be determined individually for each sample using reflectivity and photoluminescence (PL) measurements. The latter yields actual values for the bandgap energy around RT, whereas reflectivity should be used to probe the band-to-band transition energy at low temperature, as the PL emission properties at low temperature are dominated by localized states.

1.3.2 Refractive index

The dependence of the real part of the refractive index $n(\lambda)$ of III-nitride compounds as a function of the wavelength λ below the bandgap can be approximated by the first-order Sellmeier equation, which writes:

$$n^2(\lambda) = 1 + \frac{A_0\lambda^2}{\lambda^2 - \lambda_0^2} \tag{1.18}$$

where A_0 and λ_0 are fitting parameters. Kawashima *et al.* [46] obtained the following relation

Table 1.7: Band-to-band bandgap values E_g and Varshni parameters α and β for III-nitride binary compounds, and bowing parameters b for GaN-containing ternary alloys.

	GaN [18]	AlN [18]	InN [42]
$E_g(T=0$ K) (eV)	3.51	6.25	0.69
$E_g(T=300$ K) (eV)	3.43	6.14	0.64
α (meV/K)	0.909	1.799	0.414
β (K)	830	1462	454
b(GaN and...)	–	0.6 [43]	1.4 [44]

for the refractive index of GaN below its bandgap as:

$$n^2(\lambda) = 1 + \frac{4.37\lambda^2}{\lambda^2 - 0.088}\,. \tag{1.19}$$

Baldanzi and coworkers [47] found the following best-fit parameters A_0 and λ_0 for $In_xGa_{1-x}N$ and $Al_xGa_{1-x}N$ alloys:

$$\begin{aligned}
A_0(\mathrm{In}_x\mathrm{Ga}_{1-x}\mathrm{N}) &= 3.187 + 0.962 \cdot x + 0.948 \cdot x^2 \\
\lambda_0(\mathrm{In}_x\mathrm{Ga}_{1-x}\mathrm{N}) &= 177.374 + 64.144 \cdot x - 13.737 \cdot x^2 \\
A_0(\mathrm{Al}_x\mathrm{Ga}_{1-x}\mathrm{N}) &= 3.193 - 1.219 \cdot x + 0.533 \cdot x^2 \\
\lambda_0(\mathrm{Al}_x\mathrm{Ga}_{1-x}\mathrm{N}) &= 177.545 - 83.565 \cdot x + 29.285 \cdot x^2
\end{aligned} \tag{1.20}$$

Another commonly used approximation for the refractive index $n_{\mathrm{M}_x\mathrm{Ga}_{1-x}\mathrm{N}}(E)$ of a Ga-containing ternary alloy (M being Al or In), initially proposed by Bergmann *et al.* [48], relies on the shift of the dispersion curve reported by Kawashima for GaN (Eq. 1.19) by the difference between the bandgap of this alloy and that of GaN. Subsequently, $n_{\mathrm{M}_x\mathrm{Ga}_{1-x}\mathrm{N}}(E)$ can be expressed as:

$$n_{\mathrm{M}_x\mathrm{Ga}_{1-x}\mathrm{N}}(E) = n_{\mathrm{GaN}}\left[E - \left(E_g(\mathrm{M}_x\mathrm{Ga}_{1-x}\mathrm{N}) - E_g(\mathrm{GaN})\right)\right]\,. \tag{1.21}$$

The refractive index of InAlN will be discussed in section 3.2.

1.3.3 Quantum confined Stark effect

We have discussed in section 1.1.2 the electric field resulting from the polarization along [0001] inherent to the anisotropy of the wurtzite III-nitride crystal. Whereas this electric field is screened in bulk material, it becomes a quite strong effect in narrow double heterostructures such as QWs, with theoretical estimates giving values up to 10 MV/cm in a single GaN/AlN QW [20]. Charge planes with an opposite sign build up at each interface of a QW made of material j surrounded by thick barriers made of material i, according to Eq. 1.12. Those charge planes induce an electric field $\mathbf{F}_{QW}$ in a single QW given by:

$$\mathbf{F}_{QW} = \frac{\sigma_{ij} - \sigma_{ji}}{2\epsilon_0\epsilon_{QW}}\mathbf{n}_{ij} = \frac{\sigma_{ij}}{\epsilon_0\epsilon_{QW}}\mathbf{n}_{ij} = \frac{\mathbf{P}_i - \mathbf{P}_j}{\epsilon_0\epsilon_{QW}}\,. \tag{1.22}$$

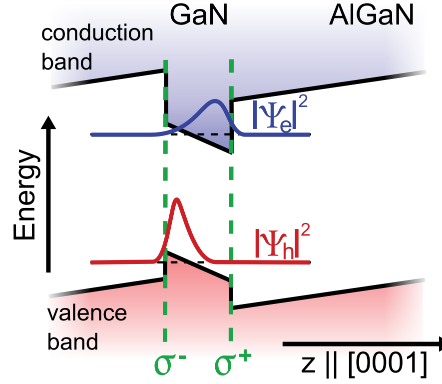

Figure 1.3: Illustration of the QCSE in a GaN/AlGaN QW. Courtesy of G. Rossbach.

This strong electric field yields a tilt of both the conduction and valence bands resulting in a triangular potential QW, which is known as the QCSE [49]. It is illustrated in Fig. 1.3, and has two major impacts on the radiative properties of the QW. On the one hand, the so-called Stark-shift originates from the triangular shape of the QW and decreases by a factor $-eL_{QW}\left\|\mathbf{F}_{QW}\right\|$ the fundamental transition energy $E_{e_1-hh_1}$ inside the QW, where e is the charge of the electron and L_{QW} is the QW thickness. As a first approximation, $E_{e_1-hh_1}$ can be expressed as [29]:

$$E_{e_1-hh_1} = E_{g,W} + e_1 + hh_1 - E_B - eL_{QW}\left\|\mathbf{F}_{QW}\right\| \tag{1.23}$$

where $E_{g,W}$ is the bandgap energy of the QW material, which is usually strained, e_1 and hh_1 are the confinement energies of the electron and the hole, respectively, and E_B is the exciton binding energy. E_B values in the range $\sim 10-50$ meV for GaN/Al$_x$Ga$_{1-x}$N QWs, which depends on x, on the QW thickness and on the electric field, have been reported [50, 51]. As a result, the large carrier energy confinement may dominate the transition energy of very thin QWs, yielding $E_{e_1-hh_1}$(thin QWs) $> E_{g,W}$ despite the QCSE. On the other hand, the term $-eL_{QW}\left\|\mathbf{F}_{QW}\right\|$ in the case of thick QWs decreases the QW transition energy below the bandgap of the well material, which means $E_{e_1-hh_1}$(thick QWs) $< E_{g,W}$.

The second effect is a spatial separation of the electron and hole wavefunctions inside the QW (Fig. 1.3), which yields a decreased oscillator strength f_{osc} according to [52]:

$$f_{osc} = \frac{2}{m_e\hbar\omega_{cv}}|d_{cv}|^2 \tag{1.24}$$

where m_e is the free electron mass, $\hbar\omega_{cv}$ is the energy of the interband transition and $d_{cv} =$

$\langle c|\mathbf{pe}|v\rangle$ is the dipolar matrix element with $|c\rangle$ and $|v\rangle$ the final and initial states of the optical transition, **p** is the electron momentum operator and **e** is the unitary polarization vector. This dipolar matrix element d_{cv} is proportional to the square modulus of the overlap integral between electron and hole envelope wave functions $f_e(z)$ and $f_h(z)$ [52]:

$$|d_{cv}|^2 \propto \left| \int f_e(z) f_h(z) dz \right|^2. \tag{1.25}$$

The oscillator strength f_{osc} is linked to the radiative lifetime τ_r through [53]:

$$\tau_r = \frac{2\pi\varepsilon_0 m_e c^3}{ne^2\omega_{cv}^2 f_{osc}} \tag{1.26}$$

where c is the speed of the light in vacuum, n is the refractive index and e is the charge of the electron. The QW internal quantum efficiency η_i, defined as the ratio between the radiative carrier recombination rate and the total recombination rate, can be expressed as:

$$\eta_i = \frac{\tau_{nr}}{\tau_r + \tau_{nr}} \tag{1.27}$$

where τ_{nr} is the non-radiative lifetime. Note that η_i is experimentally approximated by the ratio between the integrated QW PL intensity measured at RT and that measured at 4 K, assuming that η_i equals unity at 4 K [54, 55]. Thus, an increase in τ_r yields a decrease in the internal efficiency η_i. Thereby, the QCSE leads to a decrease in the optical transition energy and the QW internal efficiency. The larger the QW thickness, the bigger this effect.

1.4 Electrical properties

Non-intentionally doped (*nid*) GaN layers grown using by the MOVPE technique exhibit an electron background concentration of about ~ 10^{16} cm^{-3}. This residual n-type doping is ascribed to either nitrogen vacancies or residual oxygen impurities [56, 57, 58], with activation energies of 30 meV and 10 meV, respectively, although in some more recent studies it is considered that the conductivity of *nid* GaN solely comes from the unintentional incorporation of donor impurities such as oxygen [59].

1.4.1 *n*-type doping

The most commonly used donor impurity for achieving *n*-type doping of GaN layers is Si [60, 61, 62]. Si donors have an activation energy of about 20 meV [63], which means that nearly all donor impurities are ionized at RT, as $k_B T \approx 26$ meV at $T = 300$ K. The GaN crystalline quality starts dramatically decreasing at a doping impurity concentration of [Si]$\approx 10^{20}$ cm^{-3}. The electron mobility strongly depends on each sample characteristics (carrier concentration, crystalline quality, temperature, ...). Typical values are around 500 cm^{2}V^{-1}s^{-1} at 300 K for *nid* GaN. A RT mobility value as high as 1425 cm^{2}V^{-1}s^{-1} for [Si]$= 1.76 \cdot 10^{16}$ cm^{-3} has been reported [64]. The electron effective mass of GaN is ~ 0.20 m_0 [18]. Germanium has been proposed as an alternative GaN donor impurity [60, 65]. However, it has been only seldom used, despite some recent studies that suggest the superiority of Ge doping when compared to Si regarding achievable carrier concentration, sample surface smoothness and strain impact [66]. Indeed, Si doping has been reported to induce tensile strain, which is not the case for Ge doping even at [Ge] in the high 10^{19} cm^{-3} range.

1.4.2 *p*-type doping

Achieving satisfactory *p*-type doping of GaN layers has been for a long time the main challenge preventing the realization of III-nitride based optoelectronic devices. Mg has been quickly proposed as a possible acceptor impurity, but the use of low-energy electron beam irradiation has been required in order to obtain *p*-type conductivity in Mg-doped GaN layers [1, 67]. However, it is only in the early 1990s that Nakamura *et al.* proposed an annealing treatment to achieve efficient conduction in *p*-type doped GaN using Mg impurities [2]. Indeed, in MOVPE as-grown layers Mg impurities have been reported to form Mg-H complexes that are electrically inactive. Rapid thermal annealing is now commonly used in order to break the Mg-H bonds, which activates the acceptor behavior of Mg impurities [68]. However, the large activation energy E_A of Mg impurities, which is around 170 meV [68], means that the actual hole concentration p at RT is only about $p \approx N_A/20$, where N_A is the acceptor concentration (i.e. [Mg]-[Mg-H]), according to [69]:

$$p = \frac{N_A}{1 + g \cdot \exp\left(\frac{E_A - \Delta E}{kT}\right)} \tag{1.28}$$

where ΔE is the difference between the Fermi level and the valence band maximum and g is the degeneracy factor, which is assumed to be equal to 2. Indeed, the heavy and light hole valence bands are not degenerate in III-nitrides. As GaN layer crystalline quality degrades at [Mg]$\approx 5 \cdot 10^{19}$ cm^{-3}, the maximum achievable hole concentration is limited. Indeed, Kaufmann *et al.* reported on a maximum hole concentration equal to ~ $6 \cdot 10^{17}$ cm^{-3} for $N_A \approx 2 \cdot 10^{19}$ cm^{-3}, which then decreases for larger N_A and drops to very small values at $N_A \approx 1 \cdot 10^{20}$ cm^{-3}

[70]. A typical value for the hole mobility in nitride-based devices at RT is about 10 $cm^2V^{-1}s^{-1}$, for a hole concentration of about $7 \cdot 10^{17}$ cm^{-3} [71]. Calculations lead to an effective hole mass value of 1.4 m_0 for heavy holes, and 0.3 m_0 for light holes and 0.6 m_0 for holes in the split-off valence band [72].

As a result, *p*-type GaN layers exhibit a large resistivity, which is detrimental for the realization of bipolar optoelectronic devices such as VCSELs. In order to circumvent this drawback, transparent conductive electrodes are usually employed in order to improve the lateral current spreading across device mesas (see chapter 4).

2 Microcavity lasers

In this chapter, basics about semiconductor LDs are reviewed. Specificities about planar microcavity lasers are then introduced. Finally, VCSEL and VECSEL structures are presented. A brief review of standard III-V devices is stated, and specificities and the state-of-the-art of III-nitride based devices are presented. The aim of the RbGaN project, which involves the development of blue VECSELs for atomic clock applications, is also outlined.

2.1 Semiconductor laser diodes

Laser is an acronym standing for Light amplification by stimulated emission of radiation. Such devices are based on two key building blocks:

- an active medium, providing optical gain,
- a cavity, providing optical feedback.

Basically, optical gain in the active medium is obtained by inverting the population, enabling the extinction coefficient (imaginary part of the refractive index) to become negative. In such a system, the light is amplified through stimulated emission. This phenomenon is called amplified spontaneous emission (ASE) [73, 74]. The population inversion is reached through energy pumping, which can be optical, electrical or chemical. This active medium is placed in a cavity, providing optical feedback. The most commonly used cavity is the Fabry-Perot resonator, made of two mirrors facing each other. Subsequently, the light travels back and forth in this cavity, experiencing amplification through ASE during each crossing of the active medium. When the gain eventually reaches and exceeds the cavity optical losses, the spontaneous emission rate is clamped, the stimulated emission rate increases and the onset of lasing is observed. The first demonstration of electromagnetic radiation amplification inside a cavity was made in 1955 by Gordon, Zeiger and Townes [75]. Actually it was based on the amplification of microwave radiations, and was thus called a maser. A couple of years later, the concept was extended to the infrared and optical frequencies by Schawlow and Townes

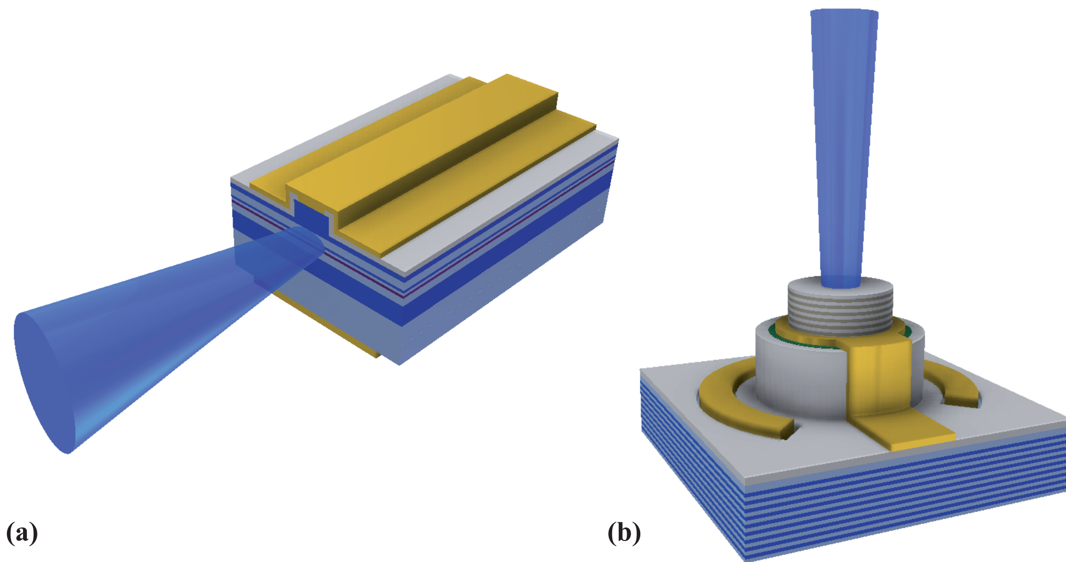

Figure 2.1: (a) An edge-emitting LD and (b) a VCSEL.

[76], which are considered as the inventors of the laser. They were awarded the Nobel Prize in Physics in 1964 and 1981, respectively.

In a semiconductor LD, light is usually generated through radiative recombinations of electrically-injected electron-hole pairs in a *p*-*n* junction. The first LD was demonstrated in 1962 by R. N. Hall *et. al* in a bulk GaAs-based *p*-*n* junction [77]. The first GaN-based LD was then demonstrated more than 30 years later, in 1996 by S. Nakamura and coworkers [5]. As discussed in section 1.4.2, the main challenge preventing the development of nitride-based optoelectronic devices was achieving an efficient *p*-type doping. Nonetheless, there are other types of semiconductor-based lasers that are not truly diode-based devices. The quantum cascade laser is based on intersubband transitions in a MQW structure and is actually a unipolar device, where a single electron can generate many stimulated photons, unlike devices based on band-to-band transitions. This principle was first proposed in 1971 by Kazarino and Suris [78] and demonstrated in 1994 by J. Faist *et al.* at Bell Laboratories [79]. Another possibility for semiconductor-based lasers relies on optical pumping for the generation of electron-hole pairs in the active region, which is no longer necessarily placed in the space charge region of a *p*-*n* junction. For instance, optical pumping is common for high power VECSELs [80, 81], whose output power can eventually exceed 100 W [82].

The cavity of the first LD was parallel to the *p*-*n* junction plane, with mirrors simply formed by the cleaved facets of the device [77]. Such devices are called edge-emitting LDs, whose emitted beam is perpendicular to the sample growth direction, but parallel to the active region [Fig. 2.1 (a)]. VCSELs are another important family of LDs, which were first demonstrated in 1979 by Soda *et al.* [83]. However, CW operation at room temperature has only been reported in 1988/1989 by Koyama and coworkers [84, 85]. Such microcavity lasers make use of DBRs as

mirrors and emit light perpendicularly to their *p*-*n* junction plane, i.e. to their active region [Fig. 2.1 (b)]. Their specificities are detailed in the forthcoming sections.

As previously said, lasing requires fulfilling two aspects: getting optical gain and feedback. First, let us recall how gain is obtained in semiconductors.

For energies higher than the bandgap, the intensity of the light transmitted I_t through a slab of a semiconductor, whose thickness is equal to l, is given by Beer-Lambert law [86]:

$$I_t = (1-R)^2 I_0 e^{-\alpha(\omega) l} \tag{2.1}$$

where R is the reflectivity of the air/semiconductor interface, I_0 is the initial intensity of the light and $\alpha(\omega)$ is the absorption coefficient of the semiconductor at the energy $\hbar\omega$.

The absorption coefficient $\alpha(\omega)$ can be written [87]:

$$\alpha(\hbar\omega) = \alpha_0(\hbar\omega)\left[f_v(\hbar\omega) - f_c(\hbar\omega)\right] \tag{2.2}$$

where $f_v(\hbar\omega)$ and $f_c(\hbar\omega)$ are the Fermi-Dirac distributions applied to quasi-Fermi levels E_{Fv} and E_{Fc} in the valence and the conduction band, respectively, and $\alpha_0(\omega)$ is given by [87]:

$$\alpha_0(\hbar\omega) = \frac{e^2 x_{vc}^2 \omega}{2\pi\varepsilon_0 \hbar n_{op} c}\left(\frac{2m_r}{\hbar}\right)^{3/2}\sqrt{\omega - \frac{E_g}{\hbar}} \tag{2.3}$$

where c is the speed of light in vacuum, e is the charge of the electron, x_{vc} is the dipolar matrix element, ε_0 is the vacuum dielectric constant, E_g is the energy bandgap of the semiconductor, n_{op} is the refractive index of the semiconductor and m_r is the reduced mass given by $\frac{1}{m_r} = \frac{1}{m_e} + \frac{1}{m_h}$, with m_e and m_h the effective masses of electrons and holes, respectively. Note that $\alpha_0(\omega) \propto E_g^{3/2}$ close to the bandgap.

Quasi-Fermi levels descript the band filling of semiconductors out of equilibrium. Basically $\alpha_0(\omega)$ gives the absorption in the case of thermodynamic equilibrium, and it is the maximal possible value of the absorption coefficient.

Under large carrier injection, $f_c(\hbar\omega)$ can eventually exceed $f_v(\hbar\omega)$, i.e. $E_{Fc} - E_{Fv} > \hbar\omega$. It then implies that $\alpha(\omega) < 0$, the absorption becomes negative and gain $g(\omega) = -\alpha(\omega)$ is obtained. The inequality $E_{Fc} - E_{Fv} > \hbar\omega$ is called Bernard-Duraffourg condition [88], and the inversion of population is reached when $f_c(\hbar\omega) > f_v(\hbar\omega)$.

Equation 2.2 indicates that the gain in a semiconductor is limited to $\alpha_0(\omega)$. Moreover, equation 2.1 shows that the amplification of the light in a semiconductor when Bernard-Duraffourg condition is fulfilled, i.e. when the inversion of population provides gain, is exponential.

Optical feedback in LDs is usually provided by a Fabry-Perot resonator. In the case of edge-emitting LDs, the reflectors are formed by the facets of the device. Their reflectivity R due to the refractive index contrast between air and the semiconductor material is given by [87]:

$$R = \frac{(n_{op} - 1)^2}{(n_{op} + 1)^2} \tag{2.4}$$

which yields $R \approx 18\%$ for a GaN-based LDs emitting at $\lambda = 420$ nm. It could be further increased by using reflective coatings on the diode facets.

Another element of relevant interest deals with the finite portion of the optical mode interacting with the gain region. This is accounted for by the confinement factor $\Gamma = \Gamma_{xy}\Gamma_z$, where xy and z refer to the plane perpendicular to and the direction of the beam propagation direction, respectively. Γ_{xy} and Γ_z can be expressed as [87]:

$$\Gamma_{xy} = \frac{\iint_{active} \left|E(x,y)\right|^2 dx\,dy}{\iint_{cavity} \left|E(x,y)\right|^2 dx\,dy}\,, \tag{2.5}$$

and

$$\Gamma_z = \frac{\int_{active} |E(z)|^2 dz}{\int_{cavity} |E(z)|^2 dz}\,. \tag{2.6}$$

These expressions correspond to the ratio between the electric field intensity in the active region and the total electric field intensity along the cavity, where the electric field can be written $E(x,y,z) = E(x,y)\cdot E(z)$. In an edge-emitting LD, Γ_z equals unity if the active region extends to the whole cavity, which is usually the case.

The losses α_m due to photon leakage through the mirrors are given by [87]:

$$\alpha_m = \frac{1}{2L} \ln \frac{1}{R_1 R_2} \tag{2.7}$$

where L is the length of the resonator and R_1 and R_2 are the reflectivity of each reflector forming the resonator. The total losses are given by $\alpha_m + \alpha_i$, where α_i corresponds to the internal losses due to absorption, scattering, etc... Thus, the threshold condition for the onset of lasing can be written [89]:

$$\langle g_{th} \rangle = \Gamma_z \langle g_{th} \rangle_{xy} = \Gamma_{xy} \Gamma_z g_{th} = \alpha_i + \alpha_m \tag{2.8}$$

where $\langle g_{th} \rangle$ is the modal gain and g_{th} is the material gain at threshold. The light intensity $I(z)$ crossing a laser cavity can then be expressed within a single pass as:

$$I(z) = I_0 e^{\overline{g} z} \tag{2.9}$$

where I_0 is the initial light intensity and $\overline{g} = \Gamma g - \alpha_i$ is the net modal gain.

The differential external efficiency η_e of a LD operating above lasing threshold is:

$$\eta_e = \eta_i \eta_t \tag{2.10}$$

where η_i is the internal quantum efficiency and $\eta_t = \frac{\alpha_m}{\alpha_m + \alpha_i}$ is the extraction efficiency considered only for the lasing mode. The optical output power P_{out} of a lasing device can be written:

$$P_{out} = \eta_e \frac{\hbar \omega}{e} (I - I_{th}) \tag{2.11}$$

where I_{th} is the threshold current and I is the operating current. η_e is called the *differential* external efficiency because it only takes into account the current above threshold and not the entire current flowing through the device. η_e can be obtained by measuring the optical output power versus the injected current:

$$\eta_e = \frac{e}{\hbar \omega} \frac{dP_{out}}{dI} \tag{2.12}$$

where $\frac{dP_{out}}{dI}$ is taken above threshold.

The wall-plug efficiency (η_{WPE}), measuring the overall power conversion, is given by:

$$\eta_{WPE} = \frac{P_{out}}{P_e} = \eta_e \frac{\hbar\omega}{eV}\left(1 - \frac{I_{th}}{I}\right) \tag{2.13}$$

where P_{out} is given by equation 2.11, $P_e = IV$ is the electric power injected into the device and V is the operating voltage.

For an operating current well above threshold, i.e. $I \gg I_{th}$, and for $\hbar\omega \approx eV$, we obtain $\eta_{WPE} \approx \eta_e$. For semiconductor-based lasers, η_{WPE} is of the order of 30 – 60%, whereas it only amounts to ~ 1% for gas-based lasers.

Finally, the carrier density in the active region is clamped above threshold, i.e. any further carrier brought into the active region above threshold is converted into a photon through stimulated emission. Thereby, the material gain is also clamped above threshold:

$$g(I > I_{th}) = g_{th}\,. \tag{2.14}$$

2.2 Planar microcavities

The longitudinal z axis of a planar microcavity is perpendicular to the plane of the active region. Thus, a few discrepancies from standard edge-emitting lasers arise. Firstly, the active region does no longer extend to the whole cavity length. Indeed, the active region thickness is very small compared to the cavity length. This means that the gain per pass is quite low (~ 1%), which is much lower than in an edge-emitting LD. Thereby, according to Eq. 2.8, lasing requires total losses below this value. Subsequently, the bare semiconductor/air interface reflectivity (~ 20%) is no longer sufficient to obtain lasing, and highly-reflective mirrors are required. Indeed, planar microcavity mirrors are made of highly-reflective DBRs ($R > 99.5\%$). Consequently, planar microcavities exhibit a large cavity quality factor Q, which is defined as [89]:

$$Q = \frac{E_0}{\Delta E} = \frac{2n_c L_c}{\lambda_0}\frac{\pi}{1-\sqrt{R_1 R_2}} \approx \frac{\lambda_0}{\Delta\lambda_0} \tag{2.15}$$

where E_0 and ΔE are the cavity optical mode energy and FWHM, respectively, L_c is the cavity length, n_c is the cavity refractive index and $R_{1,2}$ are both DBR reflectivity values. The second equality implies no other losses than α_m, and the last approximation stands for high quality factors, i.e. $E_0 >> \Delta E$. The Q factor is related to the photon lifetime in the cavity τ through

$Q = 2\pi\nu\tau$, where ν is the photon frequency.

Secondly, due to their short cavity length (~ 1 μm, whereas the edge-emitting LD cavity length is usually ~ 500 μm long), their mode spacing is often larger than their gain bandwidth, resulting in single mode operation. The mode spacing or free spectral range $\delta\lambda$ can be approximated by:

$$\delta\lambda \approx \frac{\lambda_0^2}{2n_c L_c} \tag{2.16}$$

where λ_0 is the central wavelength of the nearest transmission peak.

2.2.1 Distributed Bragg reflectors

As discussed previously, the low gain-per-pass in a microcavity laser, which is about 1% [89], means that the photons have to perform several round-trips across the cavity, i.e. across the gain medium, in order to achieve lasing in such a structure. Thus, microcavity lasers need highly-reflective mirrors, exhibiting a reflectivity over 99%. In addition, at least one of the two reflectors should present a non zero transmission in order to let the laser beam out of the cavity. As metal mirrors are limited to reflectivities ~ 95%, DBRs are required as reflectors. They are made of periodic stacks of multiple layers, alternating high and low refractive index. The optical thickness of each layer is set to a quarterwave $\lambda_0/4$, i.e. each layer physical thickness is equal to $\lambda_0/(4n)$, where λ_0 is the wavelength satisfying the Bragg condition, thus called the Bragg wavelength, and n is the refractive index of the layer. The DBR reflectivity can then eventually reach a value exceeding 0.99 thanks to the constructive interferences between the light reflected at each interface of the multiple layer stack, if it comprises enough pairs. For this reason and unlike metal mirrors, the reflectivity spectrum of a DBR exhibits a high value plateau only within a narrow spectral window, which is centered at the DBR Bragg wavelength.

The peak reflectivity R_{peak} at the Bragg wavelength λ_0 of a DBR made of layers with a low refractive index n_L and a high refractive index n_H is given by [89]:

$$R_{peak} = \left(\frac{1 - \left(\frac{n_L}{n_H}\right)^{2m}}{1 + \left(\frac{n_L}{n_H}\right)^{2m}} \right)^2 \tag{2.17}$$

where m is the number of quarter-wave pairs. More generally, if the DBR is made of m bilayers, each of them composed of a low refractive index (n_{Li} material and a high refractive index (n_{Hi} material, with $i = 1, \ldots, m$, then the reflectivity at the Bragg wavelength is expressed as [89]:

$$R_{peak} = \left(\frac{1-b}{1+b}\right)^2 , \tag{2.18}$$

$$b = \prod_{1}^{2m} \frac{n_{Li}}{n_{Hi}} . \tag{2.19}$$

In the case of m identical bilayers made of materials with a low n_L and a high n_H refractive index, surrounded by media with a refractive index n_{in} and n_{out} on the incident and transmitted side of the DBR stack, respectively, the peak reflectivity at the Bragg wavelength writes:

$$R_{peak} = \left(\frac{1-\frac{n_{out}}{n_{in}}\left(\frac{n_L}{n_H}\right)^{2m}}{1+\frac{n_{out}}{n_{in}}\left(\frac{n_L}{n_H}\right)^{2m}}\right)^2 . \tag{2.20}$$

The stopband width $\Delta\lambda_{stopband}$ of a DBR, which is the wavelength span ensuring a high reflectivity, is then given by [89]:

$$\Delta\lambda_{stopband} = \frac{2\lambda_0(n_H - n_L)}{\pi n_{eff}} \tag{2.21}$$

where n_{eff} is the effective refractive index contrast of the mirror defined as:

$$n_{eff} = 2\left(\frac{1}{n_H} + \frac{1}{n_L}\right)^{-1} . \tag{2.22}$$

Unlike for metallic mirrors, the electric field intensity partially penetrates into DBR structures. The penetration depth L_{pen} of the optical power into the DBR is written [89]:

$$L_{pen} = \frac{(L_H + L_L)}{4}\frac{n_H + n_L}{n_H - n_L}\tanh\left(2m\frac{n_H + n_L}{n_H - n_L}\right) \approx \frac{(L_H + L_L)}{4}\frac{n_H + n_L}{n_H - n_L} \tag{2.23}$$

where $L_H = \lambda_0/(4n_H)$ and $L_L = \lambda_0/(4n_L)$ are the high and low refractive index layer thickness, respectively. The last approximation stands for large numbers of pairs ($m \to \infty$).

Examples of the minimal number of quarter-wave pairs m_{min} for obtaining a reflectivity over 0.99 (using Eq. 2.20), the stopband width $\Delta\lambda_{stopband}$ and the penetration depth L_{pen}

Table 2.1: Minimal number of pairs m_{min} for achieving a reflectivity $R > 0.99$, $\Delta\lambda_{stopband}$ and L_{pen} for various DBR systems.

DBR type	λ_0 (nm)	n_1	n_2	m_{min}	$\Delta\lambda_{stopband}$ (nm)	L_{pen} (nm)
GaAs/AlAs [89]	980	3.52	2.95	14	~ 110	~ 430
ZrO_2/SiO_2	420	2.1	1.47	7	~ 100	~ 170
$GaN/Al_{0.20}Ga_{0.80}N$	420	2.49	2.40	68	~ 10	~ 1170
$GaN/In_{0.17}Al_{0.83}N$	420	2.49	2.32	36	~ 20	~ 620

for various DBR systems are given in Table 2.1. Simulated reflectivity spectra and electric field intensity profile of a 10-pair SiO_2/ZrO_2 DBR and a 42-pair $In_{0.17}Al_{0.83}N$/GaN with Bragg wavelength $\lambda_0 = 420$ nm are shown in Fig. 2.2, together with the simulated reflectivity spectrum and the standing wave electric field intensity distribution across a GaN λ cavity sandwiched between those two DBRs. The curves have been obtained using the transfer matrix method, which is described in the next section.

2.2.2 The transfer matrix method

The approach considered here is the transfer matrix formalism [90] to solve the Maxwell equations (classical treatment of the electrical field) in a given layered structure. As this set of four equations is linear, one can treat separately the propagation of each Fourier component across the structures. Each layer is defined by its dispersion (energy dependence of the refractive index) and its thickness. In the frame of the present work, only the description of the propagation of light through dielectric materials will be discussed.

We define a planar structure as made of different layers of different thicknesses and with an infinite lateral extension (implying a translational invariance along the plane). The direction perpendicular to this plane is aligned with the z-axis. The dielectric layers are assumed to be made of homogeneous materials with a uniform frequency-dependent dielectric constant, different from layer to layer. This stepwise function is the dielectric profile $\epsilon(\omega, z)$ of the structure, where ω is the propagating electromagnetic wave angular frequency. The Maxwell equation reads:

$$\nabla^2 \boldsymbol{E}(\boldsymbol{r}, z) + \left(\frac{\omega}{c}\right)^2 \epsilon(\omega, z)\boldsymbol{E}(\boldsymbol{r}, z) = 0 \tag{2.24}$$

where $\boldsymbol{r}$ is the in-plane position. Because of the in-plane invariance, the solution is of the

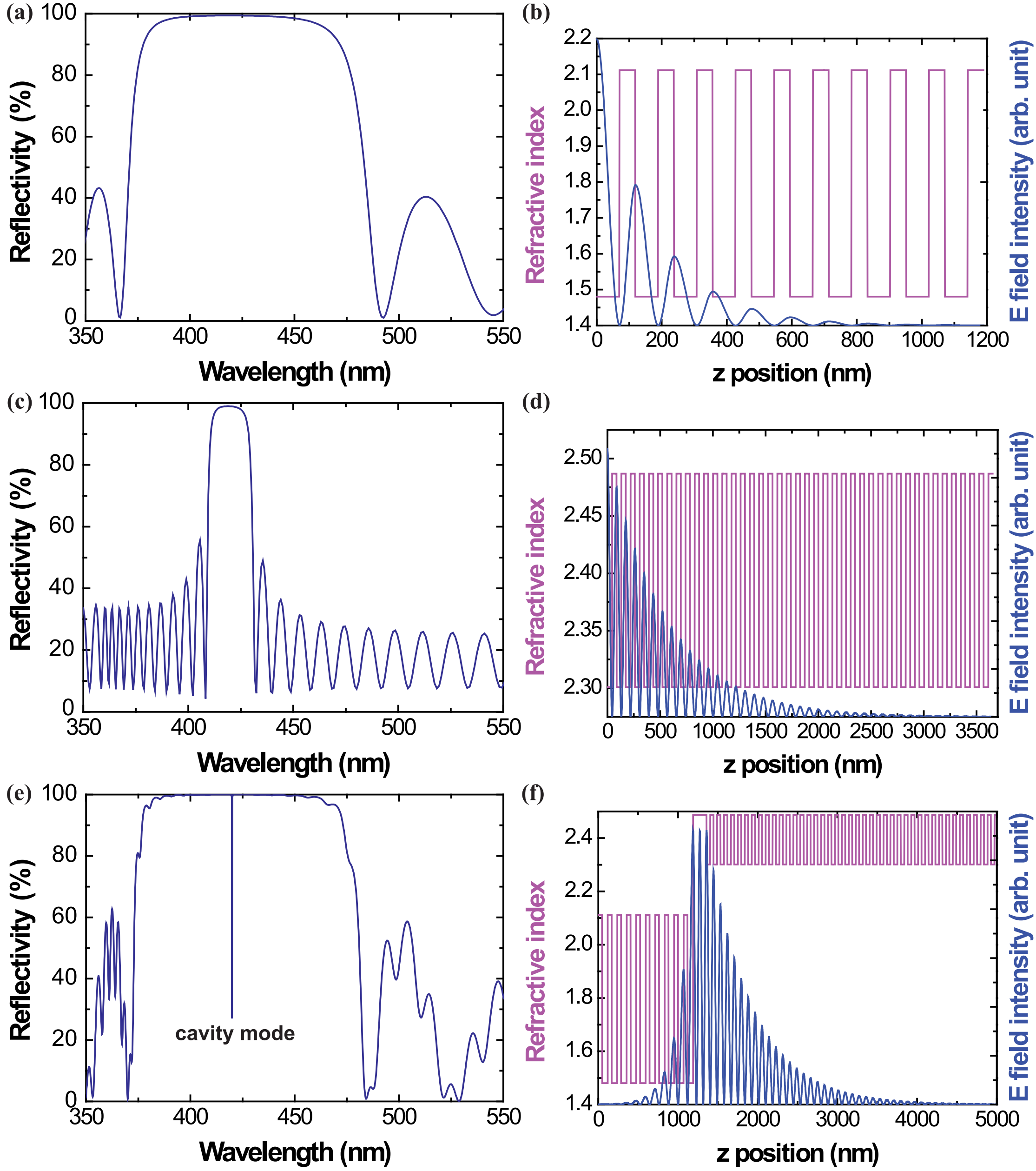

Figure 2.2: (a) Simulated reflectivity spectra and (b) electric field intensity profile of a 10-pair SiO_2/ZrO_2 DBR with $\lambda_0 = 420$ nm. (b) Simulated reflectivity spectra and (c) electric field intensity profile of a 42-pair $In_{0.17}Al_{0.83}N/GaN$ DBR with $\lambda_0 = 420$ nm. (e) Simulated reflectivity and (f) standing wave electric field intensity profile of a λ GaN cavity sandwiched between those two DBRs, exhibiting a cavity mode at $\lambda_0 = 420$ nm.

form:

$$\boldsymbol{E}_{k_\parallel}(\boldsymbol{r}, z) = \boldsymbol{e}_{k_\parallel} U_{k_\parallel}(z) e^{i\boldsymbol{k}_\parallel \boldsymbol{r}} \tag{2.25}$$

where $\boldsymbol{e}_{k_\parallel}$ is the polarization vector. Replacing Eq. 2.25 into Eq. 2.24, one finds the 1-D equation for the mode function $U_{k_\parallel}(z)$:

$$\frac{d^2 U_{k_\parallel}(z)}{dz^2} + \left(\left(\frac{\omega}{c}\right)^2 \epsilon(\omega, z) - k_\parallel^2\right) U_{k_\parallel}(z) = 0\,. \tag{2.26}$$

This equation may be separately solved in each homogeneous layer. For a layer with dielectric constant $\epsilon(\omega, z)$, one finds the following solution:

$$U_{k_\parallel}(z) = E_{\text{left}}\left(k_\parallel\right) e^{i k_z z} + E_{\text{right}}\left(k_\parallel\right) e^{-i k_z z}\,, \tag{2.27}$$

$$k_z = \sqrt{\left(\frac{\omega}{c}\right)^2 \epsilon(\omega) - k_\parallel^2} \tag{2.28}$$

which is the sum of a left-traveling and a right-traveling waves. This solution describes a propagating wave for $(\omega/c)^2 \epsilon(\omega) > k_\parallel^2$ and an evanescent wave along the z-axis otherwise. E_{left} and E_{right} are complex coefficients to be determined by the Maxwell boundary conditions at each interface between two layers. This is done within the transfer matrix formalism. For each position z in space, we define the vector $\begin{pmatrix} E_{\text{left}} \\ E_{\text{right}} \end{pmatrix}$. For an arbitrary structure, one can write the field in the form of Eqs. 2.27 and 2.28 for two points z_1 and z_2 at the boundaries of the structure [Fig. 2.3 (a)]. Maxwell boundary conditions across the structure result in a linear relation between the coefficients in z_1 and z_2:

$$\begin{pmatrix} {E_{\text{left}}}^2 \\ {E_{\text{right}}}^2 \end{pmatrix} = \begin{pmatrix} m_{11} & m_{12} \\ m_{21} & m_{22} \end{pmatrix} \begin{pmatrix} {E_{\text{left}}}^1 \\ {E_{\text{right}}}^1 \end{pmatrix} = M \begin{pmatrix} {E_{\text{left}}}^1 \\ {E_{\text{right}}}^1 \end{pmatrix} \tag{2.29}$$

where M is the transfer matrix of the structure. For a stack of different structures 1,2,3,..., the total transfer matrix M_{tot} reads:

$$M_{tot} = \ldots M_3 M_2 M_1\,. \tag{2.30}$$

Starting from the matrix of the homogeneous layers of given thicknesses, one can derive the wave propagation for arbitrarily complex planar structures by writing the elementary transfer

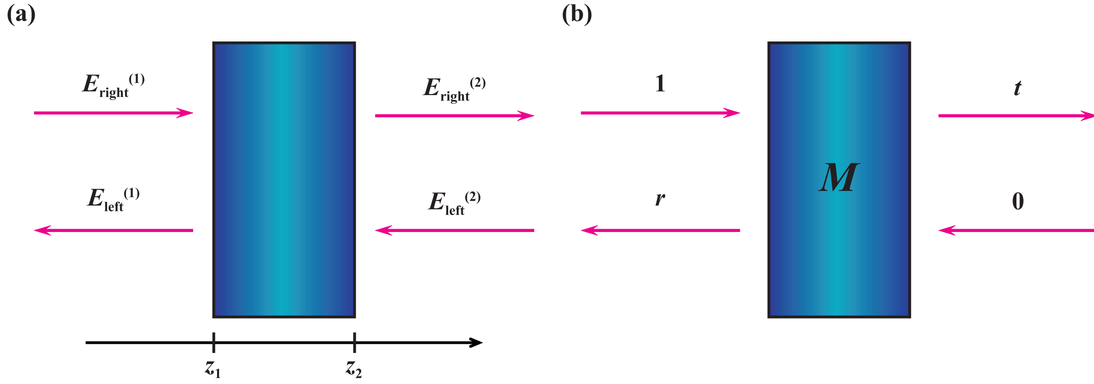

Figure 2.3: (a) Schematic representation of the left- and right-traveling waves at positions z_1 and z_2. (b) The transmitted t and reflected r waves are given by the transfer matrix M of the system.

matrices corresponding to the propagation from z_1 to z_2:

$$M_{\text{hom}} = \begin{pmatrix} e^{ik_z(z_2-z_1)} & 0 \\ 0 & e^{-ik_z(z_2-z_1)} \end{pmatrix} \tag{2.31}$$

For an interface transfer matrix, one has to consider separately TE and TM modes:

$$M_{\text{TE}} = \begin{pmatrix} \frac{k_z^{(1)}+k_z^{(2)}}{2k_z^{(2)}} & \frac{k_z^{(1)}-k_z^{(2)}}{2k_z^{(2)}} \\ \frac{k_z^{(1)}-k_z^{(2)}}{2k_z^{(2)}} & \frac{k_z^{(1)}+k_z^{(2)}}{2k_z^{(2)}} \end{pmatrix}, \tag{2.32}$$

$$M_{\text{TM}} = \begin{pmatrix} \frac{n_2^2 k_z^{(1)}+n_1^2 k_z^{(2)}}{2n_1 n_2 k_z^{(2)}} & \frac{n_2^2 k_z^{(1)}-n_1^2 k_z^{(2)}}{2n_1 n_2 k_z^{(2)}} \\ \frac{n_2^2 k_z^{(1)}-n_1^2 k_z^{(2)}}{2n_1 n_2 k_z^{(2)}} & \frac{n_2^2 k_z^{(1)}+n_1^2 k_z^{(2)}}{2n_1 n_2 k_z^{(2)}} \end{pmatrix} \tag{2.33}$$

where:

$$\begin{aligned} k_z^{(i)} &= \sqrt{\left(\frac{\omega}{c}\right)^2 \epsilon_i - k_\parallel^2}\,, \\ n_i &= \sqrt{\epsilon_i}\,. \end{aligned} \tag{2.34}$$

In the following, we consider waves originating from a wave of unitary amplitude coming from the left [Fig. 2.3 (b)]. Considering the transfer matrices under time inversion, one can derive the complex reflectivity and transmittivity coefficients:

$$r = -\frac{m_{21}}{m_{22}} ,$$
$$t = -\frac{\det(M)}{m_{22}} . \tag{2.35}$$

In the absence of absorption, the transmittance and reflectance are given by the following relations:

$$R = |r|^2 ,$$
$$T = -\frac{|t|^2}{\det(M)} . \tag{2.36}$$

2.2.3 Optical field distribution and related features

According to Eq. 2.8, the confinement factor $\Gamma = \Gamma_{xy}\Gamma_z$ is a critical parameter that governs lasing threshold in LDs. In edge-emitting LDs, $\Gamma_z \sim 1$ as previously stated. Thus, the important parameter in such devices is Γ_{xy}, which can be increased by using proper claddings for vertical confinement of the propagating mode and a ridge structure for lateral confinement of the propagating mode. In a VCSEL structure, the lateral confinement factor Γ_{xy} can be assumed to be ~ 1 and the critical parameter becomes Γ_z, as the active region plane is perpendicular to the cavity axis. Γ_z can then be expressed as $\Gamma_z = \Gamma_{fill}\Gamma_{enh}$, where Γ_{fill} is the filling factor and Γ_{enh} is the gain enhancement factor, which are given by:

$$\Gamma_{fill} = \frac{d_a}{L_{eff}} \tag{2.37}$$

and

$$\Gamma_{enh} = \frac{L_{eff}}{d_a} \frac{\int_{d_a} |E(z)|^2 \, dz}{\int_{L_{eff}} |E(z)|^2 \, dz} \tag{2.38}$$

where $L_{eff} = L_c + L_{pen,1} + L_{pen,2}$ is the effective cavity length given by the sum of the cavity length L_c and the penetration depths in both DBRs $L_{pen,1,2}$, d_a is the active region total thickness and $E(z)$ is the standing wave electric field distribution along the cavity. Thus, given a cavity length and an active region thickness, the only way to improve the Γ_z factor is tuning the active region position with respect to the electric field. Indeed, by placing a single gain

segment in an antinode of the standing wave, where the electric field can be well approximated by $E(z) = E_0 \cos(2\pi\overline{n}z/\lambda_0)$ we obtain [91]:

$$\Gamma_{enh} = 1 + \frac{\sin\left(2\pi\overline{n}d_a/\lambda_0\right)}{2\pi\overline{n}d_a/\lambda_0} \tag{2.39}$$

where $\overline{n}$ is the spatially averaged refractive index of the cavity. Thereby, a thin QW placed at an antinode of the optical field yields $\Gamma_{enh} \to 2$. For $d_a = m\lambda_0/(2\overline{n})$ with m an integer, we obtain $\Gamma_{enh} = 1$. This can be generalized in the case of M_a active sections (i.e. MQWs) with equal gain, located at positions $z_{il} \leq z \leq z_{ih}$ with $i = 1, ...M_a$, resulting in [91]:

$$\Gamma_{enh} = 1 + \frac{\sum_{i=1}^{M_a} \sin(4\pi\overline{n}z_{ih}/\lambda_0) - \sin(4\pi\overline{n}z_{il}/\lambda_0)}{\sum_{i=1}^{M_a} z_{ih} - z_{il}}\,. \tag{2.40}$$

For instance, Eq. 2.40 yields $\Gamma_{enh} = 1.52$ for five 5 nm thick $In_{0.10}Ga_{0.90}N$ QWs separated by 5 nm thick $In_{0.01}Ga_{0.99}N$ barriers centered at an antinode of the optical field standing wave for $\lambda_0 = 420$ nm such as found in devices presented in section 5.4.

2.3 The VCSEL

VCSELs are planar microcavity-based LDs, making use of highly-reflective DBRs as mirrors and emitting light vertically, i.e. perpendicularly to their gain region plane. Thanks to these particularities, they benefits from several advantages compared to standard edge-emitting LDs:

- Unlike edge-emitting LDs that require laser bar cleaving in order to define facets acting as reflectors, VCSEL vertical emission enables direct on-wafer testing.
- For the same reason, VCSELs can be processed as 2D arrays, whereas edge-emitting lasers can only form 1D arrays.
- As previously said, due to their short cavity length resulting in a large free spectral range, VCSELs usually exhibit single longitudinal mode operation.
- Thanks to their circular symmetry, VCSELs emit circular beam that are easier to collimate than elliptical beams emitted by edge-emitting lasers [Fig. 2.1].
- VCSELs exhibit a low operating current and power consumption thanks to their small active volume.

Table 2.2: Applications of VCSELs (adapted from [98]).

Technical fields	Systems
Optical communications	Local area networks, optical links, ...
Computer optics	Computer links, optical interconnects, high speed/parallel data transfer, computer mice ...
Optical memory	CD, DVD, near field, multi-beam, initializer, ...
Optoelectronic equipments	Printer, laser pointer, mobile tools, home appliances, ...
Optical information processing	Optical processors, parallel processing, ...
Optical sensing	Optical fiber sensing, bar code readers, encoders, ...
Displays	Array light sources, multi-beam search light, ...
Illuminations	High efficiency sources, micro illuminators, adjustable illuminations, ...
Biomedical sensing [97]	*in vivo* molecular monitoring, label-free biosensing, ...

- VCSELs can be modulated at high speed at low operating currents, also thanks to their small active volume.

Thanks to those unique properties, VCSELs found numerous applications, such as optical interconnects [92, 93], gas sensing [94, 95], pumping of atomic clocks [96], biomedical sensing [97] and many others that are summarized in Table 2.2.

The low gain per pass in VCSEL structures means that such devices require rather large operating current densities, which are obtained by confining small currents into small current apertures. The most common approaches used for such current confinement are ring or circular electrodes, proton implant, buried heterostructures, air-post, oxide confinement or oxide DBRs [98].

2.3.1 Standard III-V VCSELs

Standard III-V VCSELs are based on arsenides, phosphides or antimonides. "Short-wavelength" GaAs-based VCSELs operate between 650 and 1300 nm, the most common and well-established device emitting at 850 nm, with an annual production volume of the order of 100 million units for high-volume applications like data communications, computer mice, finger navigation engines for mobile devices [99]. Such devices are based on a GaAs MQW active region, doped AlGaAs DBRs and lateral oxidation as current aperture. Using strain engineering in InGaAs QW [100], adding dilute concentration of N [101] or using InGaAs QDs [102], the emission wavelength can be extended nearly up to 1300 nm. Red-emitting (650-700 nm) VCSELs can be realized using InGaP QWs [103], which find application in plastic optical fiber communications. Finally, VCSELs emitting at 980 and 1060 nm arouse growing interest thanks to enabling more efficient data transfer and higher operating temperatures [104].

Long-wavelength InP-based VCSELs emission ranges between 1.3 and 2.3 μm and are based on a buried tunnel junction (BJT) aperture for current confinement and strained InAlGaAs QWs as gain medium. The mirrors of such devices can be either monolithic InP-based DBRs [105], dielectric DBRs [106] or wafer fused GaAs-based DBRs [107], and they are usually made single-mode in order to fulfill requirements in applications such as optical fiber communications and gas sensing. Output power over 6 mW has been demonstrated in VCSELs emitting at 1.55 μm [108].

Finally, the InP-based VCSEL emission range has been extended to 2.3 μm [109]. Such devices are single mode and thermally tunable. However, because of strain considerations, the mid-infrared range (2.3 to 3.5 μm) is usually targeted using antimonide alloys. CW room temperature GaSb-based edge-emitting LDs have been recently reported with emission wavelength over 3.6 μm [110]. Nevertheless, single-mode CW VCSELs emitting at 2.3-2.6 μm were demonstrated only lately [111]. They exhibit higher tuning rates and better thermal conductivity than InP-based devices, and find applications in gas sensing.

2.3.2 III-nitride based VCSEL specificities

The two main specificities of the III-nitride material system related to VCSEL devices are:

- the large lattice parameter mismatch between the different III-nitride binary compounds (see section 1.1.1),
- the low *p*-type GaN conductivity (see section 1.4.2).

This makes the realization of nitride-based DBRs challenging because of the build up of strain in non LM superlattices, unless using LM InAlN/GaN bilayers [112]. In addition, the low *p*-type GaN conductivity makes the use of current confinement mandatory in order to avoid light absorption by the metallic top contacts. Moreover, no *p*-type doped nitride-based epitaxial DBR has been reported up to date, which means that intracavity *p*-type contacts are required. In addition, proton implant of *p*-type GaN is quite challenging and nitride-based VCSELs suffer from the lack of efficient GaN-based tunnel junctions, which prevents the use of BJT. As a result, the viable current confinement schemes for blue VCSELs are scarce. They are presented in section 5.3.

However, such blue VCSELs would find numerous applications, e.g. for high density optical data storage system, laser printing, laser mice, and micro- or picoprojectors [113].

2.3.3 Nitride-based VCSEL diodes: state-of-the-art

Only few groups have reported on blue/green nitride-based electrically-driven VCSELs so far [114, 11, 115, 116]. Amongst them, Nichia Corporation (Japan) is clearly dominating the field,

and has reported CW operation at RT of VCSELs emitting at 451 nm with 0.7 mW output power and 1.5 mA threshold current [117], and pulsed operation of VCSELs emitting at 503 nm with 22 mA threshold current [118]. Nichia, as well as Panasonic [115] and UCSB [114], proposed a device based on a fully hybrid microcavity using both top and bottom mirrors made of dielectric DBRs. They all use a thin dielectric aperture together with a TCO current spreading layer on top of the device mesa to achieve current confinement. UCSB specificity relies on the growth of their VCSEL cavity along the non polar *m*-axis, yielding no QCSE and polarization-locked emission. On the other hand, T.-C. Lu *et al.* developed monolithic VCSELs based on AlN/GaN DBRs [116], while also using the dielectric/TCO bilayer current confinement scheme. However, they report a low output power ascribed to the large dislocation density of the active region due to the large strain that builds up in such an epitaxial DBR.

2.3.4 Our approach

In this context, we propose an innovative and monolithic approach relying on a LM highly-reflective InAlN/GaN DBR. Such structures are extensively discussed in chapter 3, and present the advantage over other nitride-based DBRs to exhibit a much lower dislocation density when grown on high-quality FS GaN substrates. On the other hand, our devices also make use of a TCO layer as *p*-type contact for hole spreading. The development of such contacts is addressed in chapter 4. Finally, our final VCSEL structure is presented in chapter 5.

2.4 The VECSEL

VECSELs, also known as semiconductor disk lasers, are structures quite similar to VCSELs, with two noticeable differences: the microcavity is completed by a top external mirror rather than a DBR surmounting the epitaxial structure, and they are usually based on optical pumping rather than electric injection [119], even if there are a few reports of electrically-driven VECSELs [120, 121]. Although such devices were first reported in 1966 [122] and used on various occasion since then [123, 124], their potential has only be fully recognized in the late 1990s [125, 126]. They have been developed in order to overcome some conventional semiconductor laser limitations: generating watt-level and higher optical powers with a high quality circular beam exhibiting single lateral mode lasing. Indeed, VECSELs basically benefit from the same advantages than VCSELs, i.e. a high quality low divergence angle circular beam, on-wafer testing and ability to easily realize 2D arrays, while presenting two main advantages on VCSELs [127]:

- power scaling,
- ability to insert intracavity elements.

Power scaling is made possible by the laser mode and pump spot size scalability. In a standard electrically-driven VCSEL, the achievable lateral mode size is limited by the lateral current

spreading efficacy, which is no longer an inconvenience in the case of an optically pumped VECSEL. Indeed, VECSELs with output powers exceeding 100 W have been recently reported [82]. In addition, the external mirror enables the insertion of intracavity elements, such as spectral filters [128, 129], saturable absorber elements so as to achieve passive mode-locking [130, 131] (the cavity length defining the pulse repetition rate), transparent intracavity heat spreaders [132], intracavity absorption cells for intracavity laser absorption spectroscopy [133] or nonlinear optical elements [134].

Thanks to those specific properties, VECSELs are suited for several applications [119], like visible sources for television or projectors, spectroscopy, fluorescence-based bio-imaging (microscopy) or search for fingerprints (forensics), photodynamic therapy, or laser engineering.

2.4.1 Standard III-V VECSELs

Basically, the different material systems used in VCSELs to achieve various wavelengths can be also used for VECSELs. Indeed, such devices emitting in the 660-1300 nm wavelength range have been realized using GaAs-based compounds [135], the optical fiber communication window, which is around 1.5-1.6 μm, has been achieved using InP-based materials [136], which could also be combined to the wafer fusion technique [137], and GaSb-based alloys allowed reaching the 2.0-2.3 μm range [138]. In addition, group IV-VI semiconductor PbTe/PbEuTe and PbSe/PbEuTe-based materials systems have been used to demonstrate VECSELs emitting in the 4.5-5.0 μm region [139]. Finally, the emission wavelength range can be increased as previously said through the use of intracavity nonlinear optical elements for generating light at harmonics, as well as summing or differencing frequencies of the incoming light beams [119, 127].

2.4.2 Nitride-based VECSELs: state-of-the-art

The reports on nitride-based VECSELs are quite scarce and only concern optical pumping [16, 140, 141, 142]. The threshold power densities range between 100 and 700 kW/cm^2 for optical pulse durations of 1.7 to 5 ns, and optical output peak power as high as 300 W has been demonstrated. However, the published literature on GaN-based VECSELs only reports on external cavity lengths of the order of 2 mm, or even sample substrates used as the external cavity [16, 140], which would both prevent inserting any intracavity element, which cancels one of the main interests of VECSEL devices. In this context, the development of VECSELs with long external cavities of the order of several tens of millimeter is of high interest.

2.4.3 Nitride-based VECSELs for atomic clocks (the RbGaN project)

The RbGaN project is a collaborative work between LASPE and CSEM funded by the Swiss National Science Foundation. The purpose of this collaboration is the development of an active atomic clockwork based on a mode-locked GaN-based laser using an intracavity Rb

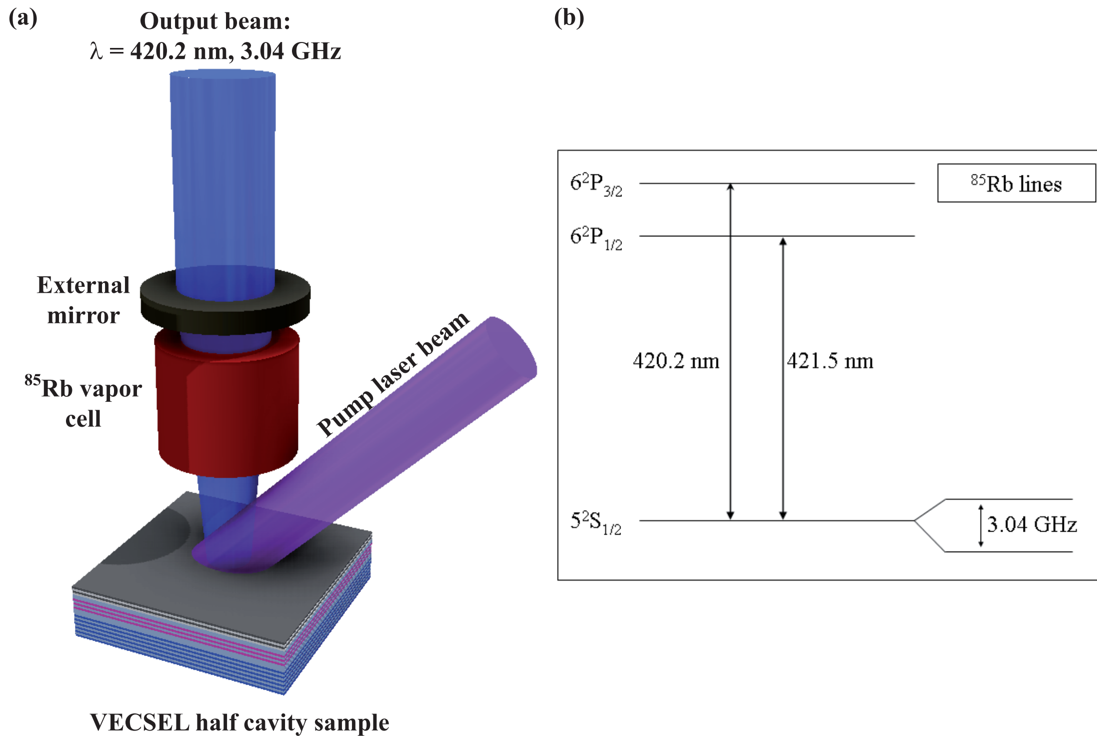

Figure 2.4: (a) Schematic drawing of the RbGaN clockwork device. (b) Detail of the ^{85}Rb hyperfine structure, corresponding to the two optical transitions of ^{85}Rb in the blue wavelength range.

atomic vapor cell absorber. The laser is made of an optically pumped VECSEL, so as to enable the introduction of intracavity elements, such as a Rb vapor cell absorber. However, this requires the development of VECSELs with long external cavities, unlike those reported so far in the literature [16, 140, 141, 142]. The VECSELs will then operate in the self mode locking regime, the spectral separation of modes in the generated optical comb being intrinsically tuned to the ground state hyperfine structure splitting in the Rb atoms. A schematic drawing of the RbGaN device is shown in Fig. 2.4 (a). The Rb hyperfine structure optical transition of interest is the $5^2S_{1/2}$-$6^2P_{3/2}$ at 420.2 nm [Fig. 2.4 (b)], which is the Rb transition line with the strongest intensity in the blue range. The Rb cell will exhibit saturation if the atomic populations of the two hyperfine ground states (F= 2 and F= 3 levels in ^{85}Rb) are coupled to the two adjacent components of the periodic frequency comb. In this way the pulse repetition rate will be locked to hyperfine splitting of the ground states. We choose the ^{85}Rb isotope with 3.04 GHz splitting of the hyperfine ground states. The cavity length required for stable mode-locking at 3.04 GHz pulse repetition rate is 49.965 mm, i.e. the pulse round-trip time inside the VECSEL cavity should correspond to the inverse of this repetition rate.

The VECSEL half-cavity sample is based on a LM InAlN/GaN bottom DBR such as those developed for our VCSELs (see chapter 3) and an InGaN QW-based active region emitting at 420 nm. Initially, the desired laser pump beam wavelength was $\lambda = 405$ nm, as LDs emitting

at this wavelength are commercially available at reasonable low costs. However, as will be discussed in chapter 6, the low absorption of the active region at this wavelength resulted in the use of a pulsed frequency-tripled Nd:YAG laser emitting at 355 nm.

3 InAlN-based distributed Bragg reflectors

In this chapter, LM InAlN/GaN DBRs grown by MOVPE are studied. Once the motivations for such DBRs are given, InAlN growth challenges are discussed. The structural and optical properties of InAlN layers nearly LM to GaN are then presented. Visible and UV DBRs grown on sapphire are briefly discussed. The growth of such epitaxial stacks on FS GaN substrates is then thoroughly addressed. Finally, further improvements for such DBRs are proposed.

3.1 On the interest of InAlN for Bragg mirrors

As seen in section 2.2, one of the main building blocks for semiconductor microcavities are DBRs. They can be either III-nitride-based epitaxial or dielectric DBRs. Whereas the former usually suffer from strain resulting from the lattice parameter mismatch between the two different semiconductor materials constituting the bilayers and require rather long growth times, the latter usually exhibit a larger refractive index contrast between the two different dielectric materials, which are usually amorphous or polycrystalline and thus suffer much less from strain, while being much easier and quicker to deposit (e.g. *via* evaporation or sputtering). However, the realization of fully hybrid microcavities (i.e. using both top and bottom dielectric DBRs) requires some challenging processing steps in order to remove the epitaxial cavity from the substrate, which furthermore makes the control of the cavity length delicate.

Early approaches for the realization of III-nitride-based Bragg mirrors relied on the use of either AlGaN/GaN [143, 144] or AlN/GaN [145] pairs. The main critical drawback of such epilayers is the large in-plane lattice parameter mismatch ($\Delta a/a$) between the different materials composing the DBR stack. Increasing the number of pairs, the build-up of the stress eventually leads to the formation of cracks and misfit dislocations, as shown in Fig. 3.1 (a). A strain compensation technique based on superlattice interlayers has been proposed in order to avoid cracks in AlN/GaN DBRs [146]. Such DBRs have been successfully used to achieve CW lasing in blue electrically-driven VCSELs grown on sapphire [116]. However this method is not suited for growth on low dislocation density FS GaN substrates. Indeed, as the stress

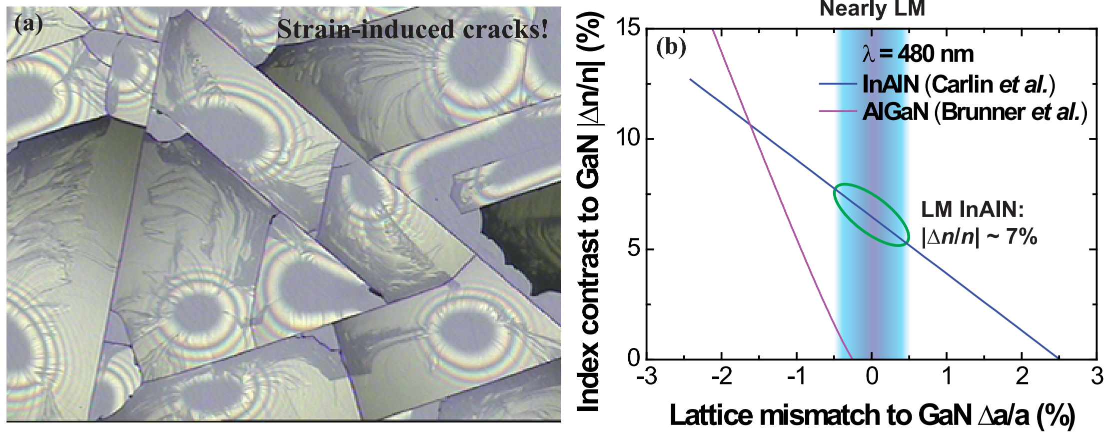

Figure 3.1: (a) Optical microscope image of strain-induced cracks. (b) Refractive index contrast $|\Delta n/n|$ vs in-plane lattice parameter mismatch $\Delta a/a$ to GaN for InAlN layers (blue curve) [147] and AlGaN (violet curve) [148] at a wavelength $\lambda = 480$ nm. The shaded blue area corresponds to InAlN or AlGaN layers nearly LM to GaN, i.e. $\|\Delta a/a\| < 0.5\%$.

accumulated within the epilayers would eventually generate additional threading dislocations, the use of such high quality substrates partially decreases its interest over sapphire ones.

In this context, the use of InAlN for the realization of highly reflective DBRs is of high interest. InAlN with an indium content of about 18% indeed exhibits a refractive index contrast to GaN $|\Delta n/n| = \left(n_{\text{InAlN}} - n_{\text{GaN}}\right)/n_{\text{GaN}}$ of about 7% [112] in the blue-violet wavelength region while being lattice-matched to GaN. For comparison, $Al_{0.46}Ga_{0.54}N$ would have the same refractive index contrast to GaN but would then suffer from a lattice parameter mismatch to GaN of about 1.20%. The refractive index contrast to GaN at a wavelength $\lambda = 480$ nm is shown in Fig. 3.1 (b) as a function of $\Delta a/a$ for InAlN (blue curve) and AlGaN (violet curve). InAlN and AlGaN refractive index values as a function of the aluminum content are taken from Carlin *et al.* [147] and from Brunner *et al.* [148], respectively, whereas in-plane lattice parameter constants come from the review article by Vurgaftman and Meyer [18]. Note that the refractive index contrast to GaN for $Al_xGa_{1-x}N$ layers should obviously never be positive, which is in fact the case in Fig. 3.1 (b) for small values of x. Actually, the curve comes from a fit of measurements made on several $Al_xGa_{1-x}N$ layers without x values between 0 and 0.1, which causes strong inaccuracy within this range. Thus, in simulations, the $Al_xGa_{1-x}N$ refractive index is usually taken as that of GaN with an offset given by the difference of their bandgaps for $0 < x < 0.1$ (Eq. 1.21).

LM InAlN/GaN quarterwave layers are serious candidates for the realization of high quality nitride-based epitaxial DBRs. Indeed, highly reflective InAlN-based DBRs have been successfully demonstrated on sapphire substrates in both the visible [149] and UV [150] regions as well as on FS GaN substrates [151]. They have been used in nitride-based polariton lasers [152], optically pumped [153] and electrically driven [154] VCSELs, as well as in optically pumped VECSELs [155]. In the next sections, the growth, structural and optical properties of

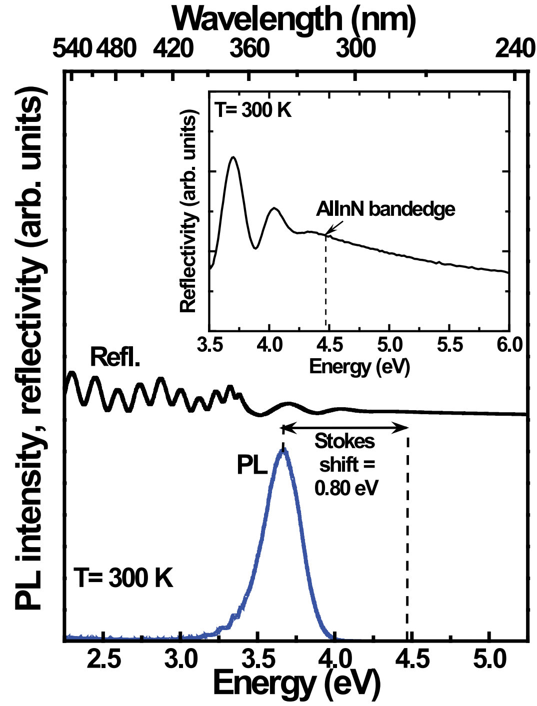

Figure 3.2: RT PL and reflectance spectra measured on a LM InAlN layer grown on sapphire, and corresponding Stokes shift. Inset: enlarged view of the reflectance spectrum close to the InAlN band edge [156].

LM InAlN layers are described. Finally, InAlN-based DBRs are presented along their structural and optical properties, and several critical issues are addressed.

3.2 Optical properties of InAlN

The $In_xAl_{1-x}N$ refractive index contrast to GaN, $\Delta n/n = \left(n_{\text{InAlN}} - n_{\text{GaN}}\right)/n_{\text{GaN}}$, at a wavelength $\lambda = 480$ nm has been determined to be [112]:

$$\frac{\Delta n}{n}\,(In_xAl_{1-x}N/GaN) = -0.127 + 0.35x \tag{3.1}$$

within the explored In content range of 6% $< x <$ 21%. Eq. 3.1 is a fit to experimental data acquired through *in situ* reflectivity measurements performed during InAlN growth. In particular, LM $In_xAl_{1-x}N$ grown on sapphire (x = 17%) exhibits $|\Delta n/n| = -6.8\%$ at $\lambda = 480$ nm. $\frac{\Delta n}{n}$ $(In_xAl_{1-x}N/GaN)$ and $\frac{\Delta n}{n}$ $(Al_xGa_{1-x}N/GaN)$ curves as a function of the lattice parameter mismatch to GaN have been plotted in Fig. 3.1 (b).

The RT bandgap of nearly-LM InAlN layers has been estimated through reflectance measure-

ments performed on sapphire/GaN/InAlN samples. The extracted fitted linear relationship between the nearly-LM $In_xAl_{1-x}N$ bandgap and its indium content $0.12 \leq x \leq 0.20$ at 300 K is [147]:

$$E_g\,(In_xAl_{1-x}N) = 6.2 - 11x\,. \tag{3.2}$$

RT PL and reflectance spectra measured on a LM InAlN layer grown on sapphire are shown in Fig. 3.2 [156]. The position of the InAlN band edge is determined to be at 4.47 eV according to the reflectance measurement. From the PL and reflectance curves, a Stokes shift value as large as 800 meV is deduced, which could possibly be ascribed to indium composition fluctuations or to the presence of deep defects or impurities acting as preferential recombination centers.

Equation 3.2 corresponds to Eq. 1.16 with a bandgap bowing parameter b of ~ 6 eV, which is in good agreement with the value determined via a $\mathbf{k}\cdot\mathbf{p}$ model including the strain-induced energy shift that allows deriving the unstrained bandgap for the whole indium composition range [157]. In this study, the InAlN bandgap is expressed as:

$$E_g\,(In_xAl_{1-x}N) = x\cdot E_g\,(InN) + (1-x)\cdot E_g\,(AlN) - b(x)\cdot x\cdot(1-x) \tag{3.3}$$

where $b(x)$ is a modified bowing parameter given by:

$$b(x) = \frac{A}{1+Cx^2}\,. \tag{3.4}$$

The best fit to the experimental data is obtained for the values $A = 6.43 \pm 0.12$ eV and $C = 1.21 \pm 0.14$, which gives the value $b\,(x = 17\%) \approx 6.2$ eV, close to that extrapolated from Eq. 3.2. The use of a composition-dependent bowing parameter is ascribed to the significant charge transfer occurring in the InAlN alloy accross the whole indium content range owing to the large electronegativity difference between aluminum and indium.

3.3 Growth and structural properties of InAlN layers

The InAlN alloy is arousing a growing interest thanks to the unique possibility to be grown lattice-matched to GaN while exhibiting both a large refractive index contrast and a huge spontaneous polarization discontinuity leading to the formation of a two-dimensional electron gas at the InAlN/GaN interface. LM InAlN has found a use in many applications, such as cladding layers in LDs [158, 159, 160, 161, 162] and in high electron mobility transistors [163]. However,

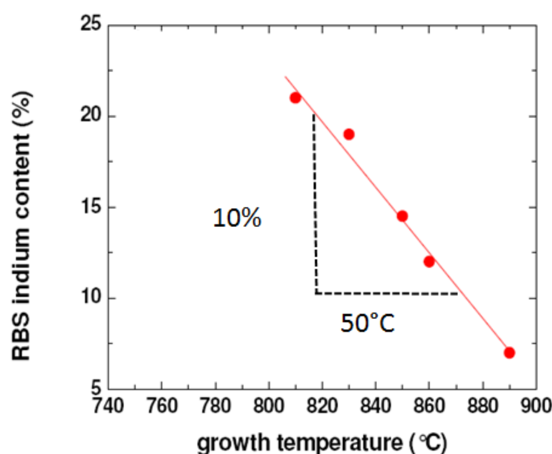

Figure 3.3: InAlN indium content measured by Rutherford backscattering spectrometry as a function of the InAlN growth temperature. A 10°C increase in the growth temperature yields a decrease of 2% in the indium content.

the growth of high quality InAlN layers remains quite challenging. The main growth parameters are reviewed and several issues are addressed hereafter, focusing on MOVPE growth, which has been used throughout this work.

3.3.1 Growth parameters

The growth of InAlN layers remains rather challenging although it has been quite extensively studied during the past few years. The huge growth temperature difference between AlN (~1100°C) and InN (~600°C) requires an intermediate growth temperature for InAlN layers restrained to a narrow window, limited on the upper side by the indium desorption rate and on the lower side by the aluminum adatoms diffusion length. Moreover, the large difference between the length and the energy of In-N and Al-N bonds is responsible for indium surface segregation [164] and phase separation [165], respectively. As surface segregation effect mainly occurs at interfaces between layers, it has a strong impact on InAlN-based superlattices. After a given thickness surface segregation reaches a steady regime where the indium atoms segregating from one layer to the upper one are fully replaced by the indium atoms segregating from the lower layer. In particular, this effect has to be taken into account when growing InAlN-based DBRs, as will be discussed in section 3.4.2. On the other hand, phase separation, related to spinodal decomposition, has a strong negative effect on the crystalline quality and the surface morphology of thick In-rich InAlN layers [166]. However, this issue is not relevant in the present work as it focuses on nearly LM $In_xAl_{1-x}N$ layers.

InAlN growth parameters have been widely studied during the past few years [37, 167, 168, 169, 170, 171, 172]. As can be seen in Fig. 3.3, increasing the growth temperature also enhances the indium desorption rate, resulting in a reduced indium incorporation [37, 167, 168, 171]. The growth temperature is actually the key parameter in order to tune the indium content

in InAlN layers. As a rule of thumb, a growth temperature rise of 10°C reduces the indium content by 2% [Fig. 3.3]. Moreover, the temperature is measured on the susceptor and thus it is not the actual sample temperature. Thereby, the temperature setpoint should take into account the thermal conductivity of the different types of substrate used. For our specific growth conditions and reactor, if the temperature setpoint corresponding to the LM condition on sapphire is T_{sapphire}, then the temperature setpoints for samples grown on $1/6^{th}$ of single side polished FS GaN substrate, on full single side polished FS GaN substrate and on full double side polished FS GaN substrate are $T_{\text{sapphire}}+15°\text{C}$, $T_{\text{sapphire}}+30°\text{C}$, and $T_{\text{sapphire}}+40°\text{C}$, respectively.

At a given growth temperature, increasing the indium precursor flux also favors indium incorporation until reaching a plateau [173, 174, 167]. However, we also found that a low TMIn flux favors the formation of V-shaped pits and accelerate the crystalline quality degradation mechanism (see section 3.4.2). Surprisingly, increasing the aluminum precursor flux also leads to an indium incorporation increase, without the saturation effect reported for the TMIn flow rate for the range of TMAl fluxes investigated [167]. This is ascribed to an InAlN growth rate increase resulting in a reduced indium desorption rate. The InAlN surface morphology can be improved by introducing a small quantity of H_2. However, a large hydrogen flux also reduces indium incorporation [37]. Another way to improve surface morphology is to increase the ammonia flux, and thus also the V/III ratio, which decrease both the surface roughness and the V-shaped pit density [37]. At first sight, the influence of the nitrogen flux seems identical to that of NH_3 [37]. The indium incorporation is improved when increasing the growth pressure, but this is detrimental to the surface roughness [37]. It has also been shown that no noticeable effect on the growth rate, the indium incorporation and the surface morphology occurs for a substrate miscut angle varying between 0 and 0.5° [172]. The carrier gas flows have a great impact on the InAlN quality. When performing growth with a low carrier gas flow, InAlN layers LM to GaN, whose absorption edge should lie in the UV range (at ~4.45 eV), exhibit a brownish aspect, indicating that light absorption occurs at visible wavelengths. Eventually the transparency of the layers is improved and thus the residual absorption is decreased when growth is carried out using a sufficiently high carrier gas flow [147].

Another highly interesting aspect deals with the residual doping in *nid* InAlN layers LM to GaN since the latter will have a strong impact on the ability to intentionally dope such an alloy, which is crucial for the fabrication of optoelectronic devices making use of n- or p-type doped layers. R. B. Chung and coworkers have studied the carbon and oxygen impurity incorporation and its dependence on the growth conditions of optimized InAlN layers, i.e. layers where no relaxation or degradation occurred, by performing secondary ion mass spectrometry measurements [167]. As far as carbon incorporation is concerned, it appears that [C] values in the $3-4\times10^{17}$ cm^{-3} range are obtained for low growth pressures (< 100 Torr). It was concluded that carbon mainly originates from the methyl groups from the decomposition of TMIn since AlN grown under identical conditions resulted in [C] values in the low 10^{17} cm^{-3}. In addition, for a given pressure, the InAlN alloy is more sensitive to carbon contamination compared with the InGaN one likely due to a binding energy between Al and C atoms stronger than that

between Ga and C. On the other hand, the incorporation of oxygen does not appear to be affected by growth parameters such as the growth pressure, the growth rate, the V/III ratio and the addition of H_2 as carrier gas to N_2. In any case, InAlN layers exhibit high [O] values (in excess of 1×10^{18} cm^{-3}), which is ascribed to the strong affinity of oxygen atoms to aluminum ones and the low growth temperatures.

3.3.2 The lattice-matched condition to GaN

The indium content fulfilling the LM condition between $In_xAl_{1-x}N$ and GaN layers is an important parameter, which has generated a great interest. It amounts to about 17% for structures grown on c-plane sapphire substrates [175] and about 18% for those grown on c-plane FS-GaN substrates [176]. This discrepancy is ascribed to the different residual strain state of GaN buffers grown on the two types of substrate. Furthermore, it is worth pointing out that an indium content satisfying the LM condition at room temperature for InAlN layers grown on any type of substrate will result in tensile strain at the InAlN growth temperature because of the difference between InAlN and GaN thermal expansion coefficients. This has to be kept in mind when growing InAlN-based structures in order to avoid cracks and/or dislocation generation.

When growing InAlN/GaN DBRs, a small strain resulting from slightly non LM InAlN layers can result in a rather large stress after the growth of more than 40 pairs. Whereas slightly compressively strained stacks of layers are pretty much stable against cracks and/or dislocations (at least up to a certain extent, as will be discussed in section 3.4.2), slightly tensely strained epilayers exhibit cracks. Actually, such cracks are widely reported for InAlN layers with an indium content below 17% [173, 174, 177]. Thus, the indium content in LM InAlN DBR stacks is usually targeted to be between 19 – 20%.

3.3.3 Structural properties, defects, and critical thickness

The InAlN layer quality has been widely reported to dramatically degrade and exhibit phase separation after a given critical thickness, despite being nearly-LM to GaN [165, 178, 179]. Moreover, the presence of V-shaped pits, not always related to threading dislocations, are usually observed, whose origin is still uncertain [177, 180, 181, 182, 183]. The pit density seems to increase with the InAlN thickness. Finally, the presence of hillocks is systematic in such layers [37, 167, 173, 174, 177, 178]. The aim of this section is to study those structural issues in (nearly-)LM InAlN layers [184].

Nearly LM InAlN samples with different thicknesses have been grown on FS GaN substrates in order to study the surface morphology changes. Precursor gas flows were set to 100 sccm (TMAl), 350 sccm (TMIn) and 400 sccm (NH_3), which are our standard growth parameters for InAlN layers used in optoelectronic devices. The growth temperature is around 850°C. AFM scans of samples whose thicknesses are 2 nm, 50 nm, 100 nm, 240 nm and 500 nm are

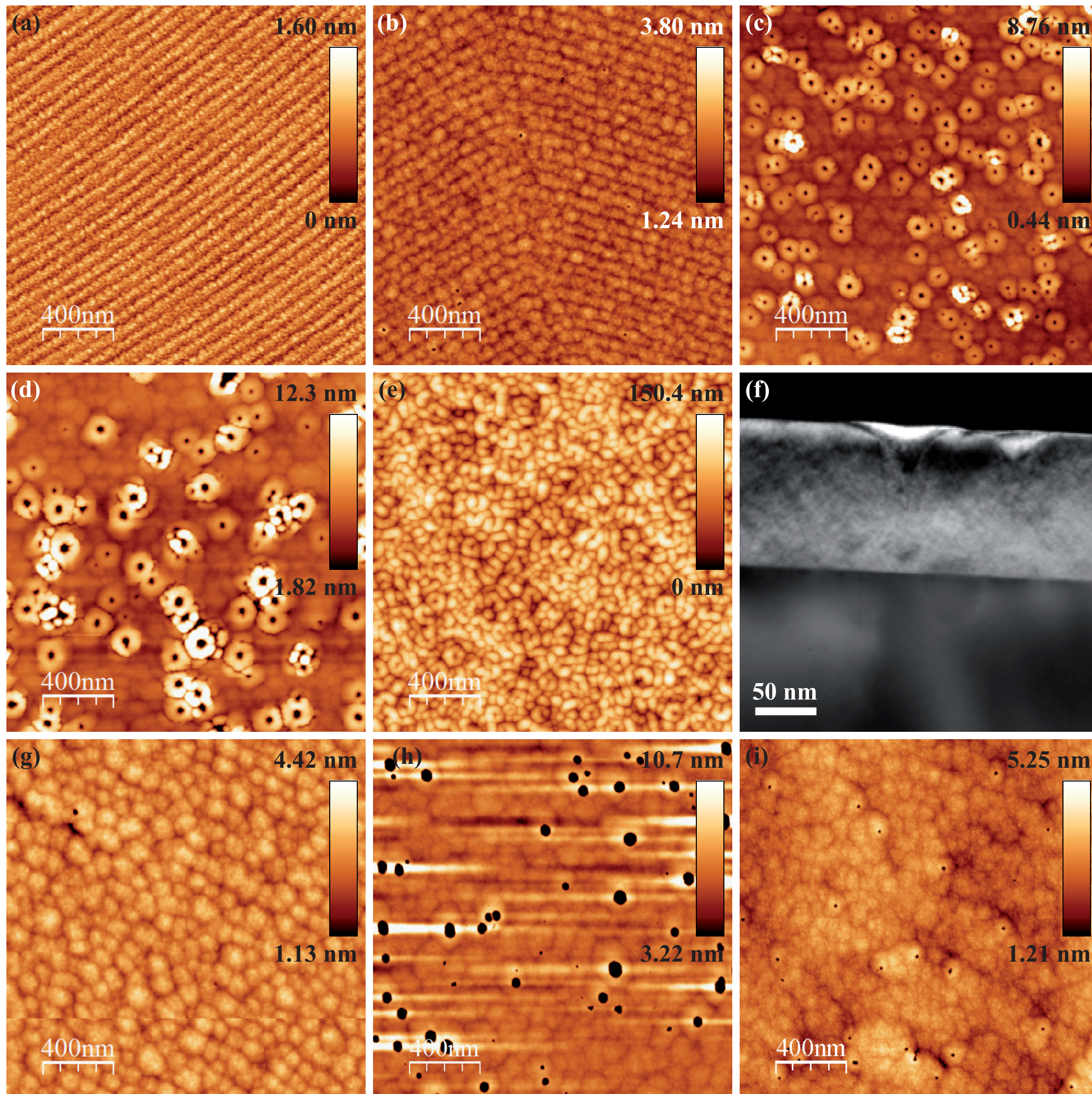

Figure 3.4: 2×2 μm^2 AFM scans of nearly LM ($x \approx 19-20\%$) $In_xAl_{1-x}N$ layers grown on FS GaN substrates, whose thicknesses are (a) 2 nm, (b) 50 nm, (c) 100 nm, (d) 240 nm and (e) 500 nm. (f) TEM cross-section view of a V-shaped pit on the 100 nm thick InAlN layer without any underlying defect or threading dislocation (courtesy of Dr. G. Périllat-Merceroz). 2×2 μm^2 AFM scans of (g) 100 and (h) 210 nm thick $In_xAl_{1-x}N$ layers grown on FS GaN substrates with $x \approx 14\%$ (tensely strained layers). (i) 2×2 μm^2 AFM scans of a 50 nm thick LM InAlN layer grown on sapphire substrate.

shown in Fig. 3.4 (a), (b), (c), (d) and (e), respectively. XRD $\omega - 2\theta$ rocking curve measurements yield indium contents around $19-20\%$ for those layers. The surface degradation mechanism can be divided into 3 overlapping phases. During the first step, hillocks are formed and they align along the atomic steps. This feature starts right at the beginning of the InAlN growth [Fig. 3.4 (a)], and results in quite regular hillocks aligned along the atomic steps after a thickness of 50 nm [Fig. 3.4 (b)]. At this thickness hillock width and height are about 100 nm

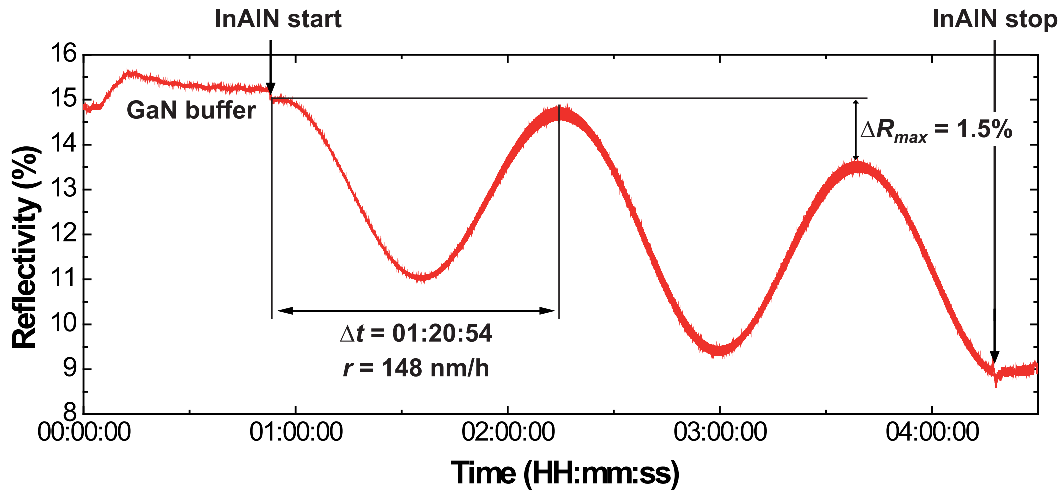

Figure 3.5: *In-situ* reflectivity measurement of a 500 nm thick InAlN layer grown on a FS GaN substrate. The decrease of the reflectivity maximal value, which is equal to ~ 1.5%, reveals a surface roughness that increases with the layer thickness. Equation 1.15 can be used to determine the InAlN growth rate r, which amounts here to 148 nm/h.

and 0.7 nm, respectively. Then the second step occurs: starting at a thickness of 50 nm (or even slightly before), V-shaped pits are appearing. Their density increases and finally stabilizes around $3-5\times10^{8}$ cm^{-2} at InAlN thicknesses ranging between 100 and 240 nm [Figs. 3.4 (c) and 3.4 (d)]. Donut-like features also appear around the V-pits, and eventually smaller V-pit rings are formed around those donuts [Fig. 3.4 (d)]. The V-pits grow and reach a diameter of about 70 nm at a thickness of 240 nm [Fig. 3.4 (d)]. However, during those two first phases the surface roughness remains fairly constant apart from the pits. The rms roughness measured on small areas (~ 200×200 nm^{2}) free of pits is around $0.3-0.4$ nm up to a thickness of 240 nm. However, during the third phase the V-pits completely coalesce yielding a strong increase in the rms roughness up to 21 nm as can be seen in Fig. 3.4 (e). The InAlN surface roughness that increases with the layer thickness is evidenced by *in-situ* reflectivity measurements, as shown in Fig. 3.5. Indeed, the maximal value of the reflectivity decreases from 15% to 13.5% after two oscillations (corresponding to about 400 nm), which can be ascribed to an increased surface roughness. This reflectivity curve yields an InAlN growth rate r = 148 nm/h, owing to Eq. 1.15. This coalescence phase seems to begin already around a thickness of 100 nm, and coalescing donuts generating new V-pits can be seen in Fig. 3.4 (d) for an InAlN thickness of 240 nm. To summarize, hillocks are formed at early stages of InAlN growth. After a thickness of about 50 nm, V-pits appear, which are growing and eventually coalescing, yielding a strong degradation of the surface morphology.

So, where do the V-pits come from? V-pit formation has been mainly ascribed to threading dislocations in this material system [180, 181, 182]. However, FS GaN substrates were used in order to ensure a low dislocation buffer (TDD ~ 4×10^{7} cm^{-2} or less) so as to minimize their impact on the structural properties of the overgrown InAlN layers. Indeed, a TEM cross-section

view of a 100 nm thick $In_{0.20}Al_{0.80}N$ layer shows a V-pit without any underlying defect such as threading dislocation or stacking mismatch boundary at its bottom [Fig. 3.4 (g)]. A few studies also report on the formation of V-pits not related to threading dislocations. Miao and coworkers ascribed those V-pits to compressive strain [177], whereas Vennéguès *et al.* observed similar features in tensely strained layers [183]. In order to exclude strain effects from the possible V-pit formation mechanism, tensely strained InAlN layers were grown on FS GaN substrates under the same growth conditions, except for a slightly higher growth temperature so as to obtain an indium content of 14%. In fact, hardly no V-pits are visible after a thickness of 100 nm as can be seen in Fig. 3.4 (g). The hillock morphology can though be recognized, with slightly larger hillocks (diameter ~ 130 nm). However, V-pits are visible after a thickness of 210 nm as shown in Fig. 3.4 (h), although no donut-like features appear. This means that both hillocks and V-pits cannot be ascribed to strain-related effects. In particular, Stranski-Krastanov island formation cannot account for those mechanisms as proposed by Krost *et al.* [185]. For comparison, a 50 nm thick LM $In_xAl_{1-x}N$ layer has been grown on sapphire (x = 17.6%). It also exhibits V-pits and hillocks as shown in Fig. 3.4 (i). Its V-pit density is $\sim 8 \times 10^8$ cm^{-2}, which is a bit higher than the TDD of a GaN buffer grown on sapphire. We thus ascribe hillock formation to kinetic roughening [186, 187], likely related to the small diffusion length of aluminum adatoms in this temperature range. We then propose that hillocks are at the origin of the V-pits: the hillock height and diameter increase when the InAlN layer thickness increases, and the hillocks eventually reach a height beyond which inclined facets between hillocks become stable, giving rise to V-defects. This is consistent with the fact that V-pits appear later for tensely strained layers, as their higher growth temperature yields an increased aluminum adatom diffusion length. This also accounts for the larger hillock size found in Fig. 3.4 (g).

Having explained the hillock and V-pit formation mechanism, we still have to describe into further details the critical crystalline quality degradation mechanism, which takes place at a thickness between 50 and 200 nm. This is illustrated in Fig. 3.6 (a), showing a high angle annular dark field scanning transmission electron microscope (HAADF STEM) cross-section image of a 500 nm thick LM InAlN layer. This is the same sample than that shown in Fig. 3.4 (e). As previously said, the V-pit diameter increases with the thickness, as the basal growth rate is faster than that on inclined facets. The indium incorporation is enhanced on the inner edges between facets of the V-pits, and decreased on the top of the outer edges of those V-pits, which is ascribed to a stronger bonding of indium adatoms on concave surfaces yielding a lower desorption rate, and *vice-versa* [184]. When V-pit coalescence occurs, columnar growth of In-rich V-pit edges and Al-rich V-pit sides is enabled, resulting in a layer with 4 different features: In-rich walls on the top of the inner V-pit edges, Al-rich walls on top of the V-pit outer edges, voids on top of the V-pits and nominal In composition elsewhere. An energy dispersive x-ray (EDX) cross-section mapping of aluminum (green) and indium (red) atoms in such a degraded InAlN layer is shown in Fig. 3.6 (b), evidencing the In-rich and Al-rich regions. A schematic drawing of this mechanism is shown in Fig. 3.6 (c). The huge surface roughness increase is evidenced in Fig. 3.6 (d), showing a HAADF STEM plan-view of the sample surface.

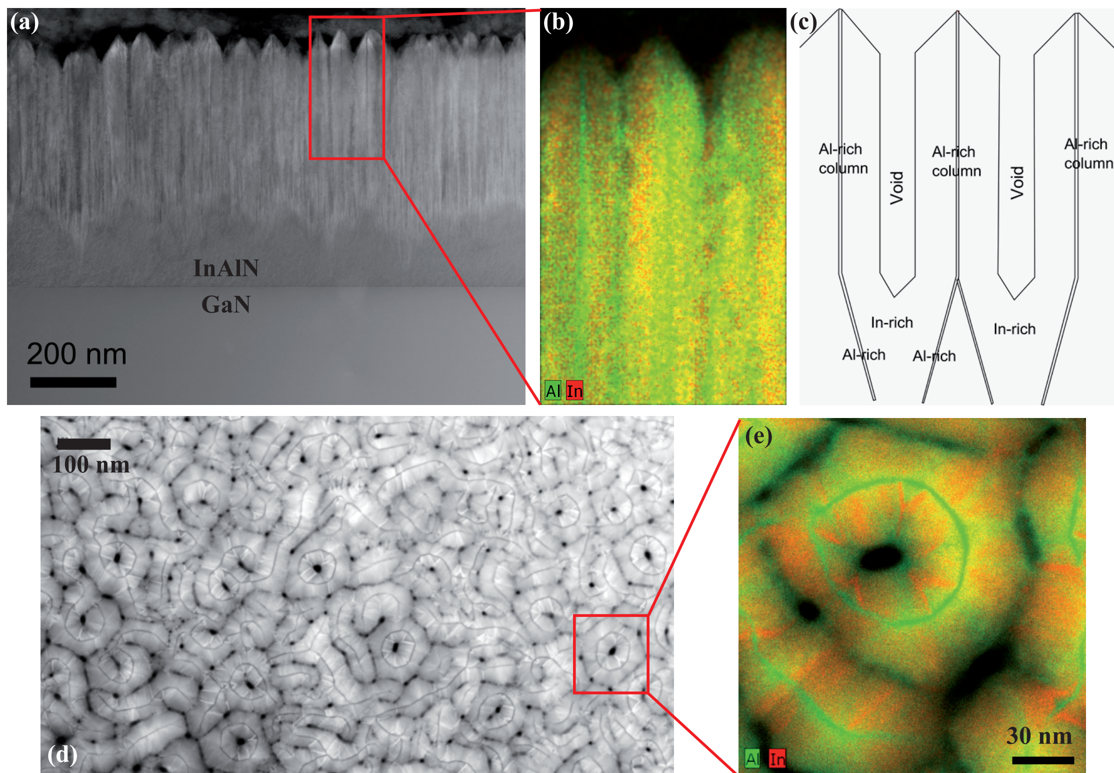

Figure 3.6: (a) HAADF STEM cross-section view of a 500 nm thick LM InAlN layer grown on FS GaN substrate. (b) Corresponding EDX map of indium (red) and aluminum (green) atoms and (c) schematic drawing. (d) HAADF STEM plan-view of the same sample at low magnification and (e) associated EDX mapping of indium (red) and aluminum (green) atoms at higher magnification. Courtesy of Dr. G. Périllat-Merceroz.

On an enlarged EDX mapping corresponding to this HAADF STEM plan view, green Al-rich walls and red In-rich edges are supporting this assumption, as can be seen in Fig. 3.6 (e). (All TEM images and EDX mapping have been performed by Dr. G. Périllat-Merceroz.)

However, as this critical crystalline quality degradation mechanism occurs only after a thickness larger than 50 nm, it does not impact on the quality of InAlN-based DBRs, though other parameters do affect their quality. They will be discussed hereafter.

3.4 Distributed Bragg reflectors

In this section InAlN-based DBRs are studied. First, DBRs grown on sapphire are introduced. Then, high quality highly reflective DBRs grown on FS GaN substrates are presented. Several parameters that strongly impact on the quality of such DBRs are addressed. Finally, DBRs for UV applications are described. Such DBRs are no longer strictly LM, as AlGaN layers replace GaN ones as the high refractive index material in order to achieve DBRs with a stopband position at wavelengths below the GaN bandgap without dramatically increasing absorption.

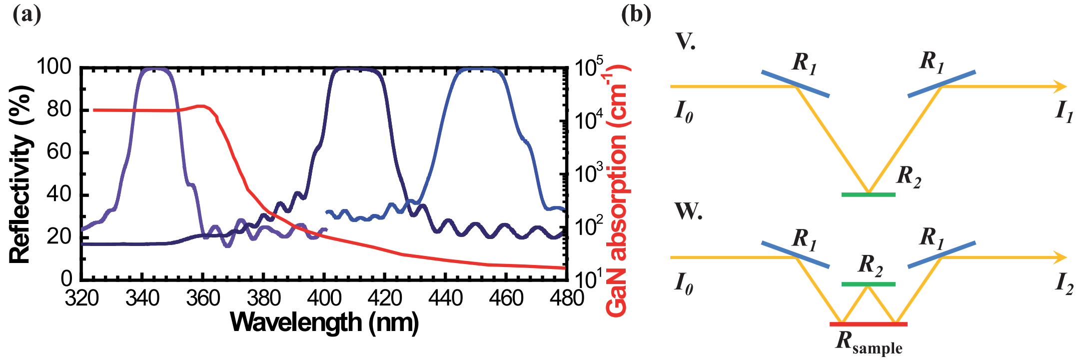

Figure 3.7: (a) InAlN-based DBR reflectivity spectra spanning the UV-blue wavelength range and GaN absorption (red curve) at 300 K as a function of the wavelength. (b) Schematic drawing of the V-W absolute reflectivity measurement. The fixed mirrors, movable mirror and sample of reflectivity R_1, R_2 and R_{sample}, respectively, are depicted in blue, green and red, respectively.

InAlN-based DBR reflectivity spectra with stopbands ranging from the UV to the blue regions are shown in Fig. 3.7 (a) together with the GaN absorption spectrum as a function of the wavelength at RT.

The reflectivity of the different DBRs are measured with a Varian Cary 500 spectrophotometer in V-W configuration, as schematically represented in Fig. 3.7 (b). Such a setup allows measuring the absolute value of the reflectivity at nearly normal incidence (~7°) without the need for a reference mirror of known reflectivity. It is made of one white light beam of intensity I_0 directed towards two fixed and one movable mirrors of reflectivity R_1 and R_2, respectively. First, the intensity of the light beam I_1 is measured in V-mode after reflecting on the 3 mirrors. Its value is given by $I_1 = R_1^2 \cdot R_2 \cdot I_0$. Then, the sample of reflectivity R_{sample} is introduced into the setup, which is set in W-mode [Fig. 3.7 (b)]. The intensity of the output beam I_2, after reflecting once on each mirror and twice onto the sample, is now given by $I_2 = R_1^2 \cdot R_2 \cdot R_{\text{sample}}^2 \cdot I_0$. The sample reflectivity is finally simply obtained by taking the square root of the ratio between intensities I_2 and I_1:

$$R_{\text{sample}} = \sqrt{\frac{I_2}{I_1}}. \tag{3.5}$$

Thereby, this setup allows measuring the absolute reflectivity value of the sample. Moreover, the Cary tool has two separate channels. The output value is then not the intensity of one beam but the ratio between the beams of both channels, which improves the measurement accuracy by taking into account lamp intensity fluctuations. However, such a measurement requires quite large and homogeneous samples, as the two reflections on the sample are about 1 cm apart, and each beam spot size on the sample is about 0.5 cm^2. Besides, transmission

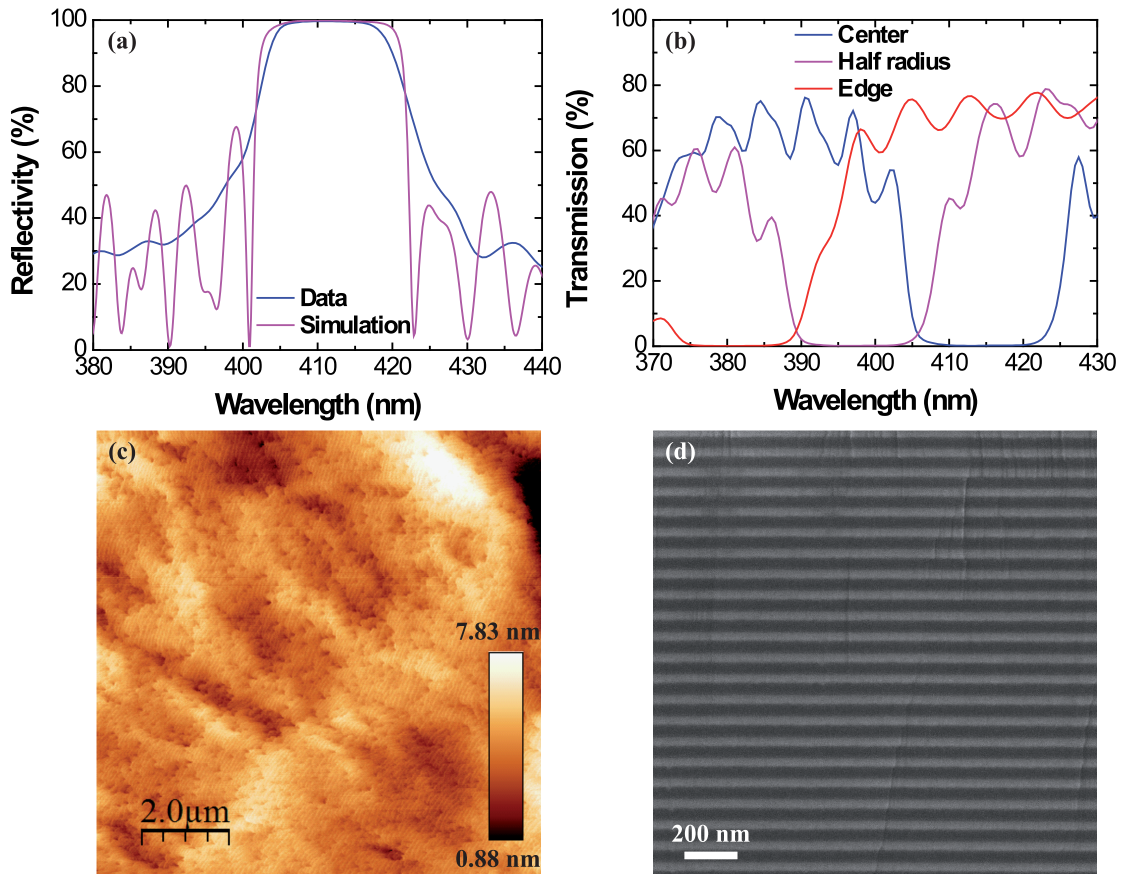

Figure 3.8: (a) Reflectivity spectrum measured on a 40-pair InAlN/GaN DBR grown on sapphire (blue curve) and corresponding transfer matrix simulation curve (violet curve). (b) Transmission spectra measured along the wafer radius exhibiting DBR stopband blueshift due to the growth wedge. (c) $10 \times 10\ \mu m^2$ AFM scan and (d) SEM cross-section view of this DBR.

measurements can also be performed using the Cary 500. Those measurements can be performed on much smaller samples as the beam spot size can be decreased down to a couple of mm^2. This has been used for instance for measuring the DBR stopband central wavelength as a function of the relative position to the center of the wafer.

3.4.1 DBRs grown on sapphire substrates

Standard InAlN-based DBRs on *c*-plane sapphire are grown on top of a 2 μm thick buffer with a TDD of the order of $\sim 8-10 \cdot 10^8$ cm^{-2} using TMIn and TMAl as metal precursors for InAlN, TEGa as metal precursor for GaN, and NH_3. The InAlN and GaN growth temperature (rate) is 835°C (~ 140 nm/h) and 1065°C (~ 700 nm/h), respectively. N_2 is used as carrier gas for both GaN and InAlN layers. The growth rates are calibrated in a separate run performed prior the the DBR growth using *in situ* reflectivity measurements to determine the thicknesses of thick InAlN and GaN layers.

The reflectivity of such a DBR made of 40 $In_{0.18}Al_{0.82}N/GaN$ bilayers is shown in Fig. 3.8 (a) (blue curve), together with the corresponding theoretical reflectivity spectrum obtained using transfer matrix simulation (violet curve). The indium content has been determined by XRD $\omega - 2\theta$ rocking curve measurements. The sample exhibits a peak reflectivity of 99.7% at a wavelength of 410 nm and a 26 nm wide stopband. This latter value might be slightly overestimated due to the fact that the reflectivity measurement probes two distinct areas on the sample whose stopbands are not exactly matching with each other, resulting in a slightly wider measured stopband value. This effect also accounts for the absence of side lobes on the reflectivity spectrum. As discussed in section 1.2, the wedge inherent to MOVPE growth results in a shift of the stopband central position along the wafer radius from 415 nm near the center to 380 nm near the edge, as shown in Fig. 3.8 (b). Note that the absorption value for this structure as could be deduced from the relation $A = 1 - R - T$ yields a large, overestimated, value because of the inhomogeneity of the area probed by the Cary setup. This results in a mean reflectivity value averaged over a broad area, that blurs the Bragg oscillations which should be visible on each side of the DBR stopband, as can be seen on the simulated reflectivity curve.

$10 \times 10\ \mu m^2$ AFM scan and SEM cross-section view of this DBR are depicted in Fig. 3.8 (c) and 3.8 (d), respectively. The interfaces between the different layers are nice and regular, but the top surface exhibits a rms roughness of ~ 1.0 nm due to the large TDD inherited from the GaN buffer. Whereas such structures are well-suited for RC-LED applications, their large TDD, important surface roughness and the low thermal conductivity of sapphire substrates are dramatically detrimental to the realization of VCSEL devices despite the high peak reflectivity achieved. Therefore, LM InAlN-based DBRs have been developed on *c*-plane FS GaN substrates.

3.4.2 DBRs grown on free-standing GaN substrates

DBR growth parameters on *c*-plane FS GaN substrates are exactly the same than that of DBRs grown on sapphire, except for a small tuning of the InAlN growth temperature setpoint, required as discussed previously. They are grown on 1 μm thick GaN buffer with a TDD of $\sim 4 \times 10^7\ cm^{-2}$.

The reflectivity of a 42-pair $In_{0.20}Al_{0.80}N/GaN$ DBR grown on a FS GaN substrate is shown in Fig. 3.9 (a) (blue curve), together with the corresponding theoretical reflectivity spectrum obtained using transfer matrix simulation (violet curve). Its peak reflectivity and stopband width amount to 99.6% at 424 nm and 26 nm, respectively. The wedge causes the same stopband position shift along the wafer radius as for DBRs grown on sapphire, as shown in Fig. 3.9 (b). Its central wavelength near the wafer center and the edge is 440 nm and 405 nm, respectively. As previously discussed for DBRs grown on sapphire, an estimation of the DBR absorption using the relation $A = 1 - R - T$ would yield an overestimated value, because of the inhomogeneity of the broad area probed by the reflectivity measurement setup.

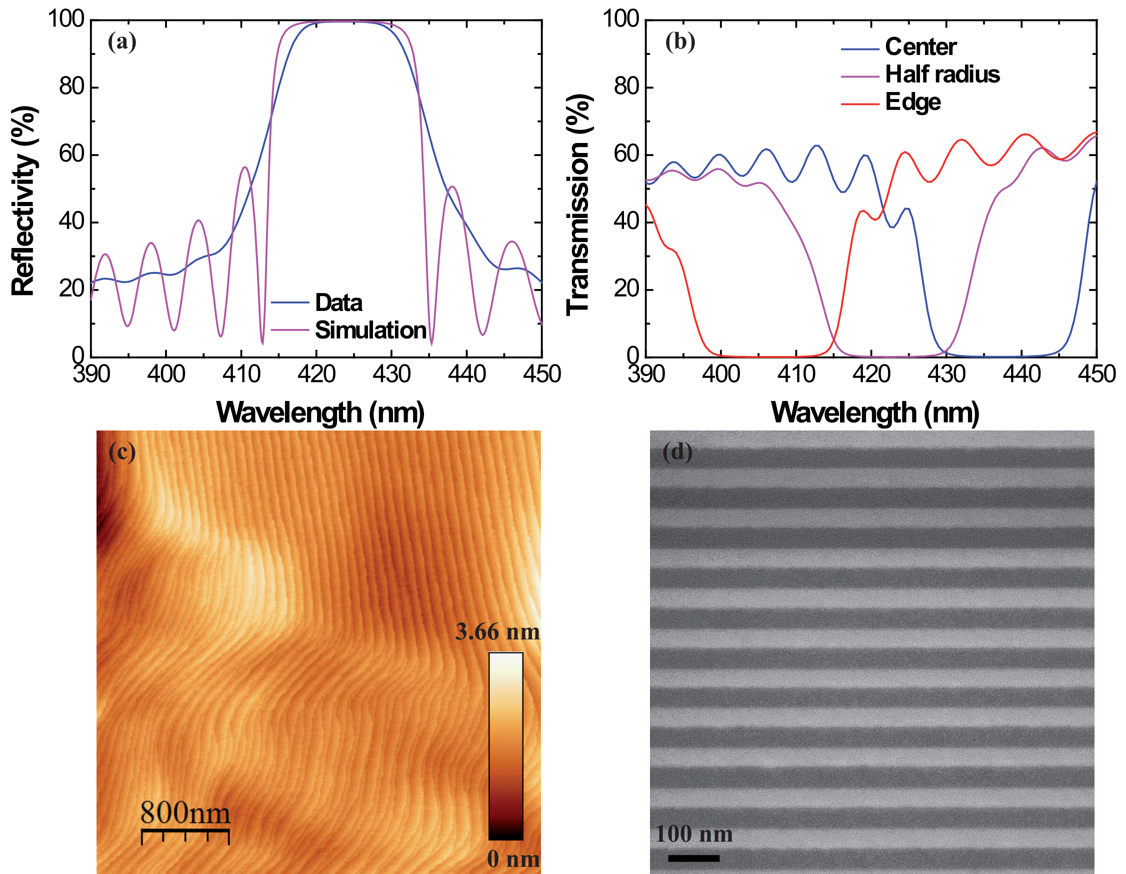

Figure 3.9: (a) Reflectivity spectrum measured on a 42-pair InAlN/GaN DBR grown on FS GaN (blue curve) and corresponding transfer matrix simulation curve (violet curve). (b) Transmission spectra measured along the wafer radius exhibiting a DBR stopband blueshift due to the growth wedge. (c) $4 \times 4\ \mu m^2$ AFM scan and (d) SEM cross-section view of this DBR.

$4 \times 4\ \mu m^2$ AFM scan and SEM cross-section view of the DBR are shown in Fig. 3.9 (c) and (d), respectively. Whereas the interfaces between the different layers are as smooth as those of DBRs grown on sapphire, the top surface now exhibits a much lower roughness. The rms roughness value is ~ 0.3 nm, which is almost that of a GaN buffer grown on FS GaN. Very regular monolayer steps can be seen in Fig. 3.9 (c). Moreover, the TDD, measured on a $10 \times 10\ \mu m^2$ AFM scan, equals that of the substrate nominal value. Thus, no further dislocations have been introduced during the DBR growth.

Another aspect of the growth of such DBRs on FS GaN substrates is worth being mentioned. As previously stated, the growth rates are calibrated through the growth of thick InAlN and GaN layers. When doing so, it could seem interesting to recycle the FS GaN wafer used for the calibration run. However, the required InAlN layer thickness is exceeding that at which critical degradation occurs. Thus, a DBR overgrown on such a calibration layer would exhibit a poor crystalline quality. An SEM cross-section view of such an InAlN calibration layer overgrown with a DBR is shown in Fig. 3.10 (a). Sawtooth-like features characterize the interface between

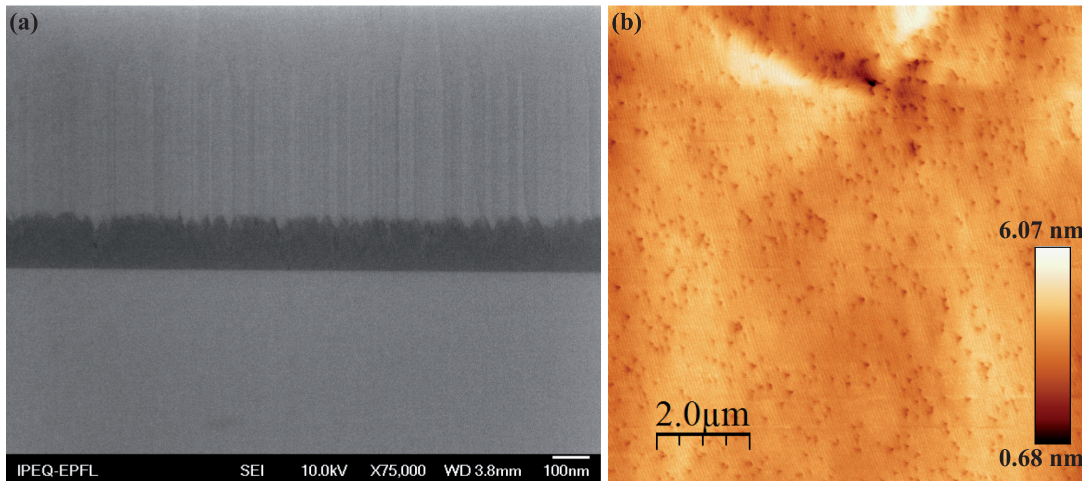

Figure 3.10: (a) SEM cross-section view of a 240 nm thick InAlN calibration layer grown prior to a DBR. (b) $10 \times 10\ \mu m^2$ AFM scan of the top surface of the DBR overgrown on the thick InAlN calibration layer.

this InAlN layer and the overgrown GaN layer. Finally, a $10 \times 10\ \mu m^2$ AFM scan of the top surface of the overgrown DBR is shown in Fig. 3.10 (b) and exhibits a huge TDD ($\sim 10^{10}$ cm^{-2}) as well as a large rms roughness ($\sim$ 1.0 nm). This cancels all the benefits of using a low dislocation density substrate. Therefore, the recycling of growth rate calibration samples should be avoided.

Effect of the indium precursor flux

The TMIn gas flow has been observed to have a critical impact on the crystalline quality of DBRs [151]. Indeed, a 42-pair LM InAlN/GaN DBR has been grown on a FS GaN substrate using standard growth parameters except for a lower indium precursor gas flux (180 instead of 350 sccm). The indium content has been determined to be 19.8% through XRD $\omega - 2\theta$ rocking curve measurement. The resulting sample peak reflectivity is decreased to only 98.6%, which is about 1% less than that of standard DBRs, corresponding to the value given by transfer matrix simulations. When having a closer look at the epitaxial structure using SEM for imaging the sample cross-section, the interfaces between InAlN and GaN layers reveal being very rough [Fig. 3.11 (a)]. On the other hand, the GaN-to-InAlN interfaces are much smoother thanks to the higher GaN growth temperature leading to a longer diffusion length of Ga adatoms that smoothens the surface. Moreover, the DBR stack exhibits a rough top surface (rms value of 1.2 nm) with a TDD of $\sim 7 \times 10^8$ cm^{-2} (more than one order of magnitude larger than that of the FS GaN substrate used for the growth), as shown in Fig. 3.11 (b). In addition, a careful study of the sample using a Nomarsky microscope reveals cracks, unlike standard LM InAlN/GaN DBRs.

Those discrepancies have been first tentatively ascribed to indium surface segregation. This

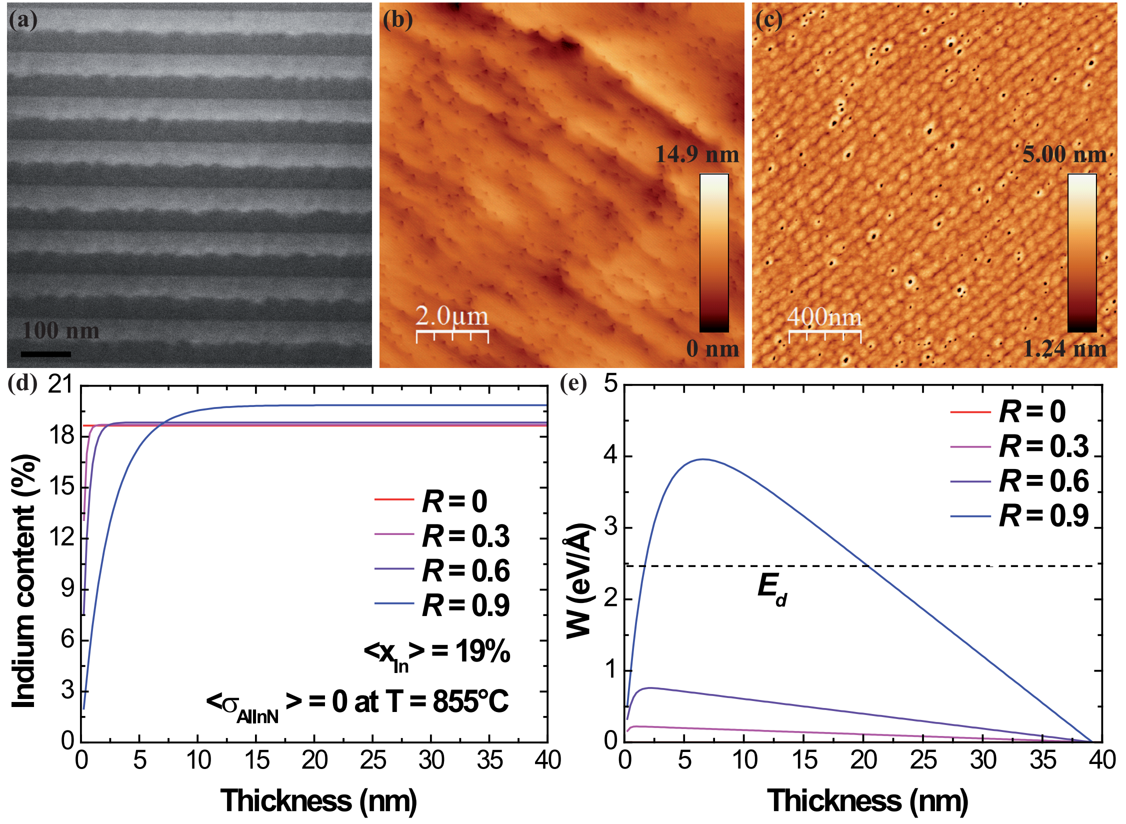

Figure 3.11: (a) SEM cross-section view and (b) $10 \times 10\ \mu m^2$ AFM scan of a DBR grown on a FS GaN substrate using a TMIn flux of 180 sccm. (c) $2 \times 2\ \mu m^2$ AFM scan of a 50 nm thick InAlN layer grown on a FS GaN substrate using a TMIn flux of 180 sccm. (d) Simulation of the indium content profiles in InAlN layers for different segregation coefficients R. (e) Corresponding work W done by the misfit stress field during the introduction of a misfit dislocation (per unit length of the dislocation) for each R value. The dotted line corresponds to the dislocation energy E_d itself.

phenomenon is well known to occur in indium-containing III-V ternary alloys [164] and can be described by a simple model [188]. The indium composition profile in $In_xAl_{1-x}N$ layers can be calculated from the expression

$$x_n = x_0\left(1 - R^n\right),\ (1 \le n \le N) \tag{3.6}$$

where x_n is the indium content in the nth ML, x_0 is the nominal indium content, R is the segregation coefficient, which gives the probability for an indium atom of the topmost ML to hop to the next ML, and N is the total number of MLs composing the InAlN layer. It has furthermore been assumed that indium atoms do not segregate to the GaN layers because of their larger growth temperature resulting in the evaporation of any indium excess at the

surface. Subsequently, the in-plane strain ε_{xx} and in-plane stress σ_{xx} (see Eq. 1.7) can be computed for each ML from the lattice parameter of the FS GaN substrate, the relaxed lattice parameter of each $In_{x_n}Al_{1-x_n}N$ ML (with x_n given by Eq. 3.6) and the elastic coefficients of InAlN, determined using Vegard's law from those of AlN and InN [18] (see section 1.1 for more details). The simulated indium composition profiles for several R coefficients calculated through Eq. 3.6 have been plotted in Fig. 3.11 (d). Due to the thermal expansion coefficient difference between InAlN and GaN layers, an average indium content of 19% is required in order to obtain an overall stress $\sigma_{\text{InAlN}} = 0$ at InAlN growth temperature. Note that the actual segregation coefficient has not been determined experimentally but it is likely very high ($R \sim 0.8 - 0.9$) if one considers the different hopping rates and atom sizes of Al and In species [189]. According to Fig. 3.11 (d), the first few InAlN MLs exhibit a very low indium content, resulting in a sublayer with a high built-in tensile strain, whose thickness strongly depends on the R coefficient. Thus, for large R values, the low In containing sublayer might eventually exceed the critical thickness at which plastic relaxation occurs. Thereby, an estimate of this critical thickness has been made using the model proposed by Holec and coworkers [27], which compares the work W done by the misfit stress field during the introduction of a misfit dislocation to the energy of the dislocation E_d itself. The critical thickness is thus reached when W exceeds E_d. As the larger R the thicker the low In containing InAlN sublayer, the critical thickness can eventually be reached in the case of large segregation coefficients, e.g. for $R = 0.9$ as shown in Fig. 3.11 (e). The poor crystalline quality of the DBR grown with a low TMIn flux could therefore be ascribed to a larger indium surface segregation phenomenon.

In order to further investigate this effect, a 50 nm thick LM InAlN layer has been grown on a FS GaN substrate using standard growth conditions except for a lower TMIn flux (180 sccm). A 2×2 μm^2 AFM scan of this sample is shown in Fig. 3.11 (c). It exhibits the same surface morphology made of hillocks aligned along ML steps as that of a similar sample grown using a 350 sccm TMIn flux [Fig. 3.4 (b)], although it suffers from a much larger V-pit density of $\sim 5 \times 10^9$ cm^{-2}. However, a careful TEM investigation reveals that those V-pits are not related to dislocation terminations, and that the TDD of the sample is of the same order of magnitude than that of the underneath FS GaN substrate. Therefore, another explanation could be related to the surfactant effect of In adatoms that reduces the kinetic roughening of InAlN layers [190, 191, 192, 193]. Thereby, the lower the TMIn flux the lower the In surfactant effect and thus the thinner the InAlN layer before the formation of V-pits. This is consistent with the fact that hillocks are smaller for the sample grown using a TMIn flux of 180 sccm (~ 90 nm) than those of the sample with a similar thickness using standard growth parameters (~ 100 nm).

Actually, both explanations could be partially correct and further experiments are required in order to fully understand the precise mechanism behind the effect of the TMIn flux on the crystalline quality of LM InAlN layers.

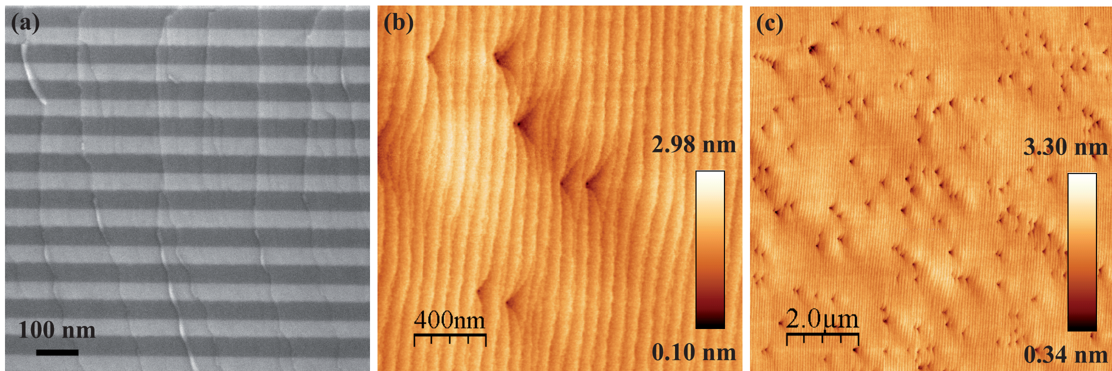

Figure 3.12: (a) SEM cross-section view, (b) 2×2 μm^2 and (c) 10×10 μm^2 AFM scans of a compressively strained 42-pair $In_xAl_{1-x}N/GaN$ DBR with $x \approx 21.3\%$.

Excess of indium in InAlN layers

It has been said previously that $In_xAl_{1-x}N$-based DBRs grown under tensile strain (i.e. with $x <$ 18% on FS GaN substrates) suffer from cracks. Conversely, an excess of indium in $In_xAl_{1-x}N$ layers is also detrimental to the crystalline quality of the DBR stack. As an example, a DBR has been grown with an indium content $x = 21.3\%$. Although an SEM cross-section view reveals homogeneous layers and smooth interfaces as shown in Fig. 3.12 (a), and the top surface exhibits a rms roughness of 0.25 nm measured on 2×2 μm^2 and 10×10 μm^2 AFM scans as depicted in Figs. 3.12 (b) and 3.12 (c), respectively, those AFM measurements also reveal a high TDD ($\sim 2 \times 10^8$ cm^{-2}), which is nearly one order of magnitude larger than that of the FS GaN substrate used for the growth. This high TDD is thus ascribed to the compressive strain resulting from an indium content $x = 21.3\%$. Thereby, indium content in LM InAlN-based DBRs grown on FS GaN substrates should be kept below 20.5%, as for that composition the DBR growth has proven to still avoid the formation of additional dislocations.

Substrate quality and photonic disorder

An element of relevant interest concerns the photonic disorder found in such DBRs. Actually, we found that this photonic disorder is strongly impacted by the quality of the FS GaN substrate used for the growth. In order to evidence this, two 42-pair InAlN/GaN DBRs have been grown on two different *c*-plane FS GaN substrates, one high quality wafer (TDD $\sim 1 \times 10^6$ cm^{-2}) and one intermediate quality wafer (TDD $\sim 4 \times 10^7$ cm^{-2}). The same standard growth conditions were employed for both samples, except for a slight variation in the layer thicknesses resulting in a stopband shift of ~20 nm. In order to quantify the photonic disorder, a dielectric 7-pair ZrO_2/SiO_2 DBR has been deposited via e-beam evaporation (see section 5.2 for more details) resulting in $\lambda/2$ GaN-ZrO_2 cavities. Afterwards the in-plane photonic disorder, which is directly linked to the DBR structural and optical properties, has been probed through two-dimensional micro-transmission mappings using the continuous spectrum of a xenon lamp as the incident light source. The light was focused in a ~2 μm wide circular spot onto the sample using a

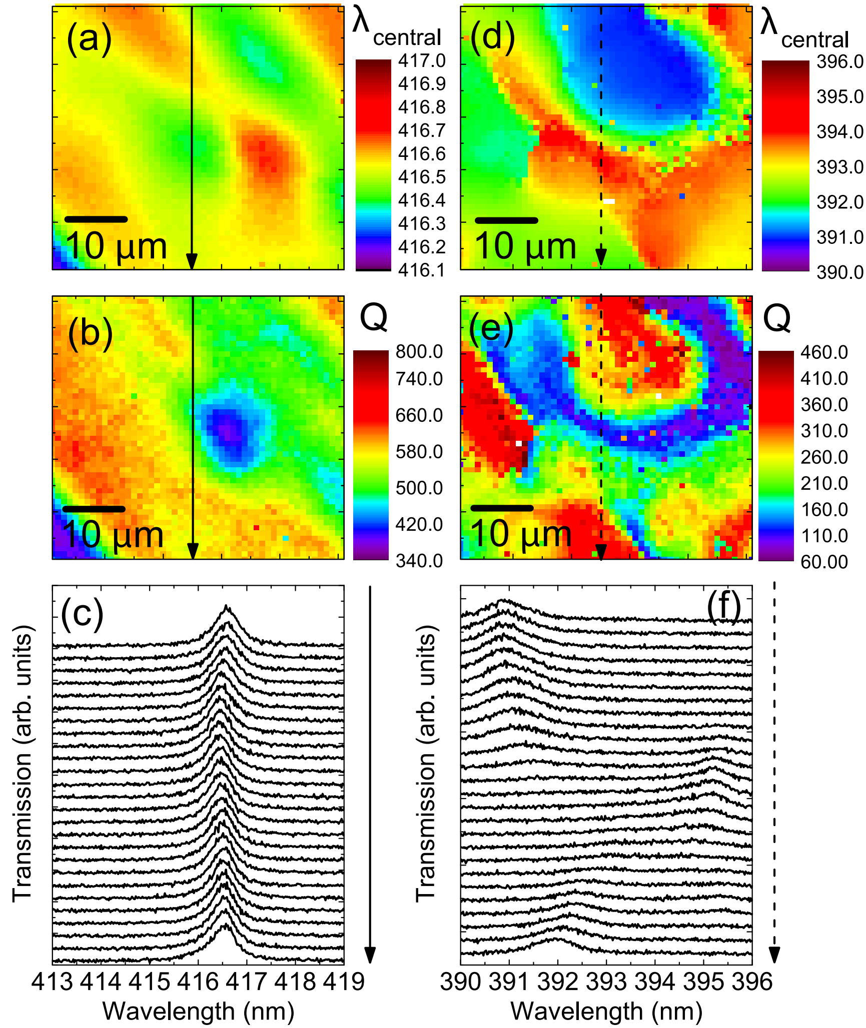

Figure 3.13: (a) and (d) micro-transmission mappings ($50 \times 50\ \mu m^2$) of the cavity mode wavelength, (b) and (e) corresponding cavity quality factor Q, and (c) and (f) transmission spectra recorded every 2 μm along the continuous and the dashed arrow on a cold cavity formed on top of a DBR structure grown on a high quality FS GaN substrate (left-hand side column) and on an intermediate quality FS GaN substrate (right-hand side column), respectively. Courtesy of M. Glauser.

long working distance near UV microscope objective ($\times$100) with a numerical aperture of 0.5. The transmitted light was then collected by a UV fiber in far-field configuration ensuring an angular selection of ~0.6°. Transmission spectra of the cavities have been acquired every micron over a $50 \times 50\ \mu m^2$ area (Fig. 3.13). For the DBR structure grown on the low dislocation density substrate (Fig. 3.13, left-hand side column) a low photonic disorder is observed. The cavity mode position is fluctuating by ±0.45 nm (~0.1%) and can be related to cavity thickness variations of ±1 nm, which is similar to the rms surface roughness determined by AFM. The quality factor (Q) for the microcavity grown onto the high-quality FS GaN substrate reaches

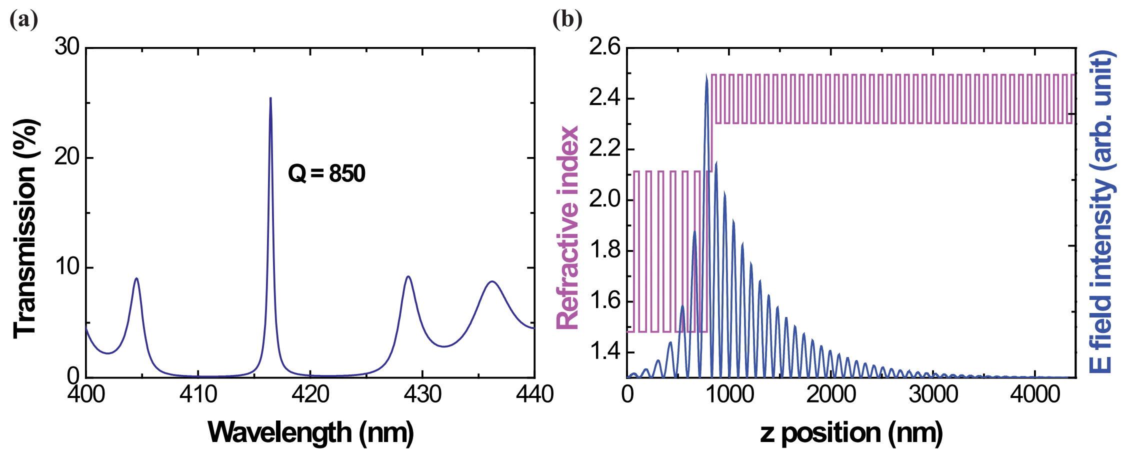

Figure 3.14: (a) Transmission spectrum of the $\lambda/2$ GaN-ZrO_2 cavity obtained using transfer matrix simulation and (b) the corresponding electric field intensity distribution along the cavity axis.

values up to 800 matching those deduced from transfer matrix simulations [Fig. 3.14]. On the other hand, for the DBR structure grown onto the intermediate dislocation density substrate (Fig. 3.13, right-hand side column), the photonic disorder is considerably increased. The Q factor only amounts to half that of the former one whereas an identical value was expected *a priori*. The difference between both samples is ascribed to different surface preparations and deficient miscut angle control over the whole wafer for the intermediate quality substrate.

Impact of a temperature ramp on InAlN layers

Another point that has to be stressed once more concerning the growth of InAlN-based DBRs is the large growth temperature difference between GaN (about 1065°C) and InAlN (about 850°C). This means that when considering the most basic approach for growing such DBRs the surface of each InAlN layer is subject to a temperature ramp up to 1065°C. Gadanecz *et al.* reported that LM InAlN layers are stable at temperatures exceeding InAlN growth temperature [194], which is confirmed by our experiments. Indeed, the growth of GaN-based cavities subsequent to that of InAlN-based DBRs is performed at temperatures higher than that used for growing InAlN layers. Nevertheless, we have not seen any sign of InAlN layer degradation once capped with a GaN layer. However, such an annealing step has a strong impact on the InAlN surface morphology [195]. Even if DBR interfaces between the different layers seem smooth and homogeneous using SEM [Fig. 3.9 (d)], a closer look using HAADF STEM reveals some dark lines at the InAlN/GaN interfaces, suggesting that indium desorption occurs during this temperature ramp. In order to further evidence this fact, a 50 nm thick LM InAlN layer has been grown on a FS GaN substrate under the same growth conditions than for those inserted in DBRs. This layer was subject to an *in situ* annealing step up to 1065°C for two minutes. Figure 3.15 (b) shows a 2×2 μm^2 AFM scan of the surface of this layer and can be compared to the unannealed sample presented in Fig. 3.4 (b). The surface morphology changed from small

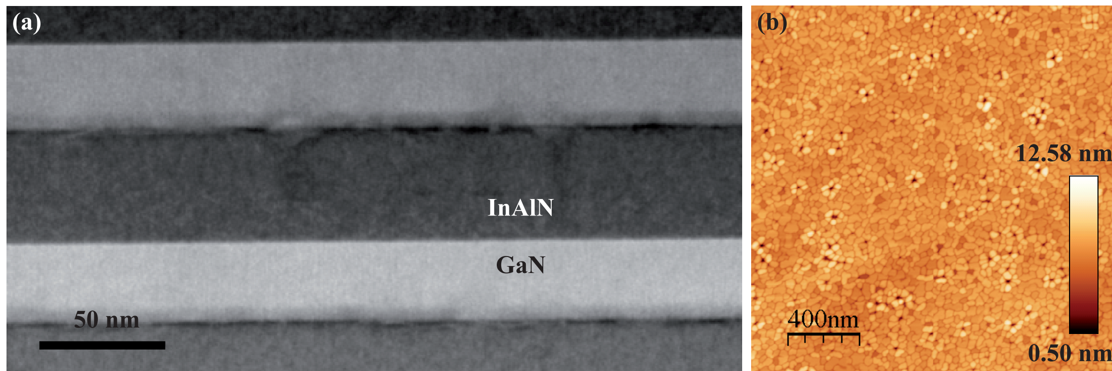

Figure 3.15: (a) Detailed HAADF STEM cross-section view of InAlN/GaN interfaces in DBRs (courtesy of Dr. G Périllat-Merceroz). (b) $2 \times 2\ \mu m^2$ AFM scan of a 50 nm thick LM InAlN after *in situ* annealing.

hillocks aligned along the atomic steps to a mesh of small cracks. To circumvent this drawback, Sadler and coworkers proposed two solutions for the growth of GaN layers used in DBRs [196]. The whole GaN layers can be grown at low temperature but it results in a finger-like GaN surface morphology, which is detrimental to the reflectivity of the DBRs. The second approach relies on the low temperature growth of a thin GaN sublayer followed by a temperature ramp and the subsequent growth of GaN at high temperature. This latter method seems much more promising since it should not alter the GaN surface morphology while preventing indium desorption at each InAlN/GaN interface. We have not experimented this technique yet but it is thought to enable further improvement of the quality of our DBRs and will be tried out during the growth of forthcoming DBR samples.

3.4.3 UV DBRs for cavity polariton study and UV VCSELs

UV DBRs proved to be key building blocks in order to achieve lasing in III-nitride microcavities. In such structures the coupling strength between the cavity photon mode and the excitons in the active material overcomes their damping rates, allowing the system to enter into a non-perturbative regime, the so-called strong-coupling regime (SCR). The new eigenmodes of the system are then the lower and upper polaritons. In the low density limit, these quasiparticles behave as bosons and polariton condensation is triggered when the ground state occupancy exceeds unity. The spontaneous decay of this macroscopic quantum state results in a nonlinear coherent emission often referred to as polariton lasing which is expected to happen at a lower threshold current density than in the case of the conventional stimulated emission ruled by the Bernard-Durrafourg condition as it is the case for VCSELs [197]. An appropriate choice for the active medium to perform SCR studies is the spectrally narrow excitonic transition of bulk GaN or that of GaN/AlGaN QWs [198]. Such an active medium requires UV DBRs. However, as the GaN absorption edge is around 375 nm [Fig. 3.7 (a)], AlGaN has to be substituted to GaN in UV DBRs. Indeed AlGaN can be grown LM to $In_xAl_{1-x}N$ by decreasing the indium content in the latter material ($x < 18\%$). A 35-pair $In_{0.15}Al_{0.85}N/Al_{0.2}Ga_{0.8}N$ DBR exhibiting a peak reflectivity

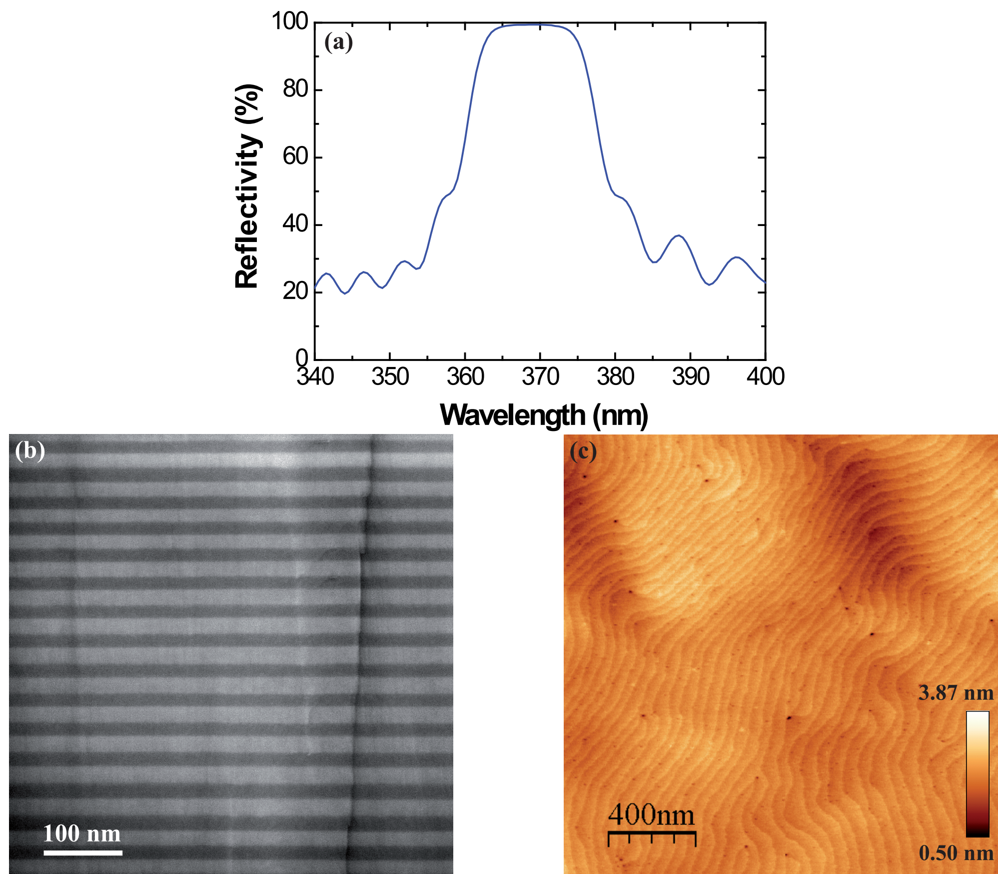

Figure 3.16: (a) Reflectivity spectrum of a 40-pair InAlN/AlGaN UV DBR, exhibiting a peak reflectivity of 99.5% at 370 nm. (b) SEM cross-section view and (c) 2×2 μm^2 AFM scan of this DBR.

of 99.3% at 340 nm has been reported [150]. As the DBR is not LM anymore to the GaN buffer layer a strain engineering solution relying on the use of short period GaN/AlN superlattices has been successfully employed to avoid the formation of cracks [150]. Moreover, the strain inherent to the use of AlGaN/InAlN bilayers grown on GaN buffers invalidates the use of high quality FS GaN substrates, meaning that the growth of such UV DBRs are performed on sapphire substrates. Nevertheless, when completed by a top dielectric DBR, high quality factor cavities can be formed. This way polariton lasing under optical pumping has been observed in such cavities using either bulk GaN as active medium [17] or GaN/AlGaN MQWs [152], which offer the advantage of a larger exciton binding energy and oscillator strength compared with their bulk counterpart.

Another active medium of interest for achieving RT polariton lasing is ZnO [199, 200]. Thanks to a lattice parameter close to that of GaN, ZnO-based microcavities can be grown on nitride-based epitaxial DBRs, which makes UV AlGaN/InAlN DBRs suitable candidates as bottom mirrors. In the frame of a collaboration with the CNRS-CRHEA in Valbonne (France), a 40-pair AlGaN/InAlN UV DBR has been grown on sapphire so as to be used as the bottom DBR for

such a ZnO microcavity. It exhibits a peak reflectivity of 99.5% at 370 nm and a stopband width of 21 nm [Fig. 3.16 (a)]. The DBR stack interfaces are smooth and the layers regular, as can be seen in Fig. 3.16 (b). However, the strain resulting from the use of AlGaN/InAlN bilayers result in a rather large TDD of $\sim 1 \times 10^{10}$ cm^{-2} despite a rather smooth surface (rms roughness of 0.60 nm) as determined with a 2×2 μm^2 AFM scan [Fig. 3.16 (c)]. Such UV DBRs would be also suited for the development of nitride-based VCSELs emitting in the UV range, e.g. using *n*- and *p*-type [201] doped InAlN to realize the *p*-*n* junction.

3.5 Further improvements

We have demonstrated high quality highly reflective LM InAlN/GaN DBRs grown on low dislocation density FS GaN substrates. Such epitaxial structures exhibit a high peak reflectivity above 99.5% while preserving the high crystalline quality of the underlying FS GaN substrate, which makes them candidates of choice for the realization of monolithic microcavities for VCSEL, VECSEL and polariton laser applications. However, further improvements can be introduced. As previously discussed, the temperature ramp up to 1065° after the growth of each InAlN layer degrades the quality of the corresponding interfaces. By introducing an additional low temperature GaN growth step at those interfaces, the overall quality of our DBRs could be further improved. This would most probably reduce the photonic disorder in our DBR cold cavities. Another interesting progress would be to introduce InAlN doping in order to obtain conductive DBR stacks, which would be a critical advance for microcavity-based optoelectronic devices as it would prevent the need for intra-cavity contacts. Whereas InAlN *n*-type doping seems quite straightforward as InAlN is intrinsically *n*-type because of the residual impurities, the main drawback in *n*-type DBRs would be to achieve efficient vertical transport of carriers through InAlN/GaN interfaces, because of the large conduction band offset between InAlN and GaN [202] as well as the free charge planes appearing at the interfaces due to the polarization mismatch between InAlN and GaN layers. This is actually an issue shared with InAlN layers used as claddings in LDs [158, 159, 160]. On the other hand, achieving efficient *p*-type doping of InAlN-based DBRs would be much more challenging, although *p*-doped InAlN has been demonstrated recently in our laboratory [201]. Finally, another route to explore would be the development and study of semi-polar and/or non-polar InAlN layers. Devices using such DBRs would have the noticeable property to exhibit a reduced QCSE in their QW-based active region. This would not only increase the oscillator strength of the QWs, but it could also result in new device properties. Thus recently, a non-polar VCSEL has been demonstrated, which exhibits polarization-locked light emission inherited from the in-plane crystalline anisotropy of the QWs [114]. In addition, a non-polar microcavity has been reported to exhibit the coexistence of strong and weak coupling regimes owing to the anisotropy of the active region [203]. However, the in-plane lattice parameter anisotropy along such an orientation would not allow for perfectly LM conditions to GaN contrarily to the situation occurring along the *c*-axis. We would rather refer to strain minimization instead.

4 Transparent conductive oxides as *p*-type contacts

In this chapter, TCO contacts to *p*-type GaN are studied. The basics about metal-semiconductor contacts are first summarized. Then, the properties of the main TCO materials are listed. Finally, the issues and challenges when using TCOs as *p*-type contacts to GaN are addressed. Several TCOs and deposition techniques are investigated, the effect of inserting a thin metallic interlayer on the contact properties are discussed and finally high quality transparent conductive sputtered ITO contacts developed by Evatec are presented as potential candidates for being used as current spreading layers in VCSEL structures.

4.1 Metal-semiconductor contacts

Metal-semiconductor contacts are a key element for the realization of many types of electronic and optoelectronic devices. The energy required for an electron to be extracted from of the metal, or in other words the work that the outside system has to do in order to remove one of the electrons out of the metal, is called the metal work function $q\phi_M$. It is defined as:

$$q\phi_M = E_0 - E_F \tag{4.1}$$

where E_0 is the vacuum energy level and E_F is the Fermi energy level of the metal. When two metals with different $q\phi_M$ are brought in contact with each other, at thermal equilibrium the energy levels of both metals must coincide. As a consequence, a potential difference called contact potential will appear at their interface. This will cause free carriers to redistribute in both layers in order to equalize potentials on each side of the interface, in other words so as to align Fermi levels. However, as the free carrier density in metals is very large, this carrier redistribution is done within a very short distance called the Debye screening length, and the free carrier density variations on either sides of the interface are not significant in terms of electrical conduction (no depletion or accumulation region appears).

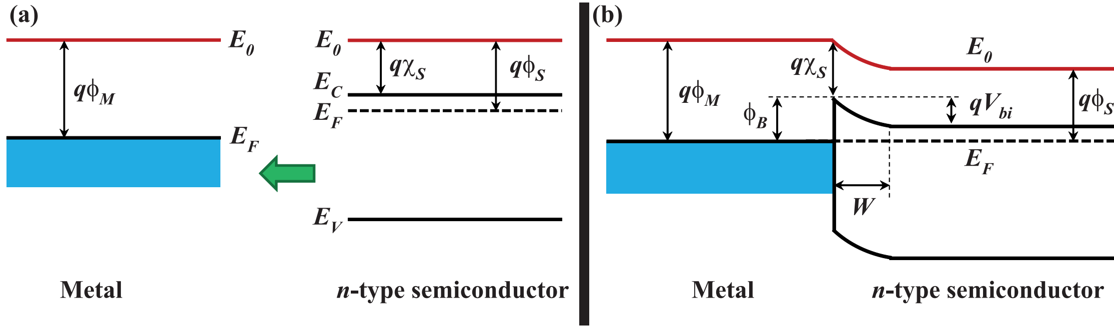

Figure 4.1: Energy-band diagrams of a metal-semiconductor system (a) before and (b) after being contacted.

Similarly, the same phenomenon happens when a metal and a semiconductor are brought into intimate contact. The semiconductor work function $q\phi_S$ is defined as:

$$q\phi_S = q\left(\chi_S + V_n\right) \tag{4.2}$$

where $q\chi_S$ is the semiconductor electron affinity, measured from the top of the conduction band E_C to the vacuum level E_0, and qV_n is the difference between the top of the conduction band E_C and the semiconductor Fermi level E_F. Therefore, a contact potential $q\phi_M - q\left(\chi_S + V_n\right)$ will build at the metal-semiconductor interface.

4.1.1 Band alignment

The contact potential causes charges with opposite signs to build up on each side of the interface. While the free carrier concentration in metals is large, that in semiconductors is relatively low. Thus, a depletion or an accumulation region appears at the surface of the semiconductor within a distance W. This accumulation of positive or negative charges (depending on the semiconductor type, *p* or *n*, and the contact potential sign) will cause energy band bending. This effect is illustrated in Fig. 4.1 for a contact potential $q\phi_M - q\left(\chi_S + V_n\right) > 0$ in the case of a *n*-type semiconductor. This band bending leads to the formation of an energy barrier at the metal-semiconductor interface whose height $q\phi_{B_n}$ is given by:

$$q\phi_{B_n} = q\left(\phi_M - \chi_S\right) \tag{4.3}$$

which is simply the difference between the metal work function and the semiconductor electron affinity, in the limiting case where there is no surface state at the semiconductor surface. The barrier height $q\phi_{B_p}$ in the case of an ideal contact between a metal and a *p*-type

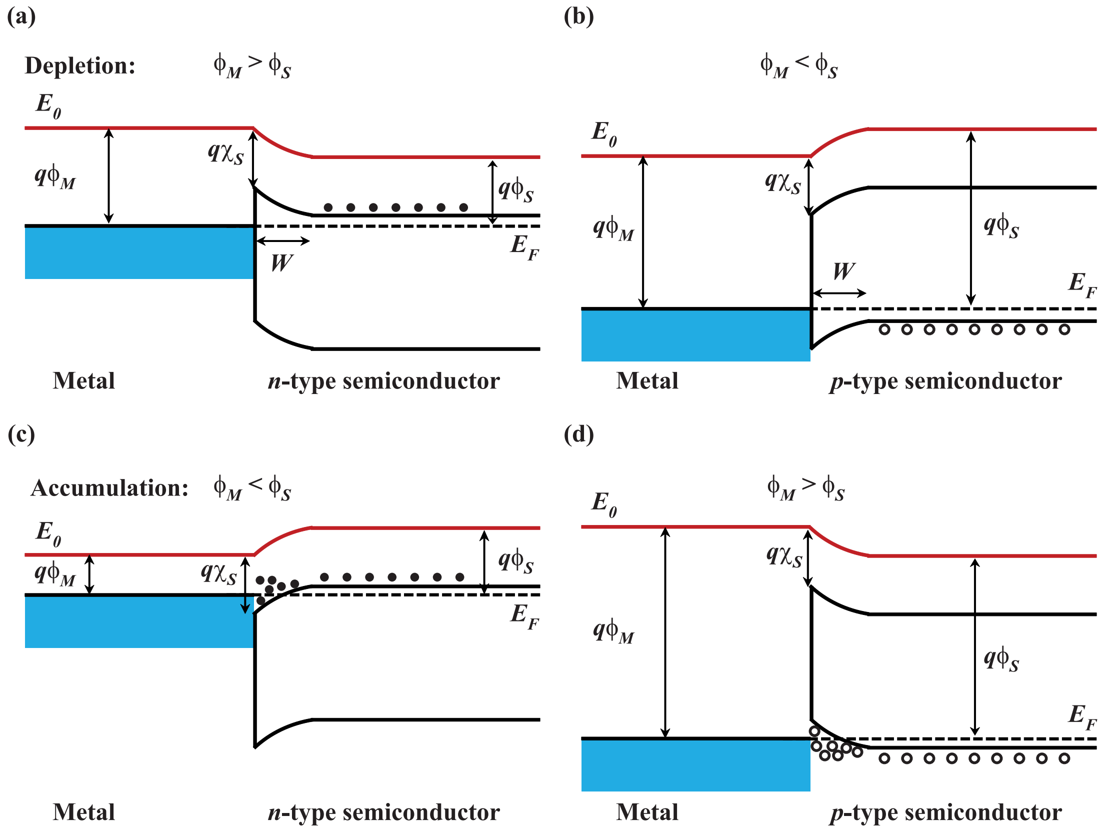

Figure 4.2: Energy-band diagrams of metal-n-[(a) and (c)] or p-[(b) and (d)] type semiconductor contacts. Depending on the difference between work functions of the metal $q\phi_M$ and of the semiconductor $q\phi_S$, the band bending results in either a depletion [(a) and (b)] or an accumulation [(c) and (d)] of charges at the metal-semiconductor interface.

semiconductor is given by:

$$q\phi_{B_p} = E_g - q\left(\phi_M - \chi_S\right) \tag{4.4}$$

where E_g is the bandgap energy of the semiconductor. Therefore, for a given semiconductor and any metal, the sum of the barrier heights on n- and p-type semiconductor is expected to be equal to the bandgap:

$$q\left(\phi_{B_n} + \phi_{B_p}\right) = E_g\,. \tag{4.5}$$

Henceforth, several cases may arise depending on the sign of the contact potential and on the semiconductor doping type, which are depicted in Fig. 4.2. A depleted region W appears when

$\phi_M > \phi_S$ (*n*-type semiconductor) or $\phi_M < \phi_S$ (*p*-type semiconductor), as shown in Figs. 4.2 (a) and 4.2 (b), respectively. On the other hand, a charge accumulation region will build up if $\phi_M < \phi_S$ (*n*-type semiconductor) or $\phi_M > \phi_S$ (*p*-type semiconductor), as can be seen in Figs. 4.2 (c) and 4.2 (d), respectively. In the depletion cases, carriers will have to overcome an energy barrier in order to pass through the metal-semiconductor interface. This results in so-called Schottky contacts, which behave like diodes, i.e. they exhibit a rectifying behavior. On the other hand, a perfect ohmic behavior is obtained in the accumulation cases.

In the case $\phi_M > \phi_S$ (*n*-type semiconductor), the depletion width W is given under the abrupt approximation that $\rho \approx qN_D$ (i.e. donors are assumed to be fully ionized) for $x < W$ and $\rho \approx 0$ and $dV/dx \approx 0$ for $x > W$ by:

$$W = \sqrt{\frac{2\epsilon_S}{qN_D}\left(V_{bi} - V - \frac{kT}{q}\right)} \tag{4.6}$$

where N_D is the donor impurity density, $\epsilon_S = \epsilon_r \epsilon_0$ is the semiconductor permittivity, and kT is the thermal energy. Thus, increasing the doping level eventually decreases the depletion width.

In the second limiting case, a large density of surface states is present on top of the semiconductor surface. If this density of surface states is large enough to accommodate all additional charges resulting from the contact potential, the space charge in the semiconductor remains unaffected and the barrier height is determined solely by the semiconductor surface properties. Thus, surface preparation prior to the formation of metallic contacts to any semiconductor is a key parameter.

According to Eq. 4.4, the barrier height on a *p*-type semiconductor is proportional to its bandgap E_g and is not affected by the doping level. Therefore, the realization of ohmic contacts to wide bandgap *p*-type semiconductors is quite challenging, as the highest work functions amongst metals are around $\sim 5.5eV$. Table 4.1 gives the values of the work functions for several metals often used as contacts to *n*- and *p*-type GaN [204].

Table 4.1: Work functions for several metals [204]. All values are given in eV.

Metal	$q\phi_M$
Al	4.28
Au	5.1
Ni	5.15
Pd	5.12
Pt	5.65
Ti	4.33

Table 4.2: Typical values for the electronic properties of *n*- and *p*-type GaN [205]. All values are given in eV.

	$q\chi_S$	$q\phi_S$
n-GaN	3.5 ± 0.1	4.3 ± 0.1
p-GaN	3.5 ± 0.1	5.9 ± 0.1

In this context, obtaining ohmic contacts to *p*-type GaN is rather challenging. Electron affinity $q\chi_S$ and typical values of the work function $q\phi_S$ for *n*- and *p*-type GaN are given in Table 4.2 [205]. Note that the semiconductor work function depends upon its doping level. Aluminum, titanium or multilayers made of both metals are often used as ohmic contacts to *n*-type GaN [206, 207, 208]. On the other hand, no real ohmic contacts can be achieved with *p*-type GaN. Nevertheless, by using proper cap layer and contact post-deposition annealing, contacts to *p*-type GaN with quasi ohmic behavior can be obtained using palladium, gold, nickel or platinum [209, 210, 211, 212, 213]. The optimization of ohmic-like contacts to *p*-type type GaN has been extensively studied. Typical values for the specific resistance of metallic contacts to *p*-type GaN are in the range of $\sim 2 \cdot 10^{-5}$ up to $\sim 4 - 510^{-4}$ Ωcm^2 [214, 215]. The effect of a heavily doped cap layer on carrier transport through the metal-semiconductor Schottky contact will be discussed in the next section.

4.1.2 Transport processes

As previously said, the barrier height in a Schottky contact between a metal and a semiconductor is determined by the metal work function, the semiconductor electron affinity and, in the case of a *p*-type semiconductor, its bandgap (cf. Eqs. 4.3 and 4.4). Thus, the barrier height cannot be influenced by the doping level. However, as will be discussed in this section, the latter can indeed impact on the carrier transport through a Schottky contact, and thus ohmic behavior can be achieved using a proper doping profile.

Unlike *p*-*n* junctions, the current transport in metal-semiconductor Schottky contacts is mainly due to majority carriers, and is ascribed to four main basic transport processes under forward bias [216]. Those processes are depicted in Fig. 4.3 for an *n*-type semiconductor and are (1) the transport of carriers from the semiconductor over the barrier into the metal, which is the dominant mechanism for moderately doped semiconductors operated at moderate temperatures, (2) quantum-mechanical tunneling of carriers through the barrier, which is important for heavily-doped semiconductors, (3) recombination in the space-charge region and (4) recombination in the neutral region, which can be seen as hole injection from the metal to the semiconductor. The inverse processes occur under reverse bias.

In a Schottky diode, the first process will be the most important one resulting in a nearly ideal behavior, the three other processes causing departure from this ideal behavior. On the other hand, the dominating mechanism in a quasi-ohmic contact will be tunneling through the

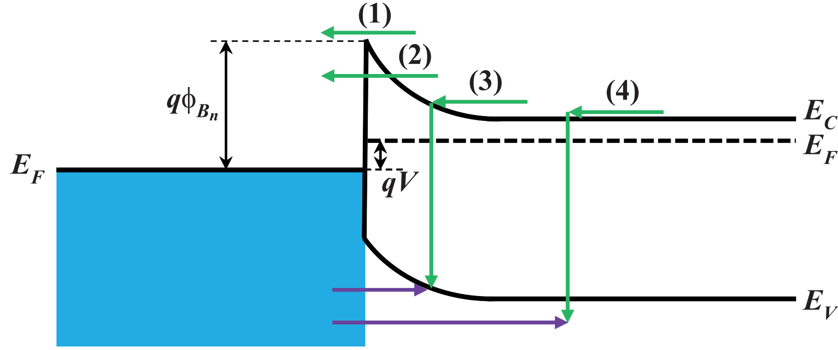

Figure 4.3: Schematization of the four basic transport processes at play in a Schottky barrier diode under forward bias V: (1) transport of carriers over the barrier $q\phi_{B_n}$, (2) tunneling of carriers through the barrier or (thermionic-) field emission, (3) recombination of carriers in the space-charge region and (4) recombination in the neutral region [216].

barrier. Field emission and thermionic-field emission theory in Schottky barriers has been pioneered by Padovani and Stratton [217]. The tunneling current density J_t is a quite complex expression, but essentially it has the form:

$$J_t \propto \exp\left(\frac{-q\phi_{B_n}}{E_{00}}\right), \tag{4.7}$$

$$\text{with } E_{00} \equiv \frac{qh}{4\pi}\sqrt{\frac{N_D}{\epsilon_S m^*}} \tag{4.8}$$

where N_D is the donor density, h is Planck constant, $\epsilon_S = \epsilon_r \epsilon_0$ is the permittivity of the semiconductor and m^* is the effective mass of the carriers. Thereby, the tunneling current increases exponentially with $\sqrt{N_D}$, meaning that ohmic behavior can be obtained using a proper doping level in the semiconductor. Practically, a thin heavily doped cap layer, whose thickness is $\sim$ 10 nm, is grown over the normally doped semiconductor layer in order to achieve ohmic contacts when the corresponding band alignment at the metal-semiconductor interface leads to a Schottky barrier.

4.2 Transparent conductive oxide properties

Several applications such as solar cells, liquid crystal displays, flat panel displays, photodetectors or LEDs require transparent electrodes made of thin films of TCO semiconductors. Since the first report of a transparent conductive CdO film by Bädeker in 1907 [218], such materials have undergone a tremendous development. They are usually made of pure or doped wide bandgap semiconductor metal oxides, most often based on SnO_2, In_2O_3 or ZnO. Commonly used doping impurities are Sb and F for SnO_2 [219, 220, 221], Sn for In_2O_3 [222],

Table 4.3: TCO semiconductors for thin-film transparent electrodes [225].

Material	Dopant or compound
SnO_2	Sb, F, As, Nb, Ta
In_2O_3	Sn, Ge, Mo, F, Ti, Zr, Hf, Nb, Ta, W, Te
ZnO	Al, Ga, B, In, Y, Sc, F, V, Si, Ge, Ti, Zr, Hf
CdO	In, Sn
ZnO-SnO_2	Zn_2SnO_4, $ZnSnO_3$
ZnO-In_2O_3	$Zn_2In_2O_5$, $Zn_3In_2O_6$
In_2O_3-SnO_2	$In_4Sn_3O_{12}$
CdO-SnO_2	Cd_2SnO_4, $CdSnO_3$
CdO-In_2O_3	$CdIn_2O_4$
$MgIn_2O_4$	
$GaInO_3$, $(Ga,In)_2O_3$	Sn, Ge
$CdSb_2O_6$	Y
ZnO-In_2O_3-SnO_2	$Zn_2In_2O_5$-$In_4Sn_3O_{12}$
CdO-In_2O_3-SnO_2	$CdIn_2O_4$-Cd_2SnO_4
ZnO-CdO-$In_2O_3SnO_2$	

and Al or Ga for ZnO [223, 224], although other dopants or compounds can be found, as shown in Table 4.3 [225]. CdO-based TCOs [226, 227, 228], despite their low resistivity, are of no practical use nowadays because of the toxicity of Cd. Besides, reports on emerging TCOs such as Ta- or Nb-doped TiO_2 [229, 230, 231] as well as on oxide multilayer films [232, 233] offer interesting alternatives, as indium is a scarce and thus expensive material, and ZnO is quite sensitive to moisture [234]. Most of the reported TCO electrodes are made of n-type degenerate semiconductors, despite a few studies on p-type TCOs [235, 236, 237].

Electrical and optical characteristics strongly depend on the deposition technique and on the choice of material. In the general case, TCO thin films used as electrodes are polycrystalline or amorphous, except for single crystals grown epitaxially, and exhibit a resistivity of the order of 10^{-3} Ω·cm or less and an average transmission above 80% in the visible range [225]. Highly transparent thin films made of metal oxides without intentional impurity doping can be obtained [238, 239]. In such layers, electrical transport is enabled by oxygen vacancies, which act as double ionized donors [240, 241]. However, those undoped oxide films are unstable at high temperature, explaining why binary compounds without impurity doping proved to be not suited for transparent electrode applications [223]. For this reason, doping metal atoms are introduced inside the oxides in order to act as donor (Table 4.3). The conductivity that can be achieved in this way is nevertheless limited by impurity scattering, which reduces the mobility of carriers. Subsequently, a compromise between carrier density and carrier mobility has to be found [225]. Absorption in TCOs comes from three different contributions: band-to-band transitions above the bandgap in the UV region, free-carrier absorption in the visible and IR range and phonon-related absorption in the far IR region. Thus, increasing the carrier density, which results in a decrease in the resistivity, also leads to larger absorption in

the visible range [242], which is detrimental to many applications.

As previously said, the characteristics of TCO thin films is strongly affected by the choice of the deposition/growth technique, e.g. vacuum e-beam or thermal evaporation, magnetron sputtering, reactive sputtering, chemical vapor deposition, pulsed laser deposition (PLD), atomic layer deposition (ALD) or sol-gel processes. The post-deposition treatments also have a great impact on the properties of TCOs, e.g. plasma treatment [243, 244] or annealing [245, 246]. In particular, the work function of ITO layers can be increased via an ICP treatment [247].

4.3 TCO contacts to *p*-type GaN

Common TCOs such as ITO or Al-doped ZnO (AZO) exhibit work functions around 4.3 – 5.0 eV [248, 249, 250] and 3.7–4.6 eV [251, 252], respectively, depending on the deposition parameters. Work functions up to ∼ 5.5 eV have been reported for rf magnetron sputtered oxides [253]. Thereby, transparent contacts to *p*-type doped GaN made of those materials will suffer from a Schottky barrier, because of the high work function of *p*-type GaN (Table 4.2). Several studies on ITO- and ZnO-based transparent contacts to *p*-type GaN and on post-deposition treatment for improving their contact resistance have been published [254, 255, 256, 257]. The use of superlattices as contact layers has also been proposed in order to improve the tunneling current across the Schottky barrier [258]. The main application of such transparent electrodes in the field of III-nitride optoelectronics deals with the increase in the light extraction efficiency of LEDs, using for instance textured ITO as the top *p*-type electrode [259, 260]. On the other hand, ITO-based current spreading layers have proven to be a key component in order to achieve lasing in III-nitride based electrically driven VCSELs [116, 154, 114, 11, 118, 115]. For this latter application, a high transparency and a flat and smooth surface are mandatory in order to minimize cavity losses (see section 5.1).

The choice of the deposition method for TCO-based contacts to *p*-type GaN is crucial, as the latter is extremely sensitive to any plasma damage, as will be discussed in section 4.3.1. The TCO material itself should be chosen wisely, as it should be highly transparent, and exhibit both a large conductivity and a low contact resistance to *p*-type GaN while being able to sustain high current densities. The study of several materials and deposition techniques is discussed in the subsequent sections. The main purpose consists in developing high-end transparent *p*-type electrodes suitable for being used as intracavity contacts in VCSEL applications, which is not trivial. Indeed, current vs voltage characteristics of VCSEL devices using defective ITO current spreading layers are shown in Fig. 4.4 (a), evidencing critical failure of devices at threshold current densities below 2 kA/cm^2, which is not sufficient to reach lasing in our III-nitride VCSELs, as the lowest threshold current density reported up to date is about 3 – 4 kA/cm^2 after an extensive structure optimization [118]. This critical failure is due to the defective ITO contacts that burn under large currents, as shown in Fig. 4.4 (b).

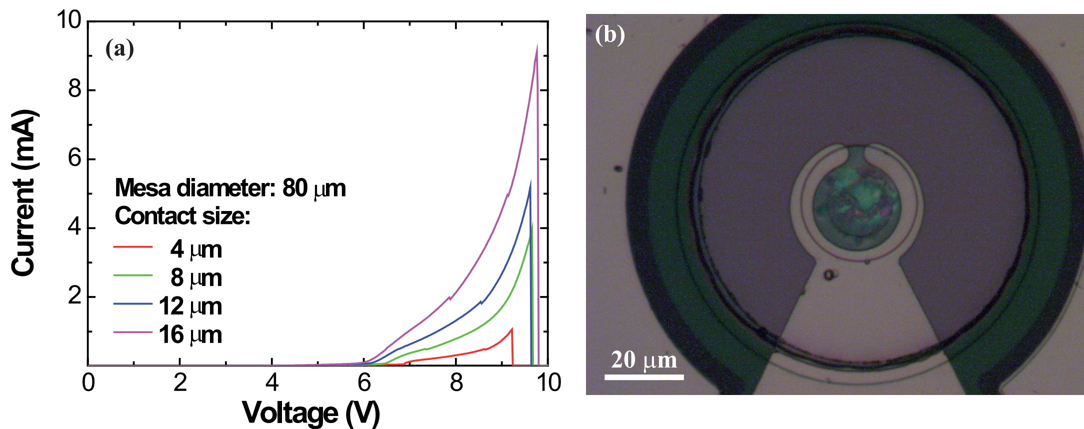

Figure 4.4: (a) Current vs voltage characteristics of a VCSEL with a defective TCO current spreading layer with a mesa diameter of 80 μm for different SiO_2 current aperture sizes. (b) Optical microscope image of such a device after critical failure.

4.3.1 Plasma damage effects on *p*-type GaN

p-type GaN is very sensitive to plasma damage, and many common TCO deposition techniques make use of a plasma, such as sputtering and ion assisted e-beam or thermal evaporation. Thus, the impact of plasma on the electrical properties of *p*-type GaN layers are of relevant interest when discussing the use of TCO-based contacts to *p*-type GaN.

Two plasma-related mechanisms have been reported to affect the electrical properties of *p*-doped GaN layers. Polyakov *et al.* investigated the H_2 plasma passivation effects on *p*-type GaN [261]. The passivation mechanism was ascribed to the introduction of hydrogen in the layer, which subsequently passivates the Mg acceptor impurities by forming Mg-H complexes, eventually reducing the hole concentration, and thus also the layer electrical conductivity. The second mechanism, as described by Cao and coworkers, is related to the creation of nitrogen vacancies in the upper 4-5 nm of the *p*-type GaN layer caused by a H_2 or Ar plasma treatment [262, 263]. These nitrogen vacancies act as donor impurities, which partially (or totally) compensate the acceptor concentration. Indeed, under high energy flux the electron concentration can exceed 10^{19} cm^{-3} and eventually yields *p*-to-*n*-type conversion. They have also reported that post-etch thermal treatment at a temperature ~ 900°C in an N_2 atmosphere effectively cures the plasma damage and restores the initial electrical properties of the *p*-type GaN layer.

4.3.2 The quest for the right material/deposition method

There are few deposition systems for TCOs at EPFL. Since Zn pollutes deposition chambers, ZnO is banned from nearly all deposition systems. In the cleanrooms of the center of Micro-NanoTechnology (CMi) at EPFL, two systems offer the possibility to deposit ITO thin films: an e-gun evaporator, that is used for the deposition of dielectric DBRs, and an rf magnetron

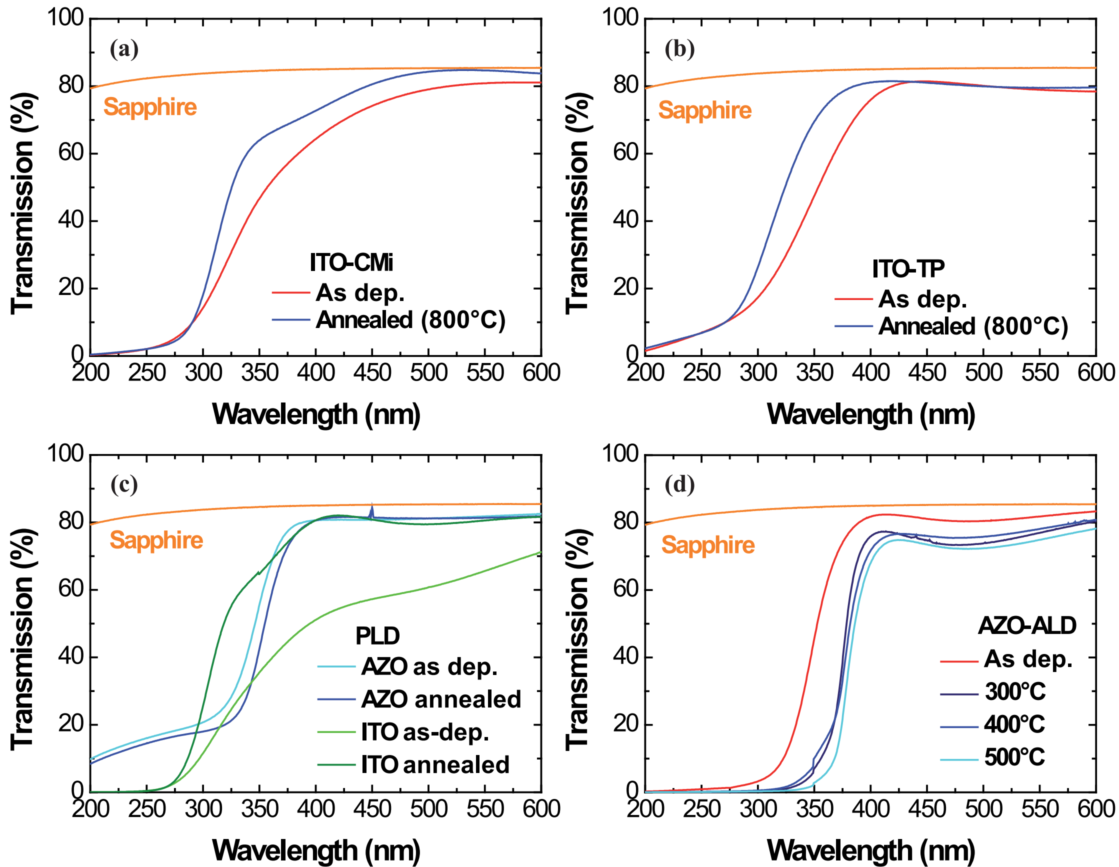

Figure 4.5: Transmission spectra measured on several TCO layers as deposited (as dep.) and after annealing: (a) 120 nm thick sputtered ITO at CMi (EPFL), (b) 100 nm thick sputtered ITO at TP (EPFL), (c) 90 nm thick AZO and 100 nm thick ITO deposited by PLD and (d) 220 nm thick AZO deposited by ALD (see text for details).

sputtering tool. The former uses an ion beam in order to densify the deposited oxide thin films. As this ion gun is started prior to the deposition itself, the *p*-type GaN surface is exposed to ion bombardment that proved to completely passivate its surface. As a result, no current could flow through the deposited ITO contacts. On the other hand, turning off the ion beam during the deposition led to ITO layers exhibiting very poor characteristics, namely a large absorption, a grayish aspect and a large resistivity. The sputtering tool is much more adapted for our purpose, allowing obtaining high quality layers. However, the different deposition parameters could not be optimized. In particular, the target-to-substrate distance is about 50 mm without the possibility to be modified, meaning a possible contact between the *p*-type GaN surface and the plasma despite the magnetron. Finally, a home-made rf magnetron sputtering tool built for teaching purposes (TP) was also available for ITO deposition. However, the overall quality of the deposited layers was not matching that of layers deposited with CMi systems. Nevertheless, ITO contacts deposited using both sputtering machines were studied, hereafter referred to as ITO-CMi and ITO-TP. Besides, ITO deposited by PLD (ITO-PLD) at University of

Table 4.4: Thicknesses and sheet resistances of different TCO layers for different annealing procedures.

Sample	Annealing procedure in N_2	Sheet resistance ($\Omega/\square$)	Thickness (nm)
ITO-CMi	–	34	120
ITO-CMi	90 s at 800°*C*	34	120
ITO-TP	–	117	100
ITO-TP	90 s at 500°C	91	100
ITO-TP	90 s at 600°C	81	100
ITO-TP	90 s at 800°C	70	100
ITO-PLD	–	23	100
ITO-PLD	90 s at 400°C	10	100
AZO PLD	–	112	90
AZO PLD	90 s at 400°C	68	90
AZO-ALD	–	40	220
AZO-ALD	90 s at 300°C	54	220
AZO-ALD	90 s at 400°C	81	220
AZO-ALD	90 s at 500°C	550	220

Palermo by Dr. Mauro Mosca, and ITO and AZO deposited by ALD at Unipress Warsaw by Dr. Henryk Teisseyre (ITO-ALD and AZO-ALD, respectively) were studied at the same time. All TCO layers were deposited at RT in order to be compatible with the lift-off technique: as TCO etching is quite challenging, selective deposition of TCO layers is much easier and convenient when using a pre-patterned photoresist. However, it requires deposition temperatures below 150°C in order not to burn the photoresist.

The different TCO layers were deposited on double-side polished sapphire substrate and on the same LED wafer after being cleaved into 6 pieces. The thickness of each TCO layer was ~ 100 nm. The first step was then to characterize the TCOs on sapphire and to test different annealing procedures on those samples, in order to determine the optimal annealing that would be subsequently applied to LED samples. In order to do so, the two main characteristics of those TCO layers were measured as deposited and after annealing, namely their transmission spectrum and their sheet resistance. The sheet resistances as a function of the annealing procedures are summarized in Table 4.4 and the transmission spectra are shown in Fig. 4.5. All sheet resistances are measured using an in-line 4-probe setup, and have been verified using 3 other measurement methods (another in-line 4-probe setup, a 4-probe setup in diamond configuration and transfer length method (TLM) measurements).

According to these results, all TCO layers exhibit improved characteristics after proper annealing except for AZO-ALD, whose both electrical and optical characteristics strongly decrease after annealing. Finally, all LED samples were annealed according to those results: ITO-CMi and ITO-TP at 800°C, AZO PLD and ITO-PLD at 400°C, all under N_2 ambient for 90 s, and

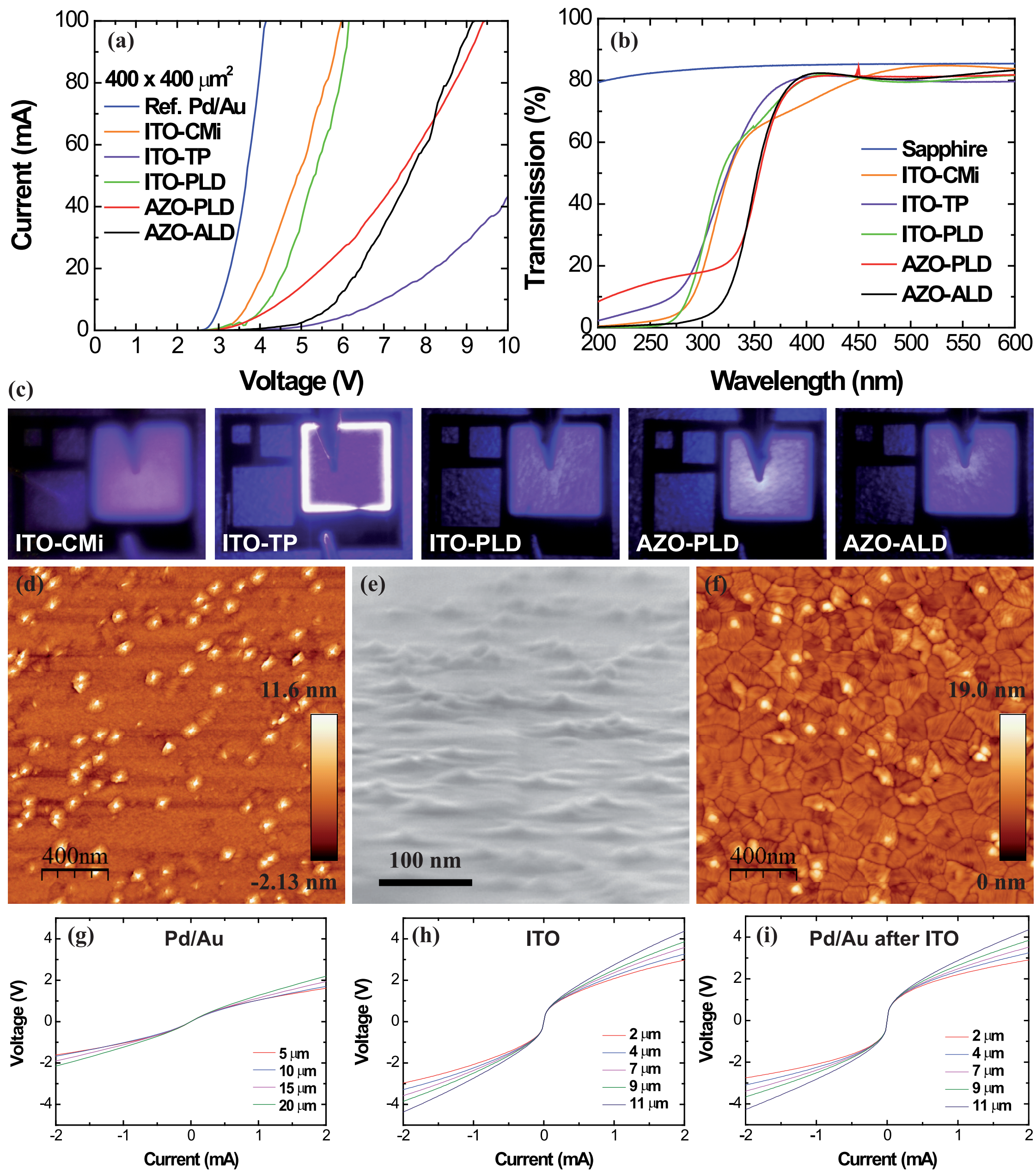

Figure 4.6: (a) Current vs voltage curves measured on 400×400 μm^2 LEDs using different TCOs as *p*-type electrode. (b) Transmission spectra of these TCOs deposited on sapphire. (c) Pictures of the different LEDs under 2 mA bias. (d) 2×2 μm^2 AFM scan and (e) SEM image of CMi sputtered ITO before annealing, and (f) 2×2 μm^2 AFM scan of the same sample after annealing. TLM measurements of (g) standard Pd/Au contacts to *p*-type GaN used as reference, of (h) ITO contacts to the same sample, and of (i) standard Pd/Au contacts to the same sample after ITO removal.

AZO-ALD was left non annealed. The resulting I-V curves are shown in Fig. 4.6 (a) together with that of an LED using a standard Pd/Au *p*-type contact, and the measured transmission

Table 4.5: TLM measurement results on the ITO-CMi LED sample. The given values have been determined under a current bias of 2 mA.

Sample	Specific contact resistance ($10^{-3}\ \Omega\cdot\mathrm{cm}^2$)	Sheet resistance ($\mathrm{k}\Omega/\square$)
Ref. Pd/Au	2.1	3.91
ITO-CMi	1.5	12.5
Pd/Au after ITO	1.0	12.8

spectra are shown altogether for comparison in Fig. 4.6 (b). As no metallic contacts were deposited on top of the different TCO layers, the current spreading efficacy was easily checked using an optical microscope. Pictures of the different TCO LEDs under 2 mA bias are shown in Fig. 4.6 (c). According to those results, the most promising TCO is the sputtered ITO from CMi. A $2\times2\ \mu\mathrm{m}^2$ AFM scan and a SEM image of such an ITO layer deposited on sapphire are shown in Figs. 4.6 (d) and 4.6 (e), respectively, and a $2\times2\ \mu\mathrm{m}^2$ AFM scan of the same layer after annealing can be seen in Fig. 4.6 (f). The corresponding rms roughness values before and after annealing are 1.54 and 1.80 nm, respectively. This is actually neither optimal nor strongly detrimental. However, despite being the most promising TCO out of these measurements, the ITO-CMi LED sample still exhibit an increase in the forward voltage of about 2 V under a current bias of 100 mA when compared to the reference sample. This could be due to two different phenomena: either the work function discrepancy between *p*-type GaN and this ITO gives rise to a large Schottky barrier, or the small target-to-substrate distance of the sputtering tool results in plasma damage of the *p*-type GaN surface, which dramatically increases the contact resistance. In order to settle this point, TLM measurements have been performed on the *p*-type contacts of the reference sample [Fig. 4.6 (g)], on the ITO-CMi LED sample [Fig. 4.6 (h)], and finally on this latter sample after removing the ITO layer using wet etching and subsequently depositing standard Pd/Au contacts [Fig. 4.6 (i)]. The resulting specific contact resistances and *p*-type GaN sheet resistances are summarized in Table 4.5.

According to those results, despite similar values for their specific contact resistance under a current bias of 2 mA, the ITO-CMi sample exhibits a much larger *p*-type GaN sheet resistance than the reference sample, as well as a strongly non ohmic behavior, which is evidenced by a voltage step of about ±1 V around 0 mA. This barrier is then also found in LED structures [Fig. 4.6 (a), ITO-CMi]. Interestingly, both features are still present after ITO removal and the deposition of Pd/Au contacts. Thereby, we ascribe those effects to *p*-type GaN surface plasma damage resulting from an insufficiently confined plasma during the ITO deposition process despite the magnetron. Indeed, the samples displayed in Fig. 4.4 were processed using ITO-CMi as the current spreading layer. Therefore, other TCOs/deposition methods have to be studied in order to achieve satisfactory characteristics for VCSEL applications.

Seeking for other TCO sources, we approached former LASPE PhD student Sylvain Nicolay, who is currently working at PV-LAB (Photovoltaics and thin film electronics laboratory), which

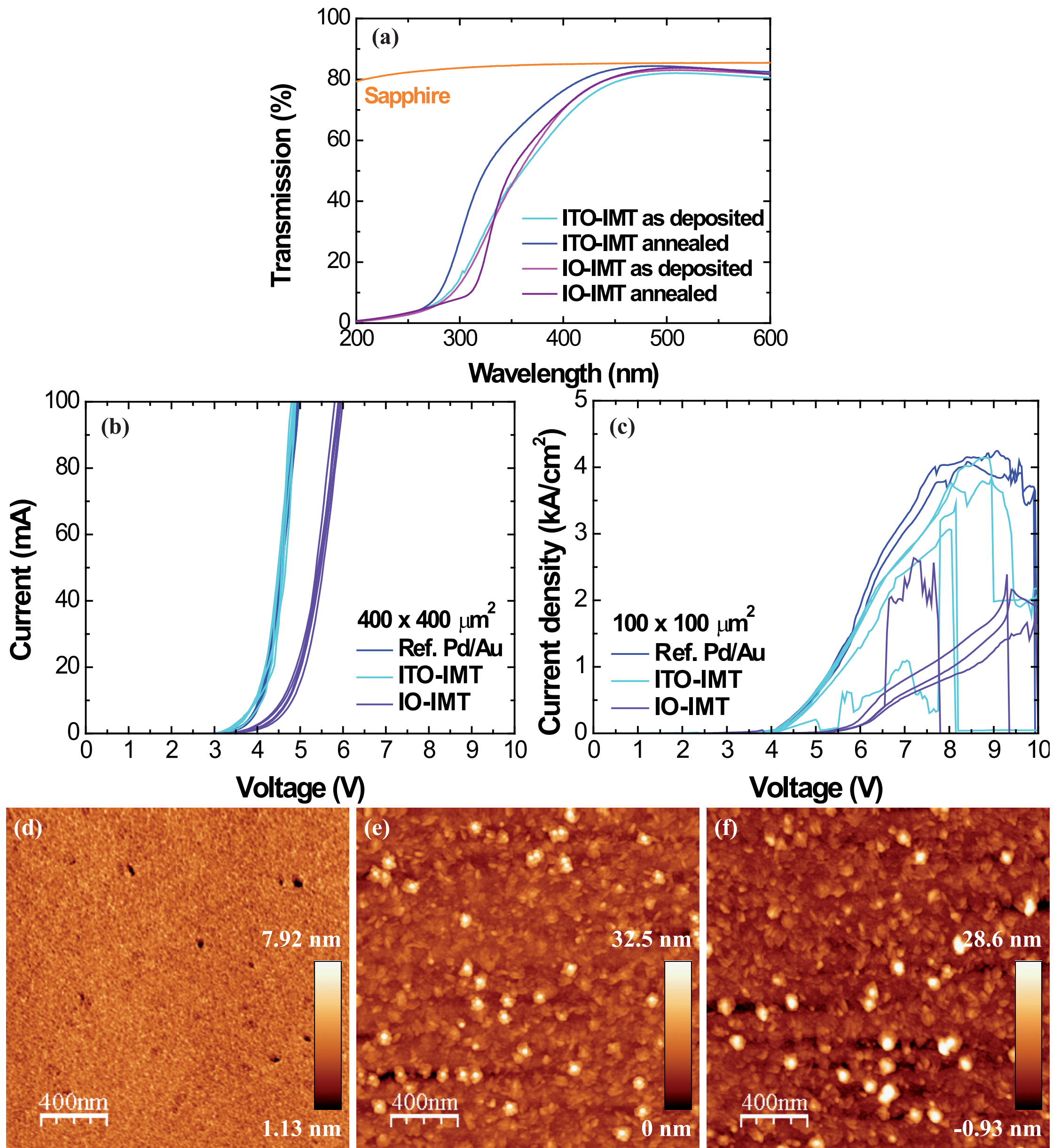

Figure 4.7: (a) Transmission spectra of IO and ITO layers deposited on sapphire measured before and after annealing. (b) Current vs voltage curves measured on $400 \times 400\ \mu m^2$ LEDs using sputtered IO or ITO as *p*-type electrodes. (c) Current density vs voltage measured on $100 \times 100\ \mu m^2$ LEDs using sputtered IO or ITO as *p*-type electrodes. $2 \times 2\ \mu m^2$ AFM scans of IO before annealing (d) and ITO before (e) and after (f) annealing.

is part of the IMT in Neuchâtel and focuses, *inter alia*, on TCOs. This way, ITO (ITO-IMT) and indium oxide (IO-IMT) were sputtered on sapphire and LED samples. Once again, the first step was to determine a proper annealing procedure for both TCOs. According to Dr. Nicolay, a standard annealing procedure is performed under N_2 ambient at a temperature of 350°C for 10 minutes. The effects of such an annealing on the TCO layer sheet resistance

Table 4.6: Thicknesses and sheet resistances of the TCO layers from IMT before and after annealing.

Sample	Annealing procedure in N_2	Sheet resistance ($\Omega/\square$)	Thickness (nm)
ITO-IMT	–	57	130
ITO-IMT	350 s at 350°C	40	130
IO-IMT	–	28	140
IO-IMT	350 s at 350°C	2250	140

are listed in Table 4.6, and the corresponding transmission spectra are shown in Fig. 4.7 (a). Whereas the transparency and sheet resistance of ITO-IMT is improved, the IO-IMT sheet resistance is dramatically increased by this annealing procedure. For this reason, the thermal treatment has been applied to the ITO-IMT LED sample, while the IO-IMT LED sample was left non annealed. I-V curves measured on those LED samples are shown in Fig. 4.7 (b). The ITO-IMT sample exhibits outstanding I-V characteristics, matching those of the reference sample, whereas the IO-IMT sample suffers from a voltage increase of about 1 V under 100 mA bias. Nevertheless, critical failure is observed below 5 kA/cm^2 and 3 kA/cm^2 for ITO-IMT and IO-IMT samples, respectively, as shown in Fig. 4.7 (c). However, the same critical failure is observed for the reference sample, which indicates a non-optimal epitaxial structure. 2 × 2 μm^2 AFM scans of the IO-IMT layer, non annealed and annealed ITO-IMT layer, all deposited on sapphire, are shown in Figs. 4.7 (d), 4.7 (e) and 4.7 (f), respectively. Whereas the IO-IMT layer exhibits a smooth surface (rms value of 0.60 nm), the ITO-IMT layer both before and after annealing exhibits a quite rough surface (rms values of 3.4 and 3.8 nm, respectively). This unfortunately disqualifies ITO-IMT for VCSEL applications, as such a large roughness would cause critical scattering losses. On the other hand, IO-IMT LED critical failure is observed at half the current densities the reference sample sustains, which therefore makes it improper to be used for VCSELs.

4.3.3 Inserting a metallic interlayer

The insertion of a very thin (~ 10 Å thick) metallic interlayer between the *p*-type GaN and the TCO contact impacts on the band alignment and thus can lower the contact resistance. Therefore, 5 LED samples were processed using the following contact schemes: standard Pd/Au as reference, 10 Å In/100 nm ITO, 10 Å Ni/100 nm ITO, 10 Å Pd/100 nm ITO, and 100 nm ITO. The resulting I-V curves measured on 400 × 400 μm^2 LEDs are shown in Fig. 4.8 (a). The insertion of those interlayers improves the LED I-V characteristics when compared to the bare ITO contact. Interestingly, the Pd/ITO LED eventually equals the reference LED performances. However, none of the ITO-based contacts sustains large current densities. Even the Pd/ITO LED suffers from critical failure at a current density ~ 4 kA/cm^2, whereas the reference sample exceeds 5 kA/cm^2 without any damage, as shown in Fig. 4.8 (b). This could be ascribed to the weakness of the bonds between the metal and the oxide, yielding important structural

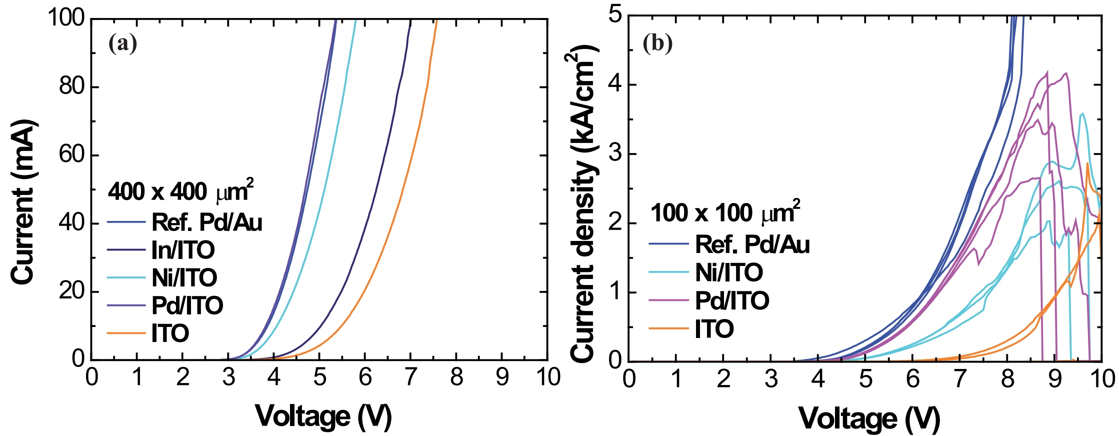

Figure 4.8: (a) Current vs voltage curves measured on 400 × 400 μm^2 LEDs using sputtered ITO and different 10 Å thick metallic interlayers as *p*-type electrodes. (b) Current density vs voltage measured on 100 × 100 μm^2 LEDs using the same *p*-type electrodes.

damage under large current densities. Moreover, all samples including a metallic interlayer exhibit a grayish aspect, evidencing a large absorption in the visible range. Consequently, this approach also proved unsuccessful.

4.3.4 Optimized sputtered ITO contacts to *p*-type GaN from Evatec

Evatec is a leading supplier of thin film deposition products and services to the global semiconductor and optics industries. In particular, they are selling sputtering systems devoted to the deposition of ITO as transparent *p*-type electrode for blue and white LEDs. Such systems are an alternative to the dominant technology in the domain, which is e-beam evaporation. They present the advantage of an easier automation of the deposition process, which results in an increase of the device mass-production yield. However, Evatec has no experience in the field of III-nitride-based devices despite their huge knowledge concerning thin film deposition. In this context, a partnership between this company and our laboratory was agreed in order to further develop and improve their ITO deposition parameters in order to realize state-of-the-art ITO contacts to *p*-type GaN.

I-V characteristics of LEDs using either a standard Pd/Au contact or ITO from Evatec are shown in Fig. 4.9 (a). The latter nearly matches the former. In addition, an ~ 70 nm thick Evatec ITO layer exhibits an absorption of only 0.8% at 420 nm as shown in Fig. 4.9 (b), which corresponds to $\alpha_{ITO} \approx 10^3$ cm^{-1}, while being highly conductive with a sheet resistivity of only 24 Ω/□. A key point relies on the absence of any plasma damage to *p*-type GaN during the sputtering of ITO. Indeed, Figures 4.9 (c), 4.9 (d) and 4.9 (e) show TLM curves measured on contacts to *p*-type GaN made of Pd/Au, ITO, and Pd/Au after removing the ITO layer, respectively. Interestingly, the ohmic behavior of Pd/Au contacts to *p*-type GaN is recovered after removing the ITO layer using wet etching, despite the non-ohmic behavior of the ITO contacts themselves. The results

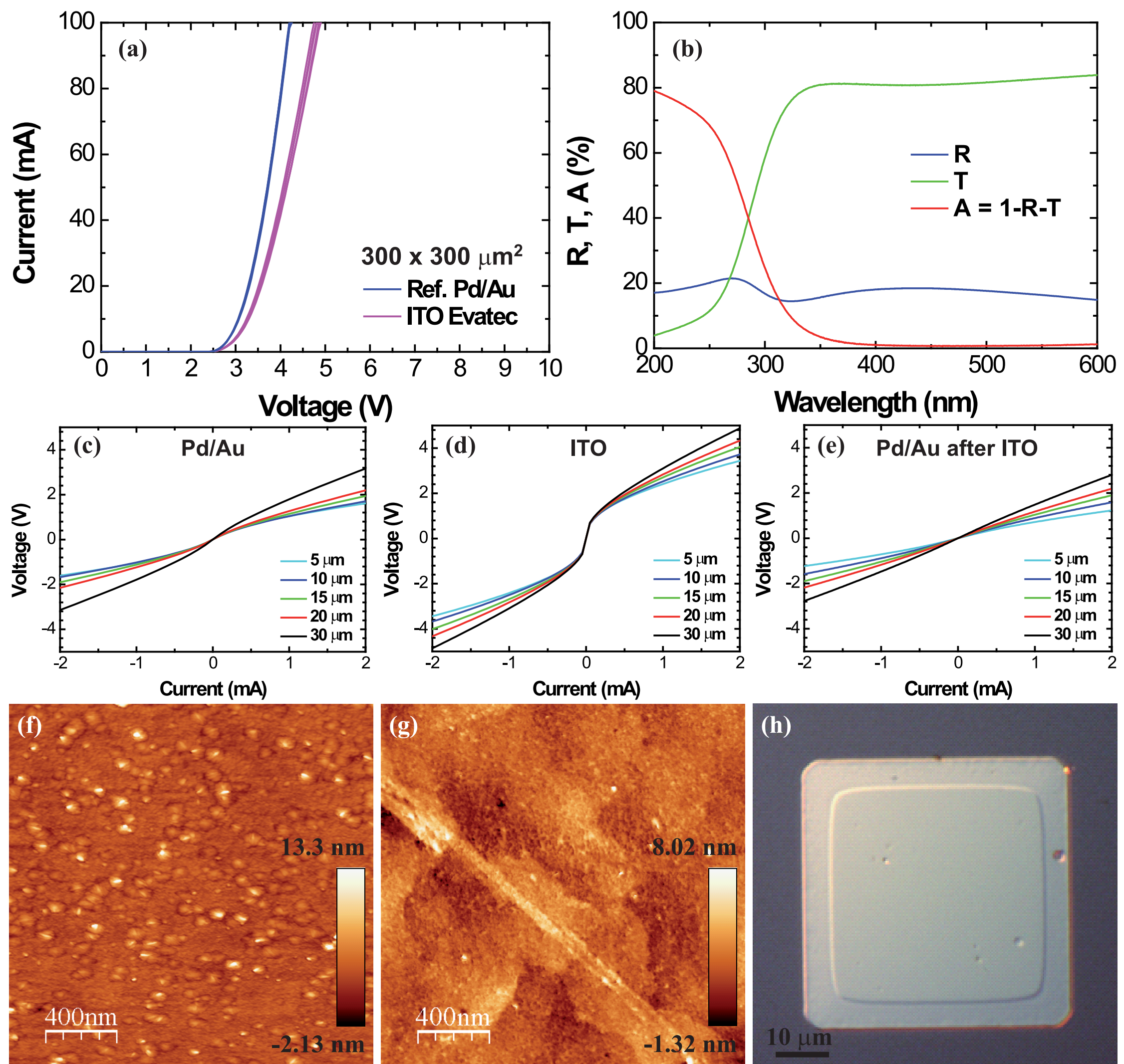

Figure 4.9: (a) Comparison of the current vs voltage curves measured on LEDs using either a standard Pd/Au *p*-type contact or a sputtered ITO layer from Evatec. (b) Reflectivity, transmission and absorption spectra measured on an ~ 70 nm thick ITO layer from Evatec deposited on sapphire. TLM measurements of (c) standard Pd/Au contacts to *p*-type GaN as reference, (d) Evatec ITO contacts to the same sample, and (e) standard Pd/Au contacts to the same sample after ITO removal. (f) 2×2 μm^2 AFM scan of the ITO layer deposited on sapphire before annealing and (g) of ITO deposited on *p*-GaN. (h) Picture illustrating the undercut effect when performing HCl-based wet etching on ITO layers.

of those TLM measurements are displayed in Table 4.7, evidencing the absence of any plasma damage caused by the sputtering step: both the Pd/Au specific contact resistance and the *p*-type GaN sheet resistance values are not affected by the ITO deposition. Regarding the ITO work function, it has been determined using Kelvin probe measurements to be in the range of 4.8 – 5.1 eV, depending on the deposition parameters and on the annealing procedure.

Table 4.7: TLM measurement results obtained on the ITO Evatec LED sample. The given values have been determined under a current bias of 2 mA.

Sample	Specific contact resistance (10^{-3} $\Omega \cdot cm^2$)	Sheet resistance ($\Omega/\square$)
Ref. Pd/Au	1.4	4320
ITO Evatec	7.9	4430
Pd/Au after ITO	1.6	4500

Finally, 2×2 μm^2 AFM scans of ITO layers deposited on sapphire and on *p*-type GaN are shown in Fig. 4.9 (f) and (g), respectively. The corresponding rms roughness values are 1.22 and 1.03 nm, respectively. Actually, the surface morphology of the ITO layers from Evatec is quite similar to that of ITO-CMi [Fig. 4.6 (d)]. Another element that is worth pointing out is the large undercut of ITO layers when performing wet etching. This effect is evidenced in Fig. 4.9 (h), where an undercut of about 5 μm can be seen after dipping the sample in HCl for only 3 minutes. Therefore, lift-off should be preferentially used in order to pattern ITO layers.

Thanks to those promising characteristics, ITO from Evatec has been selected as transparent current spreading layer for VCSEL devices. A comparison between I-V curves measured on VCSELs using non optimized (dotted lines) and optimized (solid lines) ITO current spreading layers is shown in Fig. 4.10. Results on such VCSELs are presented in the next chapter.

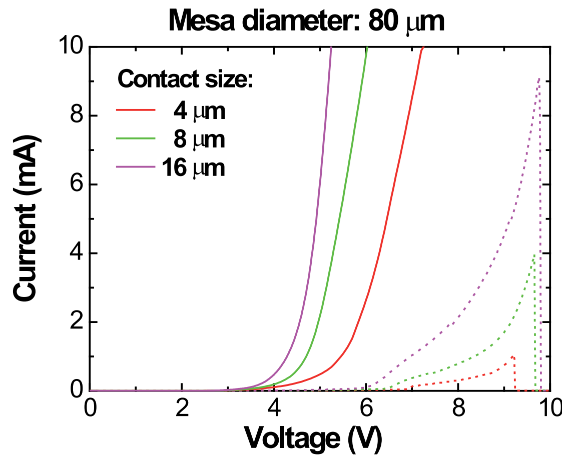

Figure 4.10: Comparison between I-V curves measured on VCSELs using non optimized (dotted lines) and optimized (solid lines) ITO current spreading layers.

5 Vertical-cavity surface-emitting lasers

In this chapter, InAlN-based blue VSCELs are studied. It is organized as follows: first, the different building blocks are presented. Amongst those, two have not been detailed yet: dielectric DBRs are thus discussed, including a brief description of their deposition process and the choice of the dielectric materials. Then, the current confinement issue is addressed, and the most promising methods are described. Finally, our optimized VCSEL design is presented, followed by the processing steps and the optical and electrical results.

5.1 Building blocks

As described in chapter 2, lasers are made of an active medium sandwiched between two mirrors. Whereas standard edge-emitting lasers have a high gain-per-pass due to their long cavity entirely filled with this active medium, which is of the order of several hundreds of microns, and thus can accommodate low reflectivity mirrors made of cleaved semiconductor/air facets, VCSEL active region is much shorter (only a few tens of nanometers), and consequently it exhibits a very low gain-per-pass. Therefore, highly-reflective DBRs are required in order to achieve lasing in such devices, as such highly reflectice DBRs would increase the cavity photon lifetime, yielding an increased number of passes before that the photon exits the cavity. Two different kinds of DBRs can then be used: nitride-based epitaxial DBRs and/or dielectric ones. Because of the difficulty to obtain high-quality highly-reflective nitride-based DBRs (as discussed in section 3.1), many groups focused on fully-hybrid VCSELs [114, 11, 118, 115]. Nevertheless, such fully-hybrid cavities present several drawbacks: it requires substrate removal and wafer bonding, rendering the process flow much more challenging. It is an issue for scaling up the production, and it also makes the precise control of the cavity length challenging. Moreover, such fully hybrid VCSELs exhibit multimode longitudinal lasing according to Eq. 2.16 because of a long cavity, required to be safely removed from the substrate, together with the large stopband width of the DBRs, yielding a short free spectral range. This thus cancels one of the advantages of VCSELs over edge-emitting lasers, namely exhibiting single longitudinal mode lasing. Another approach relied on the use of a bottom AlN/GaN DBR grown on sapphire substrate together with a top dielectric one [116], which simplifies the

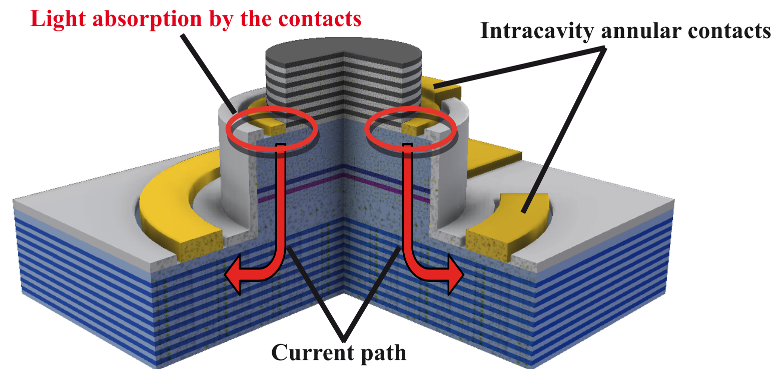

Figure 5.1: VCSEL structure without current confinement. Because of the large *p*-type GaN layer resistivity, the current flows directly below the top metallic contacts that then absorb the emitted light.

process flow. Notwithstanding, a large strain builds up in such structures, which would not make their growth on FS GaN substrates an asset. Indeed, such a geometry cannot benefit from the advantages of the use of FS GaN substrates, namely: a better crystalline quality that enables improved device characteristics and a better thermal management that improves device lifetime [23, 24, 25].

In this context, we based our approach on the use of a bottom InAlN/GaN DBR grown on a FS GaN substrate. This combines the advantages of high crystalline quality epitaxial structures together with a simple and straightforward process flow. Nevertheless, vertical electrical transport through such DBRs is quite challenging, due to the charge planes at the GaN/InAlN interfaces and to the difficulty to achieve efficient InAlN doping, especially *p*-type doping. Therefore, intracavity contacts are required for electrical injection and a top dielectric DBR is used, as it saves growth time and opens the way for the use of an intracavity TCO current spreading layer as well as for any surface treatment for current confinement. This latter point is a key factor required in order to achieve lasing in VCSEL structures because of the large resistivity of *p*-type GaN. The current has to be confined in the center of the device, otherwise it would directly flow below the metallic contacts, which would then absorb the emitted light as depicted in Fig. 5.1. In addition, confining the current into a small aperture allows achieving large current densities with small currents, which drastically limits device heating and prevents device breakdown.

Therefore, the key building blocks of our VCSELs are the following ones:

- a top dielectric DBR,
- an efficient current injection scheme, especially regarding hole spreading,
- a current confinement aperture,
- a QW-based active region,

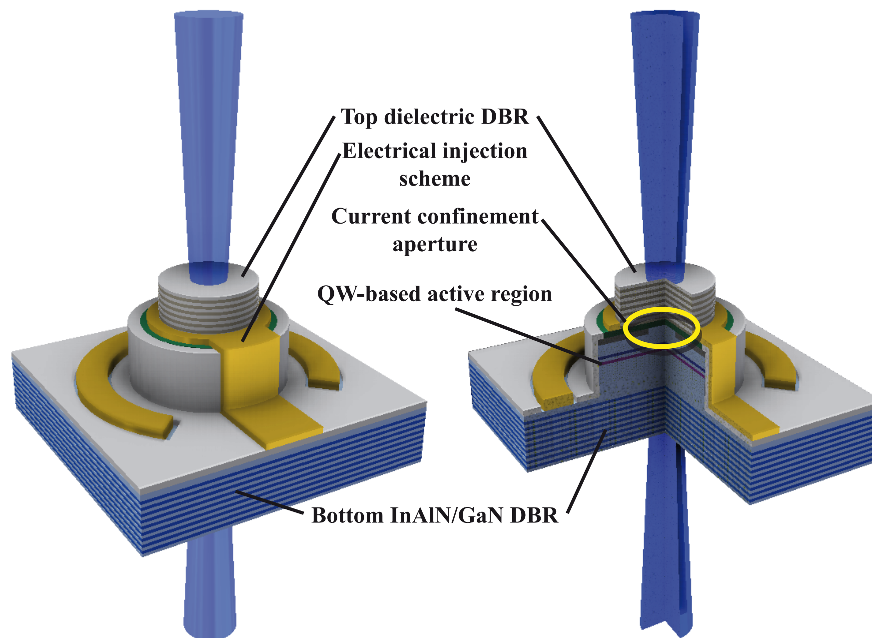

Figure 5.2: The key building blocks of our VCSEL structures: a top dielectric DBR, an efficient current injection scheme, a current confinement aperture, a QW-based active region and a bottom InAlN-based epitaxial DBR.

- a bottom InAlN-based epitaxial DBR.

Schematic drawings of a VCSEL structure where those different building blocks are depicted are shown in Fig. 5.2. InAlN-based DBRs have been extensively discussed in chapter 3 and the use of a TCO as intracavity *p*-type electrode for current injection has been studied in chapter 4. Dielectric DBRs and current confinement schemes will be presented in the forthcoming sections. A thorough study of the active region is beyond the scope of this thesis. Indeed, the QWs have been adapted from those used in the LDs developed by our laboratory. Figure 5.2 shows laser beams emitted through both top and bottom mirrors. Indeed, our VCSELs are grown on double side polished substrates. Thus, emitted light can be analyzed from both sides of the devices. The actual intensity ratio for the two laser beams will thus be given by the transmission ratio between the top and bottom DBRs.

5.2 Dielectric DBRs

As previously stated, our VCSEL structures make use of a top dielectric DBR. They present several advantages over epitaxial ones. First, a much larger refractive index contrast can be achieved between the different layers, which means that fewer pairs are required to obtain a high reflectivity, the optical field penetration depth is shorter and the stopband width is broader. Second, their deposition is usually much quicker and easier than the growth of

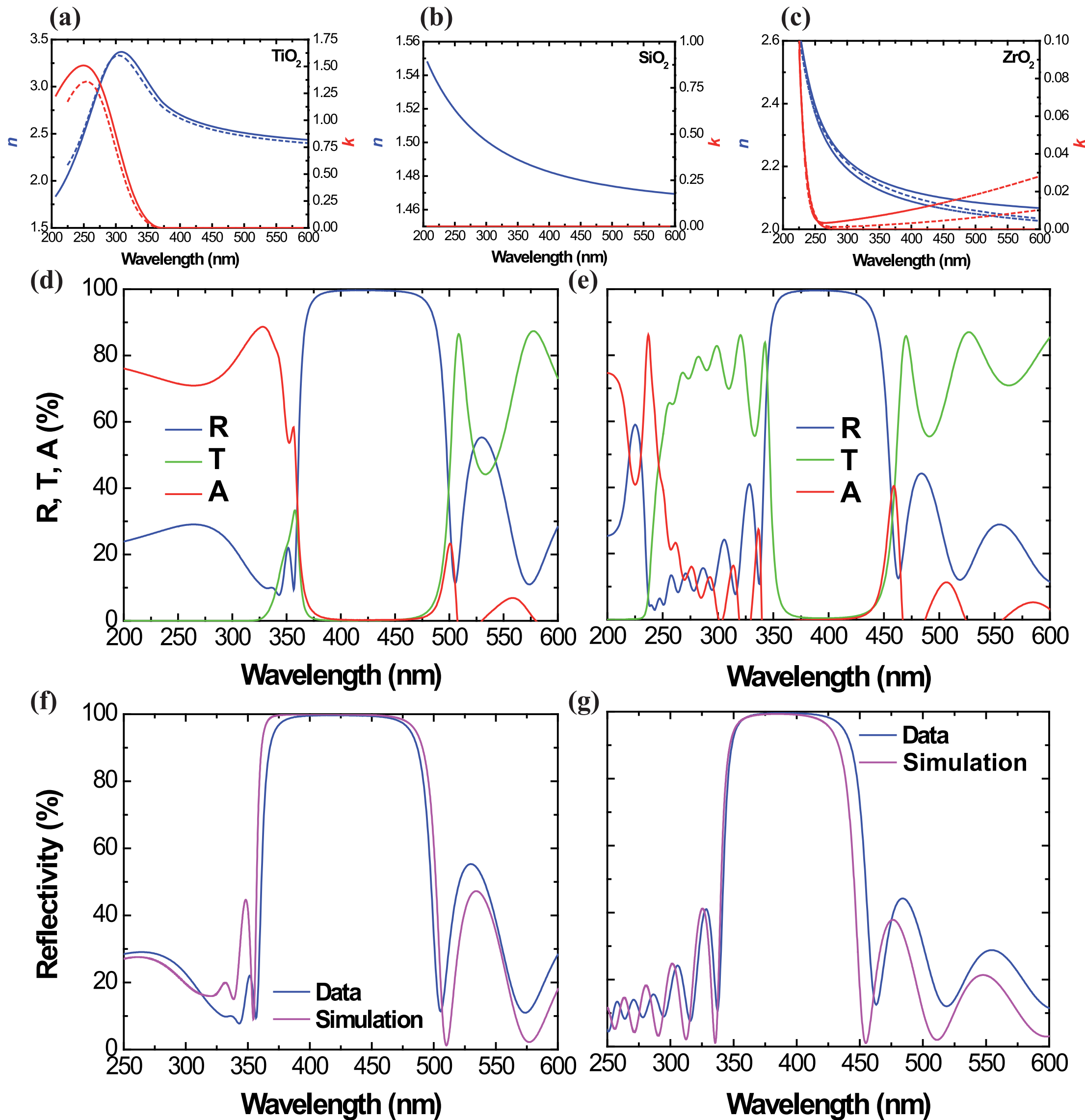

Figure 5.3: Refractive index n and extinction coefficient k of e-beam evaporated (a) TiO_2, (b) SiO_2 and (c) ZrO_2. Different curves shown on the same graph are measurements issued from different samples. Reflectivity R, transmission T and absorption A measured on (d) a 7-pair SiO_2/TiO_2 and on (e) an 8-pair SiO_2/ZrO_2 DBR. Peak reflectivities are equal to 99.7% and 99.6%, respectively. The absorption is obtained through the relation $A = 1 - R - T$. (f) and (g) comparison between the measured and simulated (using transfer matrix simulation) reflectivity spectra of the DBRs depicted in (d) and (e), respectively.

epitaxial multilayers. Moreover, it can be performed at room temperature on amorphous materials, which enables the introduction of a TCO intracavity current spreading layer as well as p-type GaN surface treatment for current confinement. Third, by properly choosing both layer materials, their absorption edge can be set at a higher energy than that of nitride-based DBRs. This latter point is critical when the microcavity structure is non-resonantly optically

pumped in order to ensure that the pump beam will not be absorbed by the top DBR stack.

The dielectric deposition is performed in a Leybold Optics LAB 600H e-beam evaporator. The tool comprises an ion beam for thin film densification that improves density, hardness and refractive index of the deposited materials. The evaporation rate is monitored *in situ* using quartz crystals, enabling a precise control of the layer thicknesses. However, the ion beam being not interrupted in-between the different layers during DBR deposition, a careful calibration had to be performed in order to take into account the deposited layer thinning while switching crucibles and e-gun ramping up and down when depositing stacks of layers such as DBRs. The base pressure, which is of the order of 1.5×10^{-6} mbar, limits thin film contaminations. Moreover, the nearly directional deposition makes this tool lift-off compatible, which is essential for the microstructuration of the DBRs.

Three different dielectric layers were used for our DBRs. SiO_2 was used as low index material in all DBR stacks. The second, high index, layer was then either made of TiO_2 or ZrO_2. The former has a higher refractive index, but also an absorption edge occuring at lower energy than the latter. SiO_2, TiO_2 and ZrO_2 films have a refractive index at 420 nm of 1.48, 2.60 and 2.09, respectively, and nearly no absorption at that wavelength. The TiO_2 absorption edge is around 360 nm, while that of ZrO_2 only occurs around 270 nm. The Refractive index and extinction coefficient of TiO_2, SiO_2 and ZrO_2 thin films for wavelengths spanning from 200 to 600 nm are shown in Figs. 5.3 (a), 5.3 (b) and 5.3 (c), respectively. Those measurements were performed by spectroscopic ellipsometry on 100 nm thick single layers deposited on silicon wafers. Thus, SiO_2/TiO_2 DBRs are mainly used for electrically-driven devices operating in the blue-violet region, where the absorption of TiO_2 is negligible. On the other hand, for non-resonantly optically pumped microcavities, where the pump beam should not be absorbed by the top dielectric stack, SiO_2/ZrO_2 DBRs are preferred, despite a longer penetration depth and a narrower stopband width.

A minimum of about 7 to 8 pairs is required in order to achieve highly-reflective DBRs with a peak reflectivity over 99.5%. Typical reflectivity and transmission spectra measured on a 7-pair SiO_2/TiO_2 and on an 8-pair SiO_2/ZrO_2 DBR are shown in Figs. 5.3 (d) and 5.3 (e), respectively. Their peak reflectivity is equal to 99.7% at 415 nm and 99.6% at 385 nm, respectively. The first DBR was deposited as top reflector on a VCSEL structure whereas the second one was used in an optically pumped flip-chiped microcavity. The reflectivity measurements have been performed in V-W configuration using a Cary 500 spectrophotometer, ensuring the determination of absolute values (see section 3.4 for more details). The absorption edge of the SiO_2/TiO_2 DBR can be seen around 360 nm, whereas that of the SiO_2/ZrO_2 DBR only occurs around 270 nm, which is consistent with ellipsometry measurements. Note that the absorption curve oscillations above the absorption edge are due to the fact that transmission measurements are performed at perpendicular incidence while reflectivity spectra are measured with an incidence angle of about 7°, which causes a slight shift of the Bragg modes. The simulated reflectivity curve of the SiO_2/TiO_2 DBR matches well the measured reflectivity spectrum [Fig. 5.3 (f)]. The simulated and measured reflectivity spectra of the SiO_2/ZrO_2 DBR

exhibit a slight discrepancy on the low energy side of the stopband [Fig. 5.3 (g)], which can be ascribed to a slight difference between the optical thicknesses of both material quarterwave layers.

Besides VCSELs and VECSELs (as will be discussed in chapter 6), such DBRs were widely used for all microcavity applications in our laboratory, as for instance light-matter coupling anisotropy studies in a non-polar nitride-based microcavity [203], the development of InGaN QWs for blue-violet polariton LDs [14], and flip-chip fully hybrid microcavities.

Another element of relevant interest deals with oxide-based conductive DBRs. Such structures can be made either from only one material, whose refractive index is tuned by varying the deposition parameters [264], or from two different TCOs, e.g. Nb-doped TiO_2 and Al-doped ZnO [265]. However, such TCO stacks do not exhibit a refractive index contrast large enough so as to benefit from very short penetration depths that would be required in order to avoid critical light absorption. Indeed, such DBRs do not exhibit a reflectivity over 90%, which is far from enough for VCSEL applications.

5.3 Current confinement scheme

A critical point concerning VCSELs is the confinement of the electrical current, required in order to obtain current densities high enough to achieve lasing while limiting device heating. As discussed in section 2.3, the current confinement schemes that are commonly used in regular III-V VCSELs are not necessarily suited for III-nitride VCSELs. In the subsequent sections, the most promising current confinement schemes are presented. Although only some of them have been successfully used to demonstrate lasing, they could definitely be further developed and combined in order to improve forthcoming devices.

5.3.1 InAlN lateral oxidation

One of the commonly used current confinement schemes in arsenide-based VCSELs is the lateral oxidation of an aluminum-rich layer positioned near the active region. As one of the main strengths of our laboratory is the mastery of LM InAlN layers, which are Al-rich, our early approach relied on the partial lateral oxidation of an $In_{0.17}Al_{0.83}N$ layer placed below the active region in the *n*-type GaN part of the cavity [266, 267]. A schematic drawing depicting the structure is shown in Fig. 5.4 (a). This scheme is quite efficient regarding the confinement of the current, but it suffers from several drawbacks. First, the insertion of an InAlN layer in the *n*-type GaN region results in a drastic increase in the series resistance. This is illustrated by an increase in the forward voltage of about 4 V under a current bias of 10 mA, as can be seen on Fig. 5.5 (a). This is due to the fact that InAlN acts like a barrier because of its large bandgap, combined to the larger InAlN resistivity when compared to that of *n*-type GaN. This increase in the forward voltage is actually stronger when adding the InAlN layer than when performing the lateral oxidation of the InAlN layer (reduced current path diameter). Moreover,

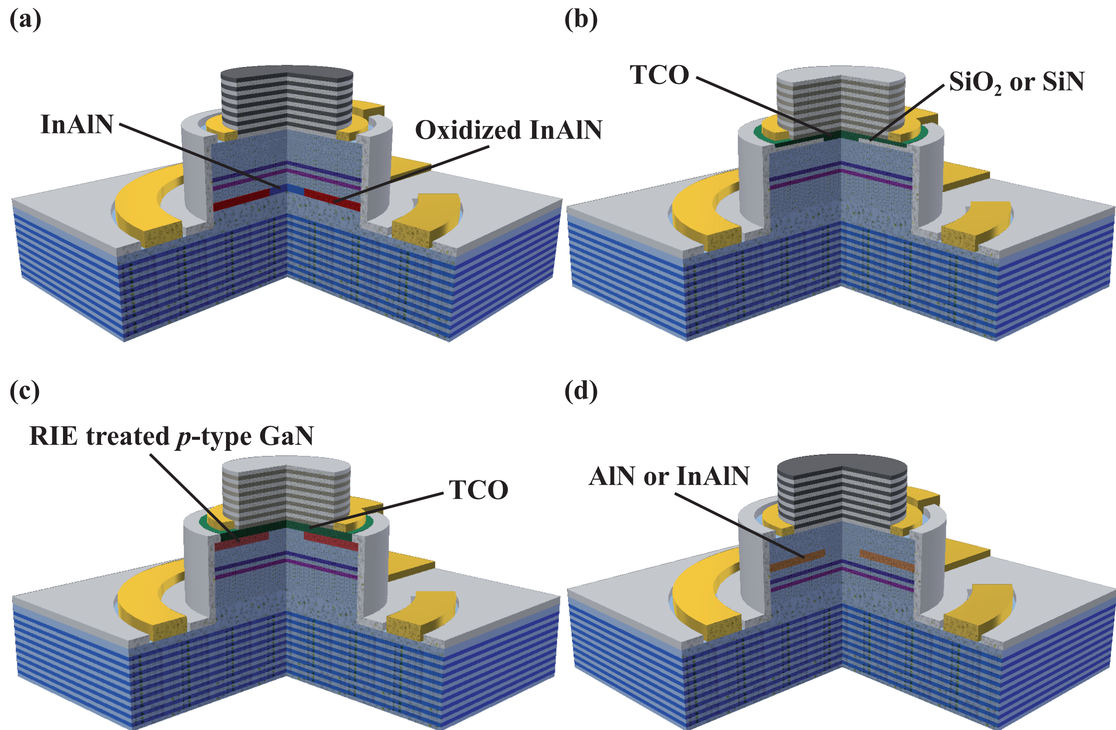

Figure 5.4: Current confinement schemes for VCSELs. (a) Lateral oxidation of a LM InAlN layer (section 5.3.1), (b) TCO current spreading layer on a dielectric current confinement layer (section 5.3.3), (c) TCO current spreading layer and RIE-based surface passivation of *p*-type GaN (section 5.3.3), and (d) buried AlN or InAlN current confinement layer (section 5.3.4).

the InAlN oxidation process is challenging to perfectly control and usually results in InAlN partial etching, which leads to a dramatical reduction of the device mechanical robustness. This effect is illustrated in Fig. 5.5 (b), where a void can be seen instead of the presence of an oxidized InAlN layer. Nevertheless, cavity effects have been observed on devices using this current confinement scheme. Electroluminescence (EL) spectra measured on such a device are shown in Fig. 5.5 (c), where the emission comes from a narrow cavity mode. A slight cavity mode emission redshift reveals device heating.

Thus, this current confinement scheme has been temporarily left aside in favor of another approach that has been in the meantime successfully used by other groups to achieve lasing in nitride-based electrically-driven VCSELs.

5.3.2 TCO and dielectric current confinement layer

Another current confinement scheme relies on the use of a dielectric (usually SiO_2 or Si_3N_4) layer deposited on top of the VCSEL mesa. This layer has a small aperture (around 4 to 20 μm) at its center that confines the current. However, it requires an intracavity current spreading layer made of a TCO on top of the dielectric layer in order to inject the current.

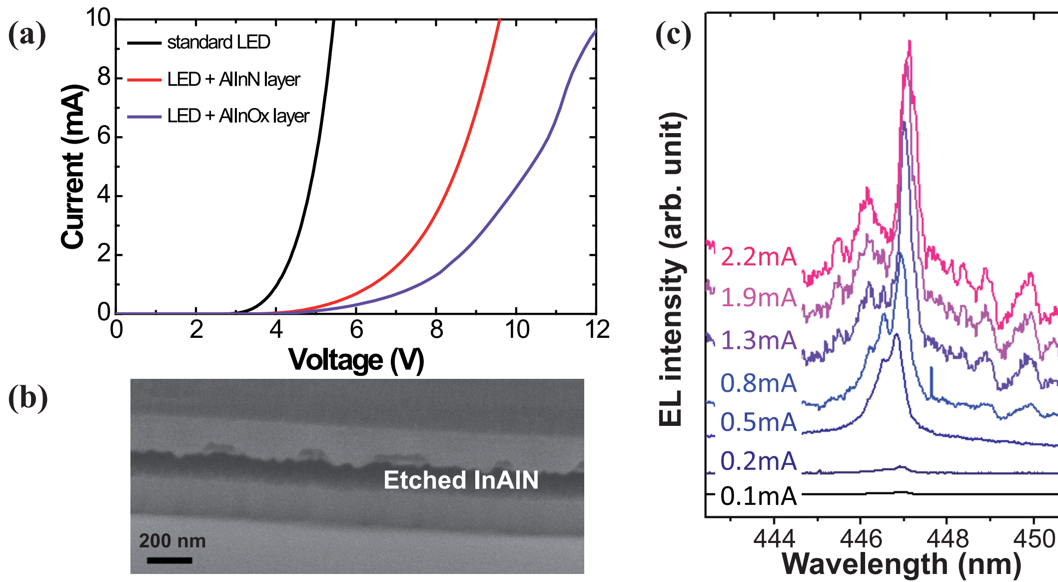

Figure 5.5: (a) I-V characteristics of a standard LED (black curve), an LED including an InAlN layer (red curve), and an LED including an InAlN layer after partial lateral oxidation. (b) EL spectra below threshold for different driving currents measured on a VCSEL including an InAlN:Ox layer for current confinement. (c) Non intentionally etched InAlN layer in a VCSEL structure. Courtesy of Dr. A. Castiglia.

This scheme is depicted in Fig. 5.4 (b). The TCO layer should exhibit both excellent optical and electrical characteristics so as to be suitable for VCSEL applications: it should exhibit a low sheet resistance as well as a low contact resistance to *p*-type GaN while ensuring an extremely low absorption. Thus, a trade-off has to be found concerning the thickness, as the thicker the layer the lower the sheet resistance but at the same time the larger the absorption. Nevertheless, the TCO layer thickness has to be sufficient in order to cover the dielectric current confinement layer sidewalls around its central aperture.

So far, this is the only method that allowed achieving lasing in electrically-driven nitride-based VCSELs [116, 114, 11, 118, 115]. The purpose of the work on TCO contacts to *p*-type GaN presented in chapter 4 was to develop such an approach in our laboratory.

5.3.3 TCO and plasma-based surface passivation

The plasma damage effects on the electrical properties of *p*-type GaN have been addressed in section 4.3.1. It has been reported to be detrimental in the case of parasitic effects during the development of TCO-based contacts to *p*-type GaN layers. However, this effect has also been used in nitride-based LEDs in order to improve light extraction [268, 269]: by using a plasma treatment to increase *p*-type GaN resistivity straight below the metallic *p*-type pad while using a TCO current spreading layer, the top-emitted light absorption by the metal pad is drastically decreased. Thus, this is an alternative approach to the dielectric current confinement layer:

the top *p*-type GaN layer of the VCSEL mesa is exposed to a plasma except for a small diameter in the center of that mesa, which will act as the current aperture. Then, the mesa is covered with a TCO current spreading layer similar to that used in the previous scheme, as illustrated in Fig. 5.4 (c). Both schemes could seem very similar, but the latter has the main advantage of preserving a flat mesa surface, preventing additional scattering losses at the dielectric layer edges. Moreover, as the TCO layer no longer needs to cover the dielectric aperture sidewalls, there is no requirement for a minimal TCO layer thickness.

The idea of using plasma treatment for the surface passivation of *p*-type GaN came from early experiments on TCO deposition on *p*-type GaN. When using the e-gun evaporator presented in section 5.2 for the deposition of ITO *p*-type contacts on LED structures, the ion beam used for oxide densification, which is started prior to the oxide deposition itself, dramatically damaged the top surface of the samples. As a result, no current could then be injected in the resulting LED devices, despite evaporated ITO exhibiting good electrical characteristics.

5.3.4 Buried current confinement layer

The last main current confinement scheme as proposed by B.-S. Cheng and coworkers [270] relies on a buried AlN current aperture placed in the *p*-type GaN region [Fig. 5.4 (d)]. Its main benefit over other methods is that it also acts as a lateral optical confinement layer. It has been successfully used in microcavity LEDs with quality factors exceeding 800. However, no lasing action has been reported in a VCSEL using such a current confinement scheme up to now.

In order to decrease the strain in such devices, the AlN layer could be replaced by a *nid* LM InAlN current aperture, which would act as a current barrier by creating a reverse bias *p*-*n*-junction. This approach would be quite similar to that using lateral oxidation of an InAlN layer, with the exception that the oxidized InAlN layer is placed in the *n*-type GaN region. However, each of these two methods would have their own strengths and weaknesses: the oxidation-based process makes the growth much easier but usually results in devices with a defective mechanical robustness, whereas the buried AlN (or InAlN) current aperture scheme requires a 3-step growth and a careful mask alignment for mesa etching.

Finally, the different approaches could be combined together. Indeed, any of the TCO-based scheme could be combined with one of the two buried (In)AlN current confinement layers. The buried current aperture would be specially interesting by the fact that it would provide lateral optical confinement to the cavity mode.

5.4 Final VCSEL design

The final VCSEL design [154] consists in: a bottom highly-reflective LM 42-pair InAlN/GaN DBR grown on a double-side polished high-quality FS GaN substrate (see section 3.4.2), a 7λ cavity made of a *pin* GaN diode structure comprising an electron blocking layer (EBL) and

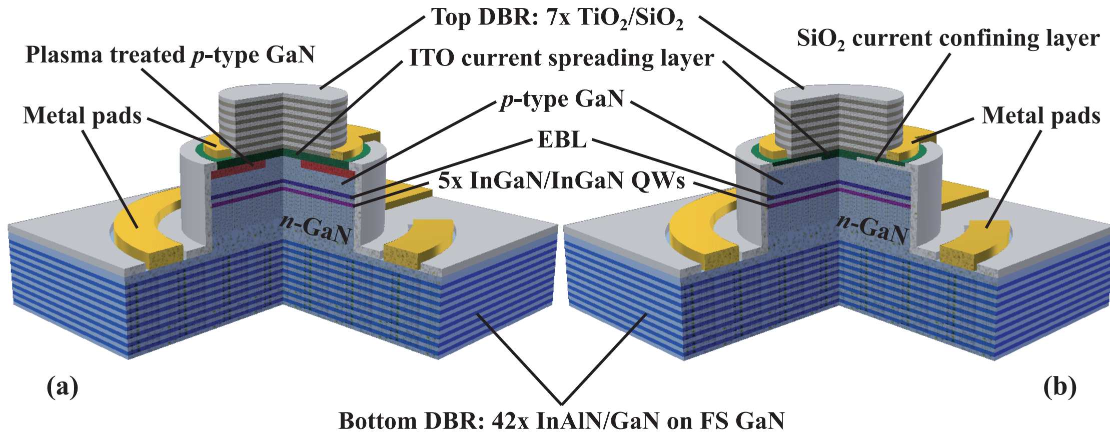

Figure 5.6: Schematic drawings of the VCSEL structures with (a) a plasma treated *p*-type GaN surface or (b) a dielectric layer for current confinement.

an active region made of 5 $In_{0.10}Ga_{0.90}N$/*n*-$In_{0.01}Ga_{0.99}N$ QWs. The top mirror is made of a 7-pair TiO_2/SiO_2 DBR such as shown in Fig. 5.3 (d). An ITO intracavity *p*-type contact forms a current spreading layer (see section 4.3). Metal pads deposited on ITO and *n*-type GaN are used for electrical injection. Two different current confinement schemes have been tested: the dielectric current confinement layer and the plasma-based *p*-type GaN surface passivation. Schematic drawings of the VCSEL designs are shown in Fig. 5.6.

The layer structure is detailed in Fig. 5.7 (a). The *n*- and *p*-type GaN layer doping levels ([Si] and [Mg]) are 5×10^{18} cm^{-3} and 2×10^{19} cm^{-3} and their thicknesses are 944 nm and 97 nm, respectively, which ensures the positioning of the active region in an antinode of the optical field. As intracavity contacts are used, the rather thick *n*-type GaN layer ensures a good lateral electric injection. Both QWs and barriers are 5 nm thick, with a thicker (10 nm) final barrier. The EBL is made of a 20 nm thick *p*-type doped $Al_{0.20}Ga_{0.80}N$ layer. A 20 nm thick heavily doped (net acceptor concentration of 5×10^{19} cm^{-3}, as determined using C-V measurements) p^+-type GaN cap layer ensures an optimal contact to a quarterwave ITO current spreading layer. The latter is placed to act as the first half-pair of the top dielectric DBR. This means that the positioning of the ITO layer is not optimal in term of absorption (it should be placed at a node of the optical field), but the purpose was to ensure a sufficient current spreading while increasing the top DBR reflectivity. The negative effects related to the large absorption due to the ITO layer will be discussed hereafter in the result section.

Transfer matrix simulation of the electric field intensity distribution along the VCSEL cavity is shown in Fig. 5.7 (b). As can be seen, the penetration depth is much shorter in the top dielectric DBR than in the bottom epitaxial one. The field distribution in the QWs and the ITO layer is detailed in Fig. 5.7 (c). As previously said, the QWs are centered at an antinode of the optical field in order to maximize the gain enhancement factor (see section 2.2). Moreover, the ITO is placed to act as a reflective layer.

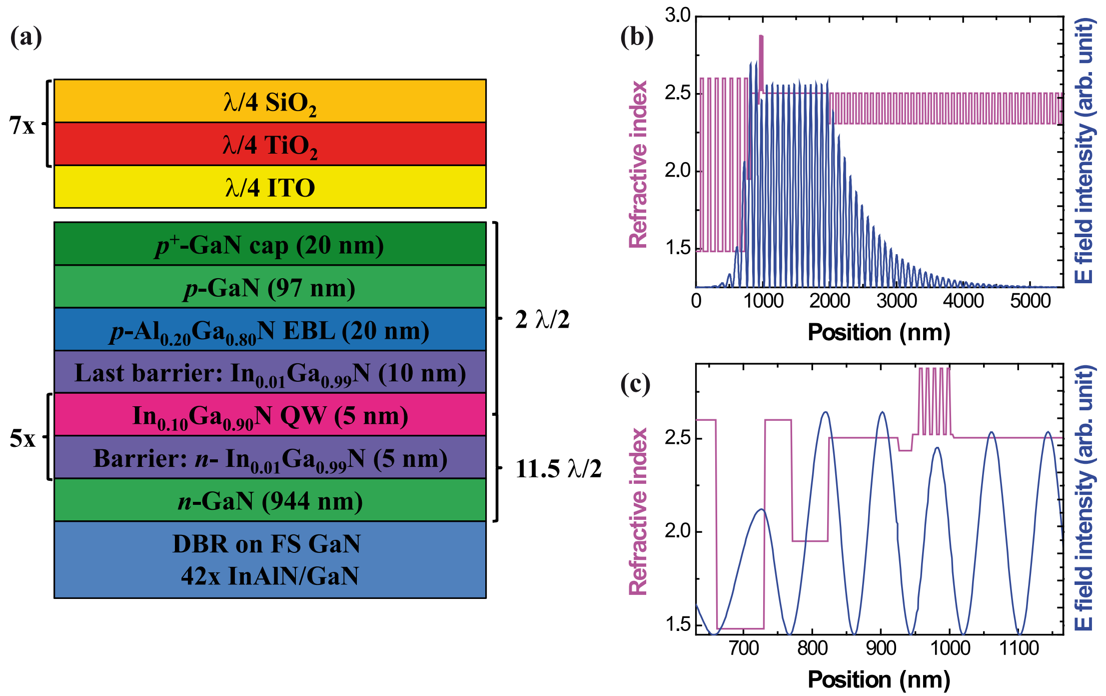

Figure 5.7: (a) VCSEL detailed layer structure. (b) Electric field intensity distribution along the VCSEL cavity. (c) Detail of the field distribution in the QWs and the ITO layer.

5.4.1 Process flow

The process steps of a VCSEL using *p*-type GaN plasma treatment for confining the current are shown in Fig. 5.8. First, mesas are etched using chlorine-based ICP down to the *n*-type GaN [Fig. 5.8 (a)]. Then, RIE using a CHF_3/Ar plasma is used for surface passivation of *p*-type GaN, while a small circular photoresist cap protects the current aperture [Fig. 5.8 (b)]. After this treatment, the ITO current spreading layer is sputtered on the mesas [Fig. 5.8 (c)]. A SiO_2 passivation layer is deposited by PECVD [Fig. 5.8 (d)] prior to the e-beam evaporation of the *p*-type pad [Fig. 5.8 (e)] and *n*-type pad [Fig. 5.8 (f)] made of Ni (30 nm)/Au (100 nm) and Ti (20 nm)/Al (80 nm)/Ti (20 nm)/Au (100 nm), respectively. Finally, the devices are covered with an e-beam evaporated 7-pair TiO_2/SiO_2 top DBR [Fig. 5.8 (g)].

The process steps for a VCSEL using a SiO_2 current confinement layer are quite similar to that of the plasma-treated structure and are shown in Fig. 5.9. Steps (c) to (g) are identical, the only dissimilarity comes from the first two steps. First, a 30 nm thick SiO_2 layer is deposited by PECVD on the epilayers. Then, this dielectric layer and the mesa are etched by RIE and by ICP, respectively, using the same photoresist mask [Fig. 5.8 (a)]. Subsequently, buffered hydrofluoric acid is used to etch a small current aperture in the center of the dielectric layer [Fig. 5.8 (b)].

The mesas have several diameters: 40, 60, 80 and 100 μm. Similarly, the current aperture diameters are equal to 4, 8, 12 and 16 μm.

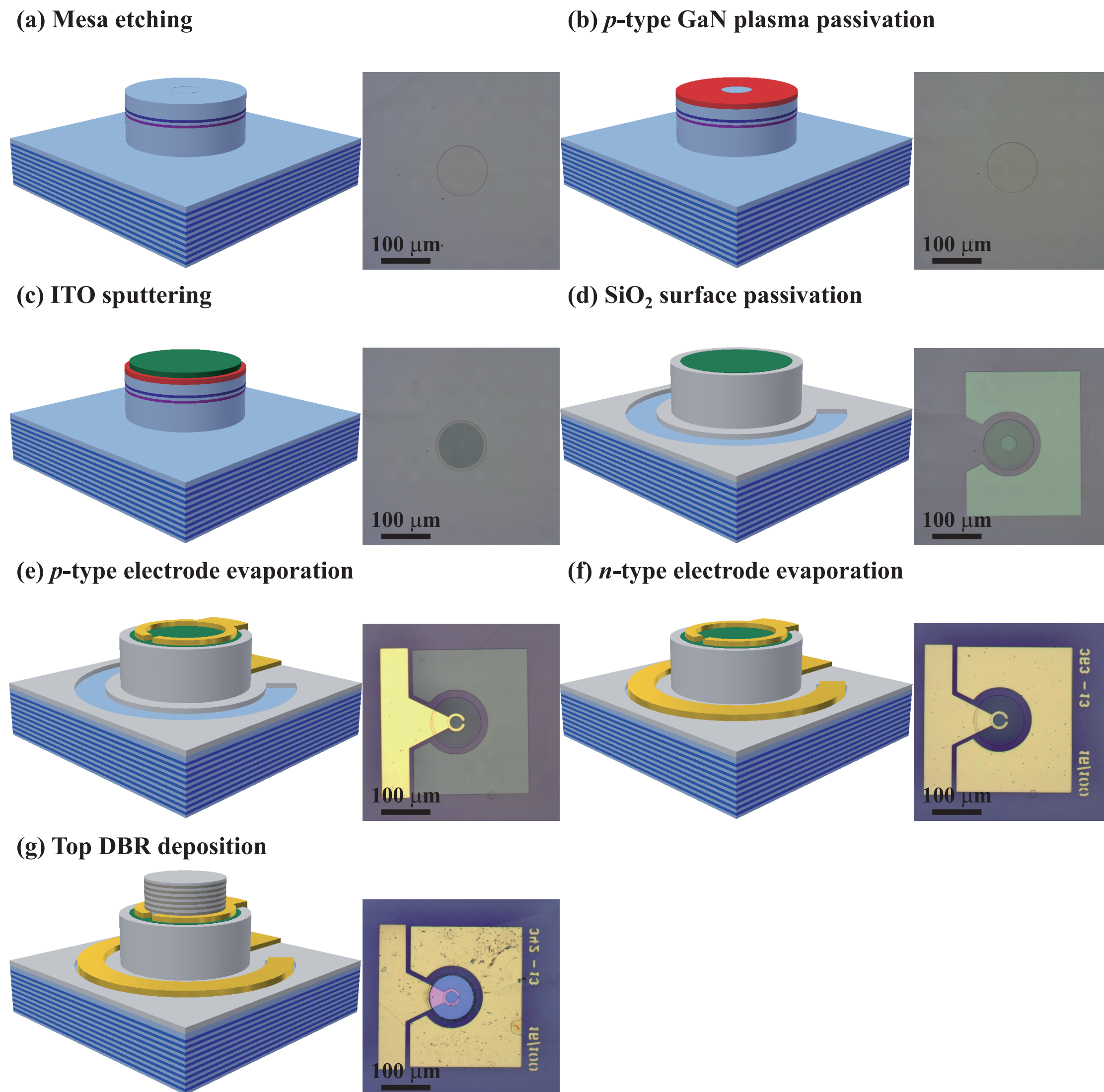

Figure 5.8: Schematic drawings and optical microscope pictures depicting the process steps of a VCSEL using *p*-type GaN plasma treatment for confining the current. Details are given in the main text.

Unfortunately, a small mistake has been made during both microfabrications, as a thin layer ($\sim 2-3$ nm thick) of Ti should have been evaporated below the *p*-type pad in order to improve its adhesion on the SiO_2 passivation layer. Indeed, the *p*-type pad were partially removed during the top DBR lift-off step, which reduced the process yield. Moreover, a technical issue during the top DBR evaporation on the plasma-treated sample resulted in a defective final pair, made of a $\lambda/2$ instead of $\lambda/4$ TiO_2 layer. Finally, most of the 4 μm wide current apertures on the SiO_2 sample were not sufficiently resolved during the corresponding photolithography step, resulting in defective devices.

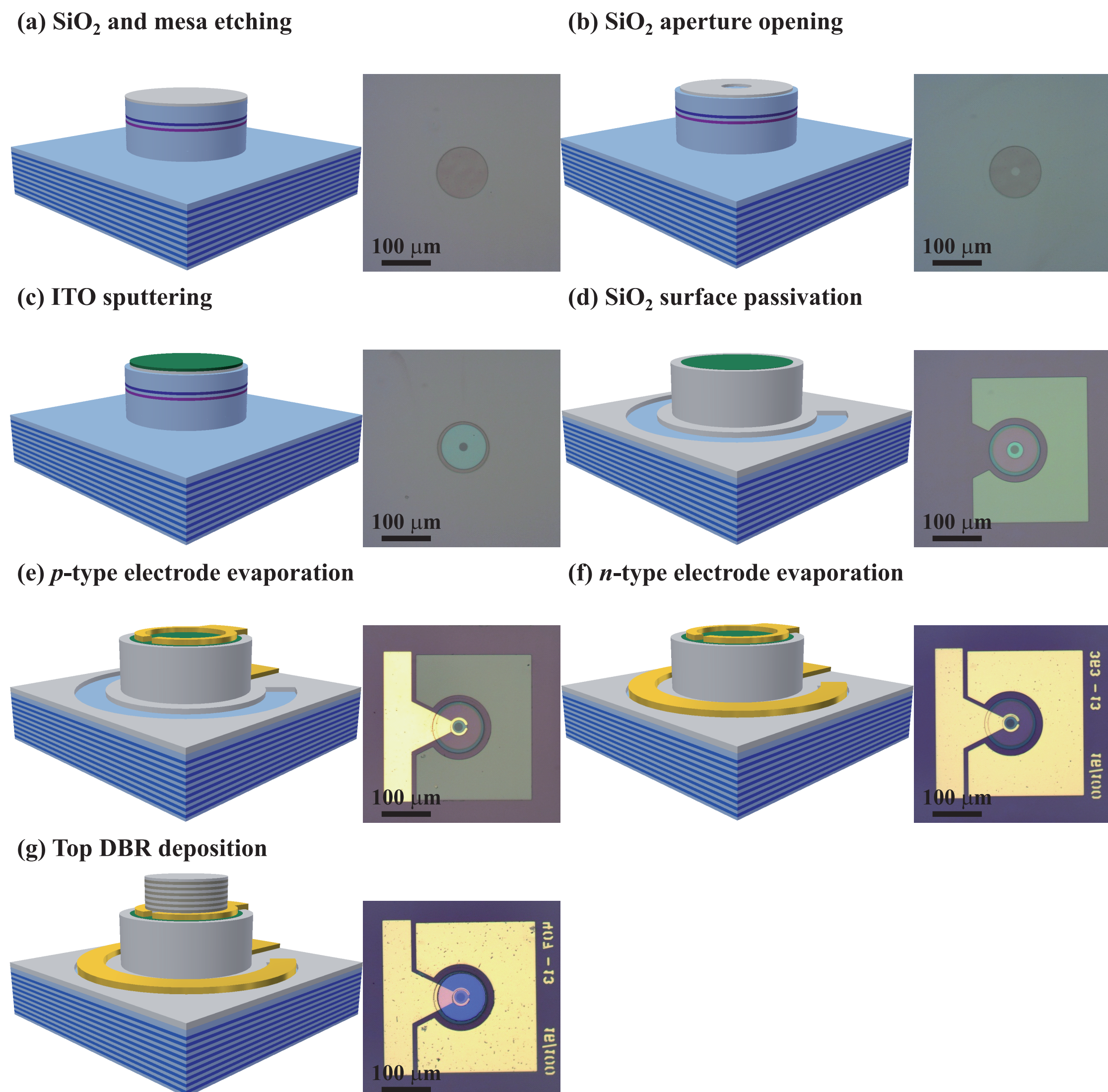

Figure 5.9: Schematic drawings and optical microscope pictures depicting the process steps of a VCSEL using a SiO_2 current confinement layer. Details are given in the main text.

5.5 Results

An SEM picture and a detailed cross-section view of the plasma-treated device are shown in Figs. 5.10 (a) and 5.10 (b), respectively. The measurements were obtained following focused ion beam (FIB) for sample milling and were performed at CIME (EPFL) by Dr. Marco Cantoni. Pictures of the unbiased plasma-treated and SiO_2 aperture devices prior to the top DBR deposition are shown in Figs. 5.10 (c) and 5.10 (e), respectively, and under a 2 mA bias in Figs. 5.10 (d) and 5.10 (f). For both devices, the emitted light only comes from the small current aperture located in the center of the mesas, which is a hint for an efficient device current confinement for both schemes. This is especially important in order to validate the

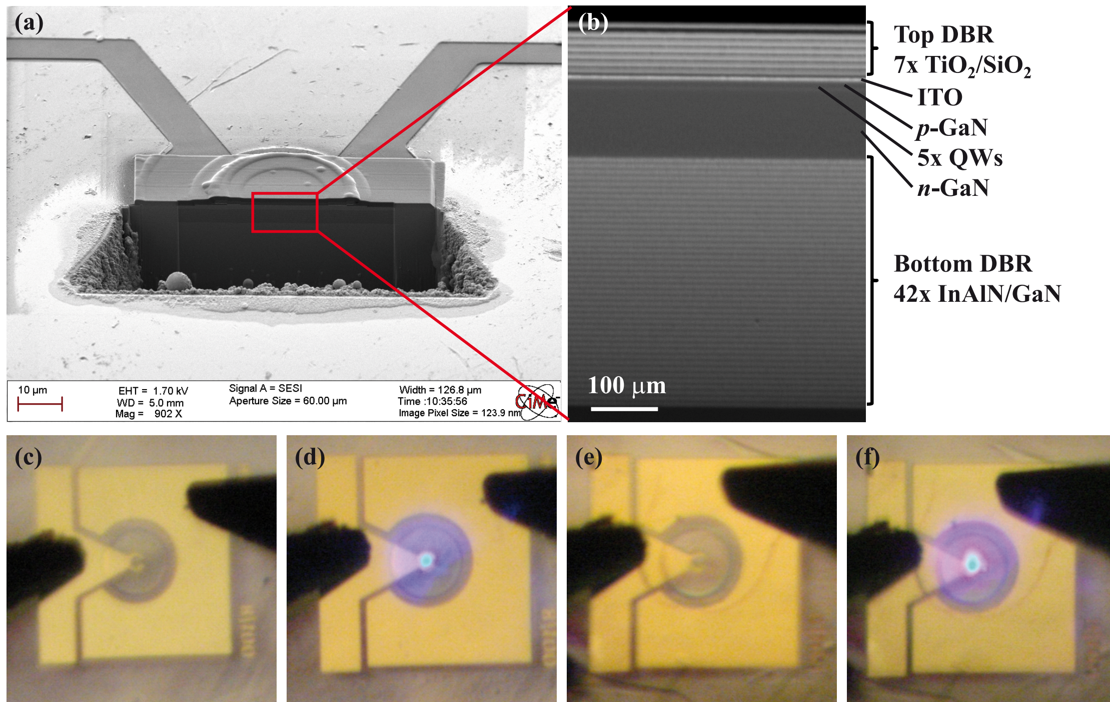

Figure 5.10: (a) SEM picture and (b) detailed cross-section view of the plasma-treated VCSEL, obtained following FIB for milling. Pictures of a plasma-treated VCSEL (c) unbiased and (d) for a 2 mA bias, and pictures of a SiO_2 aperture VCSEL (e) unbiased and (f) for a 2 mA bias, prior to the top DBR deposition.

p-type GaN plasma treatment approach.

All measurements presented in this section have been done at RT without active device cooling (e.g. Peltier cell).

I-V curves measured on both VCSEL samples with different current aperture sizes are shown in linear scale and semi-logarithmic scale in Figs. 5.11 (a) and 5.11 (c), respectively. Measurements are performed under CW injection. The device mesa diameter considered is equal to 80 μm. Despite a very slight dissimilarity in the low injection regime [Fig. 5.11 (c)] suggesting a slightly larger leakage current in the plasma-treated sample, both I-V curves are very similar, which suggests that both current confinement schemes are nearly equally efficient. The corresponding current density vs voltage curves for the plasma-treated devices are plotted in inset in Fig. 5.11 (a). The 4 and 8 μm aperture devices exhibit very similar curves, whereas the electrical injection in the 16 μm aperture VCSEL is slightly less effective, which could be related to a non perfectly homogeneous ITO contact. I-V curves measured under CW injection on plasma-treated devices with different mesa diameters are shown in Fig. 5.11 (b). Devices have a current aperture diameter of 8 μm. The different mesa diameters do not impact on the I-V characteristics of the devices. As the broader the mesa the further the *n*-type contact from the current aperture, this is a proof of an efficient lateral current spreading in the *n*-type

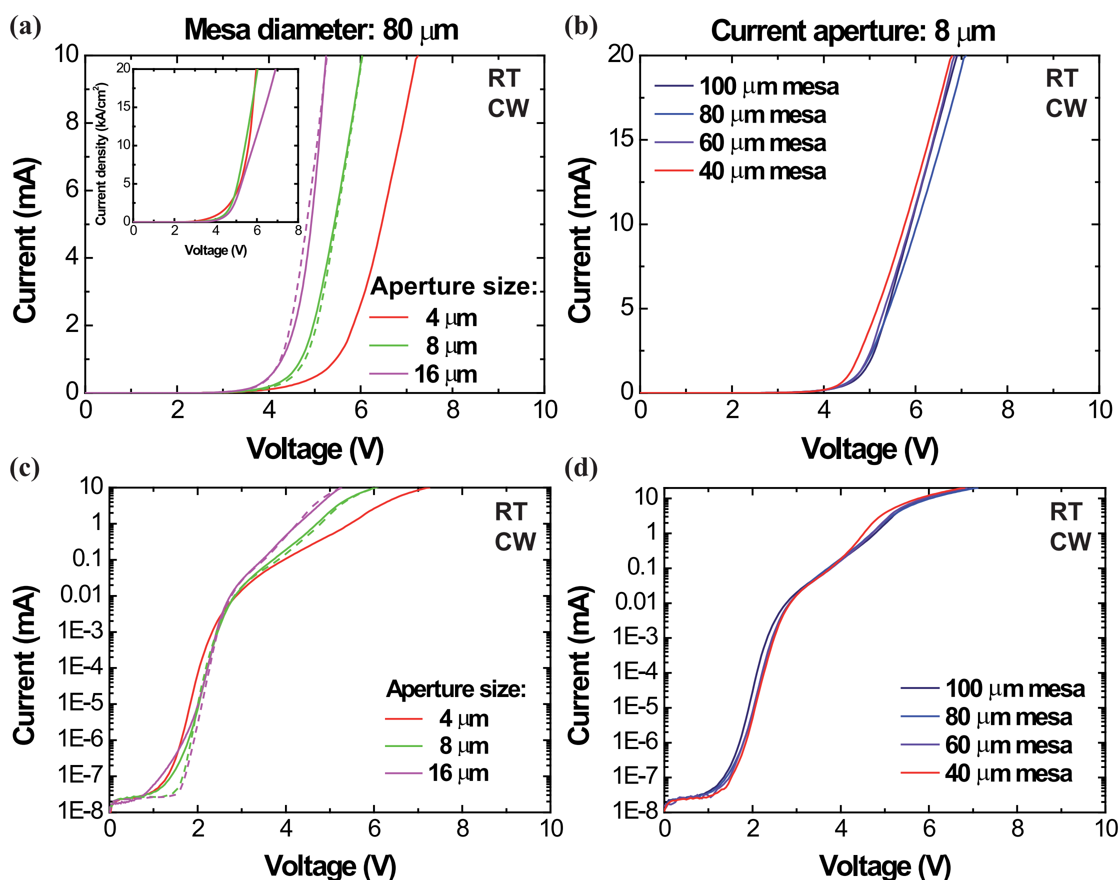

Figure 5.11: (a) Current vs voltage characteristics of plasma-treated devices (solid lines) and SiO_2 aperture devices (dotted lines) with a mesa diameter of 80 μm for different current aperture sizes in linear scale. Inset: current density vs voltage curves measured on the same plasma-treated devices. (b) Current vs voltage characteristics of plasma-treated devices with a current aperture of 8 μm for the different mesa diameters in linear scale. (c) and (d) same measurements as in (a) and (b), respectively, plotted in semi-logarithmic scale. Measurements are performed under CW injection.

GaN Layer. Moreover, the similarity between the different curves in the low injection regime [Fig. 5.11 (d)] is another good hint for the efficiency of the plasma-based current confinement. Together with the pictures shown in Figs. 5.10 (d) and 5.10 (f), these two elements allow excluding current leakage through the plasma passivated *p*-type GaN. The I-V curves presented in Fig. 5.11 (a) are to be compared to those presented in Fig. 4.4 (a) and assess the importance of high-quality ITO contact layers to *p*-type GaN for the development on VCSELs, as much larger current densities are reached without device breakdown.

The output light peak power measured from the top side as well as the cavity mode linewidth as a function of the driving current measured on a plasma-treated VCSEL with a 60 μm diameter mesa and an 8 μm current aperture are shown in Fig. 5.12 (a). Those measurements, as well as all forthcoming measurements (unless otherwise stated), were performed under

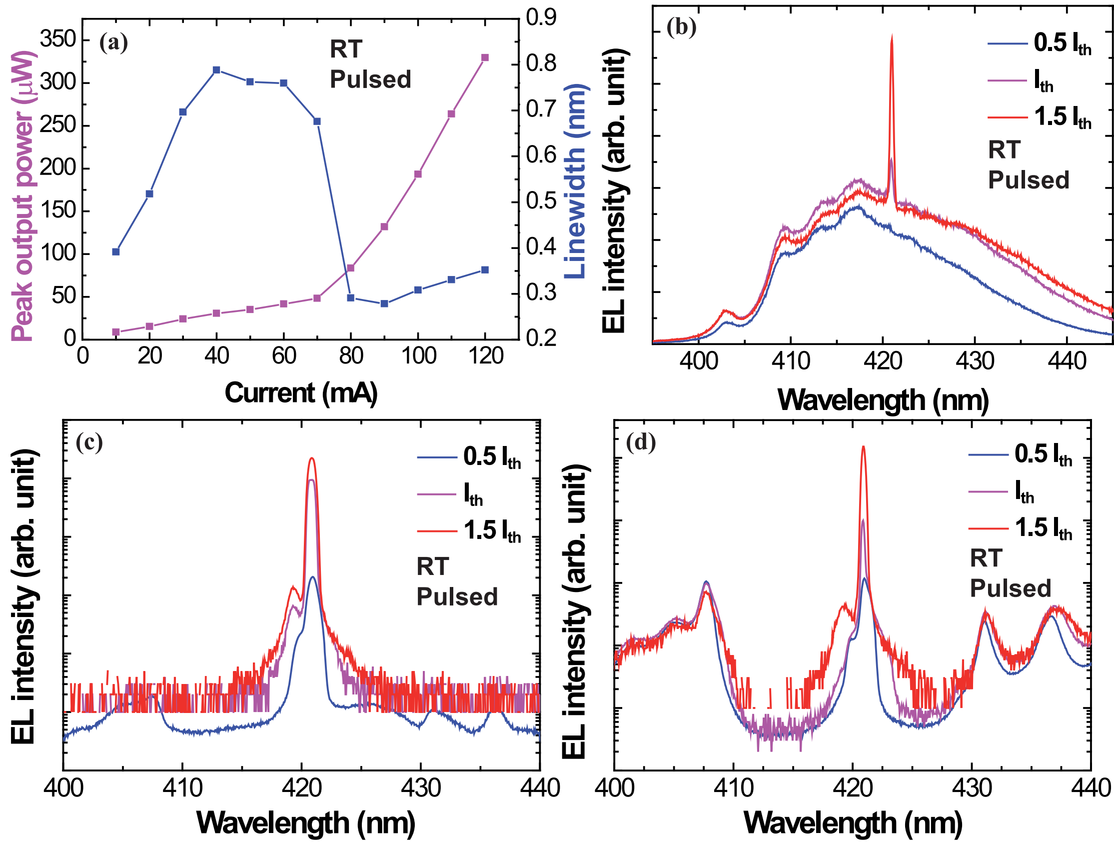

Figure 5.12: (a) Light output peak power and cavity mode linewidth vs pulsed current for the plasma-treated sample under pulsed current injection (200 ns wide pulses, 1% DC). (b) Spectra measured on the same sample from the edge, (c) the top and (d) the bottom of the device. Device mesa and current aperture diameters are equal to 60 and 8 μm, respectively.

pulsed current injection, with pulses having a length of 200 ns and a repetition rate of 50 kHz corresponding to a duty cycle (DC) of 1%. Both the nonlinear increase in the output intensity as well as the narrowing of the cavity mode linewidth at threshold are evidence for lasing in the plasma-treated VCSEL. The threshold current is about 70 mA, which corresponds to a current density of about 140 kA/cm^2. This quite large value for the threshold current density will be further discussed hereafter. Peak output powers up to 300 μW have been obtained. Below threshold, the cavity mode linewidth of a microcavity is expected to decrease when increasing the current [271]. However, our devices exhibit the reverse behavior [Fig. 5.12 (a)]. Actually, this effect is ascribed to heating effects [272] occurring in the device due to the high threshold current density. As will be disccused hereafter, heating effects are even more critical under CW injection.

EL spectra measured through the edge, the top and the bottom of a plasma-treated VCSEL for currents below, near and above lasing threshold are shown in Figs. 5.12 (b), 5.12 (c) and 5.12 (d), respectively. The cavity mode is observed at 421 nm and is well-centered with respect to the bottom nitride-based DBR, as can be seen in Fig. 5.12 (d). A slight redshift of the QW

emission above lasing threshold can be noticed through the intensity variation of the Bragg modes below and above threshold, which have inverse ratios when measured on each side of the DBR stopband [Fig. 5.12 (d)]. This shift can be ascribed to the combination of several contributions: the redshift of the QW material bandgap energy when the sample temperature increases, according to Varshni's law (Eq. 1.17), a redshift of the QW emission related to the bandgap renormalization, which depends on the $e-h$ plasma density [273, 274], the screening of the electric field inside the QWs under large carrier injection yielding a blueshift of the QW emission due to the reduction of the QCSE (Eq. 1.23), and a blueshift of the emission wavelength due to the filling of localized states in In-rich areas. However, Kuokstis *et al.* have shown that the latter is weaker than the blueshift arising from the electric field screening [275]. The observed redshift of the QW emission means that the dominant emission shift mechanism is either the bandgap renormalization, the bandgap energy redshift due to the temperature increase, or both of them. As will be seen hereafter, the actual dominant mechanism is the QW material bandgap energy decrease related to the increase of the sample temperature in the high current injection regime.

The presence of a low intensity side-peak near the main lasing mode is ascribed to photonic disorder (see section 3.4.2). The quality factor measured under a driving current of 10 mA is equal to 1080. This current is assumed to be close to the transparency current of the active region, which means that the measured quality factor should be close to the cold cavity quality factor. Of course, the quality factor of an efficient VCSEL structure far below the active region transparency is expected to be quite low, as the absorption of the QWs strongly decreases the cavity photon lifetime. The emission measured from the edge of the device shows that the QWs are not perfectly tuned with respect to the cavity mode as can be seen in Fig. 5.12 (b). The QW peak emission should match the cavity mode (zero detuning), as it corresponds to the best overlap between the cavity mode and the gain [276]. Moreover, the QW emission is fairly broad, which is highly detrimental for a microcavity laser. Indeed, Björk and coworkers showed that the spontaneous emission coupling factor β is decreased by a factor equal to the ratio between the spontaneous-emission and the cold-cavity linewidths [271].

Fourier-plane imaging of the plasma-treated VCSEL far-field emitted through the top DBR for currents below, near and above lasing threshold are shown in Figs. 5.13 (a) to 5.13 (d). Device mesa and current aperture diameters are equal to 80 and 8 μm, respectively. The parabolic dispersion curve observed for a driving current of 40 mA is characteristics of a microcavity structure emitting below lasing threshold, whereas only the lasing mode can be seen for a current of 100 mA and above. From those measurements, the beam divergence angle full width at half maximum (FWHM) has been measured below and above lasing threshold to be equal to 36° (40 mA) and 5° (100 mA), respectively.

The corresponding real space images of the near-field measured on the same device are shown in Figs. 5.13 (e) to 5.13 (h). According to Fig. 5.13 (e), the light emission below the onset of lasing is homogeneous across the whole current aperture, meaning that the current injection is uniform, i.e. the current spreading in the ITO layer is efficient. However, the lasing mode

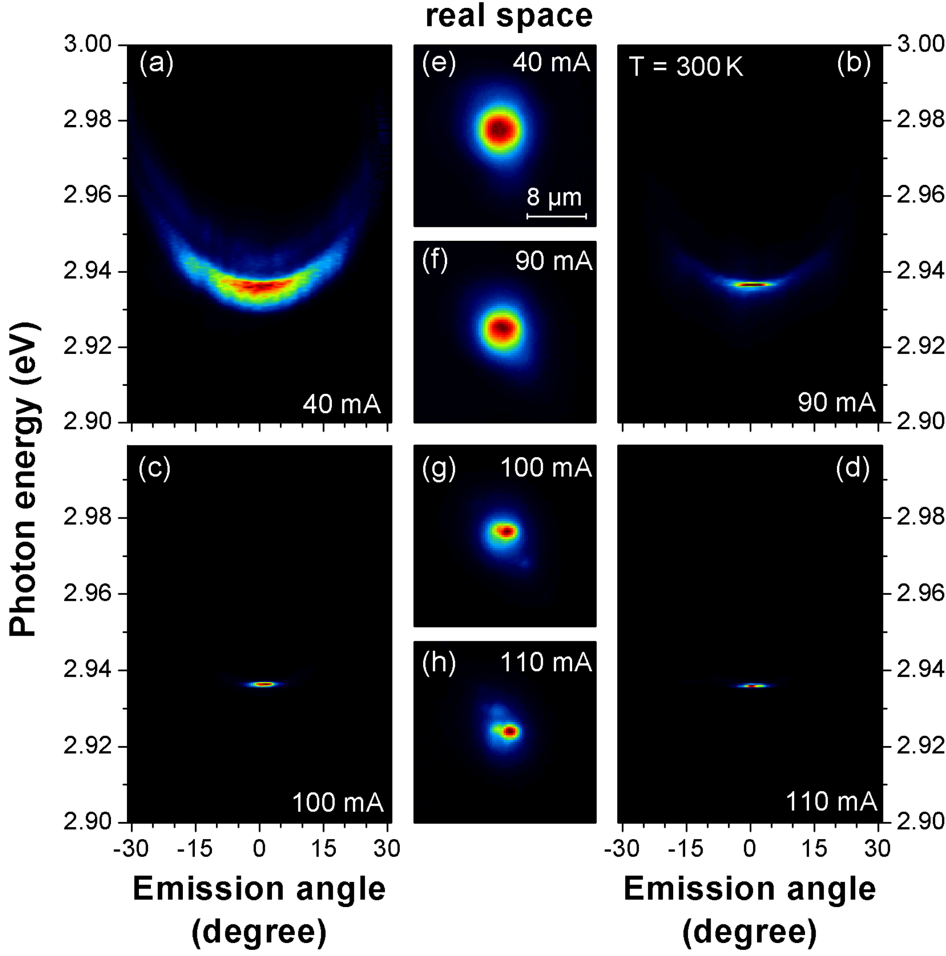

Figure 5.13: (a) to (d) Fourier-plane imaging of the cavity mode far-field emitted through the top DBR of a plasma-treated VCSEL for different pulsed currents (200 ns wide pulses, 1% DC). (e) to (h) Corresponding real space imaging of the near-field of the device for the same varying currents. Device mesa and current aperture diameters are equal to 80 and 8 μm, respectively.

spatial radius is smaller than the current aperture above lasing threshold [Figs. 5.13 (g) and 5.13 (h)]. In other words, only a small part of the injected area is actually lasing. This effect has also been reported by other groups [114, 11]. It is actually consistent with the measured beam divergence angle FWHM θ_{FWHM} above threshold, as the lasing mode radius a_p is given by [271]:

$$a_p \approx \frac{\lambda}{2\theta_{FWHM}} \tag{5.1}$$

where λ is the cavity mode wavelength and θ_{FWHM} is expressed in radian. For the θ_{FWHM} value given above, the corresponding lasing mode radius a_p amounts to 2.4 μm, which is in

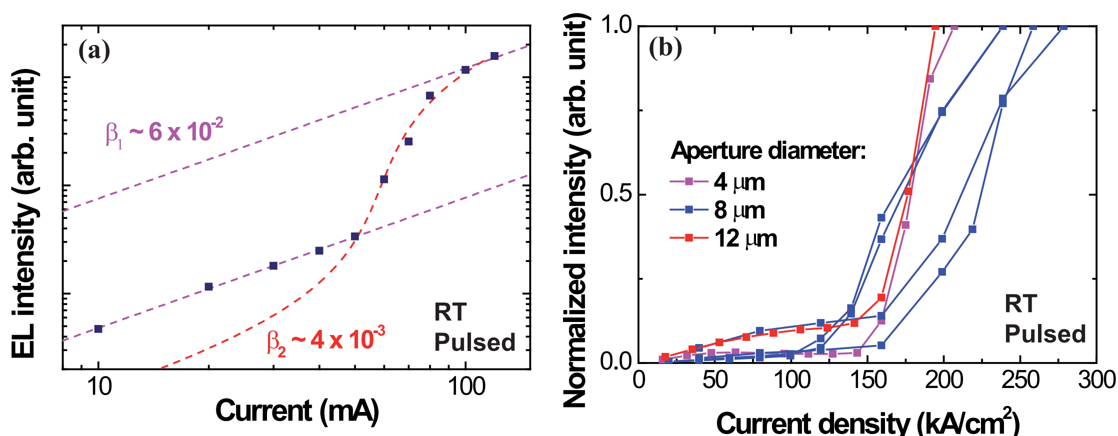

Figure 5.14: (a) Log-log plot of the integrated cavity mode intensity vs pulsed current (200 ns wide pulses, 1% DC) for a plasma-treated VCSEL. Device mesa and current aperture diameters are equal to 60 and 8 μm, respectively. The estimated values for the spontaneous emission coupling factor extracted from the curve are $\beta_1 \approx 6\times10^{-2}$ from the step intensity height at threshold, and $\beta_2 \approx 4\times10^{-3}$ from a fit of the EL curve using Eq. 5.2 (red dotted curve). (b) Cavity mode (normalized) integrated intensity vs pulsed current density (200 ns wide pulses, 1% DC) for plasma-treated devices with different current aperture diameters. Lasing threshold current densities are ranging from 120 to 150 kA/cm^2 for all aperture sizes.

good agreement with values extracted from Figs. 5.13 (g) and 5.13 (h). Photonic disorder can account for this feature, as at least two modes are coexisting within the current aperture area, as seen previously in Figs. 5.12 (c) and 5.12 (d). Indeed, those two modes may have different thresholds, and above the lowest one only one of those modes exhibits lasing.

A log-log plot of the integrated cavity mode intensity as a function of the current measured on the plasma-treated sample is shown in Fig. 5.14 (a). Device mesa and current aperture diameters are equal to 60 and 8 μm, respectively. The corresponding spontaneous emission coupling factor can been estimated from the intensity step height at threshold, or by fitting the EL curve using the following expression for the integrated mode intensity I_{out} [277]:

$$I_{out} \propto r - 1 + \sqrt{(r-1)^2 + 4\beta r} \tag{5.2}$$

where $r = I/I_{th}$ is the normalized injection rate, given by the ratio between the current I and the threshold current I_{th}. The first method yields an estimated value $\beta_1 \approx 6\times10^{-2}$. For the second one, the best fit with a value for the threshold current I_{th} equal to 60 mA is obtained for $\beta_2 \approx 4\times10^{-3}$. This discrepancy comes from an overestimation of the β factor using the first method. Indeed, the mode intensity is integrated over the whole current aperture below threshold, whereas the lasing mode spatial radius is smaller than the current aperture. This means that the intensity below threshold is integrated over at least two different spatial modes,

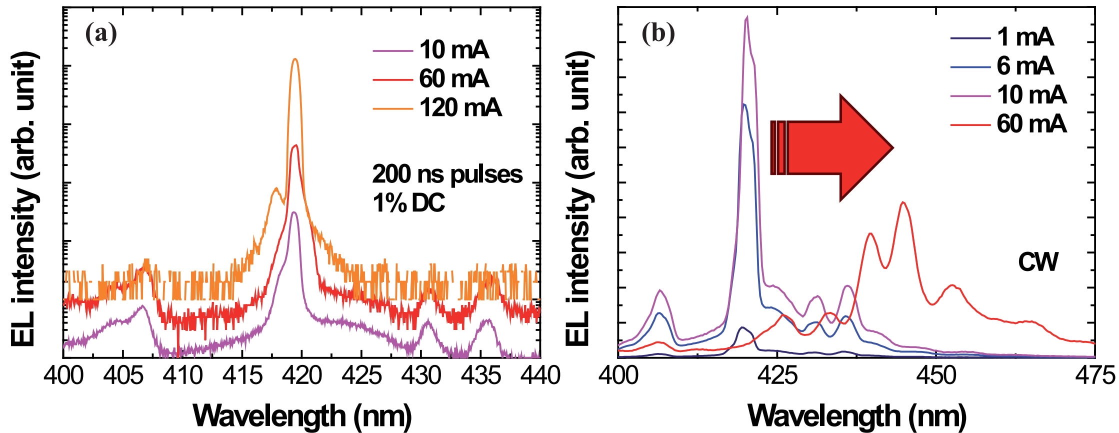

Figure 5.15: EL spectra measured (a) under pulsed injection (200 ns wide pulses, 1% DC) and (b) under CW injection on a plasma-treated sample. Device mesa and current aperture diameters are equal to 40 and 8 μm, respectively. The red arrow in (b) highlights the strong emission redshift because of critical device heating under CW injection.

while only one of those modes exhibits lasing above threshold, as discussed previously. In addition, the value $\beta_2 \approx 4 \times 10^{-3}$ is closer to value previously reported by our group for an optically pumped blue VCSEL [153].

Cavity mode integrated intensity as a function of the current density measured on several plasma-treated devices with different current apertures is depicted in Fig. 5.14 (b). The intensities have been normalized in order to compare the different curves. Threshold current densities are ranging from 120 to 150 kA/cm^2 for all current aperture diameters, which is another proof for the efficiency of both the plasma treatment for current confinement and the ITO current spreading layer.

EL spectra measured under pulsed and CW current injection on a plasma-treated VCSEL are shown in Figs. 5.15 (a) and 5.15 (b), respectively. The device has a 40 μm mesa and a 8 μm current aperture. Whereas the sample exhibits lasing under pulsed injection, no lasing action is observed in CW. Actually, the very large threshold current density causes dramatical device heating, resulting in a critical QW emission redshift as represented by the red arrow in Fig. 5.15 (b). This prevents our devices from CW lasing, as the QW emission no longer matches the cavity mode wavelength. The light is eventually emitted through the top DBR Bragg modes. Thus, the threshold current density should be drastically decreased in forthcoming samples in order to achieve CW lasing. As said previously, the emission shift comes from four different contributions. As the QW emission exhibits a redshift, the dominant mechanism was assumed to be either the bandgap renormalization or heating effects. However, as the redshift is accentuated under CW injection, it is ascribed to the temperature increase. Indeed, a larger temperature increase yielding a larger emission redshift under CW injection than under pulsed injection is consistent with this assumption.

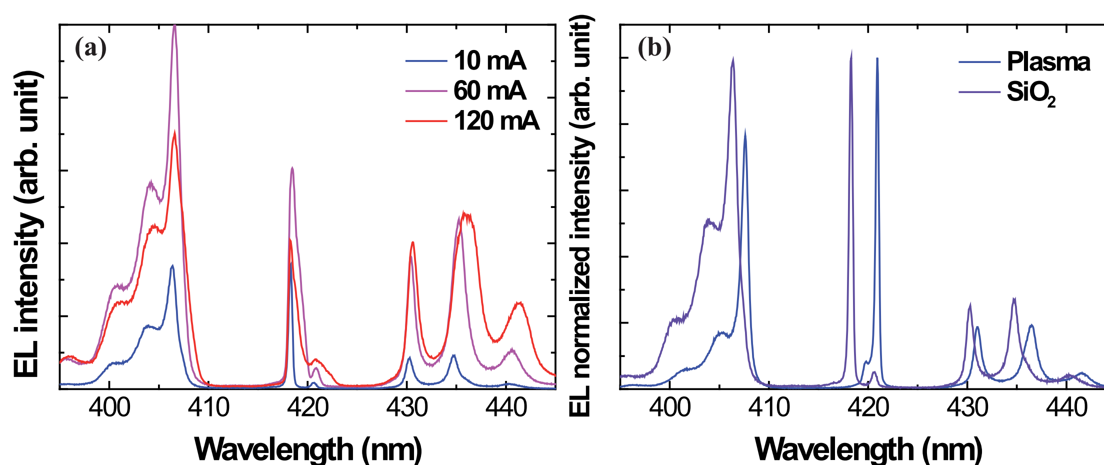

Figure 5.16: (a) EL spectra measured on the SiO_2 aperture sample under different pulsed currents (200 ns wide pulses, 1% DC) from the bottom of the device. (b) Comparison between EL spectra measured on the plasma-treated (blue line) and SiO_2 (violet line) samples under 10 mA pulsed current. The corresponding quality factors are 1080 and 950 for plasma-treated and SiO_2 samples, respectively. Both device mesa and current aperture diameters are equal to 60 and 8 μm, respectively.

EL spectra measured through the bottom DBR of a SiO_2 aperture VCSEL for different pulsed currents are shown in Fig. 5.16 (a). Device mesa and current aperture diameters are equal to 60 and 8 μm, respectively. Despite a cavity mode perfectly centered with respect to the bottom DBR stopband, a quality factor of 950 and a QW emission matching the cavity mode, no lasing has been obtained, even under pulsed injection. A comparison between the EL spectra measured through the bottom DBR of this sample (violet curve) and that of a corresponding plasma-treated sample (blue curve) is depicted in Fig. 5.16 (b). The quality factor of the plasma-treated device is $Q = 1080$, which is close to that of the SiO_2 aperture sample. Both cavity modes are well centered with respect to the bottom DBR stopband and match the QW emission. Moreover, both devices exhibit the same I-V characteristics, as depicted in Fig. 5.11 (a). This means that the discrepancy between both samples does not come from their structures but actually from their different current confinement schemes.

Preliminary simulations have been performed at Chalmers University, Sweden, in the group of Prof. Haglund in the frame of a collaboration on nitride-based VCSELs. In fact, the step at the edge of the SiO_2 current aperture would cause a large increase in the diffraction losses. On the other hand, it would provide a good lateral optical mode confinement which would result in a better overlap between the gain area (corresponding to the current aperture) and the optical mode lateral extent than for a completely planar microcavity VCSEL such as the plasma-treated VCSEL, assuming that the deposition of the ITO current spreading layer yields a planar mesa atop the dielectric current aperture. This would lead to a reduced theoretical material gain at threshold. However, assuming that the plasma treatment would decrease the refractive index of p-type GaN, the resulting index guiding would drastically improve the

overlap between the gain area and the transverse optical mode. As a result, the mode and gain region overlap would be roughly equivalent for both devices, and the increased diffraction losses for SiO_2 aperture VCSELs would account for a larger threshold than for plasma-treated samples. Together with the already large threshold for the latter devices, this could explain why lasing has not been achieved in the former samples. The required change in the refractive index value $\Delta n = n_{\mathrm{GaN}} - n_{\mathrm{GaN,RIE}}$ is of the order of $0.005 - 0.01$ if considered over the whole p-GaN layer thickness [278]. Obviously, the plasma would only affect the sample surface, thus the required Δn would be greater. Notwithstanding, further simulations and experiments, such as ellipsometry measurements on plasma treated p-type GaN samples, will be performed in order to validate these assumptions.

As previously observed, the plasma-based p-type GaN surface treatment is an efficient current confinement scheme. This means that current leakage can be excluded as a possible source for the large threshold current densities obtained. Consequently, the reasons accounting for this feature have to be found elsewhere. Actually, the ITO layer is quite thick and furthermore not positioned at a node of the optical field. The measured absorption in such a quarterwave ITO layer is as high as 0.8% (see section 4.3.4), corresponding to an absorption coefficient $\alpha_{ITO} \approx 1200$ cm^{-1}. This yields modal losses $\langle\alpha_{ITO}\rangle \approx \Gamma_z \alpha_{ITO} = 45$ cm^{-1}, which are defined in a similar way as the modal gain (Eq. 2.8). By reducing by half the ITO layer thickness (i.e. to a $\lambda/8$ layer) and placing it wisely at a node of the optical field, the ITO absorption modal losses could be decreased down to $\langle\alpha_{ITO}\rangle = 2$ cm^{-1}. Moreover, as stated in section 5.4.1, a technical issue happened during the top dielectric DBR evaporation. As a result, its reflectivity was 0.5% lower than that of the DBR deposited on the SiO_2 aperture sample as can be seen in Fig. 5.17 (a).

In order to have a quantitative idea of those two combined effects, simulations of the threshold current densities have been performed. A logarithmic dependence of the gain g to the current density J has been assumed: $g = g_0 \ln J/J_0$ [279], where g_0 is a phenomenological gain parameter and J_0 is the transparency current density of the QW-based active region. According to Eq. 2.8, the lasing condition can thus be written (under the assumption that $\Gamma_{xy} \sim 1$):

$$\underbrace{\alpha_i + \langle\alpha_{ITO}\rangle + \frac{1}{2L_{eff}} \ln\left(\frac{1}{R_{top}R_{bot}}\right)}_{\alpha_{tot}} = \langle g_{th}\rangle = \Gamma_z g_0 \ln\left(\frac{J_{th}}{J_0}\right) \tag{5.3}$$

where α_i are the cavity internal losses, L_{eff} is the effective cavity length, R_{top} and R_{bot} are the top and bottom DBR reflectivity, respectively, α_{tot} are the total losses, $\langle g_{th}\rangle$ is the modal gain at threshold, $\Gamma_z = \Gamma_{fill}\Gamma_{enh}$ is the vertical confinement factor, which is the product between the filling factor Γ_{fill} and the gain enhancement factor Γ_{enh}, and J_{th} is the threshold current density. See section 2.2.3 for more details. Thus, the current density at threshold as a function

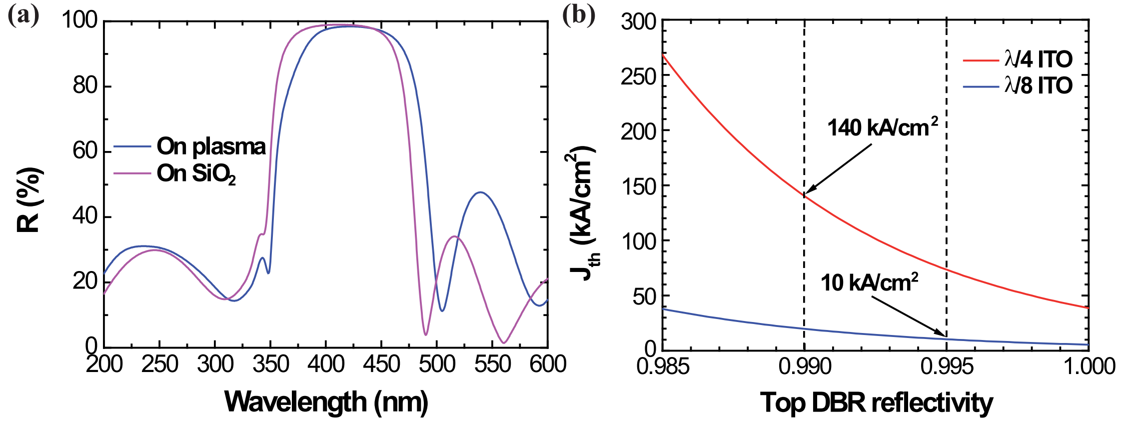

Figure 5.17: (a) Reflectivity spectra of the top DBRs evaporated on plasma-treated (blue curve) and SiO_2 aperture (violet curve) samples. (b) Threshold current density as a function of the top DBR reflectivity for the plasma-treated sample calculated using Eq. 5.3 for two different ITO layer thicknesses and positions.

of the total losses α_{tot} can be expressed as:

$$J_{th} = J_0 \exp\left(\frac{\alpha_{tot}}{\Gamma_z g_0}\right). \tag{5.4}$$

The threshold current density as a function of the top dielectric DBR peak reflectivity has been plotted in Fig. 5.17 (b) using Eq. 5.4. The red and blue curves correspond to devices with a $\lambda/4$ ITO layer placed between an antinode and a node of the optical field (similarly to the samples presented in this section) and with a $\lambda/8$ ITO layer centered at a node of the standing wave, respectively. The used parameters are $\alpha_i = 23.5$ cm^{-1}, $R_{bot} = 99.6\%$, $L_{eff} = 1.80$ μm, $\Gamma_{fill} = 0.014$ (see Eq. 2.37), $\Gamma_{enh} = 1.52$ (see Eq. 2.40). $J_0 \sim 1$ kA/cm^2 has been assumed to be a reasonable order of magnitude for the transparency current density, according to the value reported by Scheibenzuber *et al.* [280], which were measured on edge-emitting LDs grown in our laboratory using the Haki-Paoli method for modal gain determination [281]. This graph shows that the combined effect of reducing the ITO layer thickness by half, positioning it at a node of the electrical field and increasing the top DBR reflectivity, the threshold current density could be decreased from 140 kA/cm^2 down to 10 kA/cm^2, which is a value much closer to state-of-the-art thresholds reported so far [116, 11, 118, 115]. However, increasing the top DBR reflectivity would also mean decreasing the ratio of outcoupled light transmitted through the top of the device. Therefore, a trade-off has to be determined regarding the top DBR reflectivity in order to lower the threshold current density while preserving a large output power through the top DBR, or switched to a bottom emitting VCSEL geometry using substrate thinning and polishing.

5.6 Outlook

Lasing in electrically-driven blue VCSELs has been successfully demonstrated using an alternative current confinement scheme based on plasma-based *p*-type GaN surface passivation. Thus, the optimization of both the bottom InAlN-based DBRs (chapter 3) and the ITO contacts to *p*-type GaN (chapter 4) were fruitful. However, further improvements are required in order to achieve CW lasing in such devices. Amongst them, the most straightforward seems to be the correction of the thickness and position of the ITO current spreading layer. Nevertheless, a careful and in-depth study of the active region would be mandatory in order to optimize the VCSEL structure. Using an active region geometry adapted from that of edge-emitting lasers proved to be sufficient for a first try, but is not satisfactory for the long term. Moreover, the different current confinement schemes could be combined. Particularly, an InAlN buried aperture (section 5.3.4) could be used together with the plasma treatment in order to improve the optical mode lateral confinement. Another point worth mentioning is the development of conductive InAlN-based DBRs. Intracavity *n*-type contacts would no longer be required, which would allow reducing the cavity thickness and thus decrease absorption losses and increase the filling factor Γ_{fill}. Finally, a new dielectric sputtering tool has been ordered for our institute. This new machine should be more reliable than the present e-beam evaporator and will enable a better control on the thickness of the deposited layers thanks to an *in situ* reflectivity measurement system.

Furthermore, the development of such microcavity lasers opens the way for new optoelectronic devices such as polariton LEDs and LDs. However, the QW quality is much more critical in such devices as a narrow absorption broadening is required in order to reach the strong coupling regime. In particular, InGaN QW inhomogeneous broadening due to indium composition fluctuations is detrimental for that purpose. Thus, RC-LEDs using GaN QWs could be an option to explore. The drawback then would come from the larger strain and dislocation density in UV InAlN DBRs (see section 3.4.3), as well as *p*-type doping issues. Note that Tsintzos and coworkers reported on polariton LEDs made from III-arsenide materials operating up to RT [282, 283]. However, the small exciton binding energy in this material system is likely to prevent the observation of optical nonlinearities in GaAs-based microcavities at RT [284].

Finally, de Carvalho *et al.* reported recently that ordered cluster arrangements in In-containing III-nitride ternary alloys are energetically less favorable than strongly clustered configurations (i.e. a large deviation of the actual cation-site occupation of the tetrahedra from the average value) [285]. This is an intrinsic property due to the wurtzite structure of III-nitride materials system, and yields an intrinsic emission linewidth broadening, which results in a reduced overlap between the gain and the VCSEL cavity mode.

6 Vertical external cavity surface-emitting lasers

In this last chapter, the realization of long external cavity VECSELs is presented. First, the design of the active region is addressed, and two different schemes are discussed. Then, the characteristics of both schemes under optical pumping are compared, as well as their performances when used in a VCSEL configuration. Finally, the most efficient scheme is characterized in an extended external cavity configuration and the results are presented.

6.1 Active region design

As stated in section 2.4.3, the objective of the RbGaN project is the realization of an active atomic clockwork made of a mode-locked GaN-based VECSEL comprising a Rb atomic vapor cell absorber. As this VECSEL was meant to be non-resonantly optically pumped, a specific active region design had to be studied, which is quite different to that of a VCSEL. Indeed, the active region of a nitride-based electrically driven VCSEL comprises only a few ($\sim 2-5$) QWs, because of inefficient hole injection in more QWs due to their poor mobility. However, in an optically pumped VECSEL structure, this issue is no longer a concern. Instead, the active region should be thick enough and designed so as to efficiently absorb the pump beam. In this context, two different approaches have been considered, as shown in Fig. 6.1.

The first one is designed so as to absorb the pump laser beam in thick $In_xGa_{1-x}N$ barriers ($x \sim 2-3\%$), whose total thickness equals approximately 400 nm, generating electron-hole pairs that subsequently diffuse into only two InGaN QWs placed in-between the barriers for ensuring a low threshold, as depicted in Fig. 6.1 (a). In such a structure, the InGaN barriers should be thick enough in order to absorb most of the power out of the pump beam while ensuring an efficient subsequent diffusion of the generated free carriers into the QWs before they recombine. The main advantage of this scheme is the low number of QWs, resulting in a theoretical lower threshold than structures comprising a large number of QWs. Indeed, for a given amount of carriers generated by the pump beam trapped by the QWs, the free carrier density per QW will be larger for fewer QWs, which makes the population inversion easier to reach. However, as the barrier thickness is quite large, the indium content should not exceed

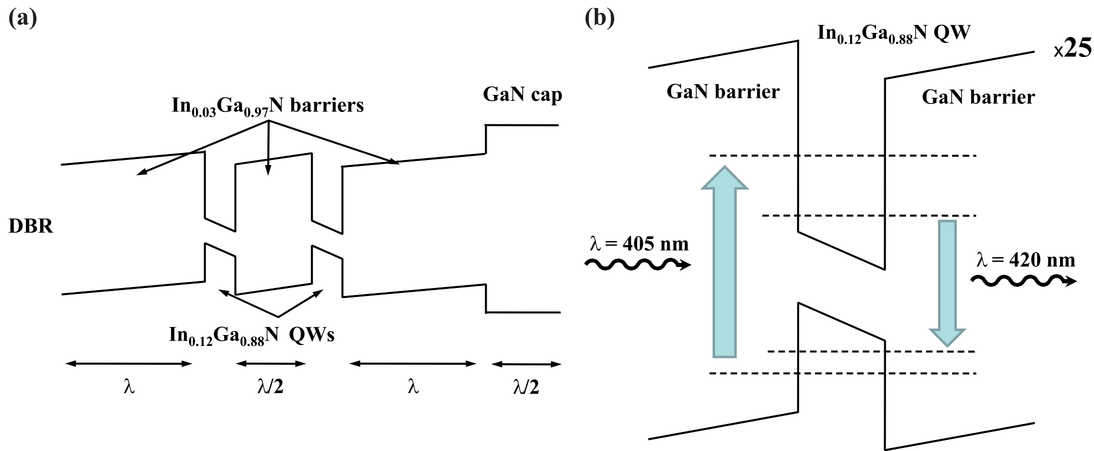

Figure 6.1: The two different active region schemes: (a) thick $In_{0.03}Ga_{0.97}N$ barriers and two $In_{0.12}Ga_{0.88}N$ QWs for pump beam absorption in the barriers and (b) standard $In_{0.12}Ga_{0.88}N$/GaN MQW approach.

~ 2 – 3% in order to preserve the overall crystalline quality. This implies that the pump laser wavelength should not be longer than ~ 370 nm. Such lasers are more expensive than more commonly used 405 nm LDs.

The second approach relies on a large number (~ 25) of InGaN/ GaN MQWs, as represented in Fig. 6.1 (b). The barriers are now transparent to the pump laser beam, which is absorbed by an excited state of the QWs, nominally at a wavelength $\lambda = 405$ nm, as such CW UV LDs are commercially available at a reasonable cost. This approach is close to the MC structures designed for strong coupling regime studies [14], which have been widely investigated in our laboratory. Nevertheless, the total thickness of absorbing material is much shorter than that of the previous scheme, which would cause a reduced part of the incident pump beam to be absorbed resulting in a larger threshold.

The subsequent sections will present the development of samples based on these two different active region schemes, then compare the obtained results. Finally, VECSEL comprising the most efficient active region will be presented, as well as their characteristics when operated in both VCSEL and external cavity configuration.

6.1.1 Thick InGaN barriers

Thick InGaN layers are quite challenging to grow [286, 287, 288]. Thus, the first step towards the realization of VECSEL structures using thick InGaN barriers consists of the optimization of the barrier growth conditions. Therefore, three samples have been grown using different barrier growth conditions, which are summarized in Table 6.1. The QW growth conditions, also given in Table 6.1, are identical for all samples, as well as their epitaxial structure, which consists in a first 166 nm thick InGaN barrier, a 2 nm thick InGaN QW, a 83 nm thick InGaN

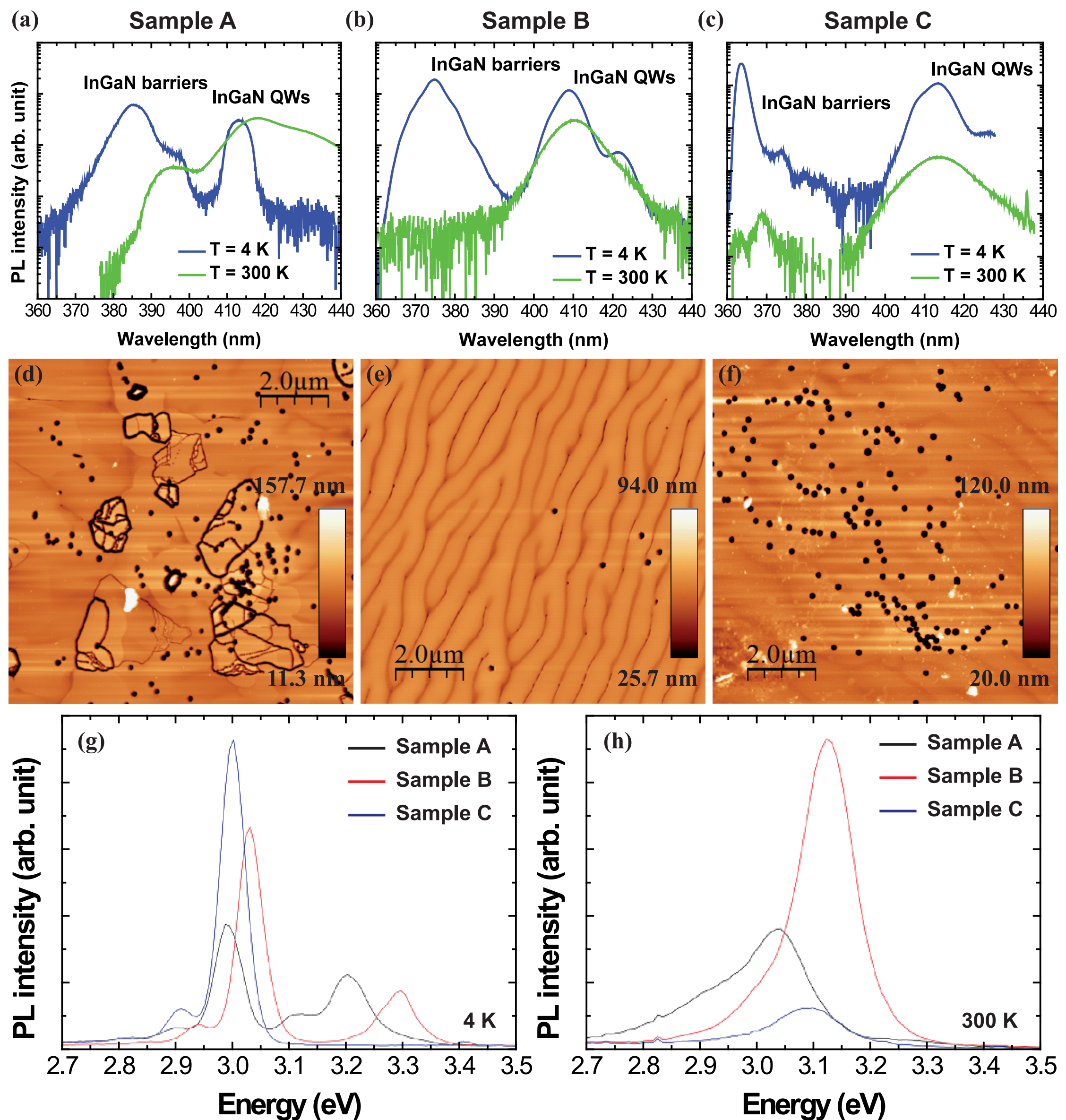

Figure 6.2: (a), (b) and (c) PL spectra measured at low and room temperature with a 325 nm HeCd laser on three different samples with thick InGaN barriers. (d), (e) and (f) $10 \times 10\ \mu m^2$ AFM scans measured on those three samples. Comparison between the PL spectra of the three different samples measured with a 325 nm HeCd laser for the same excitation power density at 4 K (g) and 300 K (h).

barrier, another 2 nm thick InGaN QW and a final 166 nm thick InGaN barrier, capped with a 84 nm thick GaN layer. All samples were grown on FS GaN substrates. The QW thickness has been set so as to minimize the QCSE, in order to avoid a critical decrease of their radiative efficiency. The TMIn flow rates were close to the lower tolerance limit of the gas flow controller, resulting in a large indium content in sample A (~ 5%). In order to decrease the indium content in samples B and C, both the growth temperatures and the TEGa flow rates have been

Table 6.1: Summary of the barrier and QW growth conditions for the study of thick InGaN barriers.

Sample	In content (%)	Growth temperature (°C)	TEGa flow rate (sccm)	TMIn flow rate (sccm)	NH_3 flow rate (sccm)
A	~ 5	845	120	10	3000
B	2.8	850	200	8	3000
C	1.7	875	200	8	3000
All QWs	~ 12	838	120	490	3000

increased, yielding indium content of 2.8% and 1.7%, respectively. PL measurements have been performed at low temperature (LT) and RT on each sample using a 325 nm CW HeCd laser. The results for each sample are shown in Figs. 6.2 (a), 6.2 (b) and 6.2 (c). The PL intensities of the different samples at LT and RT are compared in Figs. 6.2 (g) and 6.2 (h), respectively. At LT, the ratio between the emission intensities related to the QWs and the barriers is quite low (strong emission from the barriers), because of the strong carrier localization related to alloy inhomogeneities occuring in InGaN barriers. Conversely, the thermal energy at RT is sufficient for the carriers to escape from the traps, their diffusion length is large enough for them to reach the QWs, and thus QW emission is predominant at RT. However, only sample B exhibits no barrier emission at RT [Fig. 6.2 (b)]. Moreover, it also presents the strongest emission at RT [Fig. 6.2 (e)]. 10×10 μm^2 AFM scans of samples A, B and C are shown in Figs. 6.2 (d), 6.2 (e) and 6.2 (f), respectively. The surface morphology of samples A and C exhibits a large V-pit density. In addition, sample A suffers from many defects. This is surely due to the larger indium content in the InGaN barriers for this latter sample. On the other hand, sample B surface morphology reveals much less V-pits than the other two samples as well as step meandering.

The V-pits are typical of indium-containing alloys [180, 183, 286, 289, 290]. Those V-pits are ascribed to strain relaxation and surface energy minimization occurring at threading dislocations and stacking mismatch boundaries induced by stacking faults. The second feature, namely meandering or Bales and Zangwill (BZ) instability, is related to the so-called Ehrlich-Schwoebel potential barrier at the step edges, which prevents part of the diffusing adatoms to bind to a descending step during epitaxial growth [291, 292, 293]. It is most certainly due to the low growth temperature of the whole cavity. Interestingly, both effects are supposed to increase the radiative efficiency of InGaN QWs. The valleys resulting from the BZ instability have been reported to act as potential barriers in the QW planes, thus hindering non-radiative recombinations of carriers on dislocations [294], whereas V-pits provide energy barriers that screen the defects themselves [295]. However, in the present case the radiative efficiency enhancement related to the step meandering seems to be dominant over the other mechanism, as the RT PL intensity of sample B is larger than those of the other two samples.

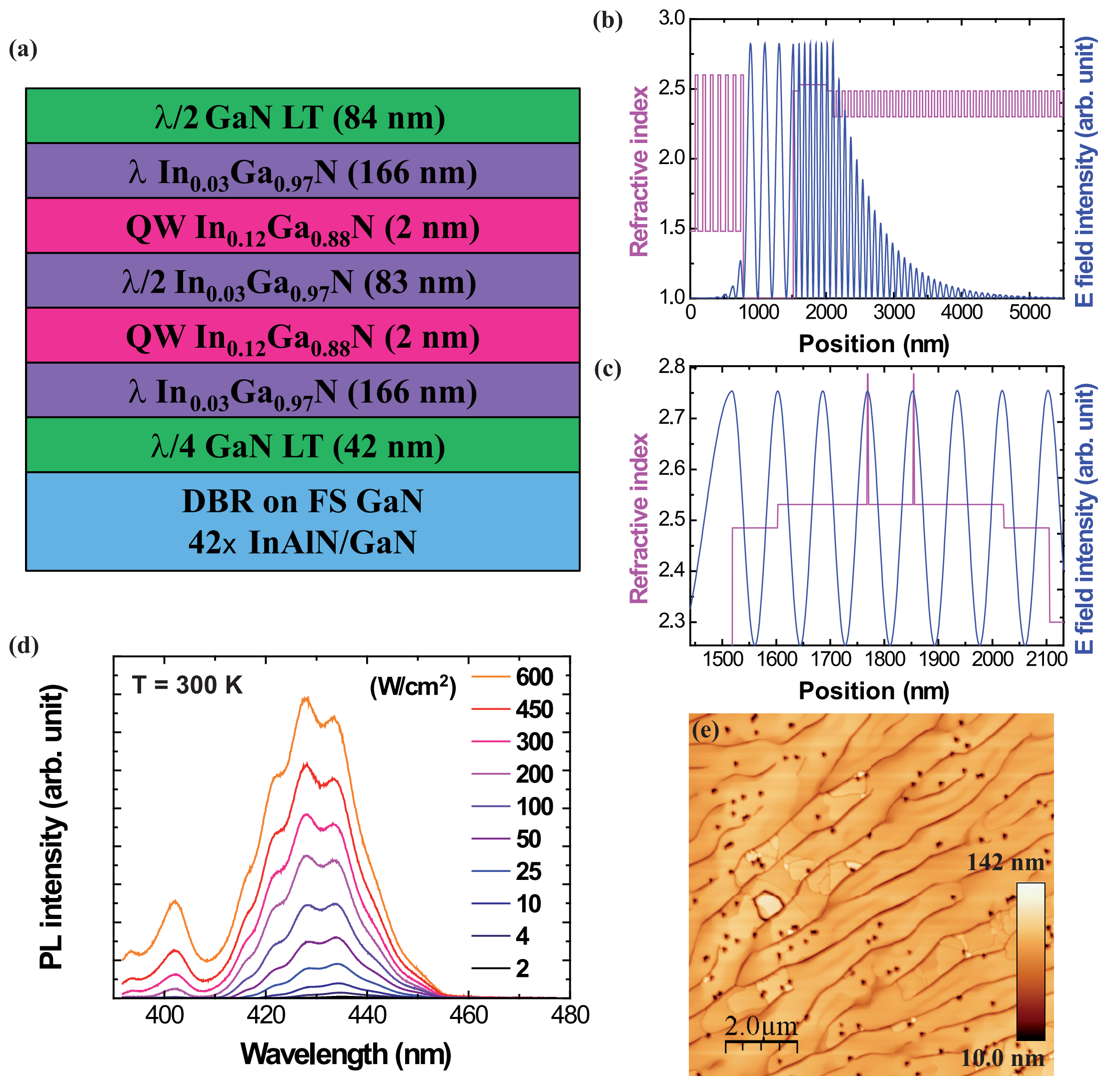

Figure 6.3: (a) Thick InGaN barrier VECSEL detailed layer structure. (b) Electric field intensity distribution along the VECSEL cavity. (c) Detail of the field in the QWs. (d) PL spectra measured with a 355 nm Nd:YAG pulsed laser at RT on the half-cavity. (e) $10 \times 10\ \mu m^2$ AFM scan of the VECSEL sample.

Thereby, sample B growth conditions have been selected for the growth of a thick InGaN barrier VECSEL sample. Its structure is depicted in Fig. 6.3 (a). It has been designed so that the QWs are placed in two consecutive antinodes of the optical field. Moreover, the two outer InGaN barrier thickness has been set so that the interferences between light reflected at the InGaN/GaN interfaces and by the DBRs are constructive. The sample has been grown over a highly reflective, low dislocation density, InAlN/GaN DBR grown on an intermediate quality FS GaN substrate, such as those presented in section 3.4.2. The electric field intensity distribution across the VECSEL structure, including a 3.5 $\lambda/2$ empty external cavity and an external mirror made of 7 TiO_2/SiO_2 bilayers, has been simulated using the transfer matrix method and is

shown in Fig. 6.3 (b). An enlarged view of the optical field intensity in the nitride-based cavity including the QWs is depicted in Fig. 6.3 (c), where both QWs can be seen at two antinodes of the field, ensuring a theoretical optimal gain enhancement factor. PL spectra measured at RT as a function of the average power density using a pulsed frequency-tripled Nd:YAG laser emitting at 355 nm on the half-cavity sample are shown in Fig. 6.3 (d). A slight emission blueshift can be seen, and can be ascribed to the screening of the internal field, yielding a decreased QCSE. Note that the PL emission peak around 400 nm does not come from the thick InGaN barriers, but can be ascribed to the QW emission modulation due to the bottom DBR.

A $10 \times 10\ \mu m^2$ AFM scan of the VECSEL sample surface is given in Fig. 6.3 (e), revealing the same two features reported previously for sample B, namely V-pits and step meandering. The corresponding rms roughness value is 12.3 nm. As will be shown hereafter, the PL intensity of this thick InGaN barrier VECSEL sample is comparable to that of a MQW VECSEL. However, its quite large surface roughness will prove detrimental to achieve lasing because of increased light scattering.

6.1.2 Multiple quantum well approach

As previously said, the second approach relies on the use of InGaN/GaN MQW. Less effort had to be spent on the growth parameter optimization, thanks to the work of Marlene Glauser on InGaN-based MQWs for polariton laser applications [14]. Indeed, two samples with a 2λ cavity comprising an active region made of 24 $In_{0.12}Ga_{0.88}N$/GaN QWs, whose total thickness correspond to 1λ, have been grown on two other parts of the same InAlN/GaN DBRs than that used for the thick InGaN barrier VECSEL sample. The QW barrier and well thicknesses amount to 4.5 and 2 nm, respectively. The barriers are n-type doped with $[\text{Si}] = 2 \times 10^{18}\ \text{cm}^{-3}$. The active region is sandwiched between two GaN layers grown at high temperature (1050°C) in order to ensure both a high quality for the overgrowth of the DBR and a smooth cavity surface morphology thanks to the larger diffusion length of Ga adatoms at high temperature. The only difference between the two MQW VECSEL samples is a slight QW growth temperature tuning in order to decrease the emission wavelength of the second grown sample. The complete structure is depicted in Fig. 6.4 (a). The MQWs are equally distributed along the growth axis, which could seem detrimental in terms of gain enhancement factor (coupling strength between the optical field and the QWs). A resonant periodic gain structure, with several groups of QWs centered at different antinodes of the optical field intensity, would indeed present a larger gain enhancement factor [141, 142]. However, a long cavity VECSEL is expected to exhibit multimode lasing, unlike short cavity VCSELs. For a given mode, the resonant periodic gain structure would be very sensitive to any displacement of the external coupling mirror, as a shift of the optical field antinode position would dramatically decrease the gain enhancement for this particular mode. Thereby, the resonant periodic gain structure would act as an additional spectral filter that would favor lasing of clusters of external cavity modes. Thus it would render such a VECSEL extremely sensitive to any cavity length fluctuation. Therefore, the equally spaced MQW structure has been selected as the active region for our

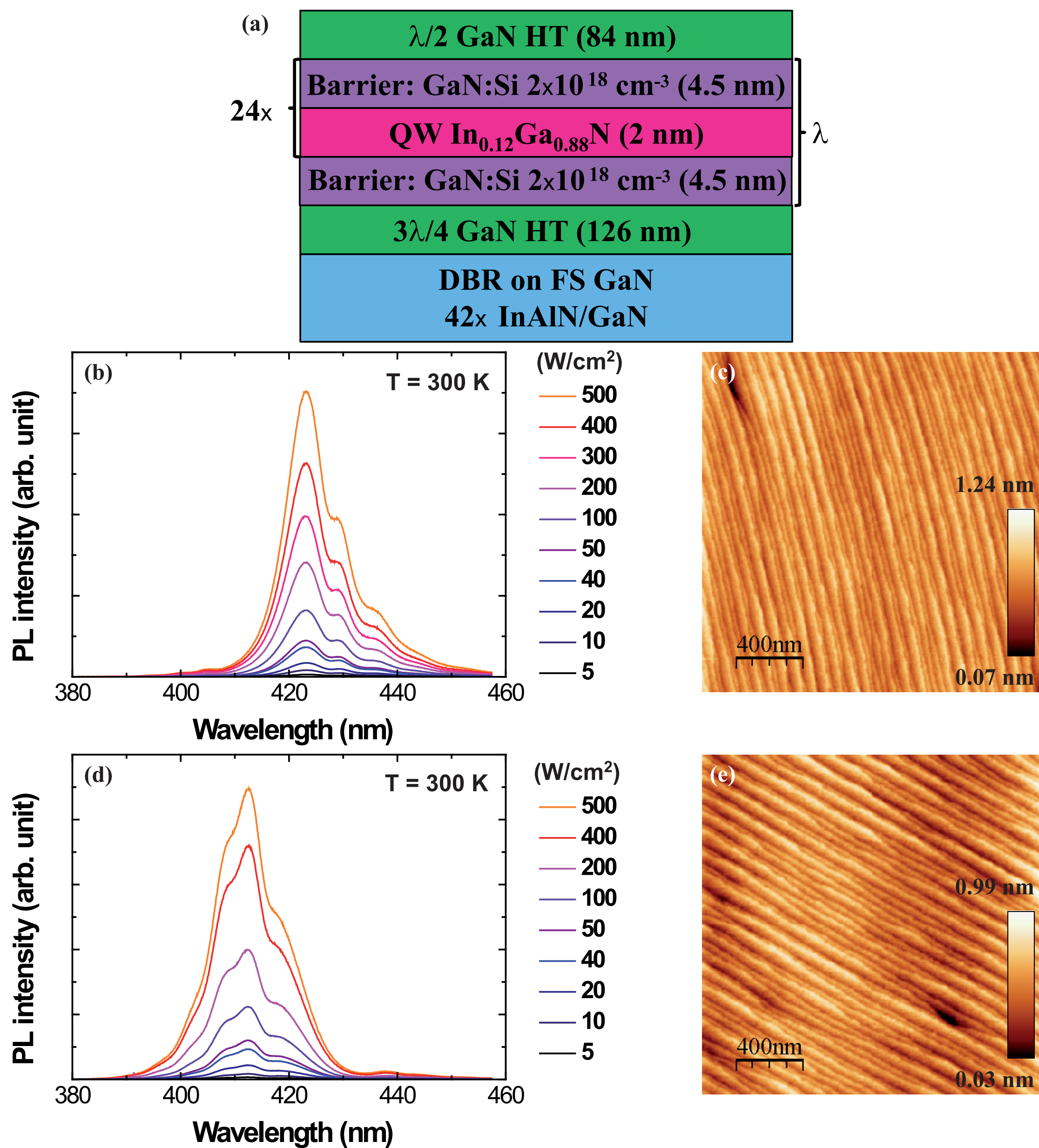

Figure 6.4: (a) MQW VECSEL detailed layer structure. (b) and (d) PL spectra measured on two different MQW VECSEL half-cavities with a 355 nm frequency-tripled Nd:YAG pulsed laser at RT. (c) and (e) 2×2 μm^2 AFM scans measured on those two samples.

long cavity MQW VECSELs.

PL spectra measured on the two different half-cavity VECSEL samples at RT with a pulsed frequency-tripled Nd:YAG laser emitting at 355 nm are shown in Figs. 6.4 (b) and 6.4 (d). Once more, no VECSEL emission blueshift is an evidence for a quite weak QCSE. 2×2 μm^2 AFM scans measured on those samples can be seen in Figs. 6.4 (c) and 6.4 (e). Those images reveal very smooth surface morphologies with rms values ~ 0.2 nm for each sample, which is an

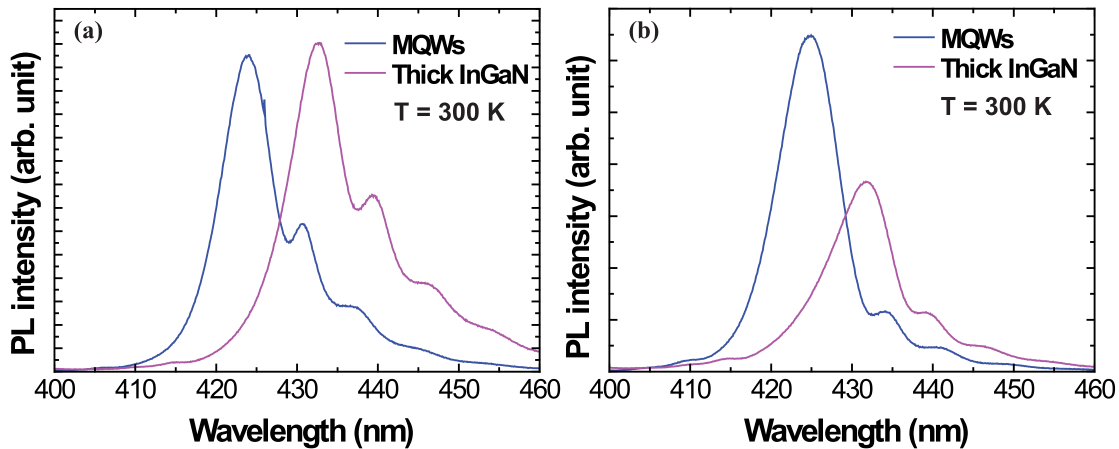

Figure 6.5: PL spectra measured on the MQW VECSEL sample (blue curves) and the thick InGaN barrier VECSEL sample (violet curves) at RT with a 325 nm CW HeCd laser (a) and with a 355 nm frequency-tripled Nd:YAG pulsed laser (b).

evidence for the high quality of our LM InAlN/GaN DBRs. Such a smooth surface morphology ensures very low scattering losses while the samples operate as surface emitting lasers, which is a requirement in order to achieve lasing in a long external cavity configuration.

6.2 Results

In this section, samples based on both active region designs are first compared. Then the results concerning our VECSEL samples operating in VCSEL and VECSEL configuration will be presented and discussed.

The RT PL spectra measured on a thick InGaN barrier and a MQW VECSEL half-cavity samples using either a CW HeCd laser emitting at 325 nm or a pulsed frequency-tripled Nd:YAG laser emitting at 355 nm are compared in Fig. 6.5. It is worth pointing out that using both pump lasers the MQW sample is pumped into the GaN barriers and not as initially planned in a QW excited state. Interestingly, the MQW sample exhibits a larger PL intensity than the thick InGaN barrier sample when pumped with the Nd:YAG laser, despite similar intensities under CW injection with the HeCd laser.

6.2.1 Operation as a VCSEL

In order to assess the quality of the different samples, they have been cleaved and a small piece of each of them has been covered with a top dielectric Bragg mirror and characterized in VCSEL configuration. The DBRs evaporated on the thick InGaN barrier sample and the two MQW samples were made of 8 and 7 pairs of SiO_2/ZrO_2 and exhibited a peak reflectivity of 99.5% and 98.5%, respectively. As no CW laser available in the lab delivered enough power so as to achieve lasing in those VCSEL samples, a frequency-tripled pulsed Nd:YAG laser, emitting

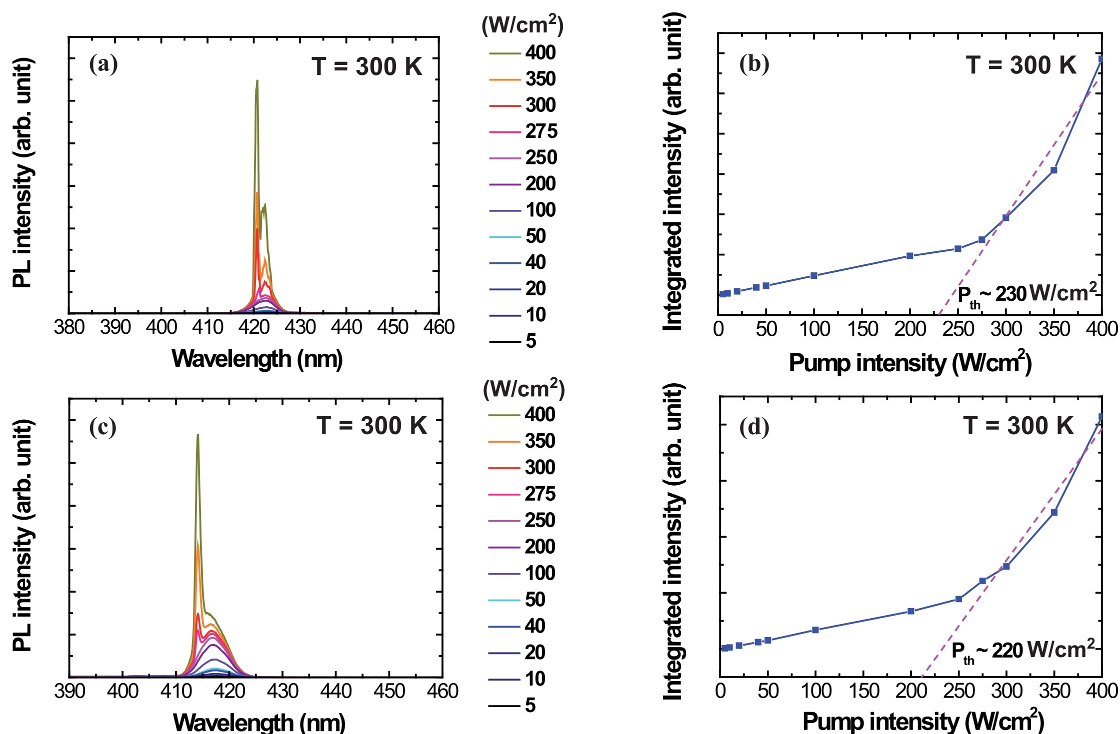

Figure 6.6: (a) and (c) PL spectra measured on the two MQW VECSEL samples shown in Fig. 6.4 after the deposition of a top dielectric DBR stack using a 355 nm frequency-tripled Nd:YAG pulsed laser at RT. (b) and (d) Corresponding L-L plots.

at 355 nm, was used as pump source. The maximum average pump power is about 12 mW. The laser beam spot size when focused on the sample is approximately 50 μm, meaning that the maximum average power density is about 600 W/cm^2.

Lasing has not been achieved for the thick InGaN sample in VCSEL configuration. This is ascribed to the large surface roughness of the sample [Fig. 6.3 (e)]. Despite the fact that the step meandering increases the QW radiative efficiency, this effect results in a large surface roughness, which dramatically increases scattering losses, preventing the sample from lasing. Thus, the thick InGaN barrier VECSEL sample has not been further measured in a long external configuration.

Unlike the thick InGaN barrier sample, lasing has been observed in both MQW samples, with a threshold power density of ~ 220 – 230 W/cm^2. Spectra measured on both samples at RT for different excitation power densities are shown in Fig. 6.6, together with the corresponding plots of the integrated mode intensity as a function of the pump intensity (L-L). Both the narrowing of the emission linewidth and the nonlinear increase in the mode intensity are clear evidence for lasing. Thus, those samples were selected for being further characterized in an extended external cavity scheme.

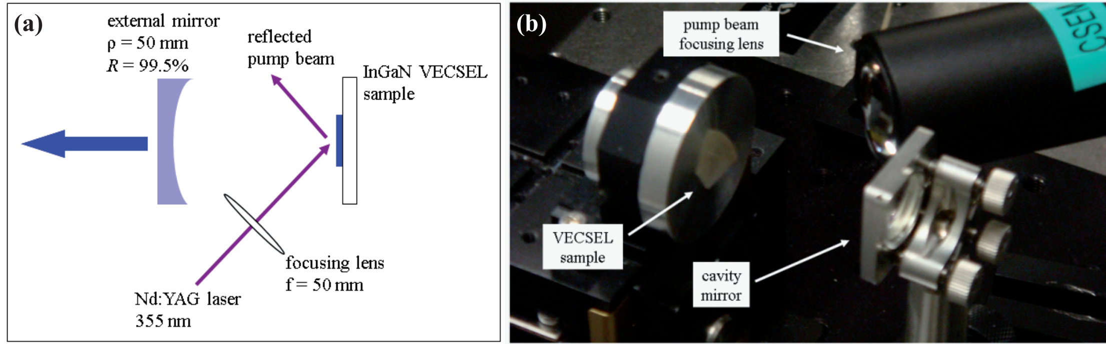

Figure 6.7: (a) Schematic drawing and (b) photograph of the setup for optical pumping of the VECSEL samples operating in an extended external cavity configuration. Courtesy of X. Zeng.

6.2.2 Operation in an extended external cavity configuration

Whereas the growth and optimization of the VECSEL samples were devoted to our group, the characterization of the final samples in VECSEL configuration has been performed by the CSEM. Thereby, the results presented in this section are courtesy of Xi Zeng [155].

Subsequently, the MQW VECSEL samples have been mounted in a long external cavity scheme. In addition to the previously mentioned pieces of sample covered with a 7-pair DBR used as reference, a less reflective 4-pair SiO_2/ZrO_2 Bragg mirror has been evaporated on another piece of both samples, exhibiting a peak reflectivity of 86.6%. As said before, the achievable power using the CW lasers available in our lab is not sufficient to achieve lasing in our VECSEL samples. Thus, two different pulsed Nd:YAG lasers are used in order to pump the samples. However, the pulse duration of those two lasers, which is equal to 10 ns and 400 ps, respectively, is shorter than the time T_b required to achieve lasing in a long external cavity VECSEL. The latter amounts to ~ 680 ns when pumped at twice the threshold for a 50 mm long cavity, according to [277]:

$$T_b = 25 \cdot \frac{T_{rt}}{(r-1)G_{th}} \tag{6.1}$$

where T_{rt} is the cavity round trip time, $r = I_{pump}/I_{th}$ is the normalized pump rate, i.e. the ratio between the pump power density I_{pump} and the power density at threshold I_{th}, and G_{th} is the cavity round trip gain at threshold. Therefore, the low reflectivity top dielectric Bragg mirror forms an auxiliary microcavity with a much shorter lasing build up time (~ 10 ps) that provides injection seeding for the external cavity, enabling lasing of a 50 mm long external cavity VECSEL.

In VECSEL configuration, the samples are mounted on a precision 3D translation stage. The external reflector is a concave mirror with a curvature radius of 50 mm with a peak reflec-

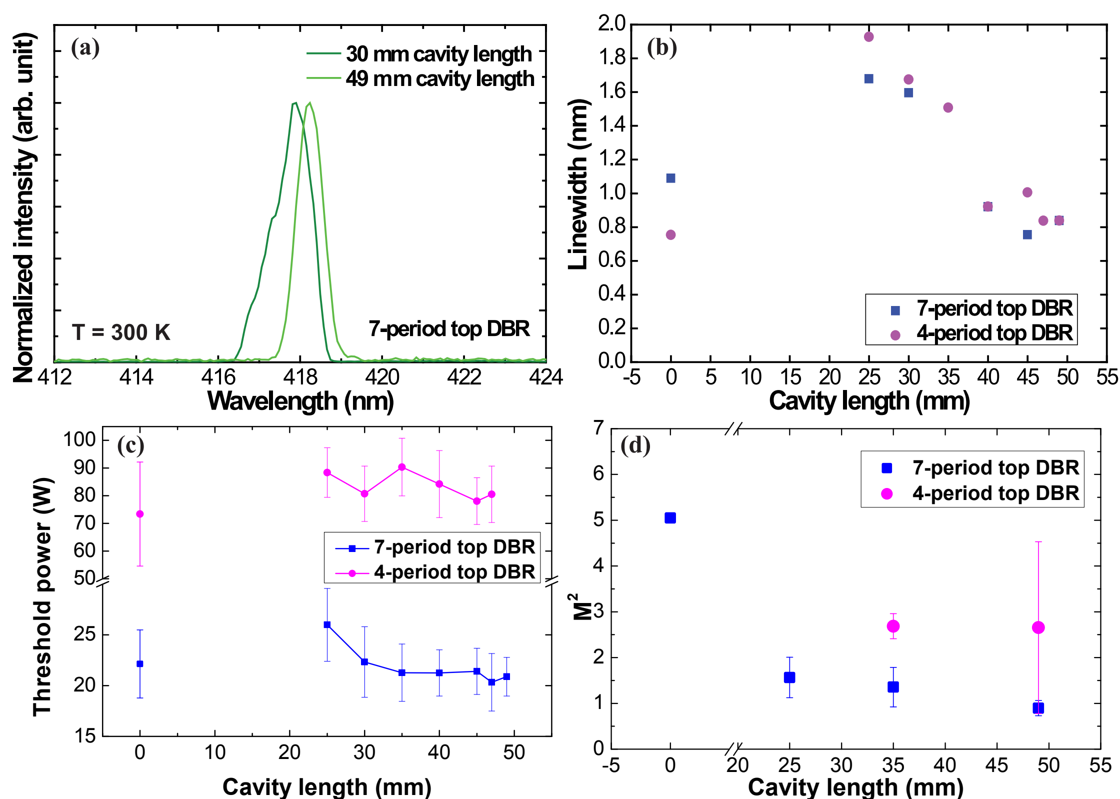

Figure 6.8: (a) PL spectra measured above threshold on the 7-period top DBR VECSEL sample for two different cavity lengths. (b) Linewidth of the lasing mode, (c) threshold power and (d) beam quality factor M^2 vs cavity length for VCSEL samples with two different top DBR stacks. Courtesy of X. Zeng.

tivity of 99.5% at 420 nm, which is mounted on a 1D translation stage allowing tuning the external cavity length from 25 to 50 mm, this latter length corresponding to the semiconfocal configuration. A schematic drawing and photograph of this setup are shown in Fig. 6.7.

In this set of experiments, the VECSEL samples are pumped using a Q-switched frequency-tripled Nd:YAG laser whose emission wavelength is 355 nm. Its pulse length and repetition rate are 400 ps and 6 kHz, respectively. The pulse peak power amounts to 5.4 kW. The pump beam incidence angle onto the sample is 45°. A neutral density filter wheel is used for attenuating the pump beam. The light output of the VECSEL cavity is analyzed using a fiber-coupled spectrometer and a CCD camera.

Examples of spectra measured on the 7-period top DBR sample above threshold for cavity lengths of 30 and 49 mm are shown in Fig. 6.8 (a). The linewidths of the lasing mode, threshold powers and beam quality factors M^2 as a function of the cavity length for the two different top DBR samples are depicted in Figs. 6.8 (b), 6.8 (c) and 6.8 (d), respectively. M^2 is defined as the ratio between the beam parameter product (given by the product of the beam divergence angle and its waist) of the VECSEL sample and that of an ideal Gaussian beam. The threshold

power decreases when increasing the cavity length from 25 to 50 mm, as expected [Fig. 6.8 (c)]. Indeed, the semiconfocal configuration offers the smallest lateral mode size onto the sample, resulting in the lowest threshold power. Moreover, the threshold pump powers measured on the 4-pair top DBR are significantly larger than those measured on the 7-pair top Bragg mirror. However, contrary to the expected behavior for a microcavity laser operating in an external cavity configuration, the VECSEL thresholds are not always smaller than the corresponding VCSEL ones. For instance, both 25 mm long cavity VECSEL thresholds are larger than those of the samples operating as VCSEL. This is ascribed to two different effects: the mismatch between the external cavity mode and the pump laser beam onto the sample, and the imperfect spatial overlap between the beam reflected from the external reflector with the initial mode of the free-running VCSEL [155].

In the same way, the lasing mode linewidth decreases when the cavity length is increased from 25 to 50 mm [Fig. 6.8 (b)] for both samples. The linewidths have been measured under the constant pump powers of 29.2 and 138 W for the 7- and 4-pair top DBR samples, respectively. The decrease in the linewidth FWHM is attributed to the fact that external cavity losses and thresholds are lower for longer cavity VECSELs, as the setup approaches and eventually reaches the semiconfocal configuration, which results in lower cold cavity linewidths. This is ascribed to the best overlap between the free running VCSEL mode and the beam reflected from the output coupling mirror.

Beam profile measurement of the VECSEL samples have been performed using a CCD camera in order to extract the beam quality factor M^2 [Fig. 6.8 (d)]. As expected, the M^2 value for the samples in VCSEL configuration are larger than those of samples in the external cavity setup. In addition, the lowest M^2 value is measured for the 7-pair top DBR sample with an external cavity length of 50 mm, i.e. corresponding nearly to the semiconfocal configuration. This is consistent with the fact that for the semiconfocal configuration the external reflector provides the strongest optical feedback.

Thus, the first long external cavity VECSELs have been demonstrated, whereas other GaN-based VECSELs reported so far were limited to 1 mm long external cavities [16, 140, 141, 142]. This will enable the integration of intracavity components, such as a Rb vapor cell absorber in the case of the RbGaN project.

6.3 Outlook

Although those results are encouraging, the threshold remains too high to allow VECSEL pumping using CW UV lasers. On the other hand, the 400 ps pulse length of the frequency-tripled Nd:YAG laser would not allow mode-locking operation after incorporation of the Rb vapor cell absorber, as the mode-locking operation establishes only after 15-20 round trips through the cavity, which takes up to ~ 6 ns for our 50 mm long VECSEL.

Thus, further experiments are planned using a high-power frequency-tripled Nd:YAG laser

with flash-lamp pumping and operating in the Q-switching regime, delivering 10 ns long pulses. Such pulses should be sufficient to observe the onset of mode-locking in the VECSEL samples.

Other points to explore would be growing further VECSEL samples onto high quality FS GaN substrates instead of intermediate quality ones, as it is expected to reduce the photonic disorder (see section 3.4.2) and thus also to reduce the lasing threshold. Furthermore, the growth conditions of the thick InGaN barrier sample could be further optimized in order to avoid the step meandering instability, for instance by increasing the growth temperature of the GaN layers, and introducing thin GaN interlayers grown at high temperature in the middle of the thicker middle barrier. Finally, as lasing has been achieved in electrically-driven VCSELs, such devices could be used to provide gain in an electrically-driven long external cavity VECSEL, although the output power of our VCSELs should be increased for that purpose.

Conclusion

In this last part, the work presented in this PhD dissertation is summarized. Finally, an outlook and perspectives on possible future work are proposed.

Summary

This PhD dissertation described how III-nitride-based VCSELs and VECSELs have been realized. Several building blocks had to be developed and optimized before being brought together in order to realize devices.

In chapters 1 and 2, the basic properties on III-nitride compounds and microcavity lasers were recalled. Some intrinsic issues related to strain, polarization and *p*-type doping inherent to the III-nitride material system were discussed. The discrepancies between standard edge-emitting LDs and microcavity lasers were presented, in particular challenges due to the low confinement factor inherent to a vertical laser cavity. Finally, standard III-V VCSELs and VECSELs and their applications were described.

In chapter 3, the optimization of highly reflective "defect-free" InAlN-based DBRs was presented. Growth and optical properties of InAlN layers were summarized. Then, the structural properties and defect issues were addressed. A systematic study of the surface morphology of nearly-LM InAlN layers with thicknesses ranging from 2 to 500 nm was presented, as well as InAlN layers under tensile strain. The surface morphology of InAlN layers was characterized by hillocks, and V-pits appearing beyond a thickness depending on the growth conditions. However, thick (~ 500 nm) InAlN layers presented a rough surface, and TEM measurements revealed In-rich and In-poor vertical planes. Those effects, namely hillocks, V-pits and critical crystalline quality degradation mechanism of thick InAlN layers were ascribed to kinetic roughening. Then, InAlN-based DBRs were discussed. First, such structures grown on sapphire were briefly presented. Secondly, the growth of such DBRs on FS GaN substrates was studied, and the impact of several parameters, such as the TMIn flux, the substrate quality, compressive strain in InAlN layers and the transition between InAlN and GaN growth conditions during DBR growths were addressed. Finally, UV DBRs were reported, and several improvements for InAlN-based DBRs were proposed.

In chapter 4, the development and optimization of low resistive TCO contacts to *p*-type GaN was described. First, the basic properties of metal-semiconductor contacts and TCOs were recalled. Then, several different TCOs and deposition techniques were investigated. The effect of inserting a thin metallic layer below the TCO on the contact properties were studied. It was concluded that plasma induced damage during the TCO layer deposition could dramatically deteriorate the *p*-type contact properties and yielded critical failure of VCSEL devices at relatively low current densities (around 2 kA/cm^2). Finally, ITO-based contacts deposited by Evatec were studied, and results showed that no plasma induced damage were hindering their electrical properties. In addition, such ITO layers exhibited a low absorption in the 400-450 nm range. Therefore, it was concluded that such transparent ITO contacts were suited for VCSEL applications.

In chapter 5, the development of VCSEL diodes was reported. First, the main VCSEL building blocks were listed, namely a top dielectric DBR, a bottom InAlN/GaN epitaxial DBR, a QW-based active region, efficient electrical injection and current confinement. Then, dielectric DBR deposition and optimization was briefly described and several promising current confinement schemes were detailed, which are lateral oxidation of an InAlN layer, a TCO current spreading on top of either a dielectric current confinement layer or plasma-based *p*-type GaN surface passivation, or a buried current confining layer. Subsequently, the final design of our VCSEL was presented together with the process flows. Finally, results were reported. Lasing at RT under pulsed electrical injection in our VCSEL diodes was demonstrated. The characteristics of our devices were described. The reason why no lasing action was observed under CW injection was ascribed to the large threshold current density reported for our VCSELs, which is due to critical absorption in the ITO current spreading layer. Therefore, it has been proposed to reduce the ITO layer thickness by half and move it at a node of the optical field standing wave in order to strongly decrease absorption, and thus decrease the threshold and achieve lasing under CW injection.

In chapter 6, VECSELs were studied. First, the development and optimization of the active region was presented. Two different active region designs were under consideration: one based on only two InGaN QWs surrounded by thick ($\sim 100-150$ nm) $In_xGa_{1-x}N$ barriers, with $0.01 < x < 0.05$, the second one based on more conventional MQWs. This latter structure proved to be better suited for VECSEL applications despite exhibiting quite similar output optical powers, because of the rough surface morphology of the former samples resulting from the meandering or BZ instability yielding large scattering losses. The MQW approach was validated in VCSEL configuration, i.e. with the top dielectric DBR directly evaporated on the surface. Subsequently, the sample was mounted in VECSEL configuration, and lasing was reported with external cavity length up to 50 mm, using a low reflectivity top dielectric DBR deposited on the surface of the half cavity VECSEL sample for injection seeding, required because of the pump beam pulse length being shorter than the lasing build up time in the external cavity. Finally, the characteristics of the VECSEL sample for various external cavity lengths were reported, and an outlook on further improvements was given.

Outlook and perspectives

Several ways to further improve VCSEL and VECSEL devices are worth mentioning. Concerning the bottom InAlN-based DBR, introducing a two-step temperature ramp at each InAlN/GaN interface during epitaxial growth could further improve the morphology of these interfaces, and thus also the overall quality of such DBRs. The development of conductive *n*- and *p*-type doped DBRs could also offer new insights on the conception of future devices. Finally, the study of semi- and non-polar DBRs would open quite interesting perspectives, as it would on the one hand decrease, or even eliminate, negative effects related to the QCSE such as the reduction of the QW internal efficiency, and on the other hand enable microcavity-based device new features such as polarization locking thanks to the III-nitride material anisotropy.

Further improvements are required in order to achieve lasing under CW injection in VCSEL diodes. The most straightforward one is to reduce the ITO contact layer and place it at a node of the optical field in order to reduce intracavity losses. However, other studies would be required in the long term, such as a careful optimization of the active region. In particular, the number of QWs and their thickness are parameters that should be carefully tuned. A large number of thick QWs would increase the confinement factor, thus also the gain-per-pass. On the other hand, thick QWs would more suffer from the QCSE, and because of the poor hole injection efficiency in QWs, an active region made of a large amount of QWs would suffer from a large transparency current density. Therefore, the right compromise should be found in order to obtain the structure design yielding the lowest threshold while ensuring a large differential external efficiency. In addition, other current confinement schemes could be further studied, in order to improve the current confinement in our structure, and couple it with efficient lateral optical mode confinement, i.e. using a buried InAlN current aperture. InAlN oxidation could also be used to realize flip-chip cavities, which could then be sandwiched between two dielectric DBRs. This could be a promising alternative to laser lift-off or PCE etching for the realization of fully hybrid VCSEL devices. It would then enable direct comparison between devices using a bottom dielectric or epitaxial DBR.

Further measurements are also required in order to study mode-locking in our VECSEL samples, as well as the effect of inserting the Rb vapor cell absorber in the external cavity. In addition, further optimizing the active region and growing samples on high-quality FS GaN substrates could also improve the performances of those devices. A careful growth optimization of the thick InGaN barrier-based VECSEL cavity in order to avoid the meandering instability and preserve a step-flow growth mode could also yield improved device characteristics.

Finally, the knowledge acquired during this PhD work could be used in order to develop new structures, such as polariton LDs, emitting either in the UV (using GaN/AlGaN QWs) or blue-violet (using InGaN/GaN QWs) range. The understanding of the thick InAlN layer crystalline quality critical degradation mechanism could be used in order to further improve InAlN cladding layers for LDs and SLEDs. Improved InAlN-based DBRs would be helpful to

demonstrate strong coupling in InGaN QW-based microcavities. Electrically-driven VCSELs could be used as injection seeding source for long external cavity VECSELs, allowing getting rid of the pump laser. Other intracavity elements could be inserted in such long external cavity VECSELs for other applications, such as nonlinear optical elements or absorption cells for absorption spectroscopy.

Bibliography

[1] Hiroshi Amano, Masahiro Kito, Kazumasa Hiramatsu, Isamu Akasaki, *P-Type Conduction in Mg-Doped GaN Treated with Low-Energy Electron Beam Irradiation (LEEBI)*, Japanese Journal of Applied Physics **28**, L2112 (1989)

[2] Shuji Nakamura, Masayuki Senoh, Takashi Mukai, *Highly P-Typed Mg-Doped GaN Films Grown with GaN Buffer Layers*, Japanese Journal of Applied Physics **30**, L1708 (1991)

[3] Shuji Nakamura, Takashi Mukai, Masayuki Senoh, *High-Power GaN P-N Junction Blue-Light-Emitting Diodes*, Japanese Journal of Applied Physics **30**, L1998 (1991)

[4] Shuji Nakamura, Takashi Mukai, Masayuki Senoh, *Candela-class high-brightness InGaN/AlGaN double-heterostructure blue-light-emitting diodes*, Applied Physics Letters **64**, 1687 (1994)

[5] Shuji Nakamura, Masayuki Senoh, Shin ichi Nagahama, Naruhito Iwasa, Takao Yamada, Toshio Matsushita, Hiroyuki Kiyoku, Yasunobu Sugimoto, *InGaN-Based Multi-Quantum-Well-Structure Laser Diodes*, Japanese Journal of Applied Physics **35**, L74 (1996)

[6] A Hangleiter, *III-V nitrides: A new age for optoelectropics*, MRS Bulletin **28**, 350 (2003)

[7] E. Feltin, A. Castiglia, G. Cosendey, L. Sulmoni, J.-F. Carlin, N. Grandjean, M. Rossetti, J. Dorsaz, V. Laino, M. Duelk, C. Velez, *Broadband blue superluminescent light-emitting diodes based on GaN*, Applied Physics Letters **95**, 081107 (2009)

[8] Matthew T. Hardy, Kathryn M. Kelchner, You-Da Lin, Po Shan Hsu, Kenji Fujito, Hiroaki Ohta, James S. Speck, Shuji Nakamura, Steven P. DenBaars, *m-Plane GaN-Based Blue Superluminescent Diodes Fabricated Using Selective Chemical Wet Etching*, Applied Physics Express **2**, 121004 (2009)

[9] Katarzyna Holc, Łucja Marona, Robert Czernecki, MichałBoćkowski, Tadeusz Suski, Stephen Najda, Piotr Perlin, *Temperature dependence of superluminescence in InGaN-based superluminescent light emitting diode structures*, Journal of Applied Physics **108**, 013110 (2010)

[10] Tien-Chang Lu, Chih-Chiang Kao, Hao-Chung Kuo, Gen-Sheng Huang, Shing-Chung Wang, *CW lasing of current injection blue GaN-based vertical cavity surface emitting laser*, Applied Physics Letters **92**, 141102 (2008)

[11] Yu Higuchi, Kunimichi Omae, Hiroaki Matsumura, Takashi Mukai, *Room-Temperature CW Lasing of a GaN-Based Vertical-Cavity Surface-Emitting Laser by Current Injection*, Applied Physics Express **1**, 121102 (2008)

[12] Dai Ohnishi, Takayuki Okano, Masahiro Imada, Susumu Noda, *Room temperature continuous wave operation of a surface-emitting two-dimensional photonic crystal diode laser*, Opt. Express **12**, 1562 (2004)

[13] Hideki Matsubara, Susumu Yoshimoto, Hirohisa Saito, Yue Jianglin, Yoshinori Tanaka, Susumu Noda, *GaN Photonic-Crystal Surface-Emitting Laser at Blue-Violet Wavelengths*, Science **319**, 445 (2008)

[14] M. Glauser, G. Rossbach, G. Cosendey, J. Levrat, M. Cobet, J.-F. Carlin, J. Besbas, M. Gallart, P. Gilliot, R. Butté, N. Grandjean, *Investigation of InGaN/GaN quantum wells for polariton laser diodes*, physica status solidi (c) **9**, 1325 (2012)

[15] Ivan Iorsh, Marlene Glauser, Georg Rossbach, Jacques Levrat, Munise Cobet, Raphaël Butté, Nicolas Grandjean, Mikhail A. Kaliteevski, Richard A. Abram, Alexey V. Kavokin, *Generic picture of the emission properties of III-nitride polariton laser diodes: Steady state and current modulation response*, Phys. Rev. B **86**, 125308 (2012)

[16] Si-Hyun Park, Jaehoon Kim, Heonsu Jeon, Tan Sakong, Sung-Nam Lee, Suhee Chae, Y. Park, Chang-Hyun Jeong, Geun-Young Yeom, Yong-Hoon Cho, *Room-temperature GaN vertical-cavity surface-emitting laser operation in an extended cavity scheme*, Applied Physics Letters **83**, 2121 (2003)

[17] S. Christopoulos, G. Baldassarri Höger von Högersthal, A. J. D. Grundy, P. G. Lagoudakis, A. V. Kavokin, J. J. Baumberg, G. Christmann, R. Butté, E. Feltin, J.-F. Carlin, N. Grandjean, *Room-Temperature Polariton Lasing in Semiconductor Microcavities*, Phys. Rev. Lett. **98**, 126405 (2007)

[18] I. Vurgaftman, J. R. Meyer, *Band parameters for nitrogen-containing semiconductors*, Journal of Applied Physics **94**, 3675 (2003)

[19] M. E. Levinshtein, S. L. Rumyantsev, M. S. Shur, *Properties of Advanced Semiconductor Materials: GaN, AlN, InN, BN, SiC, SiGe* (Wiley-Interscience Publication, New York, 2001)

[20] Fabio Bernardini, Vincenzo Fiorentini, David Vanderbilt, *Spontaneous polarization and piezoelectric constants of III-V nitrides*, Phys. Rev. B **56**, R10024 (1997)

[21] Masashi Mizuta, Shinji Fujieda, Yoshishige Matsumoto, Tsutomu Kawamura, *Low Temperature Growth of GaN and AlN on GaAs Utilizing Metalorganics and Hydrazine*, Japanese Journal of Applied Physics **25**, L945 (1986)

[22] T. Lei, M. Fanciulli, R. J. Molnar, T. D. Moustakas, R. J. Graham, J. Scanlon, *Epitaxial growth of zinc blende and wurtzitic gallium nitride thin films on (001) silicon*, Applied Physics Letters **59**, 944 (1991)

[23] Shuji Nakamura, *The Roles of Structural Imperfections in InGaN-Based Blue Light-Emitting Diodes and Laser Diodes*, Science **281**, 956 (1998)

[24] J.S. Speck, S.J. Rosner, *The role of threading dislocations in the physical properties of GaN and its alloys*, Physica B: Condensed Matter **273–274**, 24 (1999)

[25] D. S. Li, H. Chen, H. B. Yu, H. Q. Jia, Q. Huang, J. M. Zhou, *Dependence of leakage current on dislocations in GaN-based light-emitting diodes*, Journal of Applied Physics **96**, 1111 (2004)

[26] S. C. Jain, M. Willander, J. Narayan, R. Van Overstraeten, *III–nitrides: Growth, characterization, and properties*, Journal of Applied Physics **87**, 965 (2000)

[27] D. Holec, P.M.F.J. Costa, M.J. Kappers, C.J. Humphreys, *Critical thickness calculations for InGaN/GaN*, Journal of Crystal Growth **303**, 314 (2007)

[28] David Holec, Yucheng Zhang, D. V. Sridhara Rao, Menno J. Kappers, Clifford McAleese, Colin J. Humphreys, *Equilibrium critical thickness for misfit dislocations in III-nitrides*, Journal of Applied Physics **104**, 123514 (2008)

[29] R. Butté, N. Grandjean, *Effects of Polarization in Optoelectronic Quantum Structures* in *Polarization Effects in Semiconductors* (Eds. C. Wood and D. Jena, Springer US, New York, 2008)

[30] Fabio Bernardini, Vincenzo Fiorentini, David Vanderbilt, *Accurate calculation of polarization-related quantities in semiconductors*, Phys. Rev. B **63**, 193201 (2001)

[31] J. L. Weyher, H. Ashraf, P. R. Hageman, *Reduction of dislocation density in epitaxial GaN layers by overgrowth of defect-related etch pits*, Applied Physics Letters **95**, 031913 (2009)

[32] G Nataf, B Beaumont, A Bouillé, S Haffouz, M Vaille, P Gibart, *Lateral overgrowth of high quality GaN layers on GaN/Al2O3 patterned substrates by halide vapour-phase epitaxy*, Journal of Crystal Growth **192**, 73 (1998)

[33] Kensaku Motoki, Takuji Okahisa, Seiji Nakahata, Naoki Matsumoto, Hiroya Kimura, Hitoshi Kasai, Kikurou Takemoto, Koji Uematsu, Masaki Ueno, Yoshinao Kumagai, Akinori Koukitu, Hisashi Seki, *Growth and characterization of freestanding GaN substrates*, Journal of Crystal Growth **237-239, Part 2**, 912 (2002)

[34] A. Feduniewicz, C. Skierbiszewski, M. Siekacz, Z.R. Wasilewski, I. Sproule, S. Grzanka, R. Jakieła, J. Borysiuk, G. Kamler, E. Litwin-Staszewska, R. Czernecki, M. Boćkowski, S. Porowski, *Control of Mg doping of GaN in RF-plasma molecular beam epitaxy*, Journal of Crystal Growth **278**, 443 (2005)

[35] C. Skierbiszewski, Z.R. Wasilewski, I. Grzegory, S. Porowski, *Nitride-based laser diodes by plasma-assisted MBE—From violet to green emission*, Journal of Crystal Growth **311**, 1632 (2009)

[36] E. L. Piner, M. K. Behbehani, N. A. El-Masry, F. G. McIntosh, J. C. Roberts, K. S. Boutros, S. M. Bedair, *Effect of hydrogen on the indium incorporation in InGaN epitaxial films*, Applied Physics Letters **70**, 461 (1997)

[37] H. Kim-Chauveau, P. de Mierry, J-M. Chauveau, J-Y. Duboz, *The influence of various MOCVD parameters on the growth of $Al_{1-x}In_xN$ ternary alloy on GaN templates*, Journal of Crystal Growth **316**, 30 (2011)

[38] L. Liu, J.H. Edgar, *Substrates for gallium nitride epitaxy*, Materials Science and Engineering: R: Reports **37**, 61 (2002)

[39] A. Yoshikawa, E. Ohshima, T. Fukuda, H. Tsuji, K. Oshima, *Crystal growth of GaN by ammonothermal method*, Journal of Crystal Growth **260**, 67 (2004)

[40] R. Dwilinski, R. Doradzinski, J. Garczynski, L.P. Sierzputowski, A. Puchalski, Y. Kanbara, K. Yagi, H. Minakuchi, H. Hayashi, *Excellent crystallinity of truly bulk ammonothermal GaN*, Journal of Crystal Growth **310**, 3911 (2008)

[41] Shigefusa F. Chichibu, Akira Uedono, Takeyoshi Onuma, Benjamin A. Haskell, Arpan Chakraborty, Takahiro Koyama, Paul T. Fini, Stacia Keller, Steven P. Denbaars, James S. Speck, Umesh K. Mishra, Shuji Nakamura, Shigeo Yamaguchi, Satoshi Kamiyama, Hiroshi Amano, Isamu Akasaki, Jung Han, Takayuki Sota, *Origin of defect-insensitive emission probability in In-containing (Al, In, Ga) N alloy semiconductors*, Nature Materials **5**, 810 (2006)

[42] J. Wu, W. Walukiewicz, W. Shan, K. M. Yu, J. W. Ager III, S. X. Li, E. E. Haller, Hai Lu, William J. Schaff, *Temperature dependence of the fundamental band gap of InN*, Journal of Applied Physics **94**, 4457 (2003)

[43] S. R. Lee, A. F. Wright, M. H. Crawford, G. A. Petersen, J. Han, R. M. Biefeld, *The band-gap bowing of $Al_xGa_{1-x}N$ alloys*, Applied Physics Letters **74**, 3344 (1999)

[44] J. Wu, W. Walukiewicz, K. M. Yu, J. W. Ager III, E. E. Haller, Hai Lu, William J. Schaff, *Small band gap bowing in $In_{1-x}Ga_xN$ alloys*, Applied Physics Letters **80**, 4741 (2002)

[45] Y.P. Varshni, *Temperature dependence of the energy gap in semiconductors*, Physica **34**, 149 (1967)

[46] Takahiro Kawashima, Hisashi Yoshikawa, Sadao Adachi, Shunro Fuke, Kohji Ohtsuka, *Optical properties of hexagonal GaN*, Journal of Applied Physics **82**, 3528 (1997)

[47] A. Baldanzi, E. Bellotti, M. Goano, *Optical Properties of III-Nitride Ternary Compounds*, physica status solidi (b) **228**, 425 (2001)

[48] M. J. Bergmann, Jr. H. C. Casey, *Optical-field calculations for lossy multiple-layer* $Al_xGa_{1-x}N/In_xGa_{1-x}N$ *laser diodes*, Journal of Applied Physics **84**, 1196 (1998)

[49] D. A. B. Miller, D. S. Chemla, T. C. Damen, A. C. Gossard, W. Wiegmann, T. H. Wood, C. A. Burrus, *Band-Edge Electroabsorption in Quantum Well Structures: The Quantum-Confined Stark Effect*, Phys. Rev. Lett. **53**, 2173 (1984)

[50] Tae-Young Chung, K J Chang, *Exciton binding energies in GaN/AlGaN quantum-well structures*, Semiconductor Science and Technology **13**, 876 (1998)

[51] N. Grandjean, B. Damilano, S. Dalmasso, M. Leroux, M. Laügt, J. Massies, *Built-in electric-field effects in wurtzite AlGaN/GaN quantum wells*, Journal of Applied Physics **86**, 3714 (1999)

[52] G. Bastard, *Wave Mechanics Applied to Semiconductor Heterostructures, Monographies de Physique* (les éditions de physique, Les Ulis, 1988)

[53] J. Feldmann, G. Peter, E. O. Göbel, P. Dawson, K. Moore, C. Foxon, R. J. Elliott, *Linewidth dependence of radiative exciton lifetimes in quantum wells*, Phys. Rev. Lett. **59**, 2337 (1987)

[54] Satoshi Watanabe, Norihide Yamada, Masakazu Nagashima, Yusuke Ueki, Chiharu Sasaki, Yoichi Yamada, Tsunemasa Taguchi, Kazuyuki Tadatomo, Hiroaki Okagawa, Hiromitsu Kudo, *Internal quantum efficiency of highly-efficient* $In_xGa_{1-x}N$*-based near-ultraviolet light-emitting diodes*, Applied Physics Letters **83**, 4906 (2003)

[55] Tetsuya Akasaka, Hideki Gotoh, Tadashi Saito, Toshiki Makimoto, *High luminescent efficiency of InGaN multiple quantum wells grown on InGaN underlying layers*, Applied Physics Letters **85**, 3089 (2004)

[56] G. Y. Zhang, Y. Z. Tong, Z. J. Yang, S. X. Jin, J. Li, Z. Z. Gan, *Relationship of background carrier concentration and defects in GaN grown by metalorganic vapor phase epitaxy*, Applied Physics Letters **71**, 3376 (1997)

[57] M.A di Forte-Poisson, F Huet, A Romann, M Tordjman, D Lancefield, E Pereira, J Di Persio, B Pecz, *Relationship between physical properties and gas purification in GaN grown by metalorganic vapor phase epitaxy*, Journal of Crystal Growth **195**, 314 (1998)

[58] Chris G. Van de Walle, Catherine Stampfl, J *Theory of doping and defects in III-V nitrides*, Journal of Crystal Growth **189-190**, 505 (1998)

[59] Chris G. Van de Walle, Jörg Neugebauer, *First-principles calculations for defects and impurities: Applications to III-nitrides*, Journal of Applied Physics **95**, 3851 (2004)

[60] Shuji Nakamura, Takashi Mukai, Masayuki Senoh, *Si- and Ge-Doped GaN Films Grown with GaN Buffer Layers*, Japanese Journal of Applied Physics **31**, 2883 (1992)

[61] Shuji Nakamura, Takashi Mukai, Masayuki Senoh, *Si-Doped InGaN Films Grown on GaN Films*, Japanese Journal of Applied Physics **32**, L16 (1993)

[62] C. Yuan, T. Salagaj, A. Gurary, A. G. Thompson, W. Kroll, R. A. Stall, C.-Y. Hwang, M. Schurman, Y. Li, W. E. Mayo, Y. Lu, S. Krishnankutty, I. K. Shmagin, R. M. Kolbas, S. J. Pearton, *Investigation of n- and p-type doping of GaN during epitaxial growth in a mass production scale multiwafer-rotating-disk reactor*, Journal of Vacuum Science & Technology B: Microelectronics and Nanometer Structures **13**, 2075 (1995)

[63] J. Jayapalan, B. J. Skromme, R. P. Vaudo, V. M. Phanse, *Optical spectroscopy of Si-related donor and acceptor levels in Si-doped GaN grown by hydride vapor phase epitaxy*, Applied Physics Letters **73**, 1188 (1998)

[64] D. Huang, F. Yun, M.A. Reshchikov, D. Wang, H. Morkoç, D.L. Rode, L.A. Farina, Ç. Kurdak, K.T. Tsen, S.S. Park, K.Y. Lee, *Hall mobility and carrier concentration in free-standing high quality GaN templates grown by hydride vapor phase epitaxy*, Solid-State Electronics **45**, 711 (2001)

[65] P.R. Hageman, W.J. Schaff, Jacek Janinski, Zuzanna Liliental-Weber, *n-type doping of wurtzite GaN with germanium grown with plasma-assisted molecular beam epitaxy*, Journal of Crystal Growth **267**, 123 (2004)

[66] S. Fritze, A. Dadgar, H. Witte, M. Bügler, A. Rohrbeck, J. Bläsing, A. Hoffmann, A. Krost, *High Si and Ge n-type doping of GaN doping - Limits and impact on stress*, Applied Physics Letters **100**, 122104 (2012)

[67] Isamu Akasaki, Hiroshi Amano, Masahiro Kito, Kazumasa Hiramatsu, *Photoluminescence of Mg-doped p-type GaN and electroluminescence of GaN p-n junction LED*, Journal of Luminescence **48, Part 2**, 666 (1991)

[68] W. Götz, N. M. Johnson, J. Walker, D. P. Bour, R. A. Street, *Activation of acceptors in Mg-doped GaN grown by metalorganic chemical vapor deposition*, Applied Physics Letters **68**, 667 (1996)

[69] T. Tanaka, A. Watanabe, H. Amano, Y. Kobayashi, I. Akasaki, S. Yamazaki, M. Koike, *p-type conduction in Mg-doped GaN and* $Al_{0.08}Ga_{0.92}N$ *grown by metalorganic vapor phase epitaxy*, Applied Physics Letters **65**, 593 (1994)

[70] U. Kaufmann, P. Schlotter, H. Obloh, K. Köhler, M. Maier, *Hole conductivity and compensation in epitaxial GaN:Mg layers*, Phys. Rev. B **62**, 10867 (2000)

[71] P Kozodoy, S Keller, S.P DenBaars, U.K Mishra, *MOVPE growth and characterization of Mg-doped GaN*, Journal of Crystal Growth **195**, 265 (1998)

[72] A. Kasic, M. Schubert, S. Einfeldt, D. Hommel, T. E. Tiwald, *Free-carrier and phonon properties of n - and p -type hexagonal GaN films measured by infrared ellipsometry*, Phys. Rev. B **62**, 7365 (2000)

[73] L. Allen, G.I. Peters, *Superradiance, coherence brightening and amplified spontaneous emission*, Physics Letters A **31**, 95 (1970)

[74] C.H. Willis, *Master equation for amplified spontaneous emission*, Physics Letters A **36**, 187 (1971)

[75] J. P. Gordon, H. J. Zeiger, C. H. Townes, *The Maser—New Type of Microwave Amplifier, Frequency Standard, and Spectrometer*, Phys. Rev. **99**, 1264 (1955)

[76] A. L. Schawlow, C. H. Townes, *Infrared and Optical Masers*, Phys. Rev. **112**, 1940 (1958)

[77] R. N. Hall, G. E. Fenner, J. D. Kingsley, T. J. Soltys, R. O. Carlson, *Coherent Light Emission From GaAs Junctions*, Phys. Rev. Lett. **9**, 366 (1962)

[78] R.F. Kazarino, R.A. Suris, *Possibility of amplication of electromagnetic waves in a semiconductor with a superlattice*, Soviet Physics Semiconductors-USSR **5**, 707 (1971)

[79] Jérôme Faist, Federico Capasso, Deborah L. Sivco, Carlo Sirtori, Albert L. Hutchinson, Alfred Y. Cho, *Quantum Cascade Laser*, Science **264**, 553 (1994)

[80] H. Q. Le, W. D. Goodhue, P. A. Maki, S. Di Cecca, *Diode-laser-pumped InGaAs/GaAs/AlGaAs heterostructure lasers with low internal loss and 4-W average power*, Applied Physics Letters **63**, 1465 (1993)

[81] J.V. Sandusky, S.R.J. Brueck, *A CW external-cavity surface-emitting laser*, IEEE Photonics Technology Letters **8**, 313 (1996)

[82] T.-L. Wang, B. Heinen, J. Hader, C. Dineen, M. Sparenberg, A. Weber, B. Kunert, S.W. Koch, J.V. Moloney, M. Koch, W. Stolz, *Quantum design strategy pushes high-power vertical-external-cavity surface-emitting lasers beyond 100 W*, Laser & Photonics Reviews **6**, L12 (2012)

[83] Haruhisa Soda, Ken ichi Iga, Chiyuki Kitahara, Yasuharu Suematsu, *GaInAsP/InP Surface Emitting Injection Lasers*, Japanese Journal of Applied Physics **18**, 2329 (1979)

[84] Fumio Koyama, Susumu Kinoshita, Kenichi Iga , Opto-Electronics Conference (OEC'88), Tokyo, Post-Deadline Paper, PD-4, October 1988

[85] Fumio Koyama, Susumu Kinoshita, Kenichi Iga, *Room-temperature continuous wave lasing characteristics of a GaAs vertical cavity surface-emitting laser*, Applied Physics Letters **55**, 221 (1989)

[86] M. Born, E. Wolf, *Principles of Optics* (Cambridge University Press, Cambridge, 1999)

[87] E. Rosencher, B. Vinter, *Optoelectronics* (Cambridge University Press, 2001)

[88] Maurice G. A. Bernard, Georges Duraffourg, *Laser Conditions in Semiconductors*, physica status solidi (b) **1**, 699 (1961)

[89] C. Wilmsen, H. Temkin, L. A. Corzine, *Vertical-Cavity Surface-Emitting Lasers* (Cambridge University Press, Cambridge, 1999)

[90] V. Savona, *Confined photon systems: Fundamentals and applications* in *Linear optical properties of semiconductor microcavities with embedded quantumwells* (Eds. H. Benisty *et al.*, Springer Verlag, Berlin, New York, 1999)

[91] Rainer Michalzik, Karl Joachim Ebeling, *Operating Principles of VCSELs* in *Vertical-Cavity Surface-Emitting Laser Devices* (Eds. H. Li and K. Iga, Springer, Berlin, 2002)

[92] R.T. Chen, Lei Lin, Chulchae Choi, Y.J. Liu, B. Bihari, L. Wu, S. Tang, R. Wickman, B. Picor, M.K. Hibb-Brenner, J. Bristow, Y.S. Liu, *Fully embedded board-level guided-wave optoelectronic interconnects*, Proceedings of the IEEE **88**, 780 (2000)

[93] Laurent Schares, Jeffrey A. Kash, Fuad E. Doany, Clint L. Schow, Christian Schuster, Daniel M. Kuchta, Petar K. Pepeljugoski, Jean M. Trewhella, Christian W. Baks, Richard A. John, Lei Shan, Young H. Kwark, Russell A. Budd, Punit Chiniwalla, Frank R. Libsch, Joanna Rosner, Cornelia K. Tsang, Chirag S. Patel, Jeremy D. Schaub, Roger Dangel, Folkert Horst, Bert J. Offrein, Daniel Kucharski, Drew Guckenberger, Shashikant Hegde, Harold Nyikal, Chao-Kun Lin, Ashish Tandon, Gary R. Trott, Michael Nystrom, David P. Bour, Michael R. T. Tan, David W. Dolfi, *Terabus: Terabit/second-class card-level optical interconnect technologies*, IEEE Journal of Selected Topics in Quantum Electronics **12**, 1032 (2006)

[94] Scott T. Sanders, Jian Wang, Jay B. Jeffries, Ronald K. Hanson, *Diode-Laser Absorption Sensor for Line-of-Sight Gas Temperature Distributions*, Appl. Opt. **40**, 4404 (2001)

[95] Scott Sanders, Daniel Mattison, Lin Ma, Jay Jeffries, Ronald Hanson, *Wavelength-agile diode-laser sensing strategies for monitoring gas properties in optically harsh flows: application in cesium-seeded pulse detonation*, Opt. Express **10**, 505 (2002)

[96] J. Kitching, S. Knappe, M. Vukicevic, L. Hollberg, R. Wynands, W. Weidmann, *A microwave frequency reference based on VCSEL-driven dark line resonances in Cs vapor*, IEEE Transactions on Instrumentation and Measurement **49**, 1313 (2000)

[97] J. S. Harris, T. O'sullivan, T. Sarmiento, M. M. Lee, S. Vo, *Emerging applications for vertical cavity surface emitting lasers*, Semiconductor Science and Technology **26**, 014010 (2011)

[98] K. Iga, *Surface-emitting laser-its birth and generation of new optoelectronics field*, IEEE Journal of Selected Topics in Quantum Electronics **6**, 1201 (2000)

[99] Anders Larsson, *Advances in VCSELs for Communication and Sensing*, IEEE Journal of Selected Topics in Quantum Electronics **17**, 1552 (2011)

[100] E. Soderberg, J.S. Gustavsson, P. Modh, A. Larsson, Zhenzhong Zhang, J. Berggren, M. Hammar, *High-Temperature Dynamics, High-Speed Modulation, and Transmission Experiments Using 1.3-μm InGaAs Single-Mode VCSELs*, Journal of Lightwave Technology **25**, 2791 (2007)

[101] A Ramakrishnan, G Steinle, D Supper, C Degen, G Ebbinghaus, *Electrically pumped 10 Gbit/s MOVPE-grown monolithic 1.3 mu m VCSEL with GaInNAs active region*, Electronics Letters **38**, 322 (2002)

[102] JA Lott, NN Ledentsov, VM Ustinov, NA Maleev, AE Zhukov, AR Kovsh, MV Maximov, BV Volovik, ZI Alferov, D Bimberg, *InAs-InGaAs quantum dot VCSELs on GaAs substrates emitting at 1.3 μm*, Electronics Letters **36**, 1384 (2000)

[103] Klein Johnson, Mary Hibbs-Brenner, William Hogan, Matthew Dummer, Kabir Dogubo, Garrett Berg, *Record high temperature, high output power red VCSELs*, Proceedings of SPIE **7952** (2011)

[104] Alex Mutig, Philip Moser, James A. Lott, Philip Wolf, Werner Hofmann, Nikolay N. Ledentsov, Dieter Bimberg, *High-speed 850 and 980 nm VCSELs for High-Performance Computing Applications*, Proceedings of SPIE **8308** (2011)

[105] T.C. Lu, J.Y. Tsai, J.T. Chu, Y.S. Chang, S.C. Wang, *InP/InGaAlAs distributed Bragg reflectors grown by low-pressure metal organic chemical vapor deposition*, Journal of Crystal Growth **250**, 305 (2003)

[106] Junji Kinoshita, Tomoyuki Miyamoto, Yutaka Onishi, Fumio Koyama, *Characterization of Single-Wavelength Optically Pumped GaInAsP/InP Vertical-Cavity Surface-Emitting Lasers with Dielectric Mirrors*, Japanese Journal of Applied Physics **43**, 5928 (2004)

[107] A. Syrbu, A. Mircea, A. Mereuta, A. Caliman, C.A. Berseth, G. Suruceanu, V. Iakovlev, M. Achtenhagen, A. Rudra, E. Kapon, *1.5-mW single-mode operation of wafer-fused 1550-nm VCSELs*, IEEE Photonics Technology Letters **16**, 1230 (2004)

[108] Andrei Caliman, Alexandru Mereuta, Grigore Suruceanu, Vladimir Iakovlev, Alexei Sirbu, Eli Kapon, *8 mW fundamental mode output of wafer-fused VCSELs emitting in the 1550-nm band*, Opt. Express **19**, 16996 (2011)

[109] M. Ortsiefer, G. Boehm, M. Grau, K. Windhom, E. Roenneberg, J. Rosskopf, R. Shau, O. Dier, M. C. Amann, *Electrically pumped room temperature CWVCSELs with 2.3 μm emission wavelength*, Electronics Letters **42**, 640 (2006)

[110] K. Vizbaras, M. C. Amann, *3.6 mu m GaSb-based type-I lasers with quinternary barriers, operating at room temperature*, Electronics Letters **47**, 980 (2011)

[111] Alexander Bachmann, Shamsul Arafin, Kaveh Kashani-Shirazi, *Single-mode electrically pumped GaSb-based VCSELs emitting continuous-wave at 2.4 and 2.6 μm*, New Journal of Physics **11**, 125014 (2009)

[112] J.-F. Carlin, M. Ilegems, *High-quality AlInN for high index contrast Bragg mirrors lattice matched to GaN*, Applied Physics Letters **83**, 668 (2003)

[113] Tien-Chang Lu, Tzeng-Tsong Wu, Shih-Wei Chen, Po-Min Tu, Zhen-Yu Li, Chien-Kang Chen, Cheng-Hung Chen, Hao-Chung Kuo, Shing-Chung Wang, Hsiao-Wen Zan, Chun-Yen Chang, *Characteristics of Current-Injected GaN-Based Vertical-Cavity Surface-Emitting Lasers*, IEEE Journal of Selected Topics in Quantum Electronics **17**, 1594 (2011)

[114] Casey Holder, James S. Speck, Steven P. DenBaars, Shuji Nakamura, Daniel Feezell, *Demonstration of Nonpolar GaN-Based Vertical-Cavity Surface-Emitting Lasers*, Applied Physics Express **5**, 092104 (2012)

[115] T. Onishi, O. Imafuji, K. Nagamatsu, M. Kawaguchi, K. Yamanaka, S. Takigawa, *Continuous Wave Operation of GaN Vertical Cavity Surface Emitting Lasers at Room Temperature*, IEEE Journal of Quantum Electronics **48**, 1107 (2012)

[116] Tien-Chang Lu, Shih-Wei Chen, Tzeng-Tsong Wu, Po-Min Tu, Chien-Kang Chen, Cheng-Hung Chen, Zhen-Yu Li, Hao-Chung Kuo, Shing-Chung Wang, *Continuous wave operation of current injected GaN vertical cavity surface emitting lasers at room temperature*, Applied Physics Letters **97**, 071114 (2010)

[117] Kunimichi Omae, Yu Higuchi, Kyosuke Nakagawa, Hiroaki Matsumura, Takashi Mukai, *Improvement in Lasing Characteristics of GaN-based Vertical-Cavity Surface-Emitting Lasers Fabricated Using a GaN Substrate*, Applied Physics Express **2**, 052101 (2009)

[118] Daiji Kasahara, Daisuke Morita, Takao Kosugi, Kyosuke Nakagawa, Jun Kawamata, Yu Higuchi, Hiroaki Matsumura, Takashi Mukai, *Demonstration of Blue and Green GaN-Based Vertical-Cavity Surface-Emitting Lasers by Current Injection at Room Temperature*, Applied Physics Express **4**, 072103 (2011)

[119] S. Calvez, J.E. Hastie, M. Guina, O.G. Okhotnikov, M.D. Dawson, *Semiconductor disk lasers for the generation of visible and ultraviolet radiation*, Laser & Photonics Reviews **3**, 407 (2009)

[120] G.A. Keeler, D.K. Serkland, K.M. Geib, G.M. Peake, A. Mar, *Single transverse mode operation of electrically pumped vertical-external-cavity surface-emitting lasers with micromirrors*, IEEE Photonics Technology Letters **17**, 522 (2005)

[121] P. Kreuter, B. Witzigmann, D. J. H. C. Maas, Y. Barbarin, T. Suedmeyer, U. Keller, *On the design of electrically pumped vertical-external-cavity surface-emitting lasers*, Applied Physics B - Lasers and Optics **91**, 257 (2008)

[122] G. E. Stillman, M. D. Sirkis, J. A. Rossi, M. R. Johnson, Jr. N. Holonyak, *Volume excitation of an ultrthin single-mode CdSe laser*, Applied Physics Letters **9**, 268 (1966)

[123] C.B. Roxlo, R.S. Putnam, M.M. Salour, *Optically pumped semiconductor platelet lasers*, IEEE Journal of Quantum Electronics **18**, 338 (1982)

[124] H. Q. Le, S. Di Cecca, A. Mooradian, *Scalable high-power optically pumped GaAs laser*, Applied Physics Letters **58**, 1967 (1991)

[125] M. Kuznetsov, F. Hakimi, R. Sprague, A. Mooradian, *High-power (>0.5-W CW) diode-pumped vertical-external-cavity surface-emitting semiconductor lasers with circular TEM_{00} beams*, IEEE Photonics Technology Letters **9**, 1063 (1997)

[126] M Kuznetsov, F Hakimi, R Sprague, A Mooradian, *Design and characteristics of high-power (> 0.5-W CW) diode-pumped vertical-external-cavity surface-emitting semiconductor lasers with circular TEM_{00} beams*, IEEE Journal of Selected Topics in Quantum Electronics **5**, 561 (1999)

[127] O. Okhotnikov, *Semiconductor Disk Lasers* (Wiley-VCH, Berlin, 2010)

[128] S. Giet, H.D. Sun, S. Calvez, M.D. Dawson, S. Suomalainen, A. Harkonen, M. Guina, O. Okhotnikov, M. Pessa, *Spectral narrowing and locking of a vertical-external-cavity surface-emitting laser using an intracavity volume Bragg grating*, IEEE Photonics Technology Letters **18**, 1786 (2006)

[129] S. Giet, C.-L. Lee, S. Calvez, M. D. Dawson, N. Destouches, J.-C. Pommier, O. Parriaux, *Stabilization of a semiconductor disk laser using an intra-cavity high reflectivity grating*, Opt. Express **15**, 16520 (2007)

[130] Ursula Keller, Anne C. Tropper, *Passively modelocked surface-emitting semiconductor lasers*, Physics Reports **429**, 67 (2006)

[131] D. Lorenser, D.J.H.C. Maas, H.J. Unold, A.-R. Bellancourt, B. Rudin, E. Gini, Dirk Ebling, U. Keller, *50-GHz passively mode-locked surface-emitting semiconductor laser with 100-mW average output power*, IEEE Journal of Quantum Electronics **42**, 838 (2006)

[132] J. Rautiainen, A. Härkönen, V.-M. Korpijärvi, P. Tuomisto, M. Guina, O. G. Okhotnikov, *2.7 W tunable orange-red GaInNAs semiconductor disk laser*, Opt. Express **15**, 18345 (2007)

[133] A. Garnache, A. A. Kachanov, F. Stoeckel, R. Planel, *High-sensitivity intracavity laser absorption spectroscopy with vertical-external-cavity surface-emitting semiconductor lasers*, Opt. Lett. **24**, 826 (1999)

[134] T. D. Raymond, W. J. Alford, M. H. Crawford, A. A. Allerman, *Intracavity frequency doubling of a diode-pumped external-cavity surface-emitting semiconductor laser*, Opt. Lett. **24**, 1127 (1999)

[135] Jennifer Hastie, Stephane Calvez, Martin Dawson, Tomi Leinonen, Antti Laakso, Jari Lyytikäinen, Markus Pessa, *High power CW red VECSEL with linearly polarized TEM_{00} output beam*, Opt. Express **13**, 77 (2005)

[136] H. Lindberg, A. Strassner, E. Gerster, A. Larsson, *0.8W optically pumped vertical external cavity surface emitting laser operating CW at 1550 nm*, Electronics Letters **40**, 601 (2004)

[137] Jussi Rautiainen, Jari Lyytikäinen, Alexei Sirbu, Alexandru Mereuta, Andrei Caliman, Eli Kapon, Oleg G. Okhotnikov, *2.6 W optically-pumped semiconductor disk laser operating at 1.57-μm using wafer fusion*, Opt. Express **16**, 21881 (2008)

[138] B. Rosener, N. Schulz, M. Rattunde, C. Manz, K. Kuhler, J. Wagner, *High-Power High-Brightness Operation of a 2.25-μm (AlGaIn)(AsSb)-Based Barrier-Pumped Vertical-External-Cavity Surface-Emitting Laser*, IEEE Photonics Technology Letters **20**, 502 (2008)

[139] M. Rahim, M. Arnold, F. Felder, K. Behfar, H. Zogg, *Midinfrared lead-chalcogenide vertical external cavity surface emitting laser with 5 μm wavelength*, Applied Physics Letters **91**, 151102 (2007)

[140] Si-Hyun Park, Heonsu Jeon, *Microchip-Type InGaN Vertical External-Cavity Surface-Emitting Laser*, Optical Review **13**, 20 (2006)

[141] R. Debusmann, N. Dhidah, V. Hoffmann, L. Weixelbaum, U. Brauch, T. Graf, M. Weyers, M. Kneissl, *InGaN-GaN Disk Laser for Blue-Violet Emission Wavelengths*, IEEE Photonics Technology Letters **22**, 652 (2010)

[142] Thomas Wunderer, John E. Northrup, Zhihong Yang, Mark Teepe, André Strittmatter, Noble M. Johnson, Paul Rotella, Michael Wraback, *In-well pumping of InGaN/GaN vertical-external-cavity surface-emitting lasers*, Applied Physics Letters **99**, 201109 (2011)

[143] K. E. Waldrip, J. Han, J. J. Figiel, H. Zhou, E. Makarona, A. V. Nurmikko, *Stress engineering during metalorganic chemical vapor deposition of AlGaN/GaN distributed Bragg reflectors*, Applied Physics Letters **78**, 3205 (2001)

[144] F. Natali, D. Byrne, A. Dussaigne, N. Grandjean, J. Massies, B. Damilano, *High-Al-content crack-free AlGaN/GaN Bragg mirrors grown by molecular-beam epitaxy*, Applied Physics Letters **82**, 499 (2003)

[145] H. M. Ng, T. D. Moustakas, S. N. G. Chu, *High reflectivity and broad bandwidth AlN/GaN distributed Bragg reflectors grown by molecular-beam epitaxy*, Applied Physics Letters **76**, 2818 (2000)

[146] G. S. Huang, T. C. Lu, H. H. Yao, H. C. Kuo, S. C. Wang, Chih-Wei Lin, Li Chang, *Crack-free GaN/AlN distributed Bragg reflectors incorporated with GaN/AlN superlattices grown by metalorganic chemical vapor deposition*, Applied Physics Letters **88**, 061904 (2006)

[147] J.-F. Carlin, C. Zellweger, J. Dorsaz, S. Nicolay, G. Christmann, E. Feltin, R. Butté, N. Grandjean, *Progresses in III-nitride distributed Bragg reflectors and microcavities using AlInN/GaN materials*, physica status solidi (b) **242**, 2326 (2005)

[148] D. Brunner, H. Angerer, E. Bustarret, F. Freudenberg, R. Höpler, R. Dimitrov, O. Ambacher, M. Stutzmann, *Optical constants of epitaxial AlGaN films and their temperature dependence*, Journal of Applied Physics **82**, 5090 (1997)

[149] R. Butté, E. Feltin, J. Dorsaz, G. Christmann, J.-F. Carlin, N. Grandjean, M. Ilegems, *Recent Progress in the Growth of Highly Reflective Nitride-Based Distributed Bragg Reflectors and Their Use in Microcavities*, Japanese Journal of Applied Physics **44**, 7207 (2005)

[150] E. Feltin, J.-F. Carlin, J. Dorsaz, G. Christmann, R. Butté, M. Laügt, M. Ilegems, N. Grandjean, *Crack-free highly reflective AlInN/AlGaN Bragg mirrors for UV applications*, Applied Physics Letters **88**, 051108 (2006)

[151] Gatien Cosendey, Jean-François Carlin, Nils A. K. Kaufmann, Raphaël Butté, Nicolas Grandjean, *Strain compensation in AlInN/GaN multilayers on GaN substrates: Application to the realization of defect-free Bragg reflectors*, Applied Physics Letters **98**, 181111 (2011)

[152] Gabriel Christmann, Raphaël Butté, Eric Feltin, Jean-François Carlin, Nicolas Grandjean, *Room temperature polariton lasing in a GaN/AlGaN multiple quantum well microcavity*, Applied Physics Letters **93**, 051102 (2008)

[153] E. Feltin, G. Christmann, J. Dorsaz, A. Castiglia, J.-F. Carlin, R. Butté, N. Grandjean, S. Christopoulos, G. Baldassarri Höger von Högersthal, A.J.D. Grundy, P.G. Lagoudakis, J.J. Baumberg, *Blue lasing at room temperature in an optically pumped lattice-matched AlInN/GaN VCSEL structure*, Electronics Letters **43**, 924 (2007)

[154] Gatien Cosendey, Antonino Castiglia, Georg Rossbach, Jean-François Carlin, Nicolas Grandjean, *Blue monolithic AlInN-based vertical cavity surface emitting laser diode on free-standing GaN substrate*, Applied Physics Letters **101**, 151113 (2012)

[155] X. Zeng, D. L. Boïko, G. Cosendey, M. Glauser, J.-F. Carlin, N. Grandjean, *Optically pumped long external cavity InGaN/GaN surface-emitting laser with injection seeding from a planar microcavity*, Applied Physics Letters **101**, 141120 (2012)

[156] R Butté, J-F Carlin, E Feltin, M Gonschorek, S Nicolay, G Christmann, D Simeonov, A Castiglia, J Dorsaz, H J Buehlmann, S Christopoulos, G Baldassarri Höger von Högersthal, A J D Grundy, M Mosca, C Pinquier, M A Py, F Demangeot, J Frandon, P G Lagoudakis, J J Baumberg, N Grandjean, *Current status of AlInN layers lattice-matched to GaN for photonics and electronics*, Journal of Physics D: Applied Physics **40**, 6328 (2007)

[157] E. Sakalauskas, H. Behmenburg, C. Hums, P. Schley, G. Rossbach, C. Giesen, M. Heuken, H. Kalisch, R. H. Jansen, J. Bläsing, A. Dadgar, A. Krost, R. Goldhahn, *Dielectric function and optical properties of Al-rich AlInN alloys pseudomorphically grown on GaN*, Journal of Physics D: Applied Physics **43**, 365102 (2010)

[158] A. Castiglia, E. Feltin, J. Dorsaz, G. Cosendey, J.-F. Carlin, R. Butté, N. Grandjean, *Blue laser diodes including lattice-matched $Al_{0.83}In_{0.17}N$ bottom cladding layer*, Electronics Letters **44**, 521 (2008)

[159] A. Castiglia, E. Feltin, G. Cosendey, A. Altoukhov, J.-F. Carlin, R. Butté, N. Grandjean, *$Al_{0.83}In_{0.17}N$ lattice-matched to GaN used as an optical blocking layer in GaN-based edge emitting lasers*, Applied Physics Letters **94**, 193506 (2009)

[160] A. Castiglia, J.-F. Carlin, E. Feltin, G. Cosendey, J. Dorsaz, N. Grandjean, *Emission characteristics of GaN-based blue lasers including a lattice matched $Al_{0.83}In_{0.17}N$ optical blocking layer for improved optical beam quality*, Applied Physics Letters **97**, 111104 (2010)

[161] R. Charash, H. Kim-Chauveau, J-M. Lamy, M. Akther, P. P. Maaskant, E. Frayssinet, P. de Mierry, A. D. Dräger, J-Y. Duboz, A. Hangleiter, B. Corbett, *Cleaved-facet violet laser diodes with lattice-matched $Al_{0.82}In_{0.18}N$/GaN multilayers as n-cladding*, Applied Physics Letters **98**, 201112 (2011)

[162] H. Kim-Chauveau, E. Frayssinet, B. Damilano, P. De Mierry, L. Bodiou, L. Nguyen, P. Vennéguès, J.-M. Chauveau, Y. Cordier, J.Y. Duboz, R. Charash, A. Vajpeyi, J.-M. Lamy, M. Akhter, P.P. Maaskant, B. Corbett, A. Hangleiter, A. Wieck, *Growth optimization and characterization of lattice-matched $Al_{0.82}In_{0.18}N$ optical confinement layer for edge emitting nitride laser diodes*, Journal of Crystal Growth **338**, 20 (2012)

[163] J. Kuzmik, *Power electronics on InAlN/(In)GaN: Prospect for a record performance*, IEEE Electron Device Letters **22**, 510 (2001)

[164] J. Massies, F. Turco, A. Saletes, J.P. Contour, *Experimental evidence of difference in surface and bulk compositions of $Al_xGa_{1-x}As$, $Al_xIn_{1-x}As$ and $Ga_xIn_{1-x}As$ epitaxial layers grown by molecular beam epitaxy*, Journal of Crystal Growth **80**, 307 (1987)

[165] A. Redondo-Cubero, K. Lorenz, R. Gago, N. Franco, M.-A. di Forte Poisson, E. Alves, E. Munoz, *Depth-resolved analysis of spontaneous phase separation in the growth of lattice-matched AlInN*, Journal of Physics D: Applied Physics **43**, 055406 (2010)

[166] C. Hums, J. Bläsing, A. Dadgar, A. Diez, T. Hempel, J. Christen, A. Krost, K. Lorenz, E. Alves, *Metal-organic vapor phase epitaxy and properties of AlInN in the whole compositional range*, Applied Physics Letters **90**, 022105 (2007)

[167] Roy B. Chung, Feng Wu, Ravi Shivaraman, Stacia Keller, Steven P. DenBaars, James S. Speck, Shuji Nakamura, *Growth study and impurity characterization of $Al_xIn_{1-x}N$ grown by metal organic chemical vapor deposition*, Journal of Crystal Growth **324**, 163 (2011)

[168] K. Lorenz, S. Magalhaes, N. Franco, N. P. Barradas, V. Darakchieva, E. Alves, S. Pereira, M. R. Correia, F. Munnik, R. W. Martin, K. P. O'Donnell, I. M. Watson, *$Al_{1-x}In_xN$/GaN bilayers: Structure, morphology, and optical properties*, physica status solidi (b) **247**, 1740 (2010)

[169] T. C. Sadler, M. J. Kappers, R. A. Oliver, *Investigation of optimum growth conditions of InAlN for application in distributed Bragg reflectors*, Journal of Physics: Conference Series **209**, 012015 (2010)

[170] Junki Ichikawa, Yusuke Sakai, Zhitao Chen, Kazuhisa Fujita, Takashi Egawa, *Effect of Growth Temperature on Structural Quality of InAlN Layer Lattice Matched to GaN Grown by Metal Organic Chemical Vapor Deposition*, Japanese Journal of Applied Physics **51**, 01AF07 (2012)

[171] Guangyu Liu, Jing Zhang, Xiao-Hang Li, G.S. Huang, Tanya Paskova, Keith R. Evans, Hongping Zhao, Nelson Tansu, *Metalorganic vapor phase epitaxy and characterizations of nearly-lattice-matched AlInN alloys on GaN/sapphire templates and free-standing GaN substrates*, Journal of Crystal Growth **340**, 66 (2012)

[172] Thomas Sadler, Fabien Massabuau, Menno Kappers, Rachel Oliver, *The negligible effects of miscut on indium aluminium nitride growth*, physica status solidi (c) **9**, 461 (2012)

[173] T.C. Sadler, M.J. Kappers, R.A. Oliver, *The effect of temperature and ammonia flux on the surface morphology and composition of $In_xAl_{1-x}N$ epitaxial layers*, Journal of Crystal Growth **311**, 3380 (2009)

[174] Thomas C. Sadler, Menno J. Kappers, Rachel A. Oliver, *The effects of varying metal precursor fluxes on the growth of InAlN by metal organic vapour phase epitaxy*, Journal of Crystal Growth **314**, 13 (2011)

[175] K. Lorenz, N. Franco, E. Alves, I. M. Watson, R. W. Martin, K. P. O'Donnell, *Anomalous Ion Channeling in* AlInN/GaN *Bilayers: Determination of the Strain State*, Phys. Rev. Lett. **97**, 085501 (2006)

[176] V. Darakchieva, M. Beckers, M.-Y. Xie, L. Hultman, B. Monemar, J.-F. Carlin, E. Feltin, M. Gonschorek, N. Grandjean, *Effects of strain and composition on the lattice parameters and applicability of Vegard's rule in Al-rich $Al_{1-x}In_xN$ films grown on sapphire*, Journal of Applied Physics **103**, 103513 (2008)

[177] Z. L. Miao, T. J. Yu, F. J. Xu, J. Song, L. Lu, C. C. Huang, Z. J. Yang, X. Q. Wang, G. Y. Zhang, X. P. Zhang, D. P. Yu, B. Shen, *Strain effects on $In_xAl_{1-x}N$ crystalline quality grown on GaN templates by metalorganic chemical vapor deposition*, Journal of Applied Physics **107**, 043515 (2010)

[178] K. Lorenz, N. Franco, E. Alves, S. Pereira, I.M. Watson, R.W. Martin, K.P. O'Donnell, *Relaxation of compressively strained AlInN on GaN*, Journal of Crystal Growth **310**, 4058 (2008)

[179] S. Kret, A. Wolska, M. T. Klepka, A. Letrouit, F. Ivaldi, A. Szczepańska, J.-F. Carlin, N. A. K. Kaufmann, N Grandjean, *TEM and XANES study of MOVPE grown InAIN layers with different indium content*, Journal of Physics: Conference Series **326**, 012013 (2011)

[180] Z. L. Miao, T. J. Yu, F. J. Xu, J. Song, C. C. Huang, X. Q. Wang, Z. J. Yang, G. Y. Zhang, X. P. Zhang, D. P. Yu, B. Shen, *The origin and evolution of V-defects in $In_xAl_{1-x}N$ epilayers grown by metalorganic chemical vapor deposition*, Applied Physics Letters **95**, 231909 (2009)

[181] Anas Mouti, Jean-Luc Rouvière, Marco Cantoni, Jean-Francois Carlin, Eric Feltin, Nicolas Grandjean, Pierre Stadelmann, *Stress-modulated composition in the vicinity of dislocations in nearly lattice matched $Al_xIn_{1-x}N$/GaN heterostructures: A possible explanation of defect insensitivity*, Phys. Rev. B **83**, 195309 (2011)

[182] J. Song, F. J. Xu, X. D. Yan, F. Lin, C. C. Huang, L. P. You, T. J. Yu, X. Q. Wang, B. Shen, K. Wei, X. Y. Liu, *High conductive gate leakage current channels induced by In segregation around screw- and mixed-type threading dislocations in lattice-matched $In_xAl_{1-x}N$/GaN heterostructures*, Applied Physics Letters **97**, 232106 (2010)

[183] P. Vennégués, B.S. Diaby, H. Kim-Chauveau, L. Bodiou, H.P.D. Schenk, E. Frayssinet, R.W. Martin, I.M. Watson, *Nature and origin of V-defects present in metalorganic vapor phase epitaxy-grown $In_xAl_{1-x}N$ layers as a function of InN content, layer thickness and growth parameters*, Journal of Crystal Growth **353**, 108 (2012)

[184] G. Périllat-Merceroz, G. Cosendey, J.-F. Carlin, R Butté, N. Grandjean, *Intrinsic degradation mechanism of nearly lattice-matched InAlN layers grown on GaN substrates*, submitted to J. Appl. Phys. (2012)

[185] A. Krost, C. Berger, P. Moser, J. Bläsing, A. Dadgar, C. Hums, T. Hempel, B. Bastek, P. Veit, J. Christen, *Stranski-Krastanov transition and self-organized structures in low-strained AlInN/GaN multilayer structures*, Semiconductor Science and Technology **26**, 014041 (2011)

[186] Dietrich E. Wolf, *Kinetic roughening of vicinal surfaces*, Phys. Rev. Lett. **67**, 1783 (1991)

[187] J.W. Evans, P.A. Thiel, M.C. Bartelt, *Morphological evolution during epitaxial thin film growth: Formation of 2D islands and 3D mounds*, Surface Science Reports **61**, 1 (2006)

[188] K. Muraki, S. Fukatsu, Y. Shiraki, R. Ito, *Surface segregation of In atoms during molecular beam epitaxy and its influence on the energy levels in InGaAs/GaAs quantum wells*, Applied Physics Letters **61**, 557 (1992)

[189] N. Grandjean, J. Massies, M. Leroux, *Monte Carlo simulation of In surface segregation during the growth of $In_xGa_{1-x}As$ on GaAs(001)*, Phys. Rev. B **53**, 998 (1996)

[190] J. Massies, N. Grandjean, *Surfactant effect on the surface diffusion length in epitaxial growth*, Phys. Rev. B **48**, 8502 (1993)

[191] N. Grandjean, J. Massies, V. H. Etgens, *Delayed relaxation by surfactant action in highly strained III-V semiconductor epitaxial layers*, Phys. Rev. Lett. **69**, 796 (1992)

[192] S. Nicolay, E. Feltin, J.-F. Carlin, M. Mosca, L. Nevou, M. Tchernycheva, F. H. Julien, M. Ilegems, N. Grandjean, *Indium surfactant effect on AlN/GaN heterostructures grown by metal-organic vapor-phase epitaxy: Applications to intersubband transitions*, Applied Physics Letters **88**, 151902 (2006)

[193] S. Keller, S. Heikman, I. Ben-Yaacov, L. Shen, S. P. DenBaars, U. K. Mishra, *Indium-surfactant-assisted growth of high-mobility AlN/GaN multilayer structures by metalorganic chemical vapor deposition*, Applied Physics Letters **79**, 3449 (2001)

[194] A. Gadanecz, J. Bläsing, A. Dadgar, C. Hums, A. Krost, *Thermal stability of metal organic vapor phase epitaxy grown AlInN*, Applied Physics Letters **90**, 221906 (2007)

[195] H.R. Brice, T.C. Sadler, M.J. Kappers, R.A. Oliver, *The effect of annealing on the surface morphology of strained and unstrained $In_xAl_{1-x}N$ thin films*, Journal of Crystal Growth **312**, 1800 (2010)

[196] Thomas C. Sadler, Menno J. Kappers, Rachel A. Oliver, *Optimisation of GaN overgrowth of InAlN for DBRs*, physica status solidi (c) **6**, S666 (2009)

[197] A. Imamoglu, R. J. Ram, S. Pau, Y. Yamamoto, *Nonequilibrium condensates and lasers without inversion: Exciton-polariton lasers*, Phys. Rev. A **53**, 4250 (1996)

[198] E. Feltin, D. Simeonov, J.-F. Carlin, R. Butté, N. Grandjean, *Narrow UV emission from homogeneous GaN/AlGaN quantum wells*, Applied Physics Letters **90**, 021905 (2007)

[199] Marian Zamfirescu, Alexey Kavokin, Bernard Gil, Guillaume Malpuech, Mikhail Kaliteevski, *ZnO as a material mostly adapted for the realization of room-temperature polariton lasers*, Phys. Rev. B **65**, 161205 (2002)

[200] R. Shimada, J. Xie, V. Avrutin, Ü. Özgür, H. Morkoç, *Cavity polaritons in ZnO-based hybrid microcavities*, Applied Physics Letters **92**, 011127 (2008)

[201] Yoshitaka Taniyasu, Jean-François Carlin, Antonino Castiglia, Raphaël Butté, Nicolas Grandjean, *Mg doping for p-type AlInN lattice-matched to GaN*, Applied Physics Letters **101**, 082113 (2012)

[202] Ragh Charash, Hyonju Kim-Chauveau, Agam Vajpeyi, Mahbub Akther, Pleun P. Maaskant, Eric Frayssinet, Philippe de Mierry, Jean-Yves Duboz, Brian Corbett, *Current transport through AlInN/GaN multilayers used as n-type cladding layers in edge emitting laser diodes*, physica status solidi (c) **8** (2011)

[203] G. Rossbach, J. Levrat, A. Dussaigne, G. Cosendey, M. Glauser, M. Cobet, R. Butté, N. Grandjean, H. Teisseyre, M. Bockowski, I. Grzegory, T. Suski, *Tailoring the light-matter coupling in anisotropic microcavities: Redistribution of oscillator strength in strained m-plane GaN/AlGaN quantum wells*, Phys. Rev. B **84**, 115315 (2011)

[204] H. B. Michaelson, *Relation Between an Atomic Electronegativity Scale and the Work Function*, IBM Journal of Research and Development **22**, 72 (1978)

[205] C. I. Wu, A. Kahn, N. Taskar, D. Dorman, D. Gallagher, *GaN (0001)-(1 × 1) surfaces: Composition and electronic properties*, Journal of Applied Physics **83**, 4249 (1998)

[206] B. P. Luther, S. E. Mohney, T. N. Jackson, M. Asif Khan, Q. Chen, J. W. Yang, *Investigation of the mechanism for Ohmic contact formation in Al and Ti/Al contacts to n-type GaN*, Applied Physics Letters **70**, 57 (1997)

[207] S. Ruvimov, Z. Liliental-Weber, J. Washburn, K. J. Duxstad, E. E. Haller, Z.-F. Fan, S. N. Mohammad, W. Kim, A. E. Botchkarev, H. Morkoç, *Microstructure of Ti/Al and Ti/Al/Ni/Au Ohmic contacts for n-GaN*, Applied Physics Letters **69**, 1556 (1996)

[208] Zhifang Fan, S. Noor Mohammad, Wook Kim, Özgür Aktas, Andrei E. Botchkarev, Hadis Morkoç, *Very low resistance multilayer Ohmic contact to n-GaN*, Applied Physics Letters **68**, 1672 (1996)

[209] Y. Koide, T. Maeda, T. Kawakami, S. Fujita, T. Uemura, N. Shibata, M. Murakami, *Effects of annealing in an oxygen ambient on electrical properties of ohmic contacts to p-type GaN*, Journal of Electronics Material **28**, 341 (1999)

[210] Ja-Soon Jang, Seong-Ju Park, Tae-Yeon Seong, *Formation of low resistance Pt ohmic contacts to p-type GaN using two-step surface treatment*, Journal of Vacuum Science and Technology B: Microelectronics and Nanometer Structures **17**, 2667 (1999)

[211] L. Zhou, W. Lanford, A. T. Ping, I. Adesida, J. W. Yang, A. Khan, *Low resistance Ti/Pt/Au ohmic contacts to p-type GaN*, Applied Physics Letters **76**, 3451 (2000)

[212] D. Qiao, L. S. Yu, S. S. Lau, J. Y. Lin, H. X. Jiang, T. E. Haynes, *A study of the Au/Ni ohmic contact on p-GaN*, Journal of Applied Physics **88**, 4196 (2000)

[213] J.T. Trexler, S.J. Pearton, P.H. Holloway, M.G. Mier, K.R. Evans, R.F. Karlicek, *Comparison of Ni/Au, Pd/Au, and Cr/Au metallizations for ohmic contacts to p-GaN*, Materials Research Society Symposium Proceedings **449**, 1091 (1997)

[214] H.K. Cho, T. Hossain, J.W. Bae, I. Adesida, *Characterization of Pd/Ni/Au ohmic contacts on p-GaN*, Solid-State Electronics **49**, 774 (2005)

[215] Ja-Soon Jang, In-Sik Chang, Han-Ki Kim, Tae-Yeon Seong, Seonghoon Lee, Seong-Ju Park, *Low-resistance Pt/Ni/Au ohmic contacts to p-type GaN*, Applied Physics Letters **74**, 70 (1999)

[216] E.H. Rhoderick, *Metal-semiconductor contacts*, Solid-State and Electron Devices, IEE Proceedings I **129**, 1 (1982)

[217] F.A. Padovani, R. Stratton, *Field and thermionic-field emission in Schottky barriers*, Solid-State Electronics **9**, 695 (1966)

[218] K. Bädeker, *Concerning the electricity conductibility and the thermoelectric energy of several heavy metal bonds*, Annalen der Physiks **22**, 749 (1907)

[219] J.L. Vossen, E.S. Poliniak, *The properties of very thin R.F. sputtered transparent conducting films of SnO_2:Sb and In_2O_3:Sn*, Thin Solid Films **13**, 281 (1972)

[220] J.-C. Manifacier, L. Szepessy, J.F. Bresse, M. Perotin, R. Stuck, *In_2O_3:(Sn) and SnO_2:(F) films — Application to solar energy conversion; part 1 — Preparation and characterization*, Materials Research Bulletin **14**, 109 (1979)

[221] J.-C. Manifacier, L. Szepessy, J.F. Bresse, M. Perotin, R. Stuck, *In_2O_3 : (Sn) and SnO_2 : (F) films - application to solar energy conversion part II — Electrical and optical properties*, Materials Research Bulletin **14**, 163 (1979)

[222] Georg Rupprecht, *Untersuchungen der elektrischen und lichtelektrischen Leitfähigkeit dünner Indiumoxydschichten*, Zeitschrift für Physik A Hadrons and Nuclei **139**, 504 (1954)

[223] Tadatsugu Minami, Hidehito Nanto, Shinzo Takata, *Highly Conductive and Transparent Aluminum Doped Zinc Oxide Thin Films Prepared by RF Magnetron Sputtering*, Japanese Journal of Applied Physics **23**, L280 (1984)

[224] Y.M. Li, A. Van Schepdael, E. Roets, J. Hoogmartens, *Optimized methods for capillary electrophoresis of tetracyclines*, Journal of Pharmaceutical and Biomedical Analysis **15**, 1063 (1997)

[225] Tadatsugu Minami, *Transparent conducting oxide semiconductors for transparent electrodes*, Semiconductor Science and Technology **20**, S35 (2005)

[226] X. Wu, T. J. Coutts, W. P. Mulligan, *Properties of transparent conducting oxides formed from CdO and ZnO alloyed with SnO_2 and In_2O_3*, The 43rd national symposium of the American Vacuum Society **15**, 1057 (1997)

[227] T. J. Coutts, D. L. Young, X. Li, W. P. Mulligan, X. Wu, *Search for improved transparent conducting oxides: A fundamental investigation of CdO, Cd_2SnO_4, and Zn_2SnO_4*, Journal of Vacuum Science & Technology A: Vacuum, Surfaces, and Films **18**, 2646 (2000)

[228] Antonino Gulino, Francesco Castelli, Paolo Dapporto, Patrizia Rossi, Ignazio Fragalà, *Synthesis and Characterization of Thin Films of Cadmium Oxide*, Chemistry of Materials **14**, 704 (2002)

[229] Taro Hitosugi, Yutaka Furubayashi, Atsuki Ueda, Kinnosuke Itabashi, Kazuhisa Inaba, Yasushi Hirose, Go Kinoda, Yukio Yamamoto, Toshihiro Shimada, Tetsuya Hasegawa, *Ta-doped Anatase TiO_2 Epitaxial Film as Transparent Conducting Oxide*, Japanese Journal of Applied Physics **44**, L1063 (2005)

[230] Yutaka Furubayashi, Taro Hitosugi, Yukio Yamamoto, Kazuhisa Inaba, Go Kinoda, Yasushi Hirose, Toshihiro Shimada, Tetsuya Hasegawa, *A transparent metal: Nb-doped anatase TiO_2*, Applied Physics Letters **86**, 252101 (2005)

[231] Meng-Chi Li, Chien-Cheng Kuo, Ssu-Hsiang Peng, Sheng-Hui Chen, Cheng-Chung Lee, *Preparation of Low Resistivity Transparent Conductive Nb-Doped TiO_2 Films by the Co-sputtering Method*, Japanese Journal of Applied Physics **51**, 025504 (2012)

[232] Tadatsugu Minami, *Transparent and conductive multicomponent oxide films prepared by magnetron sputtering*, Papers from the 45th National Symposium of the American Vacuum Society **17**, 1765 (1999)

[233] Chunyan Song, Hong Chen, Yi Fan, Jinsong Luo, Xiaoyang Guo, Xingyuan Liu, *High-Work-Function Transparent Conductive Oxides with Multilayer Films*, Applied Physics Express **5**, 041102 (2012)

[234] Yongsheng Zhang, Ke Yu, Desheng Jiang, Ziqiang Zhu, Haoran Geng, Laiqiang Luo, *Zinc oxide nanorod and nanowire for humidity sensor*, Applied Surface Science **242**, 212 (2005)

[235] H. Sato, T. Minami, S. Takata, T. Yamada, *Transparent conducting p-type NiO thin films prepared by magnetron sputtering*, Thin Solid Films **236**, 27 (1993)

[236] H. Kawazoe, M. Yasukawa, H. Hyodo, M. Kurita, H. Yanagi, H. Hosono, *P-type electrical conduction in transparent thin films of* $CuAlO_2$, Nature **389**, 939 (1997)

[237] J. Tate, M.K. Jayaraj, A.D. Draeseke, T. Ulbrich, A.W. Sleight, K.A. Vanaja, R. Nagarajan, J.F. Wager, R.L. Hoffman, *p-Type oxides for use in transparent diodes*, Thin Solid Films **411**, 119 (2002)

[238] K.L. Chopra, S. Major, D.K. Pandya, *Transparent conductors—A status review*, Thin Solid Films **102**, 1 (1983)

[239] A. Dawar, J. Joshi, *Semiconducting transparent thin films: their properties and applications*, Journal of Materials Science **19**, 1 (1984)

[240] Radhouane Bel Hadj Tahar, Takayuki Ban, Yutaka Ohya, Yasutaka Takahashi, *Tin doped indium oxide thin films: Electrical properties*, Journal of Applied Physics **83**, 2631 (1998)

[241] B. Stjerna, C. G. Granqvist, *Optical properties of* SnO_x *thin films: Theory and experiment*, Applied Physics Letters **57**, 1989 (1990)

[242] C. G. Granqvist, *Transparent conductive electrodes for electrochromic devices: A review*, Applied Physics A: Materials Science & Processing **57**, 19 (1993)

[243] Keiichi Furukawa, Yoshihisa Terasaka, Hideaki Ueda, Michio Matsumura, *Effect of a plasma treatment of ITO on the performance of organic electroluminescent devices*, Synthetic Metals **91**, 99 (1997)

[244] Z.H. Huang, X.T. Zeng, X.Y. Sun, E.T. Kang, Jerry Y.H. Fuh, L. Lu, *Influence of plasma treatment of ITO surface on the growth and properties of hole transport layer and the device performance of OLEDs*, Organic Electronics **9**, 51 (2008)

[245] Hamid Reza Fallah, Mohsen Ghasemi, Ali Hassanzadeh, Hadi Steki, *The effect of annealing on structural, electrical and optical properties of nanostructured ITO films prepared by e-beam evaporation*, Materials Research Bulletin **42**, 487 (2007)

[246] L. Kerkache, A. Layadi, E. Dogheche, D. Rémiens, *Physical properties of RF sputtered ITO thin films and annealing effect*, Journal of Physics D: Applied Physics **39**, 184 (2006)

[247] Kwang Ho Lee, Ho Won Jang, Ki-Beom Kim, Yoon-Heung Tak, Jong-Lam Lee, *Mechanism for the increase of indium-tin-oxide work function by O_2 inductively coupled plasma treatment*, Journal of Applied Physics **95**, 586 (2004)

[248] Kiyoshi Sugiyama, Hisao Ishii, Yukio Ouchi, Kazuhiko Seki, *Dependence of indium–tin–oxide work function on surface cleaning method as studied by ultraviolet and x-ray photoemission spectroscopies,* Journal of Applied Physics **87**, 295 (2000)

[249] M. G. Mason, L. S. Hung, C. W. Tang, S. T. Lee, K. W. Wong, M. Wang, *Characterization of treated indium–tin–oxide surfaces used in electroluminescent devices,* Journal of Applied Physics **86**, 1688 (1999)

[250] Y. Park, V. Choong, Y. Gao, B. R. Hsieh, C. W. Tang, *Work function of indium tin oxide transparent conductor measured by photoelectron spectroscopy*, Applied Physics Letters **68**, 2699 (1996)

[251] X. Jiang, F. L. Wong, M. K. Fung, S. T. Lee, *Aluminum-doped zinc oxide films as transparent conductive electrode for organic light-emitting devices*, Applied Physics Letters **83**, 1875 (2003)

[252] T.W. Kim, D.C. Choo, Y.S. No, W.K. Choi, E.H. Choi, *High work function of Al-doped zinc-oxide thin films as transparent conductive anodes in organic light-emitting devices*, Applied Surface Science **253**, 1917 (2006)

[253] A. Klein, C. Karber, A. Wachau, F. Sauberlich, Y. Gassenbauer, R. Schafranek, S.P. Harvey, T.O. Mason, *Surface potentials of magnetron sputtered transparent conducting oxides*, Thin Solid Films **518**, 1197 (2009)

[254] T. Margalith, O. Buchinsky, D. A. Cohen, A. C. Abare, M. Hansen, S. P. DenBaars, L. A. Coldren, *Indium tin oxide contacts to gallium nitride optoelectronic devices,* Applied Physics Letters **74**, 3930 (1999)

[255] Ray-Hua Horng, Dong-Sing Wuu, Yi-Chung Lien, Wen-How Lan, *Low-resistance and high-transparency Ni/indium tin oxide ohmic contacts to p-type GaN*, Applied Physics Letters **79**, 2925 (2001)

[256] Jae-Hong Lim, Dae-Kue Hwang, Hyun-Sik Kim, Jin-Yong Oh, Jin-Ho Yang, R. Navamathavan, Seong-Ju Park, *Low-resistivity and transparent indium-oxide-doped ZnO ohmic contact to p-type GaN*, Applied Physics Letters **85**, 6191 (2004)

[257] June O Song, Kyoung-Kook Kim, Seong-Ju Park, Tae-Yeon Seong, *Highly low resistance and transparent Ni/ZnO ohmic contacts to p-type GaN*, Applied Physics Letters **83**, 479 (2003)

[258] S.J. Chang, C.S. Chang, Y.K. Su, R.W. Chuang, Y.C. Lin, S.C. Shei, H.M. Lo, H.Y. Lin, J.C. Ke, *Highly reliable nitride-based LEDs with SPS+ITO upper contacts*, IEEE Journal of Quantum Electronics **39**, 1439 (2003)

[259] R. H. Horng, C. C. Yang, J. Y. Wu, S. H. Huang, C. E. Lee, D. S. Wuu, *GaN-based light-emitting diodes with indium tin oxide texturing window layers using natural lithography*, Applied Physics Letters **86**, 221101 (2005)

[260] Shyi-Ming Pan, Ru-Chin Tu, Yu-Mei Fan, R.-C. Yeh, Jung-Tsung Hsu, *Improvement of InGaN-GaN light-emitting diodes with surface-textured indium-tin-oxide transparent ohmic contacts*, IEEE Photonics Technology Letters **15**, 649 (2003)

[261] A. Y. Polyakov, N. B. Smirnov, A. V. Govorkov, K. H. Baik, S. J. Pearton, B. Luo, F. Ren, J. M. Zavada, *Hydrogen plasma passivation effects on properties of p-GaN*, Journal of Applied Physics **94**, 3960 (2003)

[262] X. A. Cao, S. J. Pearton, A. P. Zhang, G. T. Dang, F. Ren, R. J. Shul, L. Zhang, R. Hickman, J. M. Van Hove, *Electrical effects of plasma damage in p-GaN*, Applied Physics Letters **75**, 2569 (1999)

[263] X.A. Cao, A.P. Zhang, G.T. Dang, F. Ren, S.J. Pearton, J.M. Hove, R.A. Hickman, R.J. Shul, L. Zhang, *Plasma damage in p-GaN*, Journal of Electronic Materials **29**, 256 (2000)

[264] Martin F. Schubert, J.-Q. Xi, Jong Kyu Kim, E. Fred Schubert, *Distributed Bragg reflector consisting of high- and low-refractive-index thin film layers made of the same material*, Applied Physics Letters **90**, 141115 (2007)

[265] Cheng-Chung Lee, Meng-Chi Li, Sheng-Hui Chen, Chien-Cheng Kuo, *Transparent Conductive Distributed Bragg Reflectors Composed of High and Low Refractive Index Transparent Conductive Films*, Japanese Journal of Applied Physics **51**, 052602 (2012)

[266] A. Castiglia, D. Simeonov, H. J. Buehlmann, J.-F. Carlin, E. Feltin, J. Dorsaz, R. Butté, N. Grandjean, *Efficient current injection scheme for nitride vertical cavity surface emitting lasers*, Applied Physics Letters **90**, 033514 (2007)

[267] Raphaël Butté, Gabriel Christmann, Eric Feltin, Antonino Castiglia, Jacques Levrat, Gatien Cosendey, Alexei Altoukhov, Jean-François Carlin, Nicolas Grandjean, *Room temperature polariton lasing in III-nitride microcavities, a comparison with blue GaN-based vertical cavity surface emitting lasers*, Proceedings of SPIE **7216** (2009)

[268] D.S. Kuo, K.T. Lam, K.H. Wen, S.J. Chang, T.K. Ko, S.J. Hon, *GaN-based LEDs with Ar plasma treatment*, Materials Science in Semiconductor Processing **15**, 52 (2012)

[269] Young-Bae Lee, Ryohei Takaki, Hisao Sato, Yoshiki Naoi, Shiro Sakai, *High efficiency GaN-based LEDs using plasma selective treatment of p-GaN surface*, physica status solidi (a) **200**, 87 (2003)

[270] Bo-Siao Cheng, Yun-Lin Wu, Tien-Chang Lu, Ching-Hsueh Chiu, Cheng-Hung Chen, Po-Min Tu, Hao-Chung Kuo, Shing-Chung Wang, Chun-Yen Chang, *High Q microcavity light emitting diodes with buried AlN current apertures*, Applied Physics Letters **99**, 041101 (2011)

[271] Gunnar Björk, Henrich Heitmann, Yoshihisa Yamamoto, *Spontaneous-emission coupling factor and mode characteristics of planar dielectric microcavity lasers*, Phys. Rev. A **47**, 4451 (1993)

[272] Christian Lauer, Markus-Christian Amann, *Calculation of the linewidth broadening in vertical-cavity surface-emitting lasers due to temperature fluctuations*, Applied Physics Letters **86**, 191108 (2005)

[273] Y. J. Wang, S. J. Xu, Q. Li, D. G. Zhao, H. Yang, *Band gap renormalization and carrier localization effects in InGaN/GaN quantum-wells light emitting diodes with Si doped barriers*, Applied Physics Letters **88**, 041903 (2006)

[274] Takehiko Nagai, Takeshi J. Inagaki, Yoshihiko Kanemitsu, *Band-gap renormalization in highly excited GaN*, Applied Physics Letters **84**, 1284 (2004)

[275] E. Kuokstis, J. W. Yang, G. Simin, M. Asif Khan, R. Gaska, M. S. Shur, *Two mechanisms of blueshift of edge emission in InGaN-based epilayers and multiple quantum wells*, Applied Physics Letters **80**, 977 (2002)

[276] K.D. Choquette, H.Q. Hou, *Vertical-cavity surface emitting lasers: moving from research to manufacturing*, Proceedings of the IEEE **85**, 1730 (1997)

[277] A. E. Siegman, *Lasers* (University Science Books, Sausalito, CA, 1986)

[278] Å. Haglund (Private communication, 2012)

[279] L. A. Coldren, S. W. Corzine, *Diode Lasers and Photonic Integrated Circuits* (Wiley-Interscience Publication, New York, 1995)

[280] W. G. Scheibenzuber, U. T. Schwarz, L. Sulmoni, J. Dorsaz, J.-F. Carlin, N. Grandjean, *Recombination coefficients of GaN-based laser diodes*, Journal of Applied Physics **109**, 093106 (2011)

[281] Basil W. Hakki, Thomas L. Paoli, *cw degradation at 300 K of GaAs double-heterostructure junction lasers. II. Electronic gain*, Journal of Applied Physics **44**, 4113 (1973)

[282] S. I. Tsintzos, N. T. Pelekanos, G. Konstantinidis, Z. Hatzopoulos, P. G. Savvidis, *A GaAs polariton light-emitting diode operating near room temperature*, Nature **453**, 372 (2008)

[283] S. I. Tsintzos, P. G. Savvidis, G. Deligeorgis, Z. Hatzopoulos, N. T. Pelekanos, *Room temperature GaAs exciton-polariton light emitting diode*, Applied Physics Letters **94**, 071109 (2009)

[284] M Saba, C Ciuti, J Bloch, V Thierry-Mieg, R Andre, LS Dang, S Kundermann, A Mura, G Bongiovanni, JL Staehli, B Deveaud, *High-temperature ultrafast polariton parametric amplification in semiconductor microcavities*, Nature **414**, 731 (2001)

[285] Luiz Cláudio de Carvalho, André Schleife, Jürgen Furthmüller, Friedhelm Bechstedt, *Distribution of cations in wurtzitic* $In_xGa_{1-x}N$ *and* $In_xAl_{1-x}N$ *alloys: Consequences for energetics and quasiparticle electronic structures*, Phys. Rev. B **85**, 115121 (2012)

[286] Ig-Hyeon Kim, Hyeong-Soo Park, Yong-Jo Park, Taeil Kim, *Formation of V-shaped pits in InGaN/GaN multiquantum wells and bulk InGaN films*, Applied Physics Letters **73**, 1634 (1998)

[287] N. A. El-Masry, E. L. Piner, S. X. Liu, S. M. Bedair, *Phase separation in InGaN grown by metalorganic chemical vapor deposition*, Applied Physics Letters **72**, 40 (1998)

[288] Hisao Sato, Tomoya Sugahara, Yoshiki Naoi, Shiro Sakai, *Compositional Inhomogeneity of InGaN Grown on Sapphire and Bulk GaN Substrates by Metalorganic Chemical Vapor Deposition*, Japanese Journal of Applied Physics **37**, 2013 (1998)

[289] X. H. Wu, C. R. Elsass, A. Abare, M. Mack, S. Keller, P. M. Petroff, S. P. DenBaars, J. S. Speck, S. J. Rosner, *Structural origin of V-defects and correlation with localized excitonic centers in InGaN/GaN multiple quantum wells*, Applied Physics Letters **72**, 692 (1998)

[290] H. K. Cho, J. Y. Lee, G. M. Yang, C. S. Kim, *Formation mechanism of V defects in the InGaN/GaN multiple quantum wells grown on GaN layers with low threading dislocation density*, Applied Physics Letters **79**, 215 (2001)

[291] Martin Rost, Pavel Šmilauer, Joachim Krug, *Unstable epitaxy on vicinal surfaces*, Surface Science **369**, 393 (1996)

[292] Masha Vladimirova, Alberto Pimpinelli, Arnaud Videcoq, *A new model of morphological instabilities during epitaxial growth: from step bunching to mounds formation*, Journal of Crystal Growth **220**, 631 (2000)

[293] F. Nita, A. Pimpinelli, *When Smoothening Makes It Rough: Unhindered Step-Edge Diffusion and the Meandering Instability on Metal Surfaces*, Phys. Rev. Lett. **95**, 106104 (2005)

[294] N. Grandjean, E. Feltin, R. Butté, J.-F. Carlin, S. Sonderegger, B. Deveaud, J.-D. Ganière, *Growth mode induced carrier localization in InGaN/GaN quantum wells*, Philosophical Magazine **87**, 2067 (2007)

[295] A. Hangleiter, F. Hitzel, C. Netzel, D. Fuhrmann, U. Rossow, G. Ade, P. Hinze, *Suppression of Nonradiative Recombination by V-Shaped Pits in* GaInN/GaN *Quantum Wells Produces a Large Increase in the Light Emission Efficiency*, Phys. Rev. Lett. **95**, 127402 (2005)

Gatien Cosendey – Physicist Engineer

Personal information
Born in Lausanne (VD) on
March 23rd 1985
Nationality: Swiss
Marital status: Single

Contact information
E-mail gatien.cosendey@gmail.com
Work: +41 (0) 21693 54 29
Mobile: +41 (0) 79 789 53 63
Home: +41 (0) 21 921 57 33

Private address
Av. de Corsier 2
CH-1800 Vevey (VD)
Switzerland

Current work address
Institute of Condensed Matter Physics
Station 6, EPFL
CH-1015 Lausanne, Switzerland

Work experience and research activity

May 2008 – present (PhD thesis)

École Polytechnique Fédérale de Lausanne (EPFL), Switzerland
Laboratory of Advanced Semiconductors for Photonics and Electronics (LASPE, Prof. N. Grandjean)

- Experimental research in the field of GaN-based optoelectronic devices.
- Skills and expertise: microfabrication in cleanroom environment, crystal growth, material and device characterization.
- Supervision of three master students and one lab trainee.
- Physics course teaching assistant and head teaching assistant to Prof. N. Grandjean from September 2007 to June 2010 and from September 2010 to June 2012, respectively.

September 2007 – February 2008 (Master thesis)

LASPE (Prof. N. Grandjean), EPFL, Switzerland

- Development of GaN-based blue laser diodes and superluminescent light emitting diodes.

September 2006 – July 2007 (Master internship, one day per week)

Laboratory of Nanostructures at Surfaces (LNS, Prof. H. Brune), EPFL, Switzerland

- Study of self-organization and magnetism properties of metallic nanostructures.

August 2006 – September 2006 (Full-time internship)

Harvard University, Cambridge, MA 02138, USA
Prof. E. Mazur Group, Division of Engineering and Applied Sciences

- Experimental research in the field of femtosecond laser microfabrication.

Personal profile and skills

Current research interest: GaN-based optoelectronic devices (LEDs, laser diodes, VCSELs, VECSELs, SLEDs).

Experimental skills: semiconductor epitaxy (MOCVD) and characterization (XRD, C-V profiler, AFM, SEM, photoluminescence). Device processing (microfabrication techniques in cleanroom environment) and characterization (electroluminescence, I-V characteristics).

Software skills: Office suite, LaTeX, Adobe CS3 suite, Autodesk Inventor (CAD), Mathematica, LabView, Origin.

Languages: French (mother tongue), English (fluent), German (basics).

Other experiences

Technical director, Vevey Natation Riviera, Vevey, Switzerland, January 2012 – December 2012

Group leader and instructor, Protection and Support Service (Protection Civile), ORPC Riviera, Switzerland, March 2011 – present

Completed the Venture Challenge course with a grade of 5/6, February – May 2010

Physics exam appraiser, Gymnase de Burier, La Tour-de-Peilz (VD), Switzerland, June 2009 and June 2012

Swim team captain, Vevey Natation Riviera, Vevey, Switzerland, January 2004 – July 2007

Selected as member of the Swiss delegation to the 34th International Physics Olympiad in Taipei, Taiwan, August 2 – 11, 2003

Education

May 2008 – January 2013

PhD in Photonics – EPFL, Switzerland

September 2006 – February 2008

Master of Science in Physics – EPFL, Switzerland

September 2003 – July 2006

Bachelor of Science in Physics – EPFL, Switzerland

September 2000 – July 2003

High school diploma (Maturité Fédérale), Gymnase de Burier, La Tour-de-Peilz (VD), Switzerland. Special awards: Sport and Studies, Physics.

Presentations

Invited oral presentations

G. Cosendey, A. Castiglia, J.-F. Carlin, R. Butté, and N. Grandjean, *InAlN-based blue VCSELs*, Photonics Day 2012, EPFL, Lausanne, Switzerland, November 30 2012

G. Cosendey, A. Castiglia, J.-F. Carlin, R. Butté, and N. Grandjean, *Overcoming limiting factors in blue VCSELs technology*, 39th International Symposium on Compound Semiconductors (ISCS), UCSB, Santa Barbara, USA, August 27-30 2012

G. Cosendey, A. Castiglia, A. Ducanchez, J.-F. Carlin, and N. Grandjean, *III-Nitride Based Optoelectronic Devices*, MicroNanoFabrication Annual Review Meeting, EPFL, Lausanne, Switzerland, May 18 2010

Contributed oral presentations

G. Cosendey, A. Castiglia, J.-F. Carlin, R. Butté, and N. Grandjean, *A monolithic approach towards electrically-driven blue Vertical Cavity Surface Emitting Lasers on free-standing GaN substrates*, 31st International Conference on the Physics of Semiconductors (ICPS), ETHZ, Zürich, Switzerland, July 29- August 3 2012

G. Cosendey, A. Castiglia, J.-F. Carlin, N. A. K. Kaufmann, R. Butté, and N. Grandjean, *A monolithic approach towards electrically-driven blue vertical cavity surface emitting lasers on free-standing GaN substrates*, European Semiconductor Laser Workshop (ESLW11), EPFL, Lausanne, Switzerland, September 23-24 2011

G. Cosendey, A. Castiglia, A. Ducanchez, J.-F. Carlin, and N. Grandjean, *Optimization of lattice-matched AlInN/GaN DBRs on free-standing GaN for VCSEL applications*, IWN2010, Tampa, USA, September 20-24 2010

G. Cosendey, A. Castiglia, A. Ducanchez, J.-F. Carlin, and N. Grandjean, *Lattice-matched AlInN/GaN DBRs grown on free-standing GaN substrates for VCSEL applications*, E-MRS Fall Meeting, Warsaw, Poland, September 13-17 2010

G. Cosendey, E. Feltin, A. Castiglia, L. Sulmoni, J.-F. Carlin, and N. Grandjean, *GaN-based blue lasers*, III Workshop on Physics and Technology of Semiconductors Lasers, Poland, October 4-7 2009

G. Cosendey, E. Feltin, A. Castiglia, J.-F. Carlin, A. Altoukhov, J. Levrat, G. Christmann, R. Butté, and N. Grandjean, *Towards room temperature electrically pumped blue vertical cavity surface emitting lasers*, CLEO/IQEQ 2009, Baltimore, USA, June 1-5 2009

Seminars

G. Cosendey, A. Castiglia, G. Périllat-Merceroz, J.-F. Carlin, R. Butté, and N. Grandjean, Towards nitride-based blue VCSELs, LASPE internal seminar, Les Diablerets, Switzerland, March 8-9 2012

G. Cosendey, *Émission spontanée : La diode électroluminescente*, IPEQ internal seminar, Lausanne, Switzerland, February 4-5 2010

G. Cosendey, *Émission spontanée amplifiée : La diode superluminescente*, IPEQ internal seminar, Lausanne, Switzerland, February 4-5 2010

Posters

G. Cosendey, M. Glauser, A. Castiglia, J.-F. Carlin, N. A. K. Kaufmann, R. Butté, and N. Grandjean, *Nitride-based V(E)CSELs*, Photonics Day 2011, EPFL, Lausanne, Switzerland, November 4 2011

G. Cosendey, A. Ducanchez, A. Castiglia, J.-F. Carlin, N. A. K. Kaufmann, R. Butté, and N. Grandjean, *On the Development of Nitride-based Vertical Cavity Surface Emitting Lasers on Free-standing GaN Substrates*, 9th International Conference on Nitride Semiconductors (ICNS-9), Glasgow, United Kingdom, July 10-15 2011

G. Cosendey, A. Castiglia, A. Ducanchez, J.-F. Carlin, and N. Grandjean, *Defect-free AlInN-based distributed Bragg reflectors*, Photonics Day 2010, EPFL, Lausanne, Switzerland, November 5 2010

G. Cosendey, E. Feltin, A. Castiglia, L. Sulmoni, A. Altoukhov, J.-F. Carlin, R. Butté, and N. Grandjean, *Nitride-based advanced light-emitting devices*, Photonics Day 2009, EPFL, Lausanne, Switzerland, November 6 2009

G. Cosendey, A. Castiglia, E. Feltin, A. Altoukhov, J.-F. Carlin, R. Butté, and N. Grandjean, *Improved optical confinement in blue laser diodes based on an* $Al_{0.83}In_{0.17}N$ *bottom cladding*, International Nano-Optoelectronics Workshop (iNOW 2009), Stockholm, Sweden and Berlin, Germany, August 2-15 2009

G. Cosendey, E. Feltin, A. Castiglia, A. Altoukhov, J.-F. Carlin, R. Butté, and N. Grandjean, *Nitride-based advanced light-emitting devices*, NCCR Quantum Photonics General Assembly 2009, Muenchenwiler, Switzerland, July 8-9 2009

G. Cosendey, A. Castiglia, E. Feltin, J. Dorsaz, J.-F. Carlin, R. Butté, and N. Grandjean, *GaN-based laser diodes including a lattice-matched* $Al_{0.83}In_{0.17}N$ *bottom cladding layer*, Photonics Day 2008, EPFL, Lausanne, Switzerland, October 17 2008

Book chapter

R. Butté, G. Cosendey, L. Lugani, M. Glauser, A. Castiglia, G. Perillat-Merceroz, J.-F. Carlin, and N. Grandjean, *Properties of InAlN layers nearly lattice-matched to GaN and their use for photonics and electronics*, in *III-nitride semiconductors and their modern devices*, edited by Bernard Gil, to be published by Oxford University Press (2012)

Publications as major contributor

G. Périllat-Merceroz, G. Cosendey, J.-F. Carlin, R. Butté, and N. Grandjean, *Intrinsic degradation mechanism of nearly lattice-matched InAlN layers grown on GaN substrates*, accepted for publication in J. Appl. Phys. (2013)

X. Zeng, D. L. Boïko, G. Cosendey, M. Glauser, J.-F. Carlin, and N. Grandjean, *In-depth analysis of injection-seeded long external cavity InGaN/GaN surface-emitting laser*, J. Appl. Phys. **113**, 043108 (2013)

G. Cosendey, A. Castiglia, G. Rossbach, J.-F. Carlin, and N. Grandjean, *Blue monolithic AlInN-based vertical cavity surface emitting laser diode on free-standing GaN substrate*, Appl. Phys. Lett. **101**, 151113 (2012)

X. Zeng, D. L. Boïko, G. Cosendey, M. Glauser, J.-F. Carlin, and N. Grandjean, *Optically pumped long external cavity InGaN/GaN surface-emitting laser with injection seeding from a planar microcavity*, Appl. Phys. Lett. **101**, 141120 (2012)

G. Cosendey, J.-F. Carlin, N. A. K. Kaufmann, R. Butté, and N. Grandjean, *Strain compensation in AlInN/GaN multilayers on GaN substrates: Application to the realization of defect-free Bragg reflectors*, Appl. Phys. Lett. **98**, 181111 (2011)

R. Butté, G. Christmann, E. Feltin, A. Castiglia, J. Levrat, G. Cosendey, A. Altoukhov, J.-F. Carlin, and N. Grandjean, *Room temperature polariton lasing in III-nitride microcavities: a comparison with blue GaN-based vertical cavity surface emitting lasers*, Proc. SPIE, **7216**, 721619 (2009)

Other publications

E. Hashemi, J. Gustavsson, J. Bengtsson, M. Stattin, A. Larsson, G. Cosendey, N. Grandjean, and Å. Haglund, *Engineering the Transverse Optical Guiding in Gallium Nitride (GaN)-based Vertical-Cavity Surface-Emitting Laser (VCSEL) Cavities to Reach the Lowest Threshold Gain*, submitted to Jpn. J. Appl. Phys. (2012)

J. Levrat, G. Rossbach, A. Dussaigne, G. Cosendey, M. Glauser, M. Cobet, R. Butté, and N. Grandjean, *Nonlinear emission properties of an optically anisotropic GaN-based microcavity*, Phys. Rev. B **86**, 165324 (2012)

M. Glauser, G. Rossbach, G. Cosendey, J. Levrat, M. Cobet, J.-F. Carlin, J. Besbas, M. Gallart, P. Gillot, R. Butté, and N. Grandjean, *Investigation of InGaN/GaN quantum wells for polariton laser diodes*, physica status solidi (c) **9**, 1325 (2012)

G. Rossbach, J. Levrat, A. Dussaigne, G. Cosendey, M. Glauser, M. Cobet, R. Butté, N. Grandjean, H. Teisseyre, M. Bockowski, I. Grzegory, and T. Suski, *Tailoring the light-matter coupling in anisotropic microcavities: Redistribution of oscillator strength in strained m-plane GaN/AlGaN quantum wells*, Phys. Rev. B **84**, 115315 (2011)

A. Castiglia, J.-F. Carlin, E. Feltin, G. Cosendey, J. Dorsaz, and N. Grandjean, *Emission characteristics of GaN-based blue lasers including a lattice matched $Al_{0.83}In_{0.17}N$ optical blocking layer for improved optical beam quality*, Appl. Phys. Lett. **97**, 111104 (2010)

J. Dorsaz, A. Castiglia, G. Cosendey, E. Feltin, M. Rossetti, M. Duelk, C. Velez, J.-F. Carlin, and N. Grandjean, *AlGaN-Free Blue III-Nitride Laser Diodes Grown on c-Plane GaN Substrates*, Appl. Phys. Express **3**, 092102 (2010)

M. Rossetti, J. Dorsaz, R. Rezzonico, M. Duelk, C. Velez, E. Feltin, A. Castiglia, G. Cosendey, J.-F. Carlin, and N. Grandjean, *High Power Blue-Violet Superluminescent Light Emitting Diodes with InGaN Quantum Wells*, Appl. Phys. Express **3**, 061002 (2010)

E. Feltin, A. Castiglia, G. Cosendey, L. Sulmoni, J.-F. Carlin, N. Grandjean, M. Rossetti, J. Dorsaz, V. Laino, M. Duelk, and C. Velez, *Broadband blue superluminescent light-emitting diodes based on GaN*, Appl. Phys. Lett. **95**, 081107 (2009)

A. Castiglia, E. Feltin, G. Cosendey, A. Altoukhov, J.-F. Carlin, R. Butté, and N. Grandjean, *$Al_{0.83}In_{0.17}N$ lattice-matched to GaN used as an optical blocking layer in GaN-based edge emitting lasers*, Appl. Phys. Lett. **94**, 193506 (2009)

D.S. Correa, P. Tayalia, G. Cosendey, D.S. dos Santos, R.F. Aroca, E. Mazur, and C.R. Mendonca, *Two-Photon Polymerization for Fabricating Structures Containing the Biopolymer Chitosan*, J. Nanosci. Nanotechnol. **9**, 5845 (2009)

A. Castiglia, E. Feltin, J. Dorsaz, G. Cosendey, J.-F. Carlin, R. Butte, and N. Grandjean, *Blue laser diodes including lattice-matched $Al_{0.83}In_{0.17}N$ bottom cladding layer*, Electron. Lett., **44**, 521 (2008)

C.R. Mendonca, S. Orlando, G. Cosendey, M. Winkler, and E. Mazur, *Femtosecond laser micromachining in the conjugated polymer MEH–PPV*, Appl. Surf. Sci **254**, 1135 (2007)